NATIONAL ACADEMY OF SCIENCES OF UKRAINE

SPACE RESEARCH IN UKRAINE 2018–2020

Report to COSPAR

The Report Prepared by the Space Research Institute of NAS of Ukraine and SSA of Ukraine

Scientific Editor O. FEDOROV

KYIV • AKADEMPERIODYKA • 2021

UDK 001.891(15)"2018/2020"
S78

SRI NASU-SSAU
Space Research Institute
of National Academy of Sciences of Ukraine
and State Space Agency of Ukraine
Ukraine
03680, Kyiv 187
40, Glushkov Ave., bilding 4/1
http://www.ikd.kiev.ua

NASU
National Academy of Sciences of Ukraine
Ukraine
01601, Kyiv 30
54, Volodymyrska St.
http://www.nas.gov.ua

The publication was funded within the framework of the Targeted Complex Program of the NAS of Ukraine «Scientific Bases of Functioning and Providing for Conditions for the Development of the Scientific and Publishing Complex of the NAS of Ukraine»

The edition is funded within the framework of the Nationwide Target Research and Engineering Space Program of Ukraine

Space research in Ukraine. 2018–2020 / Ed. O. Fedorov. — Kyiv:
S78 Akademperiodyka, 2021. — 142 p.

ISBN 978-966-360-425-1

Report to COSPAR summarizes the results of space research performed during the years 2018—2020. This edition presents the current state of Ukrainian space science in the following areas: Space Astronomy and Astrophysics, Earth observation and Near-Earth Space Research, Life Sciences, Space Technologies and Materials Sciences. A number of papers are dedicated to the creation of scientific instruments for perspective space missions. Considerable attention paid to applied research of space monitoring of the Earth. The collection can be useful for a wide range of readers, interested in space research.

UDK 001.891(15)"2018/2020"

ISBN 978-966-360-425-1

CONTENTS

FOREWORD

The publication represents the results of space research and developments, performed by leading Ukrainian scientific teams in the years 2018–2020. Unfortunately, during this period, Ukrainian scientists were not supported by the National Space Programme, which was not developed and adopted by the Parliament. Therefore, this edition includes the works supported by the National Academy of Sciences and international grants in the following areas: Space Astronomy and Astrophysics, Near Earth Space Research, Space Biology, Earth Observation from Space, Space Technologies and Materials Science (according to the classification of COSPAR).

Section "Space Astronomy and Astrophysics" represents the review of the Institute of Radio Astronomy on synchronous coordinated ground-based support of space missions using Ukrainian radio telescopes UTR-2.

The second section includes the results of studying the processes in the Earth's atmosphere — ionosphere — magnetosphere system. The articles of Space Research Institute specialists are devoted to the mechanisms of seismic-ionospheric coupling and creation of operational service for local geomagnetic forecast. Researchers of the Institute of Technical Mechanics present the modeling of complicated interactions of a spacecraft with Earth ionosphere. The new concept of the particle microbursts satellite experiment advanced by the team of scientists including experts of the Institute of Radio Astronomy. Three articles reviews the different aspects of the interactions of Geospace environment with natural and man-made objects.

The next series of review articles represents the Ukrainian science centers activity in the Space Biology, Space Observation of the Earth and Space Technologies. Most of them dedicated to perspective space missions and utilization of space data for assessment the sustainable development goals.

In general, the presented review illustrates the current state and multidimensionality of the subjects of Ukrainian space science. Some of the results were obtained in the framework of international projects, programs and grants, including the European program Horizon 2020, and most of the results had been reported at the annual Ukrainian Conference on Space Research, international seminars and conferences.

The collection is intended for space scientists, post-graduate students and readers interested in space research.

GROUND-BASED SUPPORT OF SPACE MISSIONS BY UKRAINIAN RADIO TELESCOPES

A. Konovalenko[1], N. Kalinichenko[1, 7], V. Zakharenko[1], O. Ulyanov[1], V. Dorovskyy[1], V. Melnik[1], A. Stanislavsky[1], P. Zarka[2], B. Cecconi[2], H. Rucker[3], V. Krupar[4], I. Bubnov[1], S. Yerin[1], P. Tokarsky[1], M. Sidorchuk[1], S. Stepkin[1], L. Lytvinenko[1], Ya. Yatskiv[5], Yu. Shkuratov[6], N. Kuhai[7, 1], N. Shevchuk[1], A. Brazhenko[8], V. Koshovyy[9], O. Ivantyshin[9], O. Lytvinenko[1], A. Romanchuk[1], A. Shevtsova[1], I. Kravtsov[1], V. Kharlanova[1]

[1] Institute of Radio Astronomy of NAS of Ukraine
[2] LESIA, Observatoire de Paris, Meudon, France
[3] Commission for Astronomy of Austrian Academy of Sciences, Austria
[4] Goddard Planetary Heliophysics Institute, Washington D.C. Metro Area,USA
[5] Main Astronomical Observatory of NAS of Ukraine
[6] V.N. Karazin Kharkiv National University, Institute of Astronomy
[7] Oleksandr Dovzhenko Hlukhiv National pedagogical university
[8] Poltava gravimetrical observatory of Institute of geophysics of NAS of Ukraine
[9] Karpenko Physiko-Mechanical Institute of NAS of Ukraine

Introduction

At present a number of space missions (Parker, Juno, STEREO, SOHO, Wind and others) intensively investigates the Sun, solar wind and solar system planets. Among other, these spacecrafts are equipped with receivers of space radio emission. In case of space craft, there is a possibility to observe space radio emission at frequencies which are less than ionospheric cutoff (less than 10 MHz). Unfortunately, spacecraft equipment usually provides relatively low sensitivity, frequency and time resolution due to the small size of the onboard antennas and design features. At the same time, mentioned above parameters of ground-based radio telescopes are several orders of magnitude higher than onboard radio astronomical systems. Furthermore, there is an overlap between the frequency bands of space (1 to 20 MHz) and ground based (8 to 80 MHz) instruments. The large effective antenna area of ground-based radio telescopes, which reaches several hundred thousand square meters, also compensates for the difference in distances between objects studied by spacecraft and ground-based radio telescopes. Thus, synchronous coordinated ground-based support of space missions is reasonable and useful. This article presents the results of such support made by Ukrainian radio telescopes UTR-2 (Fig. 1), URAN-1, 2, 3, 4, GURT (Fig. 1), RT-32 [1].

Ground-based support of solar space missions

On 12 August 2018 the spacecraft Parker Solar Probe (PSP) was launched. The spacecraft performs NASA mission on remote and in-situ investigation of the solar corona at close vicinity from the Sun in order to improve the quality and reliability of forecast of critical space-weather events affecting the Earth. The mission general aim is to make considerable contribution to the current understanding of coronal plasma heating, solar wind acceleration and Coronal Mass Ejections (CME) onset. Elliptical orbit with periodical close approaches to the Sun called perihelia has been chosen. In total 26 perihelia ranging from 35.6 solar radii in the beginning to 10 solar radii in the end of the mission have been planned. Some starting orbits are shown in Fig. 2.

The advantage of the PSP spacecraft is the possibility of *in-situ* determination of the plasma temperature and density, magnetic and electric fields, energies and directions of energetic particles, local plasma waves etc. at distances up to 10 solar radii from the Sun. At the same time there is a critical drawback. Due to weight and power consumption restrictions the onboard radio telescope operating in frequency band 10 kHz — 19.2 MHz has low sensitivity and time and frequency resolutions. From this point of view observational support by the ground-based radio telescopes seems useful [2, 3]. By now 5 PSP perihelia were covered by the ground-based observations using Ukrainian radio telescopes UTR-2, URAN-2 and GURT (Table 1). All perihelia except the second and the fifth ones were characterized by extremely low activity.

One of the most energetic manifestations of solar activity is Coronal Mass Ejections (CME), which usually occur during intense solar flares. On 6 September, 2017 the extremely intense flare of class X9.3 occurred.

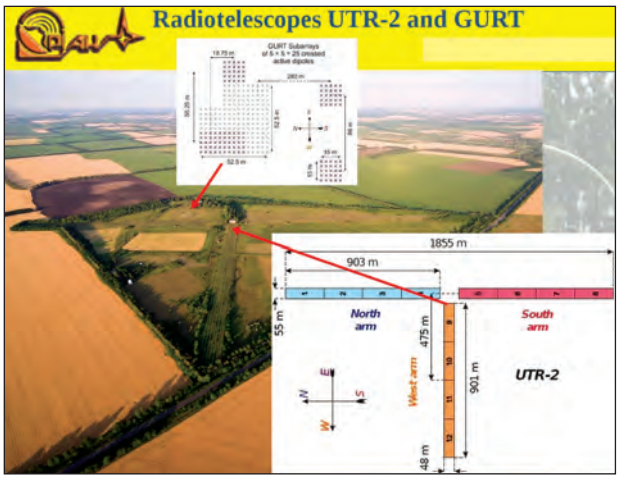

Fig. 1. Radiotelescopes UTR-2 and GURT

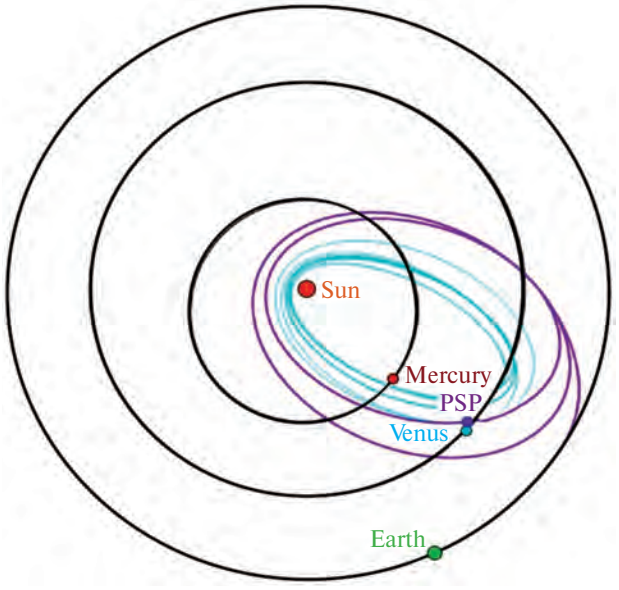

Fig. 2. Orbits of the Parker Solar Probe (PSP) and its location on 9 July 2020

Table 1

The list of Parker Solar Probe Perihelia supported by Ukrainian radio telescopes

Perihelion		Distance from the Sun		Ukrainian radio telescopes supported corresponding session
N	Date	In Gm	In Rs	
1	November, 5, 2018	24.8	35.6	URAN-2
2	April, 4, 2019[2]	24.8	35.6	URAN-2, GURT
3	September, 1,2019[1]	24.8	35.6	UTR-2, URAN-2, GURT
4	January, 29, 2020	19.4	27.9	UTR-2, URAN-2, GURT
5	June, 7, 2020	19.4	27.9	UTR-2, URAN-2, GURT

This flare initiated fast and massive CME. Its velocity exceeded 1000 km/s and mass was about 10^{16}g. The CME in its turn was a source of solar Type IV burst which was observed by radio telescopes URAN-2 (Ukraine), NDA (France) and by the radiometer onboard STEREO/A spacecraft (Fig. 3).

The flux of this burst lasted for more than two hours exceeded 1000 s.f.u. in the decameter band (1 solar flux unit equals 10^4 Jy). It was preceded by the group of type III and type II bursts. The former were generated by the sub-relativistic electron beams while the latter were associated with the intense spherical shock wave propagated with velocity of about 1000 km/s. According to the data obtained from radio telescopes URAN-2, NDA, STEREO/A-SWAVES a number of the CME parameters were retrieved. The plasma density inside the CME at distances of 9.8 Rs reached about $2.7 \cdot 10^6$ cm^{-3}, what was several times of magnitude higher than the coronal plasma density at such distances. The magnetic field required for holding the CME plasma appeared to be higher than 10^{-2} G. Taking into account high speed of the CME with dense and hot (up to 1MK) plasma in its core one may expect that the spacecraft will be affected by high gas kinetic pressure and CME wind pressure. Such environment can affect the functionality of the PSP vehicle.

Parker Solar Probe is equipped with set of devices performing in-situ measurements of different plasma parameters such as density, temperature, magnetic and electric fields etc. One of the important instruments is radiometer, which records solar radio emission at frequencies below 19 MHz. Since its frequency band overlaps with the working frequency band of effective ground-based low-frequency radio telescopes then it enables not only to superimpose the data from adjacent frequency bands but also to perform cross-calibration of the onboard PSP radiometer using calibrated data of UTR-2 and URAN-2 radio telescopes in common frequency band.

During the perihelion 2 (Table 1) the Parker Solar Probe observed a number of type III bursts. One of them is shown in Fig. 4.

One of the important results of this paper was defining of the dependence of the type III durations on frequency in wide frequency range from 10 kHz up to 10 MHz. It was shown that the durations of the type III bursts at 10 MHz slightly exceeded 10 s. We have identified some of the type III bursts observed by PSP in the data obtained from radio telescopes URAN-2 and GURT in much wider frequency band 8—70 MHz (see Fig. 4, *a*, *b*) and found good agreement between space-borne and ground-based data in common frequency band. Such long durations correspond to the second harmonic emission of the type III bursts. Thus, we concluded that all observed by PSP Type III

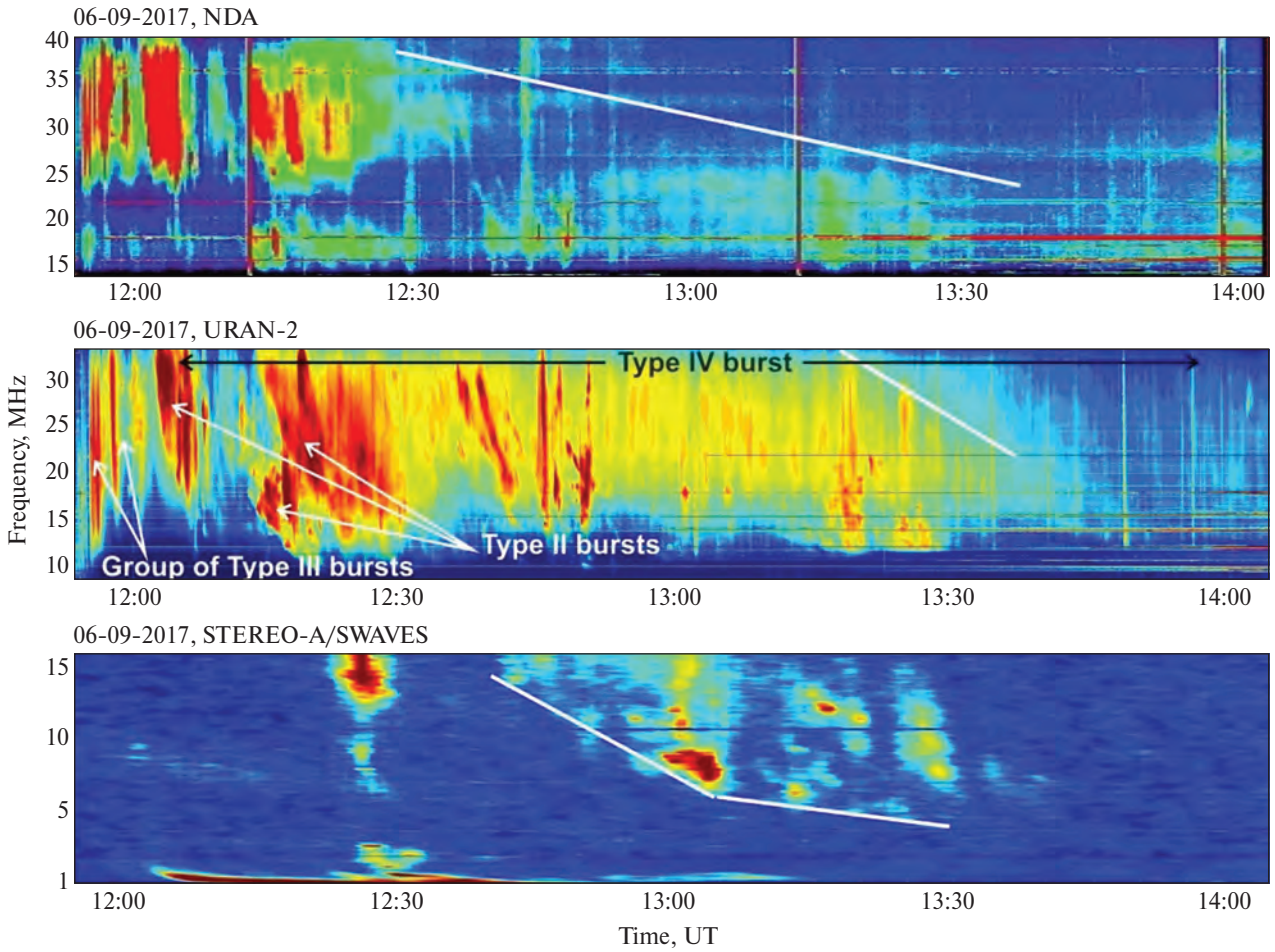

Fig. 3. The dynamic spectra of Type IV burst, Type III bursts groups and Type II burst according to NDA, URAN-2 and STEREO A

bursts were generated exclusively at second harmonic. This result is important itself, because until recently it was commonly excepted that interplanetary type III bursts (at frequencies below 1 MHz) could be generated either at fundamental or at the harmonic of the local plasma frequency.

Detection of interplanetary coronal mass ejections by synchronized observations with the radio telescopes UTR-2, URAN-2 and space missions

Coronal mass ejection is a giant eruption of 10^{11}—10^{13} kg of magnetized plasma from solar corona that propagates outward into interplanetary space disturbing the ambient solar wind. Solar wind structure that is the interplanetary counterpart of CME is generally referred to as interplanetary coronal mass ejection (ICME). ICMEs frequently cause geomagnetic storms, so the knowledge on dynamics of ICMEs is important, particularly from the viewpoint of the space weather. However, dynamics of ICMEs is little understood, because, in particular, ICME observations depend on a limited number of spacecraft. It is known that slow ICMEs accelerate and fast ICMEs decelerate as a result of interaction with the ambient solar wind and magnetic field. The radial evolution of the ICME propagation speed takes place between the solar corona and 2—4 AU (astronomical units). The deceleration of ICME speed does not also follow a simple radial law over the mentioned above distance range in the inner heliosphere. Thus, the more points on the speed vs distance dependence we have, the better prediction of ICMEs parameters (arrival time and speed) can be made.

We have proposed a technique for detecting and tracking ICMEs, which is based on the synchronized observations of the interplanetary scintillations (IPS) with ground-based radio telescopes and in *sity* measurements on board of spacecraft [4]. Fig. 5 and Fig. 6 show two cases of ICME detection made by using IPS data (radio source 3C144) of years 2011 and 2013 correspondingly. Here are the variations of scintillation index (Fig. 5, *a*; Fig. 6, *a*) and power spectrum (Fig. 5, *b*, Fig. 6, *b*) obtained by IPS method, as well as changes of proton density (Fig. 5, *c*, Fig. 6, *c*) and solar wind velocity (Fig. 5, *d*, Fig. 6, *d*) measured on the Earth's orbit by space craft "Wind". "Wind" data is extracted from NASA/GSFC's OMNI

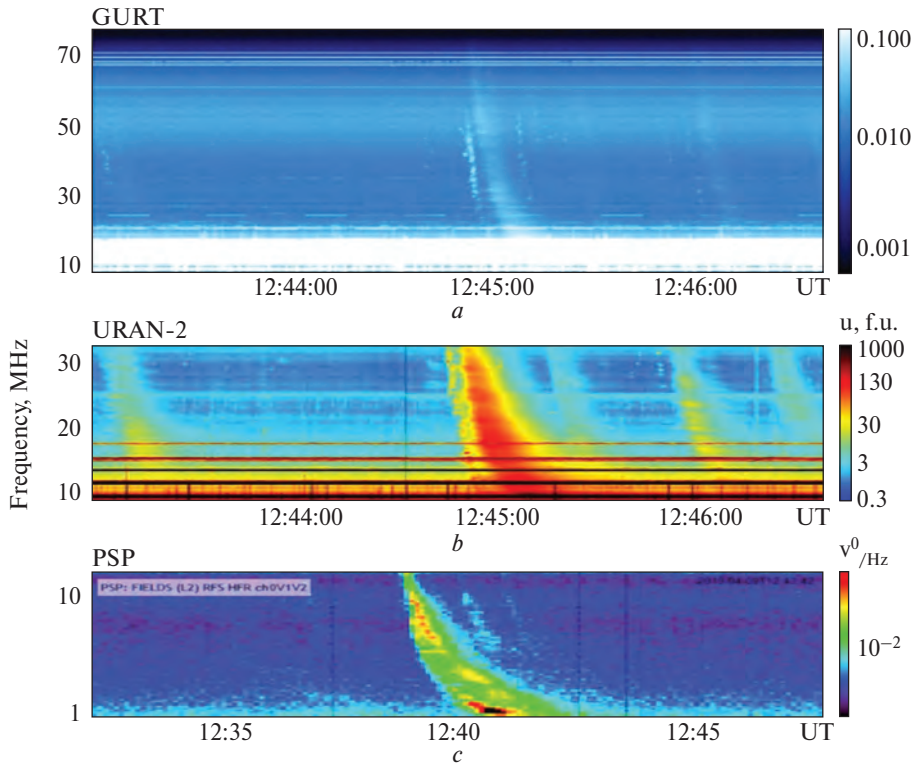

Fig. 4. Dynamic spectra of Type IIIb and Type III bursts at 12:45 UT on 9 April 2019 observed by GURT (*a*), URAN-2 (*b*) and PSP (*c*)

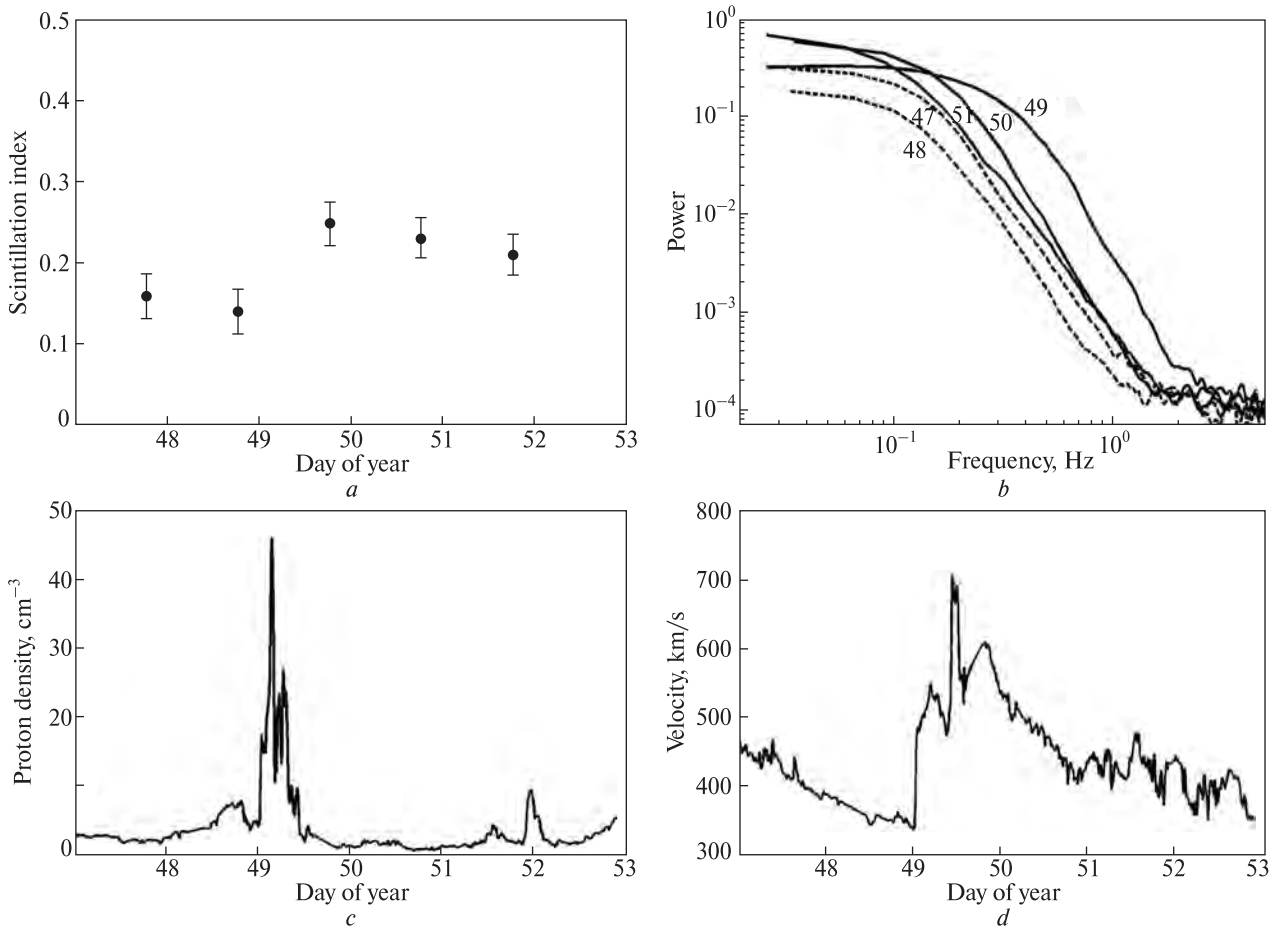

Fig. 5. IPS parameters (scintillation index (*a*) and power spectrum, (*b*)) and solar wind parameters (proton density (*c*) and solar wind velocity (*d*))

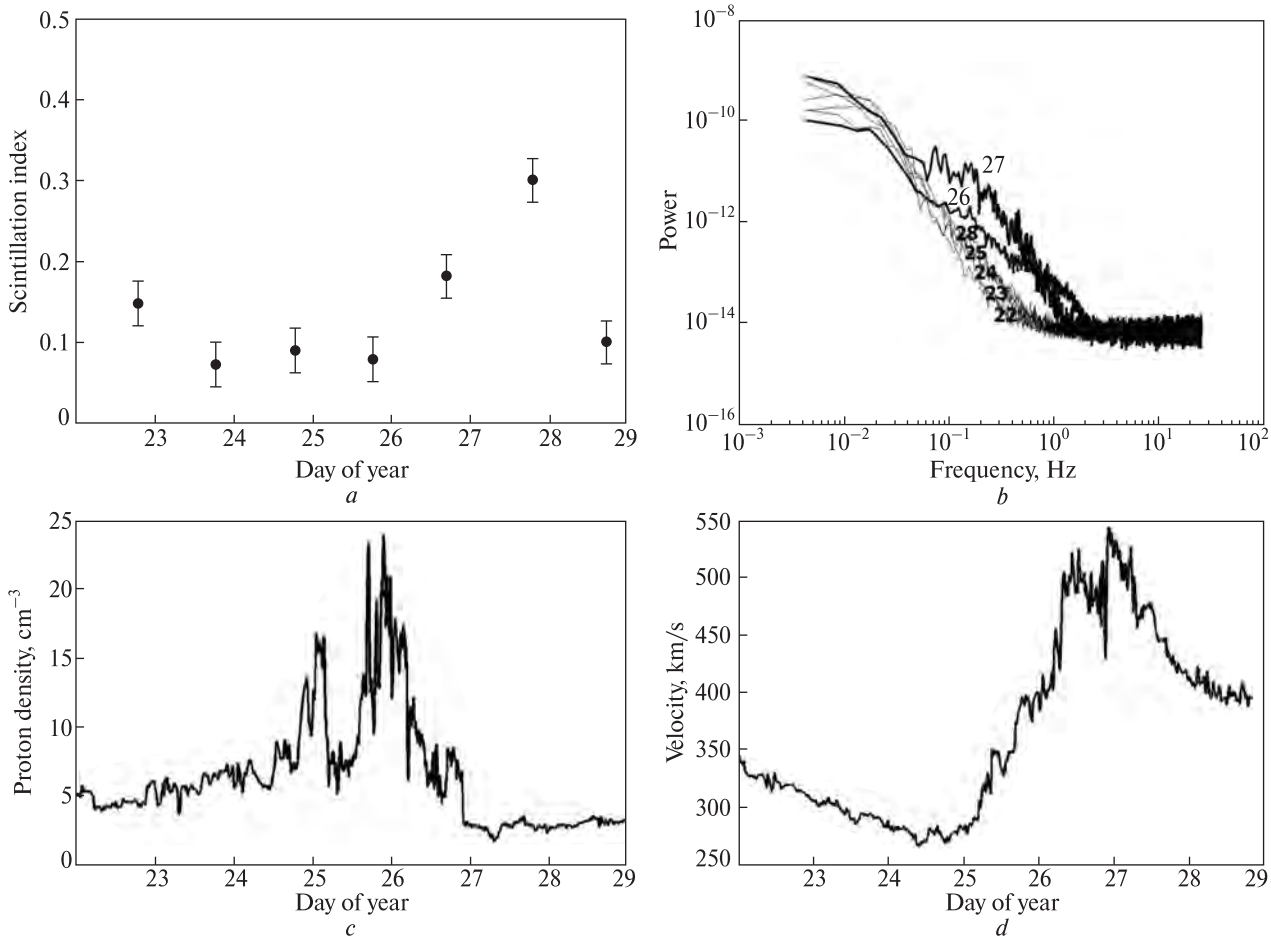

Fig. 6. The scintillation index (*a*) and power spectrum (*b*) obtained by IPS method and proton density (*c*) and solar wind velocity (*d*) measured on the Earth's orbit by the spacecraft "Wind"

data set through OMNIWeb page (https://omniweb.gsfc.nasa.gov). It is clearly seen that the scintillation index and the width of power spectrum are highly correlated with the proton density and the solar wind velocity correspondingly. The abrupt increase of the scintillation index on day 49 (Fig. 5, *a*) and day 27 (Fig. 6, *a*) is connected with the appearance of ICME on the lines of sight to the observed radio source (3C144). The width of the power spectrum (Fig. 5, *b*, Fig. 6, *b*) during the period of the observations is mainly determined by the changes of the solar wind velocity (Fig. 5, *d*, Fig. 6, *d*).

Ground-based support of Juno mission

Since 2016, the spacecraft Juno has been operating in the orbit of Jupiter. Juno mission is designed for 36 revolutions around Jupiter with revolution period ~53.5 days: from July 2016 to the end of 2021. Ukrainian low-frequency radio telescopes (primarily UTR-2) conduct constant observations together with the Juno spacecraft as part of ground support missions.

From the beginning of 2018 to the summer of 2020, observation sessions were held during the closest approach of Juno to the planet (perijove — PJ): from PJ11 to PJ28 (Table 2).

The observations at the radio telescope UTR-2 are carried out in two modes: a) correlation mode of signals of North-South and East-West antennas of UTR-2 with two receivers [5]: beam ON – direction to Jupiter, beam OFF — 1° away from Jupiter, b) waveform mode (WF): only one receiver, beam ON. In addition, starting from June 2019, observations of radio emission from Jupiter, which are controlled by the satellites Io and Ganymede, are being carried out. These studies are conducted in conjunction with the newly built NenuFAR telescope (Nancay, France). Observation data from the UTR-2, URAN and GURT telescopes are stored on a server in Japan (Future University, Hakodate).

Below are some observations from ground support for the Juno mission. As a rule, PJ do not coincide with the maxima of the storms of S-bursts, controlled by satellites Io and Ganymede. However, the sensitivity of UTR-2 allows the detection of low-intensity radiation of various types of bursts. The data of the Juno mission's ground support radio telescopes will be compared with

the data of the spacecraft in order to search for new features or types of radio emission from Jupiter.

Fig. 7 shows a data file after pre-processing in one observation session. The red ellipse marks the characteristic emission Io-A S-bursts.

In Fig. 8. S-bursts are shown in more detail. Some of them have complex modulation. Modulation parameters change very quickly when changing from one band to another, with center frequencies of approximately 24 and 28 MHz.

Development and testing of a low-frequency antenna prototype for the lunar far-side radio telescope

In recent years, there has been a renewed interest in returning to the Moon for both scientific and exploratory reasons. On the one hand, the Moon provides the perfect training ground for building large-scale bases that can be extremely useful for the future exploration of other planets like Mars. On the other hand, the existence of a radio quiet zone on the lunar far side would allow us to observe very low frequency emission from many various cosmic objects not available for ground-based observations due to ionospheric cut-off. So, it is assumed that the lunar observatory will include an antenna for receiving cosmic radio emission. Radio astronomy institute of NAS of Ukraine has a unique experience in the creation of large low frequency antennas and antenna elements for them. We have created a radio astronomy antenna for lunar observatory [6, 7] using, in particular, experience accumulated during the creation of the antenna element for the radio telescope GURT. As in the case of the radio telescope GURT, the antenna

Table 2

Observations with UTR-2 and GURT telescopes as part of ground support for the Juno

PJ	Date	Observation time (UT)	Mode	Telescopes
11	07.02.2018, 08.02.2018	1:00–7:00 (3:30–7:00 WF) 0:00–7:38 (6:30–7:38 WF)	ON,OFF,WF ON,OFF,WF	UTR-2 GURT
12	31.03.2018, 01.04.2018	6:30–7:38 2:30–4:00 (WF)	ON,OFF ON,OFF,WF	UTR-2 GURT
13	23.05.2018 24.05.2018	16:26–0:20 16:22–18:22	ON,OFF	UTR-2 GURT
14	15.07.2018 16.07.2018	16:00–20:38 12:42–17:00	ON,OFF	UTR-2 GURT
15	06.09.2018 07.09.2018	12:30–17:30 09:30–14:30	ON,OFF	UTR-2 GURT
16	29.10.2018 30.10.2018	06:40–14:40 06:38–14:38	ON,OFF	UTR-2 GURT
17	21.12.2018 22.12.2018	04:00–12:00 04:00–12:00	ON,OFF	UTR-2 GURT
18	12.02.2019 13.02.2019	01:20–09:20 01:16–09:16	ON,OFF	UTR-2 GURT
19	06.04.2019 07.04.2019	22:10–06:10 (5:20–6:10 WF) 22:06–06:06	ON,OFF,WF ON,OFF	UTR-2 GURT
20	29.05.2019 30.05.2019	18:18–02:30 18:22–02:34	ON,OFF	UTR-2
21	20.07.2019 21.07.2019	14:30–22:38 (14:30–16:00 WF) 14:34–22:42	ON,OFF,WF ON,OFF	UTR-2
22	11.09.2019 12.09.2019	11:30–19:00 11:04–19:08 (11:30–13:00 WF)	ON,OFF,WF	UTR-2
23	03.11.2019 04.11.2019	08:20–16:10 08:12–16:06 (8:30–13:30WF)	ON,OFF ON,OFF,WF	UTR-2
24	26.12.2019 27.12.2019	05:50–13:20 05:46–13:16	ON,OFF	UTR-2
25	17.02.2020 18.02.2020	02:56–11:02 03:00–11:06	ON,OFF	UTR-2
26	10.04.2020 11.04.2020	23:48–08:16 (1:40–3:40 WF) 23:52–08:20 (2:20–5:00 WF)	ON,OFF,WF ON,OFF,WF	UTR-2
27	01.06.2020 02.06.2020	23:02–04:52 20:28–04:48	ON,OFF	UTR-2
28	25.07.2020 26.07.2020	16:42–00:50 16:38–00:46 (21:16–00:46 WF)	ON,OFF	UTR-2

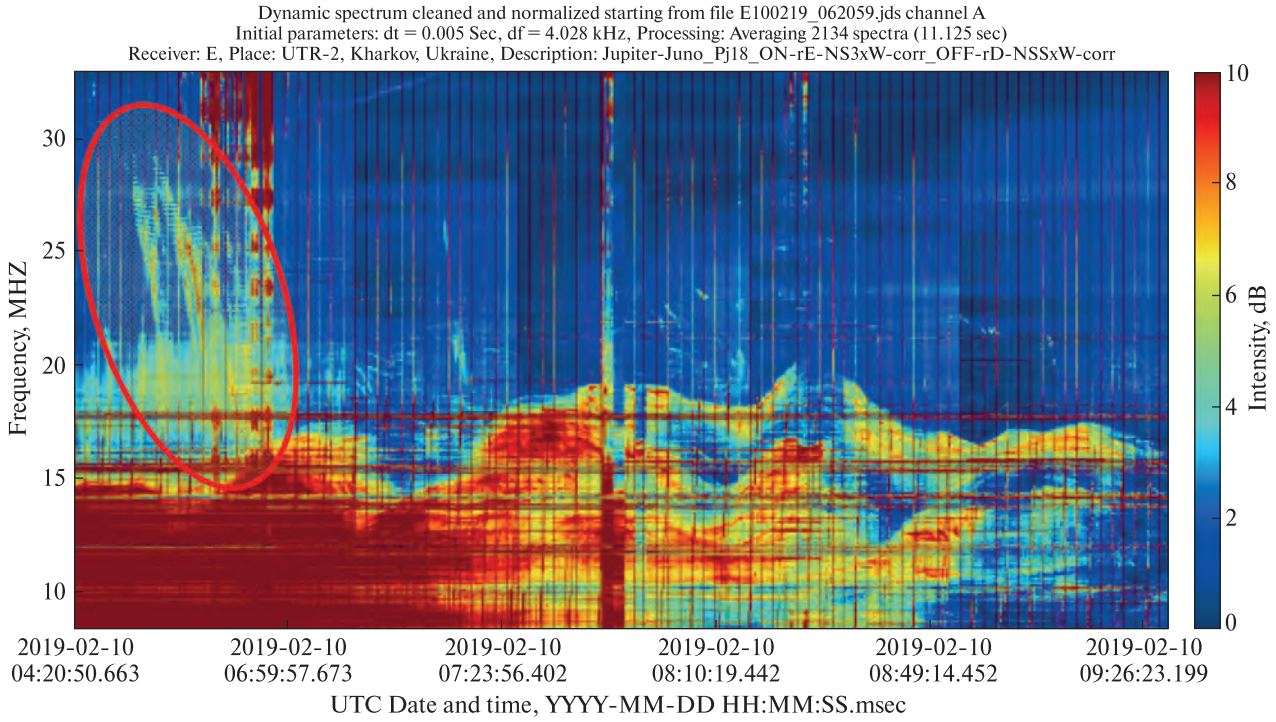

Fig. 7. Observations of Jupiter on February 10, 2019 (PJ18). The red ellipse marks the characteristic emission of S-bursts. Mode: correlation; beam — ON; North-South antenna of UTR-2. Time resolution: 5 ms; frequency range: 8.25-33.0 MHz

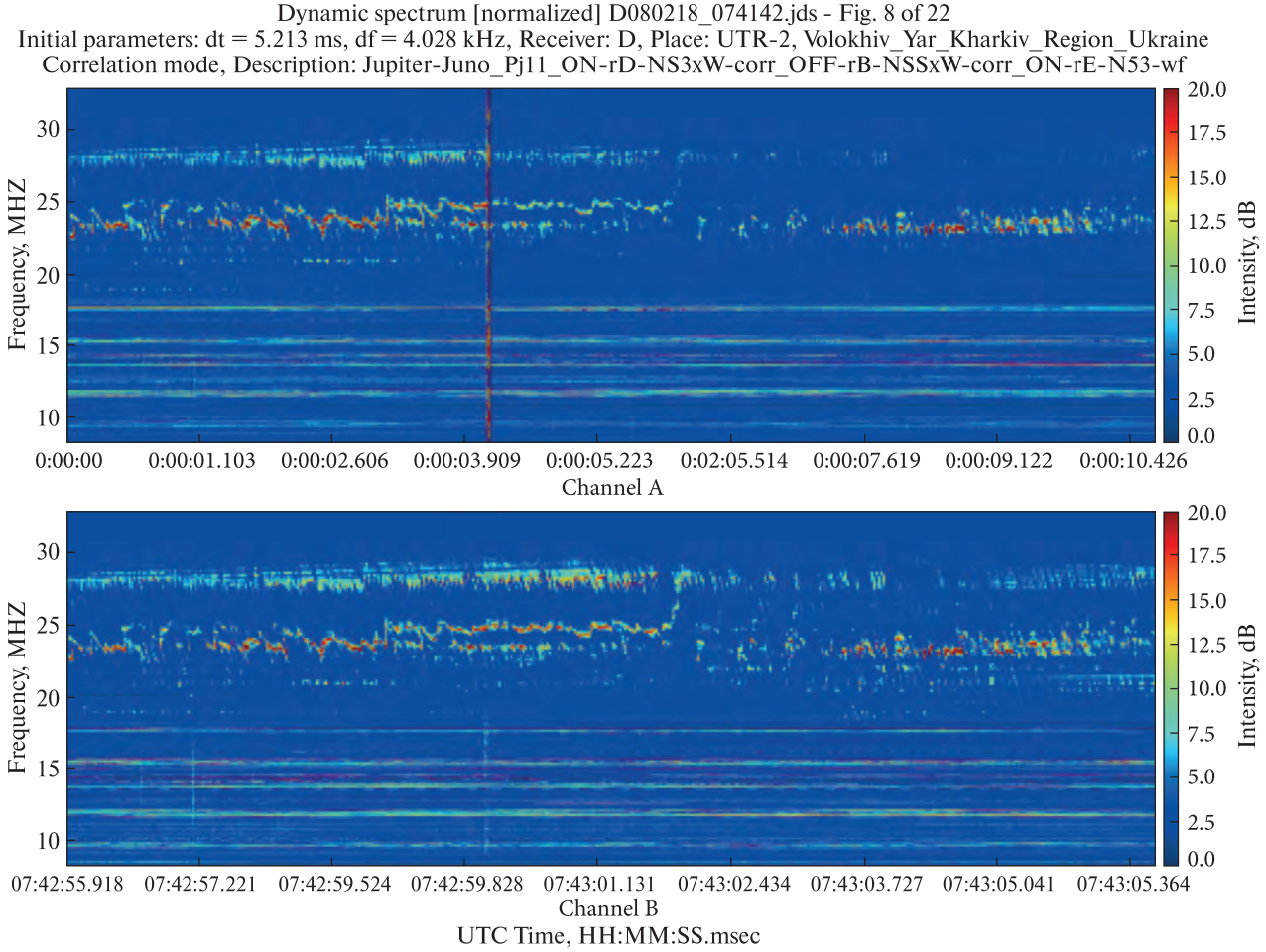

Fig. 8. The sequence of S-bursts with complex modulation. Observations of Jupiter on February 8, 2018 (PJ11). Top panel: North-South antenna, bottom panel: East-West antenna of UTR-2. Mode: correlation; time resolution: 5 ms; frequency range: 8.25–33.0 MHz

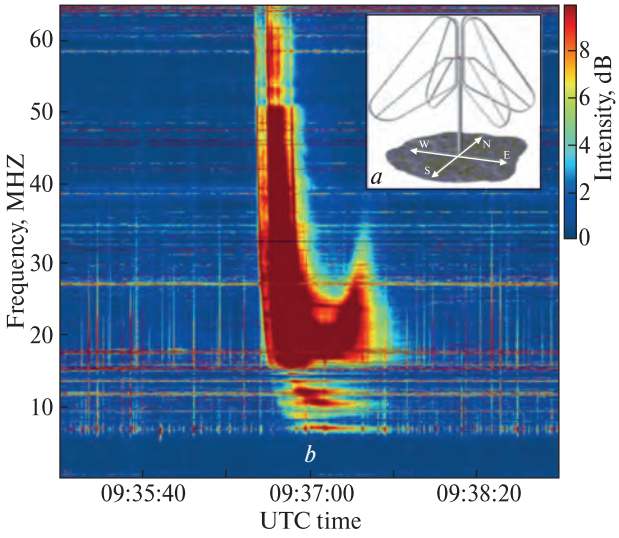

Fig. 9. (*a*) the design of the lunar radio astronomy antenna prototype, (*b*) the time-frequency spectrum of the solar U-shaped burst on June 5, 2020 registered during test observations

for lunar observatory is an active dipole. The dipole provide optimal "radio astronomical sensitivity", which is determined primarily by the contribution of the amplifier noise temperature to the noise temperature of the active dipole. Its design can be seen in Fig. 9, *a*. The dipole arm lengths along the midline are 2.8 m, the angle of inclination to the horizon is 45°, and the dipole terminals are located at a height of $h = 3.2$ m above the ground.

It is made of copper tubes having a diameter of 12 mm. A low-noise amplifier (LNA) on the In-GaAs-Al transistor ATF38143 is used. The LNA nominal gain is Gamp ≈ 22 dB, the effective noise temperature is about 50 K, and the 3-rd order nonlinear distortion coefficient is more than 30 dB/μV. The operational frequency band is 4 to 40 MHz. When testing, the prototype of lunar radio astronomy antenna has shown its high performance. For example, we managed to register a solar U-shaped radio burst (Fig. 9, *b*). The space-based observations by STEREO A and WIND at this time confirm our detection.

Ukrainian radio telescopes RT-32 and KTNA-200

Ukraine, as one of the countries that possesses unique space technologies, is making great efforts to develop and restore them. One of the important elements of the ground space infrastructure of any country with space technology is the presence of powerful transmitting-receiving antenna stations and radio telescopes. All over the world, such systems are networked. In radio astronomy, such networks are used for very long base radio interferometry (VLBI). Using VLBI methods and technologies allow us to build brightness distribution maps of various astrophysical objects with high angular resolution. The EVN (European VLBI Net) is one of the example of such networks in radio astronomy. Another example of a worldwide network is DSN (Deep Space Network). This NASA network is used to support deep space missions, interplanetary mission and also performs radar astronomy observations. The network combines large-sized transceiver antennas, which are located in different countries.

The Ukrainian MARK-4B antenna system modernization program has been ongoing since 2018 [8, 9]. The MARK-4B is a 32 meter diameter antenna manufactured by the Japanese company NEC. This antenna located near the town Zolochiv, Lvivs' region. Such beam wave-guide antennas were used in different countries as telecommunications antennas

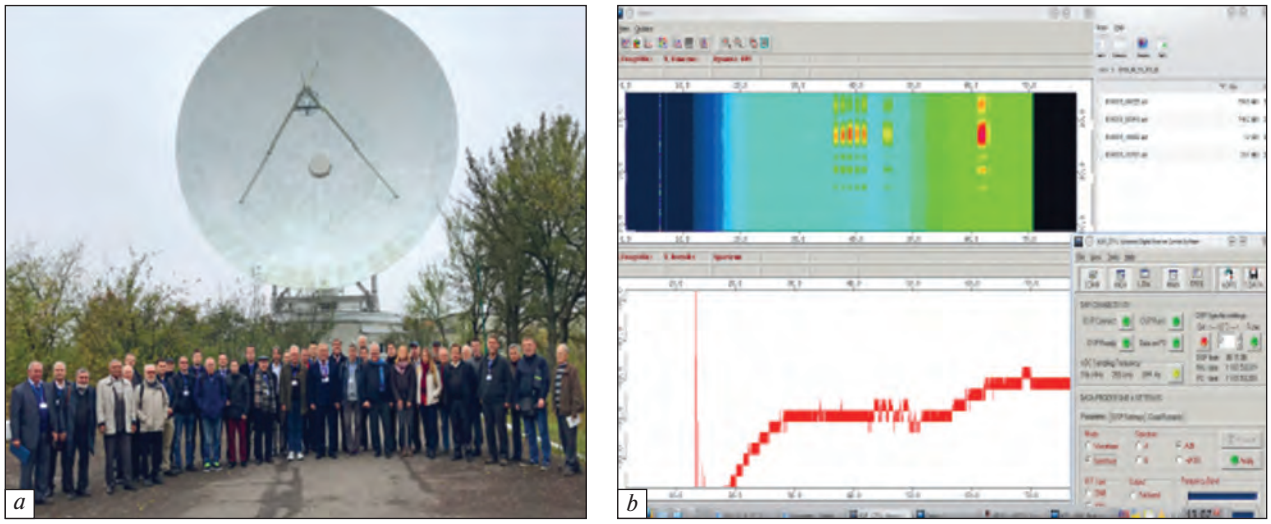

Fig. 10. Participants of an international workshop on the background of RT-32 radio telescope (*a*). An example of test recording of the radiation spectrum of the Intelsat 10–02 satellite (*b*)

for geostationary communication satellites. The Ukrainian MARK-4B antenna system is transformed into the radio telescope RT-32. The radio telescope KTNA-200 is located next to RT-32. In 2020 a project was developed to modernize this 25-meter radio telescope into the station supporting of deep space missions. In accordance with the modernization plans for these two radio telescopes, RT-32 (see Fig. 10, *a*) is operating in a single dish receiving mode in C and K bands (4.7–6.8 GHz and 20–26 GHz). Additionally, it is going to operate in the receiving mode in X (8–12 GHz) band.

Currently, the RT-32 is equipped with a wide-band corrugated conical feed horn, its own guidance and control system, a cesium frequency standard, cryogenic receivers in C and K bands, which operate in two orthogonal polarization in each of the ranges, two-channel broadband digital recorders, time server, GNSS stations, radiometric receiver and has some service facility. It is planned that RT-32 will be used as a radio astronomy radio telescope in C and K bands, including VLBI mode, and as a receiving station to support deep space missions in X band. Now a stage of research operation and testing of all RT-32 systems is realized. This radio telescope, provided it is will equipped with appropriate recording equipment, is already capable of receiving signals from satellites (see Fig. 10, *b*). After modernization, which will take 3–4 years, as we hope, the KTNA-200 radio telescope will operate to support long-range space missions in transmitting and receiving modes in S and X bands.

Conclusions

Ukrainian radio telescopes UTR-2, URAN-1, 2, 3, 4, GURT, RT-32 and KTNA-200 have a large potential for ground-based support of space missions. Such coordinated observations with ground-based and space-borne facilities have provide new unprecedented knowledge on different components of the solar and planetary sporadic radio emission as well as on the mechanisms of their generation, formation and propagation of the shock waves in the solar corona and in the interplanetary plasma. On the other hand, creation and modernization of new antennas in different frequency ranges enable us to participate in many international radio astronomy programs like lunar far-side radio telescope or EVN and DSN networks.

Acknowledgment

This study was supported by Target Complex Program of NAS of Ukraine for Scientific Space Studies for 2018–2022 (projects "Ground-based support by UTR-2-URAN-GURT low-frequency radio telescope system of international and Ukrainian space missions" and "Creation of low-frequency radio astronomical elements and systems for the study of objects in the Universe from the surface of the Moon"). The SOHO/ LASCO data used here are produced by a consortium of the Naval Research Laboratory (USA), Max-Planck-Institut fuer Aeronomie (Germany), Laboratoire d'Astronomie (France), and the University of Birmingham (UK). SOHO is a project of international cooperation between ESA and NASA. We acknowledge use of NASA/GSFC's Space Physics Data Facility's OMNIWeb (or CDAWeb or ftp) service, and OMNI data ("Wind" spacecraft data).

REFERENCES

1. Konovalenko A., Sodin L., Zakharenko V., Zarka P., Ulyanov O., Sidorchuk M., Stepkin S., Tokarsky P., Melnik V., Kalinichenko N., Stanislavsky A., Koliadin V., Shepelev V., Dorovskyy V., Ryabov V., Koval A., Bubnov I., Yerin S., Gridin A., Kulishenko V., Reznichenko A., Bortsov V., Lisachenko V., Reznik A., Kvasov G., Mukha D., Litvinenko G. Khristenko A., Shevchenko V. V., Shevchenko V. A., Belov A., Rudavin E., Vasylieva I., Miroshnichenko A., Vasilenko N., Olyak M., Mylostna K., Skoryk A., Shevtsova A., Plakhov M., Kravtsov I., Volvach Y., Lytvinenko O., Shevchuk N., Zhouk I., Bovkun V., Antonov A., Vavriv D., Vinogradov V., Kozhin R., Kravtsov A., Bulakh E., Kuzin A., Vasilyev A., Brazhenko A., Vashchishin R., Pylaev O., Koshovyy V., Lozinsky A., Ivantyshin O., Rucker H. O., Panchenko M., Fischer G., Lecacheux A., Denis L., Coffre A., Grießmeier J.-M., Tagger M., Girard J., Charrier D., Briand C., Mann G. The modern radio astronomy network in Ukraine: UTR-2, URAN and GURT. *Experimental Astronomy*. 2016. Vol. 42, Iss. 1, P. 11–48.

2. Dorovskyy V., Melnik V., Konovalenko A., Brazhenko A., Rucker H. Spatial properties of the complex decameter type II burst observed on 31 May 2013. *Sun and Geosphere*. 2018. Vol. 13, No. 1. P. 25–30.

3. Melnik V.N., Brazhenko A.I., Konovalenko A.A., Dorovskyy V.V., Rucker H.O., Panchenko M., Frantsuzenko A. V., Shevchuk M. V. Decameter Type IV Burst Associated with a Behind-the-limb CME Observed on 7 November 2013. *Solar Physics*. 2018. Vol. 293, Iss. 3, article id. 53, 10 pp.

4. Kalinichenko N.N., Olyak M.R., Konovalenko A.A., Brazhenko A.I., Kuhai N.V., Romanchuk A.I. Large-scale structure of solar wind beyond the Earth's orbit: reconstruction using the data of two-site measurements of interplanetary scintillations in the decameter radio range. *Kinematics and Physics of Celestial Bodies*. 2019. Vol. 35, No. 1. P. 17–27.

5. Zakharenko V., Konovalenko A., Zarka P., Ulyanov O., Sidorchuk M., Stepkin S., Koliadin V., Kalinichenko N., Stanislavsky A., Dorovskyy V., Shepelev V., Bubnov I., Yerin S., Melnik V., Koval A., Shevchuk N., Vasylieva I., Mylostna K., Shevtsova A., Skoryk A., Kravtsov I., Volvach Y., Plakhov M., Vasilenko N., Vasylkivskyi Y., Vavriv D., Vinogradov V., Kozhin R., Kravtsov A., Bulakh E., Kuzin A., Vasilyev A., Ryabov V., Reznichenko A., Bortsov V., Lisachenko V., Kvasov G., Mukha D., Litvinenko G., Brazhenko A., Vashchishin R., Pylaev O., Koshovyy V., Lozinsky A., Ivantyshyn O., Rucker H.O., Panchenko M., Fischer G., Lecacheux A., Denis L., Coffre A., and Grießmeier J.-M. Digital receivers for low-frequency radio

telescopes UTR-2, URAN, GURT. *Journal of Astronomical Instrumentation*. 2016. Vol. 5, Iss. 4. id. 1641010. 19 p.

6. Stanislavsky A.A., Konovalenko A.A., Yerin S.N., Bubnov I.N., Zakharenko V.V., Shkuratov Yu.G., Tokarsky P.L., Yatskiv Ya.S., Brazhenko A.I., Frantsuzenko A.V., Dorovskyy V.V., Rucker H.O., Zarka Ph. Solar bursts as can be observed from the lunar farside with a single antenna at very low frequencies. *Astronomische Nachrichten*. 2018. Vol. 339, Iss. 7–8. P. 559–570.

7. Shkuratov Y.G., Konovalenko A.A., Zakharenko V.V., Stanislavsky A.A., Bannikova E.Y., Kaydash V.G., Stankevich D.G., Korokhin V.V., Vavriv D.M., Galushko V.G., Yerin S.N., Bubnov I.N., Tokarsky P.L., Ulyanov O.M., Stepkin S.V., Lytvynenko L.N., Yatskiv Y.S., Videen G., Zarka P., Rucker H.O. A twofold mission to the moon: Objectives and payloads. *Acta Astronautica*. 2019. Vol. 154. P. 214–226.

8. Ulyanov O.M., Reznichenko O.M., Zakharenko V.V., Antyufeyev A.V., Korolev A.M., Patoka O.M., Prisiazhnii V.I., Poichalo A.V., Voityuk V.V., Mamarev V.N., Ozhinskii V.V., Vlasenko V.P., Chmil V. M., Lebed V.I., Palamar M.I., Chaikovskii A.V., Pasternak Yu.V., Strembitskii M.A., Natarov M.P., Steshenko S.O., Glamazdyn V.V., Shubny A.S., Kirilenko A.A., Kulik D.Y., Konovalenko A.A., Lytvynenko L.M., Yatskiv Ya.S. Creating the RT-32 Radio Telescope on the Basic of MARK-4B Antenna System. 1. Modernization Project and First Results. *Radio Physics and Radio Astronomy*. 2019. Vol. 24, No. 2. P. 87–116.

9. Antyufeyev A.V., Korolev A.M., Patoka O.M., Shulga V.M., Ulyanov O.M., Reznichenko O.M., Zakharenko V.V., Prisiazhnii V.I., Poichalo A.V., Voityuk V. V., Mamarev V.N., Ozhinskii V.V., Vlasenko V.P., Chmil V.M., Lebed V.I., Palamar M.I., Chaikovskii A.V., Pasternak Yu.V., Strembitskii M.A., Natarov M.P., Steshenko S.O., Glamazdyn V.V., Shubny A.S., Kirilenko A.A., Kulik D.Y., Pylypenko A.M. Development of the RT-32 radio telescope based on the MARK-4B TsKDZ antenna system. 2. Estimation of the Possibility for Making Spectral Observations of Radio Astronomical Objects. *Radio Physics and Radio Astronomy*. 2019. Vol. 24, No. 3. P. 163–183.

ATMOSPHERIC GRAVITY WAVES — THE MOST PROBABLE MECHANISM OF SEISMIC-IONOSPHERIC COUPLING

G. Lizunov[1], V. Korepanov[2], V. Pronenko[2], O. Piankova[1]

[1] Space Research Institute of NAS of Ukraine and SSA of Ukraine
[2] Lviv Center of Space Research Institute of NAS of Ukraine

We present a comparison of several basic mechanisms of earthquake precursors reflection in the ionosphere discussed in the literature: the propagation of low-frequency electromagnetic waves; the closing of electric currents through the ionosphere; the penetration of neutral atmospheric waves. It is shown that namely atmospheric gravity waves (GW) are the most likely candidate for the role of a carrier of seismic-ionospheric interaction, which allows one to explain (i) the transport of significant energy fluxes into the ionosphere, (ii) the weak dependence of the intensity of ionospheric disturbance on the magnitude of the earthquake, (iii) the shift of ionospheric disturbances per thousand kilometers horizontally relative to the earthquake; (iv) and the generation of an ionospheric electromagnetic response. A review of the theoretical and experimental data on GW is given. The original part of the work presents the study of GW global distribution at ionospheric heights according to DE-2 satellite data and statistical analysis of observed GW relations with earthquakes. The results of the DE-2 observations are backed by comparison with the published data from the DEMETER mission.

Introduction

The ionosphere is a specific area of outer space, which is influenced by energy flows coming both from above — from the Sun, and from below — from terrestrial sources. Despite the fact that the stream from above power is predominant, the streams of energy and momentum penetrating into the ionosphere from below also make a significant contribution to the formation of the heat balance and the dynamic structure of the ionospheric plasma. Recently, the interest to the relationships between the Earth and the ionosphere increased due to multiple studies on ionospheric precursors of earthquakes, which existence is a proven fact, but which origin still has no generally accepted explanation.

Current concept of earthquake (EQ) preparation foresees an ensemble of mechanical, chemical and electromagnetic phenomena, initiated by tectonic processes and propagating upward to the Earth's surface and from there into the atmosphere and the ionosphere (e.g., [1, 2]). We shall not examine here the processes in the lithosphere preceding the EQ and generating surface anomaly of geophysical parameters (emanation of core gases, local changes in surface temperature, etc.) — we accept that this anomaly is formed as a large-scale 3D structure located around the source of a future EQ and stretching into outer space. Our interests are concentrated here to the attempt of substantiation, as detailed as it is possible now, the propagation of these surface anomalies through the atmosphere to space heights by means of various mechanisms of energy transport in the atmosphere — ionosphere — magnetosphere system.

A priori, one can specify several physical agents who may be responsible for the transfer of energy from the Earth's surface to space heights: 1) radio frequency electromagnetic radiation; 2) electric currents; 3) waves of neutral atmosphere. Following Rishbeth [3], we note that any ionospheric disturbances, including those caused by EQ preparation processes, obey the law of matter conservation: ion concentration change = = ionization – recombination +/– transport. Thus, the effectiveness of the mechanisms of impact on the ionosphere from below depends on their ability to influence photochemical reactions and plasma transport processes. The mentioned mechanisms efficiencies are compared below from this point of view. Our main goal is to re-draw attention to the internal atmospheric gravity waves (hereinafter — GWs) as the most probable agent of the seismic-ionospheric interaction. This study summarizes the ideas of our recent works [4, 5].

Mechanisms of energy transport from surface sources to the ionosphere

We want to consider here the influence of surface sources on the dense and magnetoactive layers of the ionospheric plasma located at the heights of the *E*- and *F*-regions, conventionally above 100 km. Region *D* (according to some researchers, electrostatically bounded with the lithosphere) will not be a special object of our attention.

Electromagnetic radiation. Radio frequency electromagnetic radiations (EMR) caused by surface sources are observed from space with the launch of first satellites. Moreover, EMR was the first described type of ionospheric EQ precursors (according to measurements on the Intercosmos-19 satellite [6]).

Energetically, the most powerful sources of EMR from below are lightning discharges. The worldwide thunderstorm activity determines the features of the electromagnetic environment of our planet, first of all — the stable structure of Schumann resonances with central frequencies 7.8 Hz, 14.3 Hz, 20.8 Hz, 27.3 Hz, etc [7]. Next are whistler waves, whose frequencies range from units to several tens of kHz and which serve as lightning discharge markers observable from satellites. In addition, numerous EMR events of technogenic origin are observed in the same frequency bands: power lines emissions and their harmonics, signals of navigation transmitters and broadcasting stations, etc., whose spectra show signs of nonlinear and resonant interactions with the ionosphere plasma [7–9].

If to exclude the active experiments of the ionosphere heating with powerful radio emission, it can be argued that the energy of natural and technogenic EMR is, as a rule, insufficient to modify the regular parameters of the ionosphere (it should be noted that electromagnetic pulses from lightning discharges cause detectable heating of the electron component; but its localization region is limited by the heights of the *D*-layer) [10]. As far as we are interested by the signals that might be registered by satellites, we do not discuss the processes in the *D*-layer.

Therefore, first intermediate conclusion is that EMR cannot be attributed as effective mechanism of the energy transport from surface sources to the ionosphere [3]. By this, we do not assert that EMR as EQ precursor does not exist in the ionosphere. These signals do exist and probably can be recorded. The essence of our statement, confirmed by the cited references, is that because of their very low value in comparison with background fields there, these EMR is an insignificant factor in modifying the parameters of the space environment.

Quasi-stationary electric field. The fundamentals of the atmospheric electricity theory were developed in the middle of the twentieth century and are exposed, for example, in [11]. The initial equations of quasi-stationary electromagnetic field are,

$$\nabla \cdot \vec{j} = i, \vec{j} = \sigma \cdot \vec{E}, \vec{E} = -\nabla\varphi, \qquad (1)$$

where j is the electric current density, i is the density of current sources, σ is the electrical conductivity, E is electric field, φ is electric potential; outside of sources $\nabla \cdot \vec{j} = 0$. Any conclusions regarding quasi-stationary effects in the ionosphere should not contradict the solution of these equations.

A common misconception is already the idea of the earth-ionosphere gap as a capacitor in which the lower plate (Earth's surface) is negatively charged, the upper plate (ionosphere) is positive, and the plates are separated by a quasi-neutral atmosphere. Ionosphere perturbations in this model are interpreted as a result of changes of the capacitor plates charge. In fact, there is no upper plate: the atmospheric gap between the Earth and the ionosphere is positively charged by itself. The positive space charge is in direct contact with the Earth's surface, and the altitude level with a potential of 250 kV, above which the atmosphere has to be considered as almost equipotential conductor, is located only at the foot of the ionosphere, at an altitude of about 60 km. So, the entire configuration of the Earth electric field is enclosed within the troposphere and the stratosphere, forming some kind of the "Faraday cage", which shields the ionosphere from electrical interference from below [11].

As it is known, after the electromotive forces action termination, the space charge in a conducting medium disappears in time $\tau \sim \varepsilon_0 / \sigma$, (where ε_0 is vacuum permittivity). This time is about 5 minutes at the Earth's surface; at altitude of 40 km it is about 0.1 s. At higher altitudes, particle collisions become so rare that electron inertia should be taken into account when calculating conductivity; in this case, the estimation of charge neutralization time appears as $\tau \sim \sigma/(\varepsilon_0\omega_p^2)$, where ω_p is plasma frequency. At altitude of 100 km τ is ~0.01 s. At larger times, charge separation has to be permanently maintained by an external source. Thus, an uncompensated electric charge in the atmosphere and the associated electric field may arise because of the stationary circulation of electric currents generated by sources of atmospheric electricity and partially closed through the earth below and the ionosphere above. As an example, Fig. 1 shows the electrical circuit configuration of a thundercloud. The cloud charge model is represented as an elementary dipole. The electric field above the ground is the sum of the dipole field and its electrostatic image at the Earth's surface; inside the

ground it is determined by the field of the initial dipole, depressed proportionally to the ratio of ground and air conductivity, i.e. ~10^{10} times. Because of an exponential conductivity increase with height above the cloud, a part of the electric current lines are stretched upwards to smaller resistance. With the cloud height increase the part of the current closed through the ionosphere grows [12]. The opposite is also true: the lower the current source is located, the smaller is upward electric flux. So, it is clear that the leakage of currents from underground magnetotelluric sources into the ionosphere is negligible. But as to the current generated at the upper layer of clouds ~12 km, a significant part of it reaches the ionosphere, where it flows into the global ionosphere — magnetosphere electric circuit. However, the fact is that this current is extremely small ~10^{-6}–10^{-5} μA/m^2 [13, 14], which is five to six orders of magnitude less than the background currents flowing in the *E*-region [15].

The situation is no better with the penetration of the Earth's electric field into the ionosphere, although at the surface it reaches significant values (~100 V/m at fair weather and even ~1 kV/m under thunderclouds). To confirm this, let us consider a vector tube formed by the current lines above, for example, the cloud in Fig. 1. From the equation $\nabla \cdot \vec{j} = 0$, the total current through the cross-section S of the tube is not dependent on the height: $j_0 S_0 = j(z)S(z) = \sigma(z)E(z)$ $S(z) = \text{const}$, where the index 0 refers to the lower edge of the tube. (It should be clarified that the parameter here is a combination of the components of the atmospheric conductivity tensor, in the simplest case $\sigma = \sqrt{(\sigma_{||}\cos\theta)^2 + (\sigma_p\cos\theta)^2}$, where σ_p is the Pedersen conductivity, $\sigma_{||}$ is the parallel conductivity, θ is the angle between the direction of the electric field and the Earth's magnetic field). Neglecting the change in the tube cross-section related to the divergence or focusing of current lines with height, we obtain:

$$j = j_0 = \sigma(z)E(z) = \sigma_0 E_0 = const, \text{ or } E(z) = \frac{\sigma_0}{\sigma(z)} E_0 = \frac{j_0}{\sigma(z)}.$$

Thus, the near-surface electric field perturbations are transmitted upwards with the attenuation factor $\sigma_0/\sigma(z)$. The vertical distribution of the electrical conductivity tensor components of the Earth – atmosphere — ionosphere system is presented in Fig. 2. The effective electrical conductivity $\sigma(z)$ increases from the ground to the level of 120 km (*E*-region) – by 10–13 orders of magnitude (depending on the mutual direction of the electric and magnetic fields along current line). Respectively, attenuation factor of the electric field is 10^{-10}–10^{-13}. From this, a reasonable estimation of the field of surface sources at *E*-region is about 0.1 μV/m, what is three orders of magnitude less than background ionospheric fields at the same height.

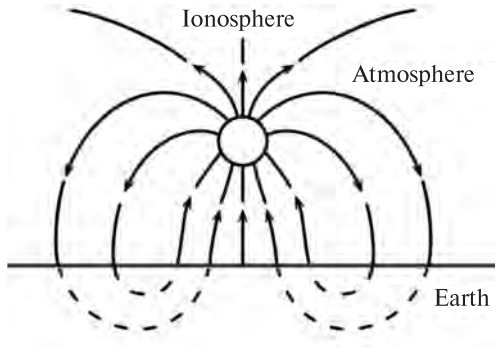

Fig. 1. Electric field of a thundercloud. The current source is represented as an elementary dipole

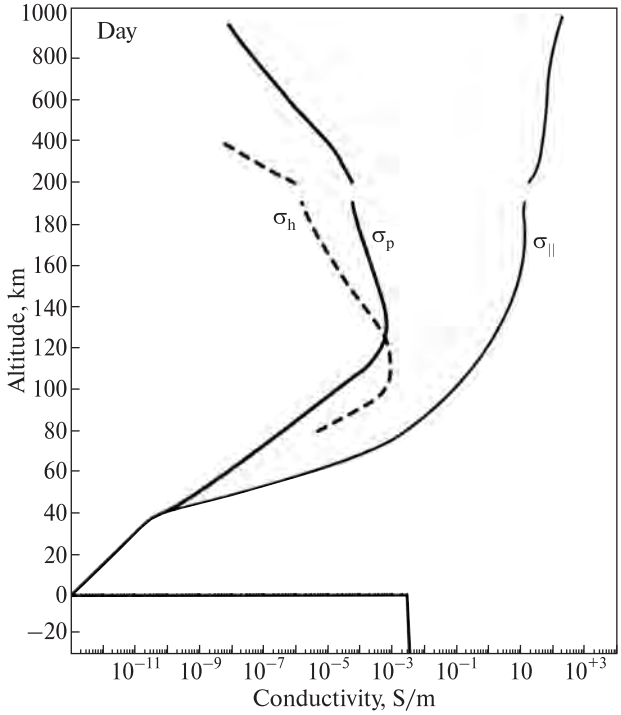

Fig. 2. Vertical profile of the electrical conductivity of the atmosphere (mean latitudes, mean solar activity, daytime)

Contrary to the foregoing, a number of publications devoted to the numerical simulation of the surface electric fields penetration into the ionosphere claim that much larger field values (up to 1 mV/m in the *E* region) have to be generated there (for example, in [16]). Such overestimates, apparently, are the result of an error in the formulation of the upper boundary condition for the differential problem (1). This question was investigated in detail in [17], where numerical experiment has been posed correctly. Fig. 3 shows an example of calculating the vertical distribution of the electric field of a model surface source 100 V/m from this work. The plots on the graph correspond to different heliophysical conditions.

Therefore, next conclusion is that a stationary electric field from Earth's surface source also cannot

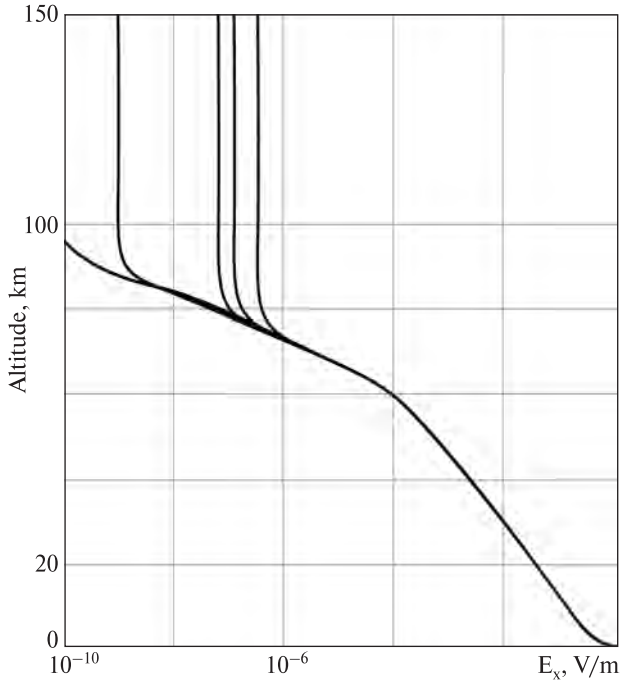

Fig. 3. Numerical calculating the altitude distribution of the horizontal component of electric field E_x produced by surface source above a point with the horizontal coordinate x_m, at which the maximum field is reached (adapted from [17]). The horizontal size of source is taken to be 100 km, the vertical electric field on the surface E_z =100 V/m. The upper split of the plot corresponds to different integral conductivities of the ionosphere

be attributed as possible mechanism of the energy transport to the ionosphere.

Neutral atmosphere waves. The Earth's atmosphere, like the atmospheres of any planets and stars, is a gravitationally stratified medium, the density of which decreases with height according to an exponential barometric law. Due to this, even weak oscillations of the surface air layers, propagating in the form of a wave process to ionospheric heights, become strong relative to the energy scale of the rarefied space environment. For example, between the surface of the Earth and an altitude of 120 km, the density of the atmosphere decreases by about 10^7 times. Correspondingly, the ratio of the energy carried by the wave to the energy contained in the same volume of the surrounding atmosphere increases by the same factor. This circumstance causes an increase in the amplitude of atmospheric disturbances with height, as it will be shown below. We note here an opposite analogy with the properties of electrostatic channel of the Earth — ionosphere coupling which is characterized by the exponential weakening of electric field perturbations.

Another fundamental consequence of the atmosphere barometric distribution is the growth with height of the coefficients of kinematic viscosity and thermal conductivity, inversely proportional to the gas density. As a result, atmospheric waves dissipate in a peculiar way: the wave energy is "seeded" in a certain height layer, the location of which does not depend on the initial amplitude of the wave, and is determined by wave's spectral characteristics — the wave number and propagation direction; this issue will be discussed in detail below. In such a way, atmospheric waves propagate through the ionosphere inducing oscillations of its plasma components and are absorbed at different altitudinal layers changing the temperature regime and photochemical equilibrium there.

We consider atmospheric waves as the most efficient agent for the energy transport into the ionosphere from below. In a wide range of atmospheric waves we select the gravity mode, propagation of which is associated with the buoyancy forces action — heated gas floats up, while cooled gas sinks [18]. The tectonic processes just create thermal sources necessary for the generation of such waves. According to [2], a list of phenomena occurring over the source of a forthcoming EQ includes: the emanation into the atmosphere of core gases (greenhouse components CO_2, CH_4, etc.) and radioactive radon; the condensation of atmospheric moisture molecules ionized by radon with an intensive release of latent heat; the mixing and convection of heated air layers. By this, a stationary dynamic structure is formed — a flow of thermal energy from ground level to the top of the clouds, which is apparently the missing link that connects atmospheric oscillations with tectonic processes.

To confirm this postulate, let us remind that seismogenic thermal anomalies are permanently recorded by remote sensing satellites in the far-infrared range in the region of a future EQ area. The typical parameters of the anomalies are as follows [19]: the heated zone corresponds to the projection of the EQ preparation area to the Earth's surface, reaching hundreds of kilometers in size; temperature difference with the surrounding region may be a few degrees; the lifetime of the anomaly is from several days to several weeks. Theoretical estimation of the generated atmospheric oscillations by such heat sources are presented in early works [19–21] and recent work [22]; relevant experimental evidence is given in [23, 24].

So, this short review explains why we are confident that GW are the most probable mechanism of energy transport from lithosphere to ionosphere. Let us try to support this postulate with the available data.

Theoretical portrait of atmospheric gravity waves

Let us consider the main properties of GW, which are important for understanding their interaction with the ionosphere [4, 5].

GW dispersion law. GW dispersion equation [18] is not too complicated, but still too cumbersome. For

analytic calculations, we recommend using the following approximate formula. Moreover, turning to a more rigorous theory for the purpose of "accurate interpretation" of experimental data or the purpose of abstract modeling is often unjustified. This is due to the fact that the parameters of the atmosphere in the altitude range from the Earth's surface to the ionosphere are known only approximately (moreover, they are taken from the atmospheric models), and with the fact that the analytical theory does not take into account all factors affecting the propagation of GW (dissipation, nonlinearity, atmosphere inhomogeneity, etc.).

GW circular frequency [25, 26]:

$$\omega = \frac{c_g k_x}{\sqrt{1+(k/k_g)^2}} = \omega_g \frac{k_x}{\sqrt{k_g^2 + k^2}}. \qquad (2)$$

Model expression for the damping decrement in approximation of weak dissipation $\nu < \omega$ [26]:

$$\nu = D(k^2 + k_g^2). \qquad (3)$$

Here $\vec{k} = \{k_x, 0, k_z\}$ is GW wave vector. OZ axis of the Cartesian coordinate system is directed vertically upwards, OX axis is selected in such a way that the wave vector lies in the XOZ plane. In formula (2), (3) the quantities ω_g, k_g, c_g are the characteristic parameters of GW theory. Specifically, ω_g is Brunt-Väisäla frequency, $k_g = (2H)^{-1}$ is a scale of wave numbers (here H is the atmosphere height scale), $c_g = \omega_g/k_g$ is the maximum GW velocity, numerically close to the speed of sound, D is the kinematical viscosity coefficient. These parameters are given in Table 1. On the phase plane, the GW dispersion curves fill the region shown in Fig. 4.

From (2) follows the expressions for components and direction of the group velocity:

$$V_{gx} = c_g \frac{1+(k_z/k_g)^2}{\left(1+(k/k_g)^2\right)^{3/2}}; \; V_{gz} = -c_g \frac{k_x k_z / k_g^2}{\left(1+(k/k_g)^2\right)^{3/2}};$$

$$\tan\psi = \frac{V_{gz}}{V_{gx}} = -\frac{k_x k_z}{k_g^2 + k_z^2}.$$

The minus sign in the second and third expressions means that the vertical components of the group and phase velocities are directed oppositely (if $k_z < 0$, then the energy propagates upward).

Fig. 5 represents the dependence of the vertical group velocity on the period and on the horizontal wavelength. The distribution has the form of a ridge, which breaks in the direction of supersonic speed $\omega/k_x > c_g$. The vertex of the distribution is reached at the point

$$k_x = -k_z = k_g, \; \omega = \omega_g / \sqrt{3},$$

where $V_{gz} = V_{gz\max} = c_g / 3^{3/2}$, $V_{gx} = 2c_g / 3^{3/2}$. Thus, the fastest upward wave transfer occurs obliquely, at an angle to the horizon $\psi = \arctan(1/2) \approx 30°$.

The region of the group velocity ridge on Fig. 5 highlights the spectral window in which the maximum flux of wave energy is transported from bottom to top of the atmosphere. Its numerical parameters are as follows: GW periods — from ten to several tens of minutes, the horizontal wavelengths from fifty to several hundred kilometers, and the horizontal phase velocities of more than a hundred meters per second. These numbers are in good agreement with the observed parameters of medium-scale traveling ionospheric disturbances. For the productive generation of such long waves, their surface sources should have horizontal dimensions of the same order as the wavelengths – in this case, mesoscopic scales. Such sources are known: these are thermal anomalies over the preparation area of the strong EQs, conglomerates of thunderstorm clouds, tsunami, weather fronts etc. At the same time, multiple non-coherent quasi-point sources of atmospheric oscillations – a plowed field heated by the sun, the work of an industrial enterprise, the wind over urban buildings, etc., – should not be effective generators of ionospheric disturbances.

Amplitude amplification and dissipation of GW. The absorption of GW energy, as well as any macroscopic movements of the atmosphere, occurs under the influence of viscosity and thermal conductivity effects, which are approximately characterized by a single kinematical coefficient of viscosity/thermal conductivity/diffusion $D = D(z)$. The value of this coefficient on the Earth's surface is quite small (~10^{-3} m^2/s), but due to the barometric distribution of atmospheric density, it grows exponentially rapidly with height. Therefore, for the same wave, the atmosphere behaves as an almost perfect liquid at low altitudes and as extremely viscous and heat-conducting fluid at high altitudes.

The theory of GW dissipation during propagation from bottom to top reveals a deep analogy with Chapman's theory describing the absorption of solar

Table 1

Parameters used for the GW theory development

Conditions	H	$2\pi / k_g$	Sound speed	c_g	$2\pi / \omega_g$	$V_{gz\max}$
Altitude 0–150 km	7 km	100 km	300 m/s	270 m/s	5.5 min	50 m/s
Altitude > 150 km high solar activity	50 km	700 km	890 m/s	870 m/s	12 min	170 m/s
Altitude > 150 km low solar activity	30 km	420 km	720 m/s	700 m/s	10 min	135 m/s

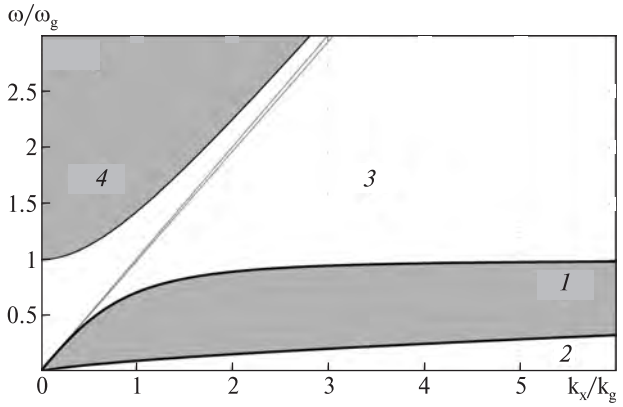

Fig. 4. Dispersion plane: GW area (*1*), dissipation area (*2*), forbidden area (*3*), acoustic wave area (*4*)

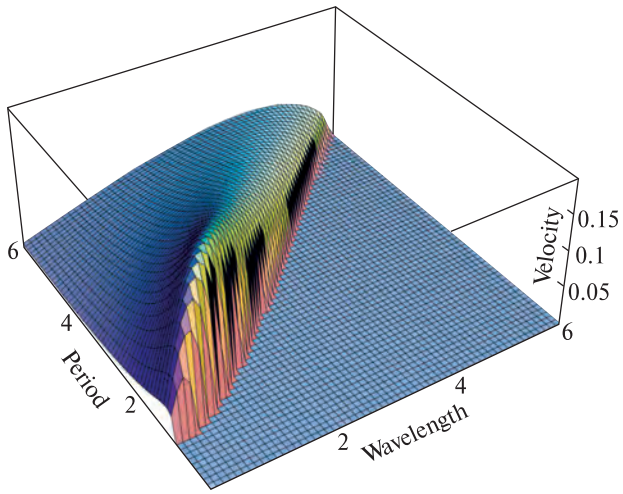

Fig. 5. The normalized vertical component of GW group velocity V_g / c_g as a function of the normalized horizontal wavelength k_g / k_x and the normalized period ω_g / ω

EUV radiation propagated from top to bottom. The equation of the vertical energy transfer of GW is:

$$\frac{dS_z}{dz} = -2\kappa S_z = -Q, \qquad (4)$$

where $S_z = V_{gz}\rho\tilde{V}^2/2$ is the density of the vertical energy flux, ρ is the density of the atmosphere, $\tilde{V}$ is the amplitude of the particle velocity, Q is the heating rate per unit volume of the atmosphere, κ is the spatial attenuation decrement of the wave (absorption coefficient), which is expressed through the temporal attenuation decrement (3) using the formula $\kappa = \nu / V_g$.

In the model of isothermal and chemically homogeneous atmosphere, the wave group velocity does not change with altitude, while the atmosphere density and kinematical viscosity coefficient, and the wave attenuation decrement depends on the height according to simple exponential laws: $\rho \sim \exp\{-z/H\}$, $\kappa \sim D \sim \exp\{+z/H\}$. In this case, equation (4) has an analytical solution.

$$Q = Q_m \exp\left\{1 + \frac{z - z_m}{H} - \exp\left(\frac{z - z_m}{H}\right)\right\}, \qquad (5)$$

where the maximum energy absorption rate Q_m is achieved at a height level z_m determined by the condition:

$$\kappa(z)\big|_{z = zm} = 1/(2H). \qquad (6)$$

Intuitively it seems that the height of GW absorption should depend on wave initial intensity — weaker waves have to decay closer to the source, stronger — at greater height. But equation (6) denies this — the parameter z_m depends on the atmosphere height scale and, through the attenuation decrement κ, on the spectral parameters of the wave, but not on its initial amplitude. This unexpected result confirms that even weak surface GW sources generate energy pumping to space heights, and each monochromatic component of GW has its proper absorption altitude.

To clarify this conclusion let us analyze the GW amplitude change. The solution of equation (5) regarding the particle velocity is:

$$\tilde{V}(z) = \tilde{V}_0\sqrt{\frac{\rho_0}{\rho(z)}}\exp\left\{-\int_0^z \kappa(z)dz\right\} = \tilde{V}_0\exp\left\{\int_0^z\left(\frac{1}{2H} - \kappa(z)\right)dz\right\}, \qquad (7)$$

where $\tilde{V}_0$ is velocity amplitude at the surface. Thus, GW evolves under the influence of two competing factors: amplification with increment $1/(2H)$ due to a change in the density of the atmosphere with height, and attenuation with decrement $\kappa = \kappa(z)$ due to viscosity and thermal conductivity. At low altitudes where the dissipation is low the amplification factor prevails, at high altitudes attenuation prevails. The maximum wave amplitude is achieved under the condition $\kappa/(2H)$, which just coincides with (6). As an example, vertical distribution (7) is plotted in Fig. 6 for a wave with the following parameters: horizontal wavelength 15 km, period 11 minutes, particle velocity $\tilde{V}_0 = 2$ cm/s. Note that the factor of the wave amplification at an altitude of 120 km is 10^3 times.

Fig. 7 shows the dependence of GW absorption height on the direction of wave propagation (group velocity) $z_m = z_m(\psi)$, calculated on the basis of the above theory. The atmosphere is modeled by two layers stitched at an altitude level of 150 km with the viscosity kinematical coefficient $D = 10^5$ m^2/s. The layer parameters are taken from Table 1. Despite the relative simplicity, such a model describes the key features of the wave field generated by surface sources of GW.

According to Fig. 7, the radiation pattern of a quasi-point GW source has a characteristic funnel shape (which fundamentally distinguishes it from the spherically isotropic radiation pattern of acoustic waves). Directly above the source the waves are absent — due to the rapid attenuation of GWs propagating at large angle to the horizon. The maximum heights of the wave field reaches 200–300 km (depending on solar activity) at distances of more than 1500 km from the source. It should be noted that the curves in the figure

characterize the height of maximum GW absorption $z_m = z_m(x)$; in fact the wave energy leaks a bit higher, within approximately still one height scale H. On the other hand, only a small part of GW initial spectrum reaches maximal heights. The majority of harmonics outside the spectral window shown in Fig. 5 are absorbed below (in the region of gray shaded space in Fig. 7).

While propagating from the Earth's surface into the ionosphere, GWs experience tremendous amplitude amplification. One can expect that the wave reaches the level of overturning $\tilde{V} \sim \omega/k$ and then balances near this level, periodically releasing excess energy and momentum into the atmosphere. In this case, the ionospheric disturbance has not to depend on the power of its source below. This conclusion allows us to explain the experimental fact established in [27] from the data of DEMETER satellite. Namely, the amplitudes of variations in the ionospheric plasma density caused by EQs were approximately the same in the widest range of earthquake magnitudes M = = 4.8–8.0 (see Fig. 2 in this paper).

Numerous theoretical and experimental data indicate that in the 70–150 km altitude range, where the atmospheric medium is already sufficiently rarefied, but the GW energy flux is still large, the GW dissipation causes the atmosphere heating by tens of Kelvin. Thus, surface thermal anomalies – the sources of GW generation – are in some way transferred to ionospheric heights. Ultimately, GWs are a significant factor in the formation of the upper atmosphere energy balance (yielding in the hierarchy of sources and sinks of a heat to the absorption of solar EUV radiation, but along with the heat influx from the thermosphere and along with the cooling due to IR radiation).

Electromagnetic disturbances generation. Due to the finite electrical conductivity of the atmosphere and the presence of the Earth's magnetic field, any atmospheric movements – wind, tides, waves – are accompanied by the electric current generation:

$$\vec{j} = \hat{\sigma} \cdot \left(\vec{E} + \tilde{\vec{V}} \times \vec{B} \right),$$

where $\hat{\sigma}$ is the tensor of atmosphere/ionosphere conductivity, $\tilde{V}$ is the velocity of neutral particles, B is induction of the Earth's magnetic field, and E is the electric field strength. In this expression, the second term in brackets describes current source created by the movement of the neutral atmosphere (dynamo-current), and the first term is a conduction current. The fundamentals of the theory of electromagnetic disturbance generation during the GW propagation have been developed in [4, 5, 28, 29]. Theoretical estimates take an especially simple form when the Earth's magnetic field is directed vertically along OZ.

As can be seen from Fig. 2, the Hall conductivity has a sharp maximum in the altitude range of

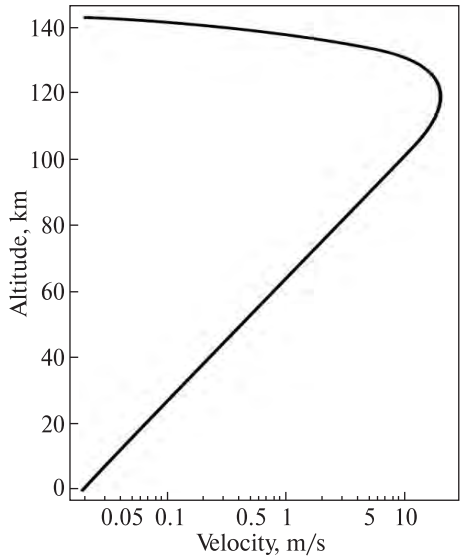

Fig. 6. Vertical distribution of the GW amplitude

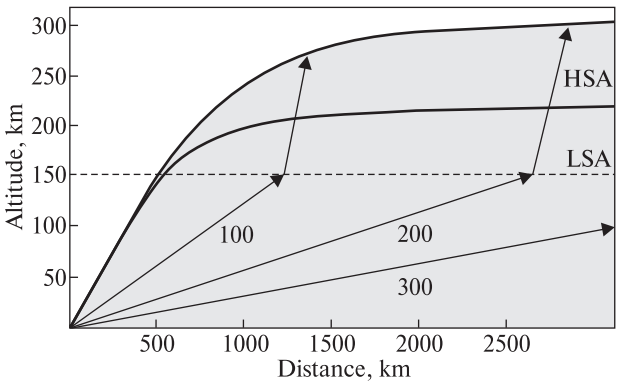

Fig. 7. GW field generated by a model point source. The dependence of the maximal height of GW propagation is shown at a low solar activity (LSA) and a high solar activity (HSA). The numbers near the plots are horizontal wavelength in km

z_d = 90–130 km (dynamo-layer), where mainly the dynamo-current jet is concentrated. Due to the small thickness of the dynamo-layer in comparison with GW vertical wavelength (typically ~100 km), the integral dynamo-current can be estimated as

$$I_{dx} = \int_0^\infty j_{dx}\, dz = \tilde{V}_{dx} B \int_0^\infty \sigma_h dz = \Sigma_h \tilde{V}_{dx} B, \qquad (10)$$

where Σ_h is integral Hall conductivity of the ionosphere, and $\tilde{V}_x$ is neutral particles velocity in the dynamo-layer.

The current source (10) is partially shunted by a conductivity current $j_{cx} = \sigma_p E_x$, and is partially closed by parallel current j_z, which is going to magnetosphere. The equivalent electrical circuit generated in this way is illustrated in Fig. 8. The calculation of the circuit parameters is made in a standard way adopted in the ionosphere electrodynamics [15].

The integral density of transverse current (dynamo current minus conductivity current) is

$$I_x = I_{dx} - I_{cx} = \frac{\Sigma'_p \Sigma_h}{\Sigma_p + \Sigma'_p} \tilde{V}_{dx} B. \quad (13)$$

The transverse electric field due to a voltage drop when current flows through the space circuit

$$E_x = \frac{\Sigma_h}{\Sigma_p + \Sigma'_p} \tilde{V}_{dx} B. \quad (14)$$

The magnetic field variation generated in the dynamo-layer (for the model of a flat current sheet)

$$\tilde{B}_y = 0.5 \mu_0 I_x. \quad (15)$$

The density of the parallel current injected into the magnetosphere

$$j_z = -\frac{\partial}{\partial x} I_x \Rightarrow |j_z| = k_x I_x. \quad (16)$$

In these formulas k_x is the GW horizontal wave number, and Σ'_p and Σ_p are the integral Pedersen conductivities in the zone of the dynamo-current generation and in the magnetically conjugate ionosphere (the sum $\Sigma_p + \Sigma'_p$ should be interpreted as the integral conductivity of entire current-carrying tube of the Earth's magnetic field), μ_0 is magnetic constant.

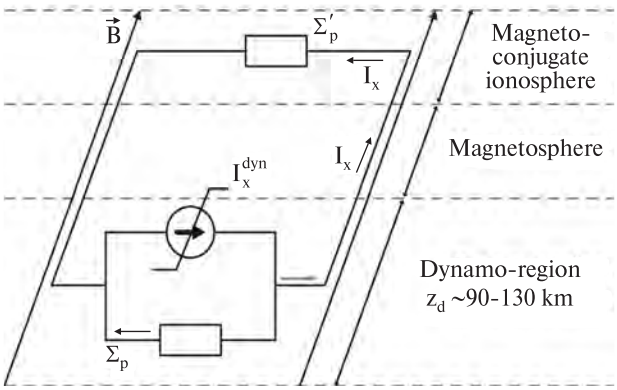

Fig. 8. Equivalent electrical circuit of GW current system

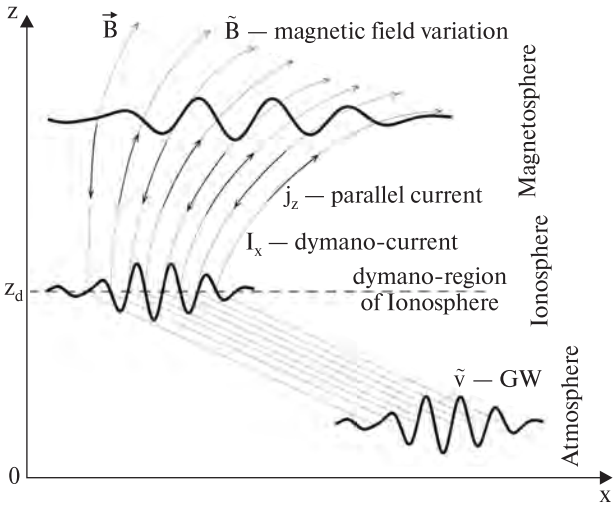

Fig. 9. Sketch of the Geospace disturbance generated by GW propagation

Thus, the value of the ionosphere response to the incoming GWs depends both on the integral Hall conductivity Σ_h, and on the conditions of the electrical circuit closing in the conjugate ionosphere. In the case of $\Sigma'_p = 0$ (idle mode), the magnetic variation is absent, and the electrical variation is maximum. In the case of $\Sigma'_p \to \infty$ (short circuit) it is opposite. With realistic parameters of the atmosphere and GW: $\Sigma_h \sim \Sigma_p \sim \Sigma'_p = 20$ Cm (day), $B = 5 \cdot 10^4$ T (mean latitudes), $\tilde{V}_{xd} = 20$ m/s (moderate amplitude GW), $k_x = 2\pi/(6 \cdot 10^4)$ m^{-1}, we find $E_x = 1$ mV/m, $\tilde{B}_y = 6.5$ nT, $j_z = 1$ μA/m^2.

The sketch in the Fig. 9 gives an idea of the set of processes accompanying GW propagation. Between the Earth's surface and the dynamo layer, GW is an ordinary wave of the neutral atmosphere (it is depicted by a wave packet at the bottom right). In the dynamo layer, the wave process is splitting. The atmospheric wave continues to propagate to the left upwards (beyond the limits of the figure) and its dissipation increases with altitude and, ultimately, the wave is absorbed at altitudes of ~200–300 km (depending on the level of solar activity and the wave spectral composition). Besides, the part of GW energy is spent at generating electromagnetic disturbance, whose horizontal structure reproduces GW profile in the dynamo-layer. Through a parallel electric current, this structure is transported upward into the magnetosphere, experiencing a geometric transformation associated with the divergence of the Earth's magnetic field lines.

So, several types of electromotive forces act on the ionosphere: surface electricity, discussed in the previous section; dynamo-effect due to the neutral atmosphere motion, including charged particles at the height of *E*-region, discussed in this section; and penetration from above of the electric fields from the magnetosphere [15]. Comparison of these factors is given in Table 2.

Observational data

The penetration of GWs from the lower layers of the atmosphere to ionospheric heights is an established experimental fact, confirmed by numerous observations when surface sources of GWs were certainly known (nuclear explosions, catastrophic EQs, etc.). As an additional example, we present the results of long-term ground-based meteorological and magnetometric observations carried out simultaneously at the Ukrainian Antarctic station "Vernadsky" (Galindez Island) and at a magnetically conjugate point in the United States (near Boston) [29]. On the basis of large-scale statistical material, it was established that the waveforms of GWs recorded in variations of meteorological parameters at the Ukrainian Antarctic Station with a certain delay (just suitable for GW to reach dynamo-layer)

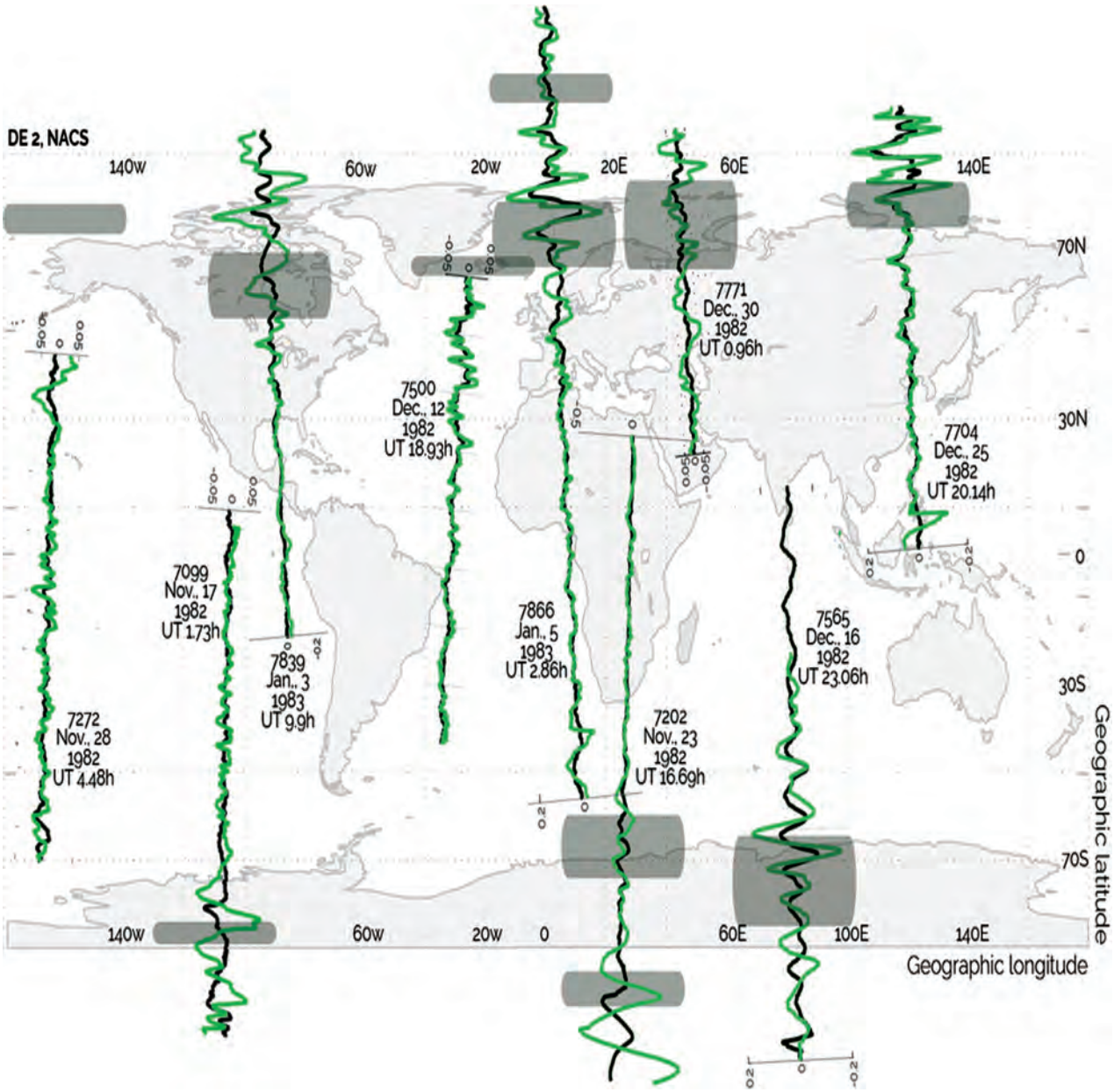

Fig. 10. GW signatures in density fluctuations of O and N2 gas components according to the DE-2 data. The dark gray areas show the current positions of the auroral oval

are reproduced in the Earth's magnetic field variations and then transmitted as magnetic disturbances to the magnetically conjugate ionosphere. The presented above theory of ionospheric-magnetospheric current systems generation is developed namely based on these observations.

Other convincing example of seismo-ionosphere coupling efficiency through GW is the registration of

Table 2

Quasi-stationary electromagnetic disturbances generated in the *E*-region by space and surface sources

Source	Current density, μA/m^2	Magnetic field, nT	Electric field, mV/m
Field of magnetospheric convection (polar caps)	10	100	10
Atmospheric tide (low latitudes)	1	10	1
GW (daytime hemisphere)	1	10	1
Fields of the Earth and weather systems	10^{-4}	10^{-3}	10^{-4}

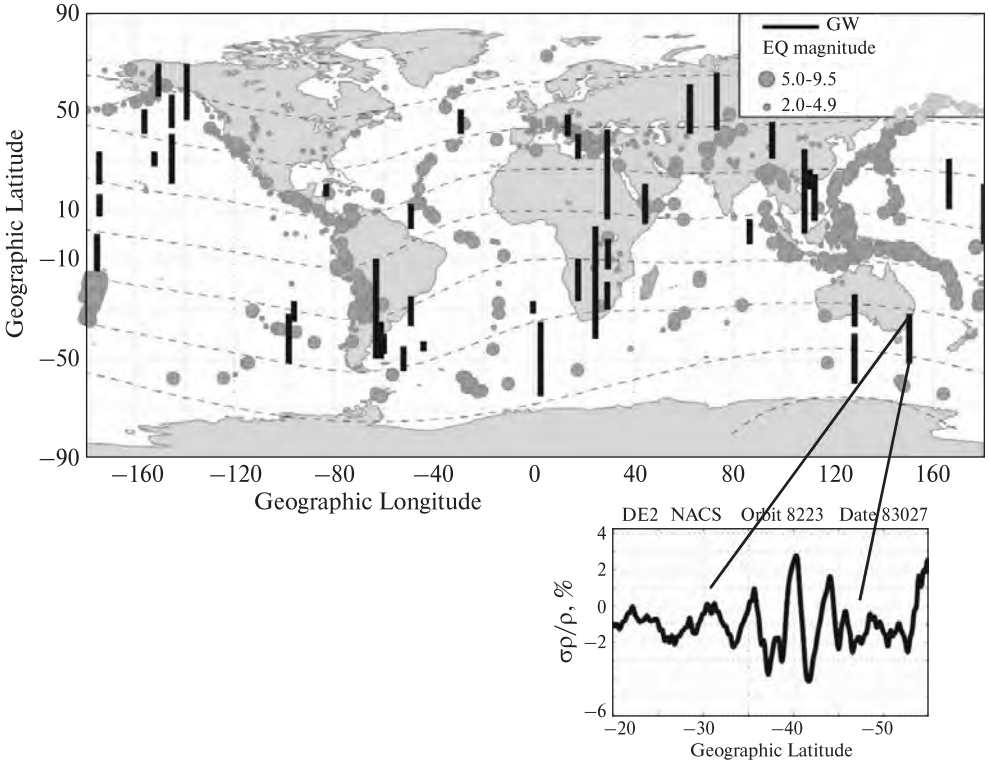

Fig 11. Georeferencing of GW bursts (solid segments) along the orbit of DE-2 and EQ epicenters (circles) for the period November 1982 – February 1983. The inlet shows GW waveform

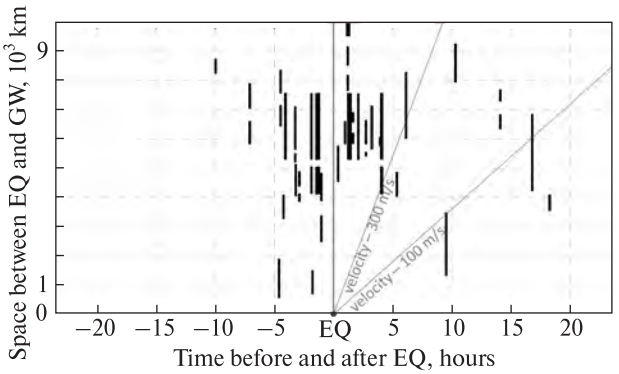

Fig. 12. Cause-and-effect diagram of EQ–GW connection

tsunami waves movement in variations of the total electron content of the ionosphere (TEC) [30]. Tsunami in the open ocean is a smooth and low water surface lifting with the speed about a fraction of centimeters per second — it is a very unproductive generator of atmosphere oscillations (in comparison, for example, with surface thermal anomalies). At the same time, the TEC value depends mainly on the electron concentration at altitude of ~250 km, where only a small part of GW spectral power penetrates. Thus, even such a weak GW source as tsunami, acting on such an inappropriate parameter as TEC, gives rise to a clearly detectable ionospheric effect.

Analysis of DE-2 satellite data. During the 1970s and early 1980s, a series of low Earth orbit satellite missions was implemented to record *in-situ* the parameters of the upper neutral atmosphere. The largest data set was obtained from DE-2 satellite operating at altitudes of 250–500 km in the period 1981–1983 in the conditions of high solar activity.

DE-2 satellite carried a set of instruments including Neutral Atmosphere Composition Spectrometer (NACS) and Wind and Temperature Spectrometer (WATS) which provided the measurement of a full set of hydrodynamic quantities of the neutral atmosphere – concentration, temperature and velocity of the gas components. This opened the possibility of calculating the spectral composition of atmospheric perturbations. Specifically, from the atmospheric particles vertical velocity $\tilde{V}_z$ (directly measured by WATS) and vertical displacement of particles δz (calculated from density variations measured by NACS), one can estimate the wave frequency $\omega \sim \tilde{V}_z / \delta z$. Further, wave vector components can be estimated using GW theory relations [18]. Algorithms for satellite data processing in order to decompose them into trend, wave process, and noise are described in [31–33].

Below are the original results described in detail in our works [4, 5]. Fig. 10 shows the georeferencing of the GW waveforms recorded at various DE-2 orbits. It can be concluded that the planetary distribution of GW consists of active high-latitude regions (Northern and Southern), where the thermosphere is strongly perturbed, and a quiet low-latitude region. The

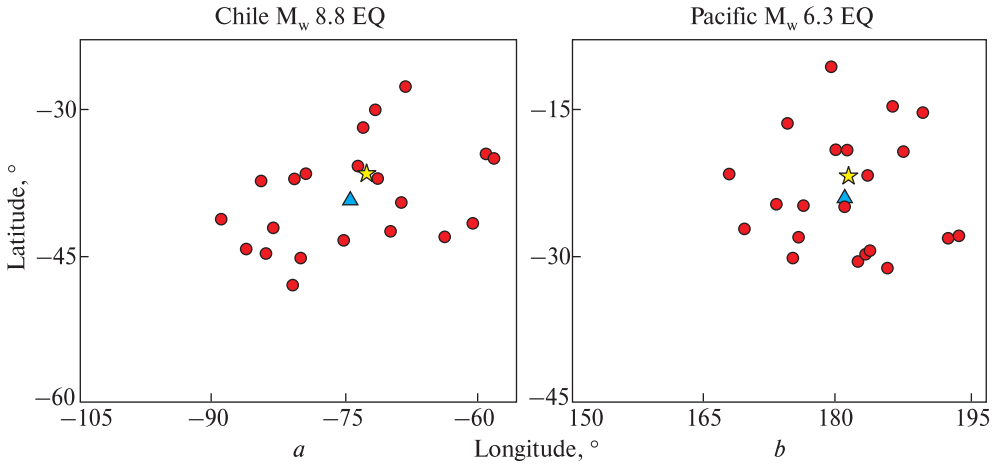

Fig. 13. Localization of ion density disturbances (circles) relative to the epicenter of a powerful EQ (triangle) according to DEMETER data (adapted from [27])

conditional boundary of the regions is at geomagnetic latitudes ~40–50 degrees [34, 35].

These data are consistent with the generally accepted idea that the main sources of thermospheric GW are the processes of gas heating and acceleration in auroras. From the generation regions in the auroral ovals, GWs propagate upward in latitude, filling the polar caps, and towards the equator, gradually attenuating at mid-latitudes. The disturbance in the active regions is so strong that makes it impossible to register GWs from surface sources. In a quiet region, on the contrary, we can extract them [35]. Since the map noticeably distorts the geographical proportions, let us specify that the quiet thermosphere occupies ~70%, and both active regions ~30% of the planet's surface. And majority of EQ-prone areas are just in quiet zone, what confirms the expedience of the research.

Further processing of DE-2 data allowed us to construct Fig. 11 which shows the location of the GW intensity bursts (wave packets) detected in the quiet region during the period November 1982 – February 1983, and the location of the epicenters of EQs that occurred during the same period. One can see that GW localization regions are mainly close to seismic ones. Taking into account that in the process of GWs propagation till ionosphere they may move for thousands of kilometers from the source, we can expect that they are caused namely by EQ. To test this assumption, we applied to the data analysis the epoch superposition method. At this, GW waveforms were the subject of theoretical analysis with the aim of calculating their spectral characteristics (frequencies, wavelengths, propagation velocities) and the set of events – EQ and GW – was selected according to the following criteria. Only strong EQs with magnitudes $M > 4.5$ were taken into account (what is the common assumption in seismic-ionospheric studies). Further, waves with phase velocity exceeding the speed of

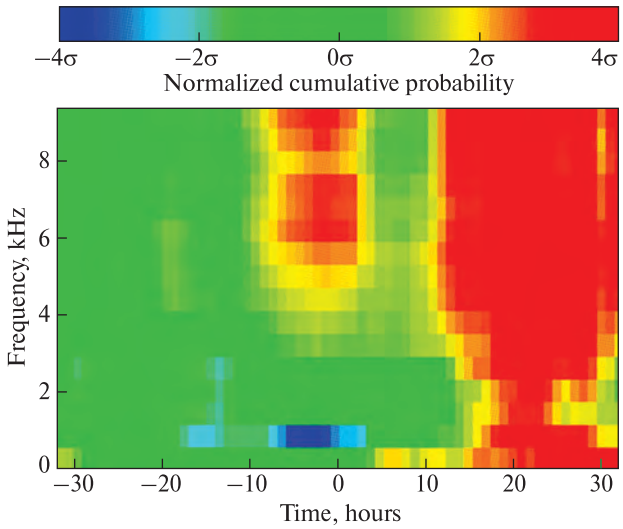

Fig. 14. Change in the plasma emissions intensity (magnetic component) relative to the EQ moment (M. Parrot, private communication). Symbol σ on the gray scale means statistical dispersion

sound in the lower atmosphere (~300 m/s) were discarded – such GWs cannot be physically generated by surface sources. In addition, were discarded the couples EQ–GW in which GWs propagated towards the epicenter (according to information on the direction of wave propagation along the satellite's orbit, determined from the order of the alternation of O and N_2 gases oscillations [36]).

Fig. 12 shows a cause-and-effect diagram, in which all registered EQs are merged to the frame origin, and GWs are placed in the time — distance coordinate system. The cluster of GW is distinguished at an average distance of 6000 km from the epicenter and at times +/– 5 hours relative to the moment of the EQ. We deliberately expanded the time window to two days to demonstrate the rarity of GW outside the cluster. The region of positive times in the diagram

we traditionally call the region of responses, although "after" does not necessarily mean "due to". In this example, the part of the cluster related to positive times lie inside the supersonic cone, and, in our opinion, cannot be associated with an EQ at time zero. We believe that all GWs in the cluster – both at negative and positive times — are generated by processes preceding the EQ, although some of the waves reached the satellite after the EQ occurrence. To the right of the sound cone there are several GWs with propagation speed of 100–150 m/s. We treat them as responses to the EQ shock.

Application of DEMETER satellite data. A special goal of the DEMETER mission (2005–2010) was to study the ionospheric EQ precursors. The statistical relationship between variations of ion density and EQ was investigated in [27] based on the data of Ion Analyzer Probe (IAP) aboard this satellite. The set of events was selected according to following conditions: EQ magnitude M > 4.8, satellite distance from the epicenter < 1500 km, Kp < 3. A time window was not specified, but the authors note that at an interval more than two weeks, any relationships of EQs and ionosphere disturbances are lost.

Fig. 13 shows an example of the localization of ionospheric disturbances selected in this way relative to the epicenter position of a future EQ. We emphasize that the circular structure of the perturbed zone is a characteristic feature of GW propagation.

Fig. 14 (courtesy of Michel Parrot, borrowed from personal presentation) shows a statistical diagram of the EMR generation in the epicentral regions of EQ, constructed in the same way. The whole data archive of IMSC experiment (Instrument Magnetometre Search Coil) onboard DEMETER satellite (about 9000 hours of measurement sessions for 15500 orbits during 6,5 years) has been processed using the epoch superposition method. The selected EQs set was limited by conditions: magnitude M > 5, hypocenter depth < 40 km. Let us pay attention that in addition of the supposed EQs precursors zone (~2–5 hours before EQ) also the area ~10 hours after the main shock is filled with a broadband noise. The only mechanism of postseismic-ionospheric interaction which may be characterized by such a delay time is the GW propagation.

Conclusions

As we showed, the EMR and/or quasistationary electric fields reaching the ionosphere are very small in comparison with the background fields there. Obviously, such small values can be neglected only when they stand next to a large values, but not zero. Regardless of its absolute value, EMR is responsible for a number of phenomena or properties of the ionosphere. Such as, for example, the precipitation of energetic particles from the radiation belts, plasma turbulization, the formation of the planet radio-frequency spectrum when viewed from space. Seismogenic EMRs also contribute to these phenomena, but their detailed quantitative study is the subject of further research.

As to the GW impact to the ionosphere from surface sources (seismogenic, weather, etc.), the discussed above theoretical and experimental patterns are generally consistent with each other. This allows us to draw a cautious conclusion that they are the most confident mechanism of lithospheric-ionospheric interaction. However, the same as for EMR, this conclusion requires further study and matching.

It should be stated that, at present state of research, even having all the information about the impending EQ (taken at least retrospectively), we are not able to calculate satisfactorily the characteristics of its ionospheric precursor. Still more, we are far from solving the inverse problem – by the observed parameters of an ionospheric disturbance to predict the parameters of a future EQ. One of the supposed cause of this is high dependence of GW propagation from ionospheric winds with unpredictable and unknown intensity and direction. In the result, even having confident satellite information about characteristic for EQ precursor ionospheric perturbation, the local source position may be determined with an error reaching about thousands of kilometers.

In our opinion, the further efforts of theorists should focus on the analysis and mathematical modeling of well-diagnosed seismic-ionospheric events ("case study" of "reference events"). As for future experiments, they should be planned in order to verify the theory – its unequivocal confirmation or refutation. Otherwise, we may expect again for the creation of speculative hypotheses that in the field of ionospheric EQ precursors have been multiplying for several decades.

To avoid this, the only issue is to plan and realize a combined ground-space experiment with synchronous registration of GW effects at the surface, atmospheric, ionospheric, and magnetospheric altitude levels. Only a cluster of satellites simultaneously registering necessary parameters at different altitudes may give exhaustive information about EQ precursors in the ionosphere. A set of scientific equipment installed on satellites must diagnose not only gas-plasma, but also the electrodynamic parameters of ionospheric disturbances (observed as standing formations with a wavelength of 100–400 km and periods of 10–50 s). Unfortunately, none of the currently planned space missions create the possibilities for carrying out such appropriate measurements. But the rapid development of cubsats, dramatically reducing the cost of manufacturing

and launch, gives a hope of the possibility of preparing and conducting such – a mandatory multipoint ground-space – experiment in the near future.

Summarizing, we can conclude that the idea of GW as an agent for transferring disturbances from surface sources to the ionosphere makes it possible to explain:

• Transportation of significant energy fluxes modifying the median parameters of *D*- and *E*- ionosphere regions (unlike to the electromagnetic radiation and quasi-stationary electric currents);

• Independence of the ionospheric response range from the intensity of the source as a result of nonlinear limitation of the GW growth with height;

• Shift of ionospheric disturbance occurring thousands of km away from the source. The time lag of about half-hour to more than ten hours;

• Transformation of the wave process in neutral atmosphere into forced magnetohydrodynamic oscillations of the ionosphere and magnetosphere.

REFERENCES

1. Molchanov, A. and Hayakawa, M. Seismo Electromagnetics and Related Phenomena: History and Latest Results. 2008. TERRAPUB Tokyo.

2. Pulinets S.A., Uzunov D.P., Karelin A.V., Davidenko D.V. Physical basis of the generation of short-term earthquake precursors. A complex model of geophysical processes in the lithosphere — atmosphere — ionosphere — magnetosphere system initiated by ionization. *Geomagnetism and aeronomy*. 2015. Vol. 55, No. 4. P. 1–19 (*in Russian*).

3. Rishbeth H. Ionoquakes: earthquake precursors in the ionosphere. *Eos*. 8 August 2006. Vol. 97, No. 2.

4. Korepanov V., Hayakawa M., Yampolski Yu., Lizunov G. AGW as seismo-ionospheric coupling response. *Phys. Chem. of the Earth*. 2009. Vol. 34. P. 485–495.

5. Lizunov G., Skorokhod T., Hayakawa M., Korepanov V. Formation of ionospheric precursors of earthquakes — probable mechanism and its substantiation. *Open Journal of Earthquake Research*. 2020. Vol. 9. P. 142–169. DOI: 10.4236/ojer.2020.92009.

6. Larkina V.I., Nalyvayko A.V., Gershenzon N.I., Liperovsky V.A., Gokhberg M.B., Shalimov S.L. Observations on the Interkosmos-19 satellite of VLF emissions associated with seismic activity. *Geomagnetism and aeronomy*. 1983. Vol. 23(5). P. 842–846 (*in Russian*).

7. Dudkin F., Korepanov V., Dudkin D., Pilipenko V., Pronenko V., Klimov S. Electric field of the power terrestrial sources observed by microsatellite Chibis-M in the Earth's ionosphere in frequency range 1–60 Hz, *Geophys. Res. Lett*. 2015. Vol. 42. DOI:10.1002/2015GL064595.

8. Bullough K., Kaiser R. Strangeways, H.J. Unintentional man-made modification effects in the magnetosphere. *Journal of Atmospheric and Terrestrial Physics*. 1985. Vol. 47. P. 1211–1223.

9. Rothkaehl H., Parrot M. Electromagnetic emissions detected in the topside ionosphere related to the human activity. *Journal of Atmospheric and Solar-Terrestrial Physics*. 2005. Vol. 67, No. 8–9. P. 821—828.

10. Nickolaenko A.P., Hayakawa M. Heating of the Lower Ionosphere Electrons by Electromagnetic Radiation of Lightning Discharges. *Geophys. Res. Let.*, 1995. Vol. 22, No. 22. P. 3015–3018.

11. Frenkel Ya.I. Theory of the phenomenon of atmospheric electricity. 2nd edition, rev. *M. KomKniga*. 2007. 160 p. (*in Russian*).

12. Mareev E.A. Achievements and prospects of research of the global electrical circuit. *Successes of physical sciences*. 2010. Vol. 180(5). P. 527–534 (*in Russian*).

13. Holzworth R.H. Quasistatic Electromagnetic Phenomena in the Atmosphere and Ionosphere. *In: Volland, H., Ed., CRC Handbook on Atmospherics, BocaRaton, FL: CRC press*. 1995. P. 235–266.

14. Bliokh P. Variations of electric fields and currents in the lower ionosphere produced by condactivity growth of the air above the future earthquake center. *Atmospheric and ionospheric electromagnetic phenomena associated with earthquakes. Ed. by M. Hayakawa. TERRAPUB, Tokyo*. 1999. P. 829–838.

15. Kelley M.C. The Earth's Ionosphere. Plasma Physics and Electrodynamics. *Academic Press. Inc. International Geophysics Series*. 1989. Vol. 43. 485 p.

16. Pulinets S.A., Boyarchuk K.A., Hegai V.V., Kim V.P., Lomonosov A.M. Quasielectrostatic model of atmosphere-thermosphere-ionosphere coupling. *Adv. Space Res*. 2000. Vol. 26, No 8. P. 1209–1218.

17. Denisenko V.V., Pomozov E.V. Penetration of the electric field from the surface layer of the atmosphere into the ionosphere. *Solar-terrestrial physics*. 2010. Iss. 16. P. 70–75 (*in Russian*).

18. Hines C.O. Internal atmospheric gravity waves at ionospheric heights. *Can. J. Phys*. 1960. Vol. 38. P. 1441–1481.

19. Tronin A.A. Atmosphere-lithosphere coupling. Thermal anomalies on the Earth surface in seismic processes. In: *Seismo Electromagnetics: Lithosphere-Atmosphere-Ionosphere Coupling, Ed. by M. Hayakawa and O.A. Molchanov, TERRAPUB, Tokyo*. 2002. P. 173—176.

20. Gokhberg M.B., Nekrasov A.K., Shalimov S.L. A new approach to the problem of lithosphere-ionosphere coupling before the earthquake. In: *Electromagnetic phenomena related to earthquake prediction, Ed. by M. Hayakawa and Y. Fujinawa, TERRAPUB, Tokyo*. 1994. P. 619–626.

21. Mareev E.A., Iudin D.I., Molchanov O.A. Mosaic source of internal gravity waves associated with seismic activity. In: *Seismo Electromagnetics: Lithosphere-Atmosphere-Ionosphere Coupling, Ed. by M. Hayakawa and O.A. Molchanov, TERRAPUB, Tokyo*. 2002. P. 335–342.

22. Chernogor L.F. The possibility of generating quasi-periodic magnetic earthquake precursors. *Geomagnetism and aeronomy*. 2019. Vol. 59, No 3. P. 1–9 (*in Russian*).

23. Nakamura T., Korepanov V., Kasahara Y., Hobara Y., Hayakawa M. An evidence on the lithosphere-ionosphere coupling in terms of atmospheric gravity waves on the basis of a combined analysis of surface pressure, ionospheric perturbations and ground-based ULF variations. *Journal of Atmospheric Electricity*. 2013. Vol. 33, No. 1. P. 53–68.

24. Yang S.S., Asano T., Hayakawa M. Abnormal gravity wave activity in the stratosphere prior to the 2016 Kumamoto earthquakes. *Journal of Geophysical Research: Space Physics*. 2019. 124. URL: https://doi.org/10.1029/2018JA026002.

25. Lighthill J. Waves in fluids. *Cambridge Mathematical Library. 2nd Edition*. 1978. 504 p.

26. Lizunov G.V., Leontyev A.Yu. Spectral ranges of AGV in the atmosphere of the earth. *Geomagnetism and aeronomy*. 2014. Vol. 54(6). P. 834–841 (*in Russian*).

27. Li M., Parrot M. Statistical analysis of an ionospheric parameter as a base for earthquake prediction. *J. Geophys. Res*. 2013. Vol. 118, No 6. P. 3731–3739. doi:10.1002/jgra.50313.

28. Pogoreltsev A.I. Production of electromagnetic field disturbances due to the interaction between acoustic gravity waves and the ionospheric plasma. *Journal of Atmospheric and Terrestrial Physics*. 1996. Vol. 58, No. 10. P. 1125–1141.

29. Yampolsky Yu.M., Zalizovsky A.V., Litvinenko L.N., Lizunov G.V., Groves K., Moldvin M. Variations of the magnetic field in the Antarctic and the conjugate region (New England), stimulated by cyclonic activity. *Radio Physics and Radio Astronomy*. 2004. Vol. 9, No. 2. P. 130–151 (*in Russian*).

30. Rolland L.M., Lognonn´e P., Astafyeva E., Kherani E.A., Kobayashi N., Mann M., Munekane H. The resonant response of the ionosphere imaged after the 2011 off the Pacific coast of Tohoku Earthquake. *Earth Planets Space*. 2011. Vol. 63, No. 7. P. 853–857.

31. Gross S.H., Reber C.A., Huang F.T. Large-scale waves in the thermosphere observed by the AE-C satellite. *The Transactions on Geoscience and Remote sensing*. 1984. GE-22(4). P. 340–351.

32. Lizunov G.V., Skorokhod T.V. On the selection of wave disturbances against the background of trends in satellite observations of the thermosphere. *Space science and technology*. 2018. Vol. 24, No. 6. P. 57–68 (*in Russian*).

33. Skorokhod T.V. Internal gravity waves in the thermosphere according to direct satellite measurements. *Thesis for scientific degree of Candidate of physical and mathematical sciences. Space Research Institute of NAS of Ukraine and SSA of Ukraine. Kyiv*. 2018. 208 p. (*in Ukrainian*).

34. Hedin A.E., Mayr H.G. Characteristics of Wavelike Fluctuations in Dynamics Explorer Neutral Composition Data. 1987. *J. Geophys. Res*. Vol. 92, No. A10. P. 11,159–11,172.

35. Skorokhod T.V., Lizunov G.V. Localized packets of acoustic-gravity waves in the ionosphere. *Geomagnetism and aeronomy*. 2012. Vol. 52, No. 1. P. 93–98 (*in Russian*).

36. Fedorenko A.K. Characteristics of atmospheric gravity characteristics in polar regions on the basis of mass spectrometric satellite spectra. *Radio Physics and Radio Astronomy*. 2009. Vol. 14, No. 3. P. 254–265 (*in Ukrainian*).

MODELING THE INTERACTION OF SPACECRAFT WITH PLASMA FLOW, ELECTROMAGNETIC RADIATION, ELECTRIC AND MAGNETIC FIELDS IN THE EARTH'S IONOSPHERE

V. Shuvalov, Yu. Kuchugurnyi, D. Lazuchenkov

Institute of Technical Mechanics of NAS of Ukraine and SSA of Ukraine

Modeling the interaction of spacecraft with the ionospheric medium, electric and magnetic fields includes three areas of research aimed at:

1. Ensuring electromagnetic compatibility and durability of materials and spacecraft's structural elements to the influence of the environment in orbit;

2. Application of the spacecraft for monitoring the parameters of the ionospheric plasma and identifying the sources of their disturbances along the sub-satellite path;

3. Using the electromagnetic force in the system "spacecraft magnet — near-satellite plasma" as the driving force of the spacecraft.

Physical modeling has been carried out on the plasma-electrodynamic set of the ITM (Fig. 1) capable to reproduce space factors such as high vacuum, ultraviolet (UV) radiation in the wavelength range of ~100—200 nm, thermal cycling ±100 °C, supersonic flows of atomic oxygen (AO) plasma, flows of high-energy (~35 keV) electrons. The plasma-electrodynamic set of the ITM had obtained the status of a scientific object "National Property of Ukraine".

Long-term spacecraft operation in the Earth's ionosphere

One of the means of ensuring the long-term operation of a spacecraft in the Earth's ionosphere is predicting the degradation of the functional characteristics of materials and structural elements influenced by the environment in orbit.

The aim of research is to obtain dependences of changes in properties, functional characteristics in time during the active operation cycle of the spacecraft. In Fig. 2, as an example, the time dependence of the degradation of the electrical power of the spacecraft's silicon batteries $P(t)/P_0$ (normalized to its initial value) during a 10-year operation in circular orbits: polar (~800 km), geostationary (~40000 km) and the orbit of GPS (~20000 km). Values of $P(t)/P_0$ vs. operation time are presented at Fig. 2.

For typical spacecraft structural materials in the ionosphere at altitudes of 200—700 km, the output dependences are: time dependences of mass-dimensional and thermo-optical characteristics; schemes of dynamic interaction in the system "AO – spacecraft material"; dependencies predicting the state of the material during long-term orbital operation.

Fig. 1. Plasma-electrodynamic set of the ITM

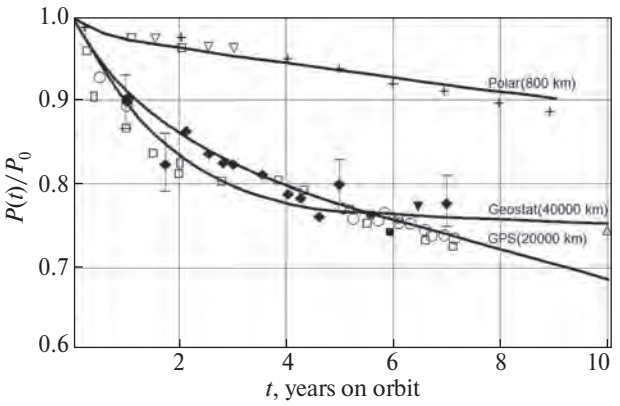

Fig. 2. Electric power loss of spacecraft solar array. Solid curves – calculated and experimental integral values of $P(t)/P_0$ under the influence of a complex of space factors; markers – measurements during solar arrays operation on various spacecraft

Dependences representing the synergistic effect of "AO + UV" on the mass loss of polymeric materials containing a monomer of the group CH_n are shown in Fig. 3.

The threshold values of the ratio Φ_v / Φ_{AO}, condition for the presence of a synergistic effect for three levels of solar activity at different altitudes in the Earth's ionosphere are determined [1].

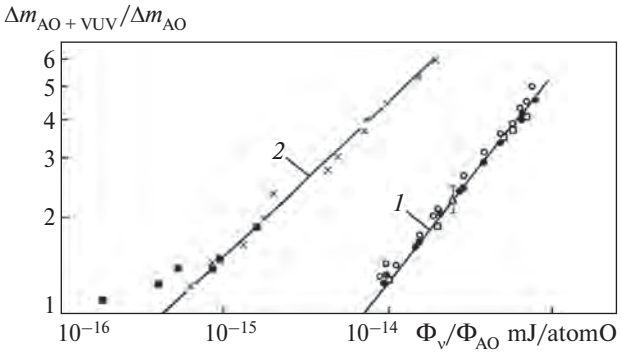

Fig. 3. Polymer mass loss vs. the ratio of UV flux density (Φ_v) to AO flux density (Φ_{AO}); *1* – polyimide kapton, *2* – polyethylene

Monitoring of kinetic parameters of ionospheric plasma and identification of sources of their disturbances

To implement the monitoring of the parameters of the neutral and charged constituents in the ionospheric plasma from the spacecraft a new generation set of scientific equipment has been developed and

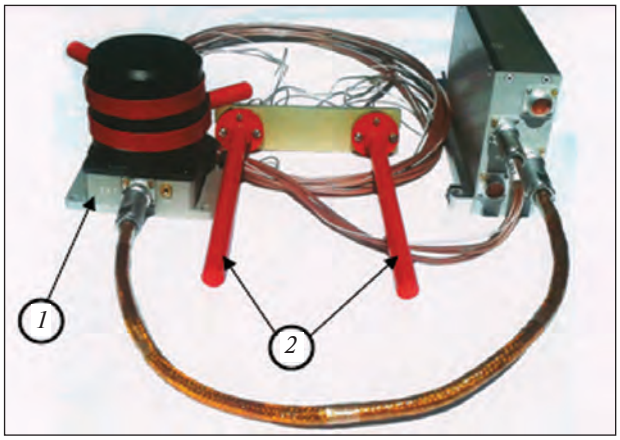

Fig. 4. The new generation equipment for spacecraft "Sich-2-1" and "Microsat". *1* – DN (detector of neutral particles); *2* – DE (detector of charged particles)

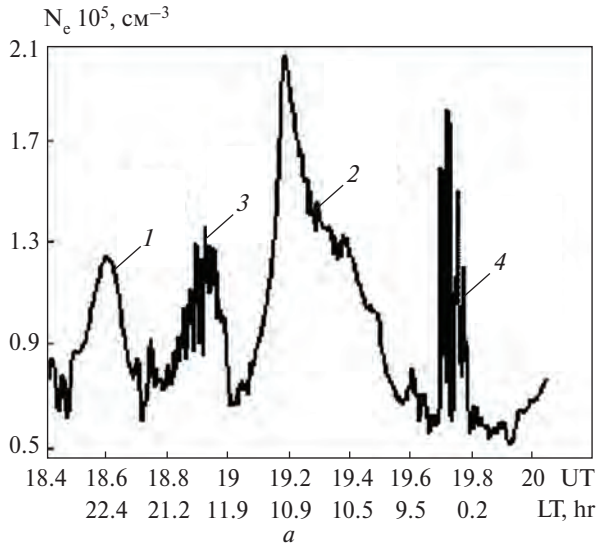

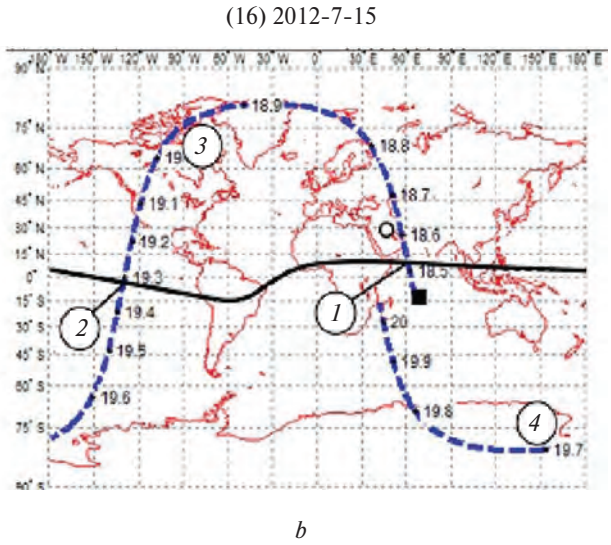

Fig. 5. Electron density on orbit (*a*) and positions of disturbance sources (*b*): N_e – electron density, UT – universal time; LT – local time; *1, 2* – equatorial ionospheric anomaly; *3, 4* – polar ovals; dashed curve – sub-satellite path; solid line – magnetic equator, marker – earthquake

Fig. 6. "Magnetized" sphere in hypersonic plasma flow

manufactured. One set of equipment is integrated in the structure of the "Sich-2-1" spacecraft; another one is prepared for the "Microsat" spacecraft. The set of the equipment is shown in Fig. 4. The previous generation equipment had successfully operated on the "Sich-2" spacecraft.

To identify the sources of perturbations of the space-time distributions of the parameters of neutral and charged particles along the spacecraft orbit, algorithms and procedures for localization the sources of natural and man-made catastrophic phenomena on the sub-satellite path have been developed. Fig. 5 shows the distribution of the electron density along the orbit of the "Sich-2" spacecraft and the positions of the disturbance sources on the sub-satellite path [2].

Dynamic interaction of a "magnetized" spacecraft with a supersonic rarefied plasma flow

The result of the dynamic interaction in the system "spacecraft's own magnetic field – ionospheric plasma" is an electromagnetic force. The natural analogue of the system is the "magnetized" planets of the solar system, which interact with the solar wind plasma flow. The details of producing the electromagnetic forces in the "magnet – plasma" system in relation to the conditions of spacecraft operation in the Earth 's ionosphere at altitudes of 200–1000 km are studied by the methods of physical modeling. It is shown that the electromagnetic force generated in the system "onboard magnet – near-satellite plasma" can effectively be used in solving the problem of preventing the pollution and cleaning the near-Earth space from space debris. Fig. 6 illustrates the structure of hypersonic rarefied plasma flow past a "magnetized" sphere on the ITM's set [3, 4].

$1 - \vec{B}_w = 0$ ("non-magnetized" sphere), $2 - \vec{B}_w \uparrow\downarrow \vec{U}_\infty$ ("magnetized" sphere, coaxial orientation of the vectors of the own magnetic field $\vec{B}_w$ and the plasma flow velocity $\vec{U}_\infty$); $3 - \vec{B}_w \perp \vec{U}_\infty$ (mutually orthogonal orientation of vectors).

Magnet with induction of $\vec{B}_w \approx 0.8...1.5$ T is proposed as a source of the spacecraft's own magnetic field. Its capability is confirmed of solving the problem of cleaning near-Earth space from space debris by deorbiting it to the dense layers of the Earth's atmosphere (where it's naturally gets combusted).

Researches were carried out within the framework of the departmental themes of the NAS of Ukraine, projects of The Target Program of the Space Scientific Research of the NAS of Ukraine and the cooperation program between the "Yuzhnoye State Design Office" and the institutes of the NAS of Ukraine.

REFERENCES

1. Shuvalov V., Reznichenko N., Tsokur A., Nosikov S. Synergetic effect of the action of atomic oxygen and vacuum ultraviolet radiation on polymers in the Earth's ionosphere. *High Energy Chemistry*. 2016. Vol. 50(3). P. 171–176. DOI: 10.1134/S0018143916030140.

2. Shuvalov V., Lazuchenkov D., Gorev N. & Kochubei G. Identification of seismic activity sources on the subsatellite track by ionospheric plasma disturbances detected with the Sich-2 onboard probes. *Advances in Space Research*. 2018. Vol. 61. P. 355–366. DOI: 10.1016/j.asr.2017.08.001.

3. Shuvalov V., Gorev N., Tokmak N., Pis'mennyi N. & Kochubei G. Control of the drag on a spacecraft in the earth's ionosphere using the spacecraft's magnetic field. *Acta Astronautica*. 2018. Vol. 151. P. 717–725. DOI: 10.1016/j.actaastro. 2018.06.038.

4. Shuvalov V., Gorev N., Tokmak N. & Kuchugurnyi Y. Drag on a spacecraft produced by the interaction of its magnetic field with the Earth's ionosphere. *Physical modelling. Acta Astronautica, Elsevier Ltd*. 2020. Vol. 166. P. 41–51. DOI: 10.1016/j.actaastro.2019.10.018.

CONCEPT OF THE PARTICLE MICROBURSTS SATELLITE EXPERIMENT WITH THE MIRA_EP COMPACT INSTRUMENT ON THE 2U CUBESAT PLATFORM

O. Dudnik[1], V. Boiko[1], O. Yakovlev[1], V. Adamenko[2], R. Antypenko[2], A. Movchaniuk[2], N. Yezerskyi[2], A. Didenko[3], I. Lazariev[3], T. Gorbachova[3]

[1] Institute of Radio Astronomy of NAS of Ukraine
[2] National Technical University of Ukraine "Igor Sikorsky Kyiv Polytechnic Institute"
[3] Institute for Scintillation Materials of NAS of Ukraine

The geomagnetic disturbances in the Earth's magnetosphere influence profoundly on the state of both the electron and proton Van Allen radiation belts, one of the important components of the space weather. In recent years, interest in registering, analyzing, discussion, and interpretation of the microbursts, i.e. short-term sharp increases of a differential flux of high-energy charged particles at LEO (Low Earth Orbit) have substantially increased. Simultaneously, new technologies have been rapidly developed, both in the area of detection of the elementary charged particles and in the construction of space microelectronics and microsatellites. In particular, over the past years, nanosatellites in the CubeSat standard were developed, manufactured and launched into LEO, whose mission was to record and study the characteristics of electron microbursts precipitating from the Earth's radiation belts.

Here, we present the concept of the satellite experiment execution on the base of 2U CubeSat nanosatellite technology. The principal core in this scientific experiment is the compact instrument which is developing in the 1U CubeSat standard and aimed to study the nature of high-energy charged particles microbursts present in the Earth magnetosphere. A functional diagram, a description of the structural modules, and some selected technical characteristics of the miniaturized electron and proton Recording Analyser MiRA_ep are shown. The principles of the production of organic single crystals and preparation of the facility to produce both types of detectors for the MiRA_ep instrument are presented. Also, we describe a conception and technical requirements to service systems of the 2U CubeSat nanosatellite to supply the scientific experiment with the MiRA_ep device.

A brief scientific rationale

A detection of subrelativistic electron microbursts at the peripheral edge of the outer electron radiation belt, at low latitudes and in the near-equatorial zone is one of the significant achievements in the study of space high energy ionizing environment. One more phenomenon is the registration of short-lived sporadically arising radiation belts in the slot between Van Allen inner and outer belts as well as below the inner electron belt. Radiation zones generated in the slot between Van Allen belts, at mid-latitudes, and particle microbursts on the edges of radiation belts are not yet studied sufficiently. Researchers have not yet proposed credible mechanisms for generating the intense electron bursts at middle and low latitudes, which is observed on LEO satellites.

Different kind of space instruments is being developed with a purpose to solve the listed scientific tasks. Engineers and elaborators of cosmic industry plan or have already implemented the miniature satellite devices for high energy elementary charged particle monitoring. As an example, it can be pointed a compact device SPEED, which Indian scientists and students from the Madras Institute of Technology developed for the registration of electrons and protons on board the nanosatellite IITMSAT. This device is aimed to study precipitating charged particles from the Van Allen radiation belts related to seismo-electromagnetic emissions. The silicon PIN and scintillation CsI(Tl) detectors are used as sensors in the RADMON (Radiation Monitor) instrument of the Finnish student nanosatellite Aalto-1 [1].

The main scientific tasks of the experiment, which we propose with the compact MiRA_ep instrument, are as follows [2]:

1. Verification of the existence the additional inner electron radiation belt at $L \sim 1.6$ for particles with energies from tens of keV to $E \sim 0.5$ MeV in geomagnetically quiet conditions;

2. Determination of the energy spectra of particles in stationary radiation belts and in microbursts outside of the belts;

3. Determination of the degree of anisotropy for directions of the electron velocities in the midpoint of the radiation belts and in micro splash at the edges of Van Allen belts and beyond belts during solar, magnetospheric and ionospheric activities.

4. Search and identification of distinctive features between micro-bursts of electrons generated due to magnetospheric, solar and interplanetary activities, and bursts correlated with seismic activity.

Prompt description of the MiRA_ep instrument

The MiRA_ep instrument as a payload of the 2U CubeSat nanosatellite will comprise of three modules: detector head, and the analog and digital units (Fig. 1). Each of the modules is a separate block, which is connected with each other with cables and connectors (Fig. 2). The DC/DC voltage converters will be installed in the analog and digital modules, which will provide these modules with necessary voltage levels.

The detector head will consist of two thin scintillation D1 and D3 detectors and one thick scintillation detector D2 of total energy absorption manufactured from the *p*-terphenyl single crystal. The head will also contain a collimating system that will restrict the angle of view in two opposite directions (Fig. 3). Detectors will be inserted into the mechanical design so that to form a bidirectional telescopic system (Fig. 4). A mechanical collimating construction will form a solid angle with a cross-cut angle of view of the device $\Delta\theta = 34°$.

The analog module will consist of three spectrometric analog electronic channels: the two identical channels will process and shape analog signals incoming from also identical thin D1 and D3 detectors. The third spectrometric electronic channel will shape the signals incoming from a thick *p*-terphenyl scintillation detector D2.

The digital processing module will sort incoming signal packets by energy and types, with the subsequent accumulation of information received.

Scintillation detectors: prototyping and preparing of the crystal growth setup

The detection and spectrometry of near relativistic electrons are carried out effectively with the usage of organic scintillators. These materials change particle motion trajectories slightly only due to their small atomic numbers. This leads to the almost full absence of the backscattering of the particles. A low density and effective atomic number of elements composing the organic scintillators make detectors to be less sensitive to the registration of X-rays and gamma-radiation in comparison with the inorganic scintillators. A short decay time ($\sim 3 \times 10^{-8}$ s) of the luminescence in comparison with a longer decay time for inorganic

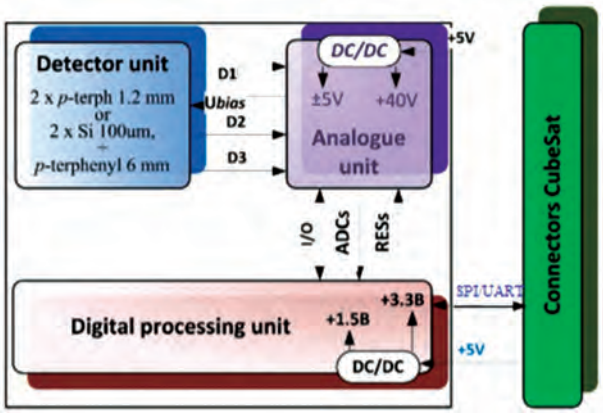

Fig. 1. A structural scheme of the MiRA_ep instrument

Fig. 2. Design view of the instrument

Fig. 3. Collimating system of the detector head

Fig. 4. A view of a manufactured prototype of the detector head (*left-hand*), and scintillation detectors in their holders (*right-hand*)

Fig. 5. An ingot of the *p*-terphenyl single crystal grown by the Bridgman method (*a*); a cylindrical workpiece of the *p*-terphenyl with the crystallographic axe's direction marking, and the *p*-terphenyl single crystal in a parallelogram form after mechanical treatment

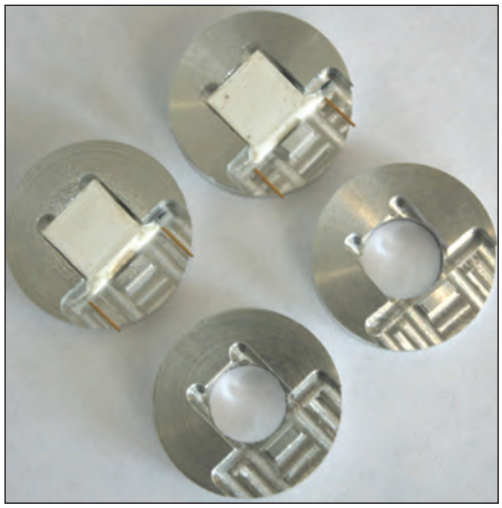

Fig. 6. Prototypes of p-terphenyl scintillation detectors for the MiRA_ep instrument

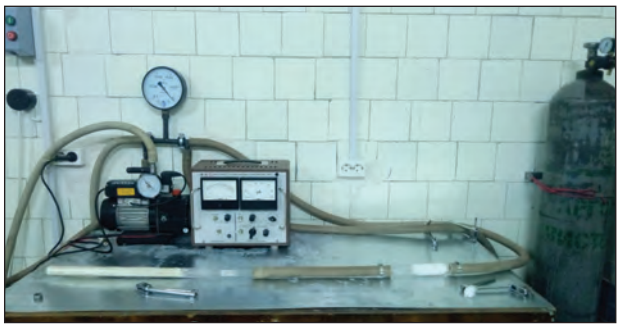

Fig. 7. Equipment for ampoule sealing-off

scintillators (~10^{-6} s and more) is an important advantage of organic scintillators. They are also highly transparent to the spectrum of their own fluorescence.

The *p*-terphenyl is one of such type of organic scintillators. It has a relatively high melting point (T = 214 °C) and a low cost. The absolute value of the light output of this scintillator is 24,950 photons / MeV. The *p*-terphenyl, doped with 1,4-diphenyl-1,3-butadiene we used as a material for sensors manufacturing of the MiRA_ep instrument.

The direction of growth of the *p*-terphenyl single-crystal usually coincides with the *c* axis of the single crystal, so the base of the cylinder matches up with the cleavage plane *ab*. The crystals oriented along the crystallographic axes *a* and *b*. Cut pieces of the single crystals are abraded to the required sizes. The polishing of the samples typically carried out using the polishing composition described in [3]. Such special polishing composition provided an improvement of the polished surface quality and increased scintillation and optical characteristics of the detectors due to the enhancement of the light collection coefficient.

The difference in the technical light yield values along the crystallographic lattice axes for the *p*-terphenyl single crystal should be also taken into consideration in the detectors' manufacturing process. Particularly, in previous works, we showed that the highest technical light yield was detected along the axis *b* of the *p*-terphenyl crystallographic lattice [4–7], carrying out studies of scintillation properties of a small cube-shaped detector along characteristic axes *a, b* and *c*.

At the initial stage of works, we executed prototyping both thin and thick scintillation detectors for the detector head of the instrument. The *p*-terphenyl single crystal with a heightened light yield was grown to produce the two thin detectors (ΔE-detectors) and a total energy absorption detector. The amount of 1.4-biphenyl-1.3-butadiene dopant was increased from 0.1 wt % (typical value) to 0.3 wt %. A cylinder of the thickness of 7 mm was cut out from the grown ingot at right angles to the growth direction of the single crystal (Fig. 5).

Fig. 6 demonstrates manufactured prototypes of E-detectors, inserted into metallic holders to be installed in the detector head of the instrument.

The production of organic single crystals consists of stages of purification of raw materials, growth, and processing of single crystals. During the purification, commercially available *p*-terphenyl is poured onto ampoule in a form of the white finely dispersed powder. A vacuum is created in an ampoule on the ampoule sealing-off table (Fig. 7) employing the vacuum pump. The latter is filled further with the cleared argon. The pumping out and filling the ampoule

with argon is repeating at least five times. After filling with argon, the ampoule is sealed-off. The sealed ampoule is placed in the facility of zone melting (Fig. 8), in which the ampoule passes 12 zones at a lifting speed of 5 mm/h. After purification by the zone melting method, the impurities are deposited in the lower part of the ampoule.

From the cleaned ingot we take the upper half to fill the growth ampoule. We fix the seed at its end before filling of the growth ampoule. The 1.4 diphenyl-1,3-butadiene(1.4biphenyl-1.3-butadiene) should be added to the growth ampoule filled with purified *p*-terphenyl. Pumping air, filling with argon, and sealing-off the growth ampoule is carried out on the special table of preparation of ampoules similar to the stage of purification (Fig. 7). The sealed-off ampoule is placed in a vertical oven with two heaters to the installation for crystal growth (Fig. 8).

The temperature of the upper half is kept at the level T = 240 °C, and the lower half at T = 125 °C. The speed of movement of the ampoule is ~1 mm/h. After the growth of the crystal, the temperature is gradually reduced to room temperature at a rate of 2 °C/h. The crystals of the required shape are cut from the single crystal ingot after its bakeout and removal from the ampoule.

Monte Carlo simulation of the light collection efficiency inside the volume of *p*-terphenyl scintillators

The efficiency of light collection for scintillation detectors on the base of the *p*-terphenyl doped with 1,4-diphenyl-1,3-butadiene for one or several PDs was evaluated. On the one hand, this efficiency is characterized by the light collection coefficient (LC). On the other hand, the LC-values are differing for different points of the scintillator volume, i.e. there is a certain range of the LC-values. This spread also characterizes the efficiency of the light collection.

The DETECT 2000 program was used to calculate the efficiency of light collection by simulating light transmission. In this program, from each selected point of the scintillator volume, the same specified number of photons (10,000 photons in our case) is emitted in random directions. The program traces the fate of each photon, noting the absorption of photons in the bulk and at the boundaries of the scintillator, reflection at the boundaries of the scintillator, and hitting the PD. In the latter case, the photon is considered as detected.

For modeling in the DETECT 2000 program, geometric models of scintillators were built in the form of rectangular parallelepipeds with dimensions of 10 × 10 × 1 mm and 15 × 15 × 5 mm, as well as PDs with dimensions of 10 × 1 mm for the first scintillator

Fig. 8. A facility for zone melting and crystal growth

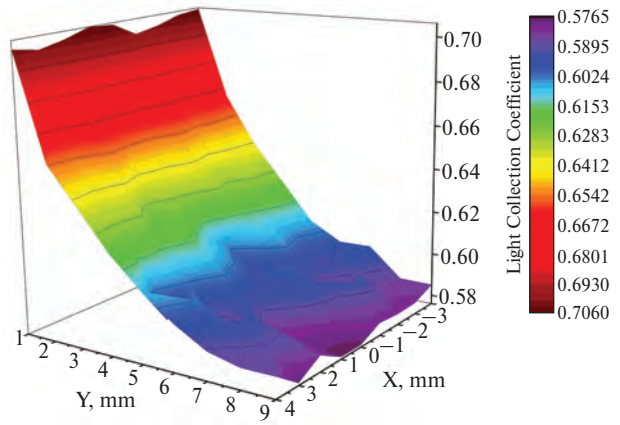

Fig. 9. Distributions of LCs over the volume of a 10 × 10 × 1 mm scintillator

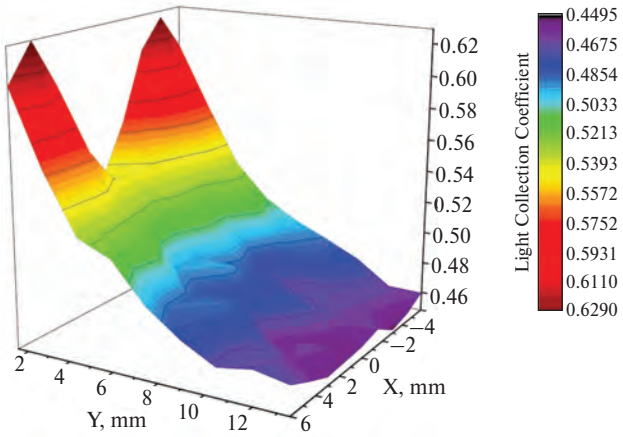

Fig. 10. Distributions of LCs over the volume of a 15 × 15 × 5 mm scintillator

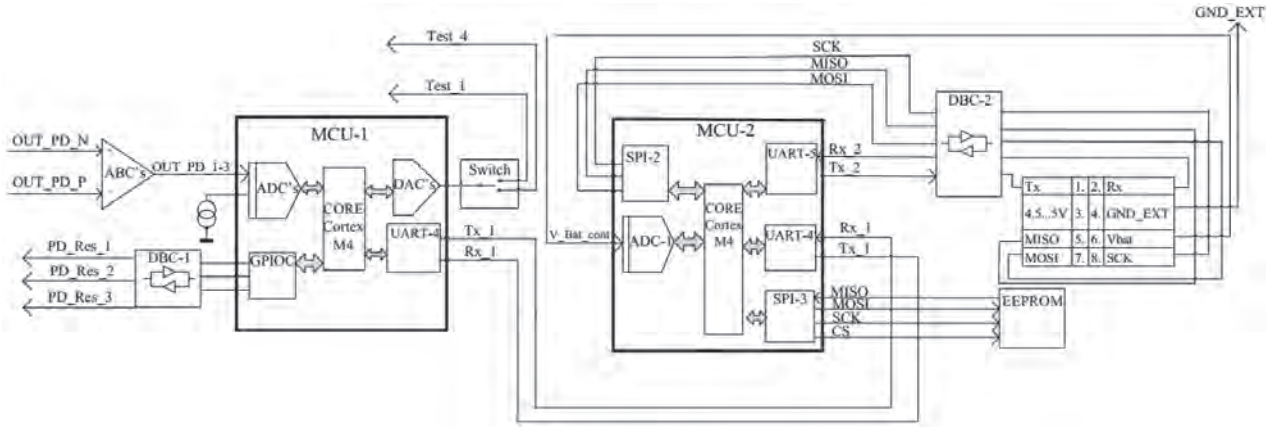

Fig. 11. Simplified functional scheme of the digital signal processing module

and 5 × 5 mm for the second one. In both cases, the PDs were in contact with one of the smallest side of the scintillator surface. We used the following optical characteristics of a PTF-based scintillator: refractive index – 1.65, a free path of scintillation light – 50 mm), and an optical PD window (refractive index – 1.45, a free path of scintillation light – 2000 mm). All the surfaces of the scintillators were polished and covered with a reflector with a reflectance of 0.98, except for the point of optical contact with the PD.

As a result of the simulation, for each point of emission in the volume of a scintillator, the LC was found as the ratio of the number of detected photons to the number of emitted ones. The dependences of the LC-values on the coordinates of the scintillation in the volume of the scintillator are shown in Fig. 9 and Fig. 10 in the form of spatial grids. The abscissa axis (Y-axis) shows the position of the flashpoint along with the scintillator height (the plane of the PD input window intersects the Y-axis at the point Y = 0). The ordinate axis (X-axis) shows the position of the scintillation across the detector width. On the axis of the applicate, the values of LC are given in relative units.

Fig. 9 shows the LC distribution over the volume of 10 × 10 × 1 mm scintillator with one photodetector 10 × 1 mm. Fig. 10 shows the LC distribution over the volume of a 15 × 15 × 5 mm scintillator with two photodetectors having active area 5 × 5 mm.

One can see from Fig. 9 and Fig. 10 that the highest light collection coefficients are observed for the cases when scintillations arise near the PD (small values of Y). When the initial locations of scintillations move away from the PD (with increasing Y), the LC decreases.

Additionally, to obtain the spatial distributions of the LC for each case of the "scintillator – PD" system, we determined the following parameters: the mean (MLC) and the relative scatter of the LC (RSLC). The obtained values of MLC and RSLC for a 10 × 10 × 1 mm scintillator are 0.62 and 0.063, and for a 15 × 15 × 5 mm scintillator, 0.5 and 0.09, respectively.

MLC-value influences the amplitude of the output pulse and PD intrinsic resolution, and RSLC value influences the resolution of the scintillator. The higher the MLC and the lower the RSLC are the better options. These parameters improve with an increase in the number of PDs.

A digital signal processing module

In an analog module containing peak detectors, the information about particle energy is obtained. However, complete information about the type and energy of the particle can be obtained only by comparing the output voltages of all three peak detectors [8]. For this reason, was developed the Digital Signal Processing (DSP) module.

The DSP module is developed on the two microcontrollers with hardware support for DSP [9]. It has such functions as the digital-to-analog conversion of three peak detectors signals of the analog module, sorting particles by the type and energy, operability testing of three channels of the analog module, storing measurement results in a FLASH drive, transferring measurement results to the on-board computer, monitoring the temperature of the digital processing module, monitoring the supply voltage. Let's consider the functioning of the digital signal processing module according to the simplified block diagram (Fig. 11).

Signals of the output voltages of peak detectors of the analog module in a form of differential voltages are fed to the input of the DSP (OUT_PD_N, OUT_PD_P). Instrumentation amplifiers (Analog buffer cascades, ABCs) convert differential signals to unipolar ones, which are digitized by 12-bit ADCs built into the first MCU-1 microcontroller. The ADC is triggered by the ready signals (PD_HP) generated by the peak detectors of the analog module. Ready signals are fed to the MCU-1 microcontroller input through a level

converter (DBC-1), which matches the logic signal levels of the digital and analog modules.

As a result of calculations in the MCU-1 core, the particles are sorted by types and energies, based on the output voltage values of the peak detectors. The MCU-1 is responsible for testing the operability of peak detectors. For this, test signals (TEST1 – TEST4) are generated using the built-in DACs, which are fed to the input of the analog module. As a result of monitoring the output voltages of the corresponding peak detectors, a decision is made about their operability/inoperability. Accumulated information about the types and grades of particles is transmitted via the UART protocol to the second microcontroller MCU-2 (Tx_1, Rx_1).

The second microcontroller MCU-2 stores information on energies and types of particles in external EEPROM storage. Information from the EEPROM is transmitted to the on-board computer via a DBC-2 level converter on request. On the MCU-2, it performs the functions of temperature measurement and supply voltage monitoring. Structurally, the digital signal processing module (Fig. 12) is made on a printed circuit board with dimensions comparable with the dimensions of the CubeSat format module. There are two auxiliary voltage converters on the board to isolate the analog and digital grounds.

The communication between analog and digital modules is via a pin header. Communication between the digital signal processing module and the on-board computer is via a second male connector. There are two auxiliary voltage converters on the board which is

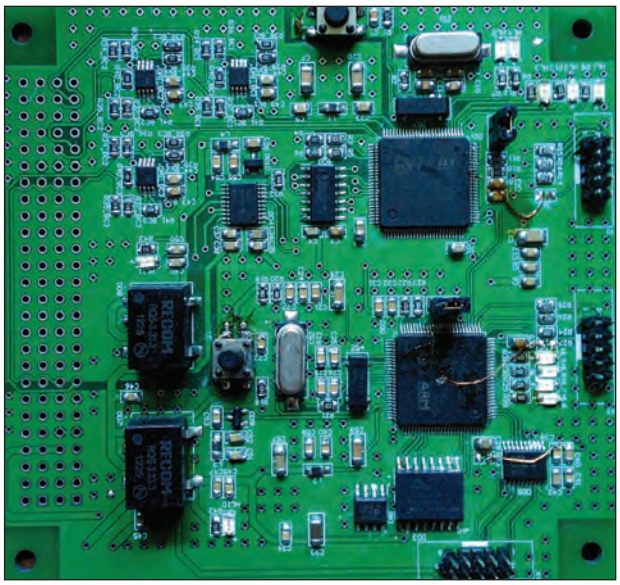

Fig. 12. Common view of digital processing module

dedicated to isolating an analog and digital ground. Communication between the digital signal processing module and the on-board computer takes place via a second male connector.

Conception and technical requirements to service systems of the nanosatellite

The rough structure of the nanosatellite for implementation of the scientific project is shown in Fig. 13. The nanosatellite is manufactured in the 2U CubeSat format and has a unified design.

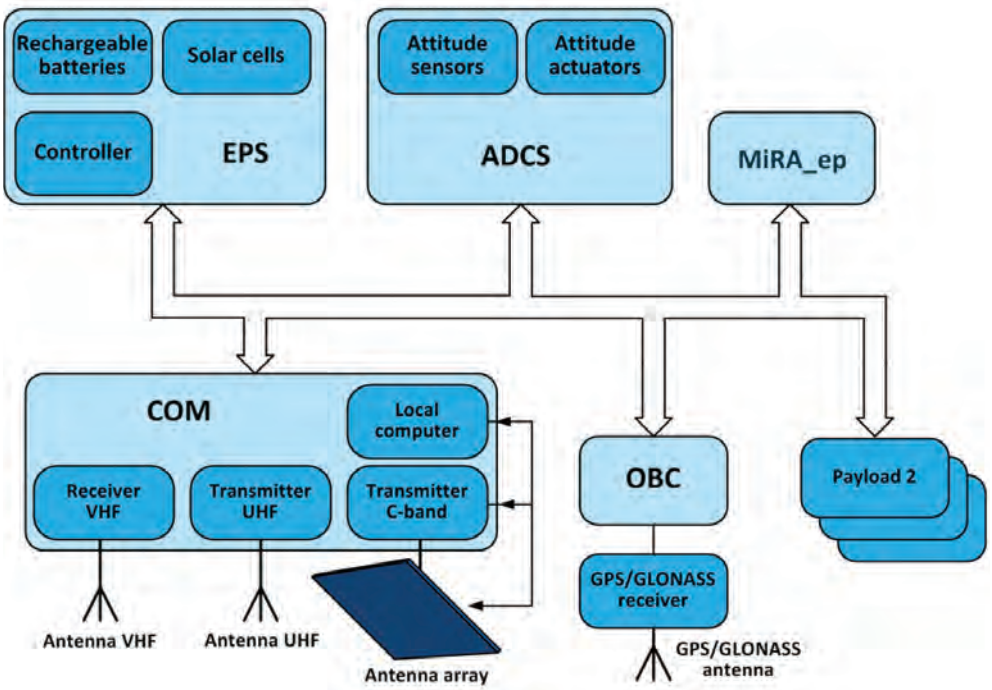

Fig. 13. The rough structure of the nanosatellite

The satellite consists of the MiRA_ep instrument as a scientific payload, electrical power system (EPS), attitude determination and control system (ADCS) with attitude sensors and actuators, onboard computer (OBC), GPS/GLONASS receiver, communication system (COM). The nanosatellite is capable to serve extra payloads with the appropriate corrections of the nanosatellite design.

The electrical power system provides a persistent power supply to all nanosatellite systems. A system uses solar cells and rechargeable batteries. The solar cells are qualified solar cells for space applications with about 30% efficiency using GaAs triple-junction technology. They are located on the satellite body. The controller provides control and optimization of the power system operation.

The attitude determination and control system holds the nanosatellite's position providing execution of scientific experiments and the accurate orientation of the communication system antennae. Expected attitude control accuracy is less than 1 degree.

The onboard computer provides control and coordination of all satellite systems and the MiRA_ep instrument, with the help of the GPS/GLONASS receiver determines the coordinates and speed of the satellite in an orbit.

The nanosatellite communication system presupposes the presence of the three independent radio channels for transmitting command messages from a ground control station to the nanosatellite, telemetry information, and scientific data from the nanosatellite to terrestrial receivers. Radio channels operate in different frequency bands independently: VHF, UHF, and C (probably X) band. The VHF uplink consists of the onboard VHF receiver with a non-directional deployable antenna system and Ground Station VHF uplink transmitter with the beam-tracking antenna system. Data rate up to 2.4 kbps. The UHF downlink consists of the onboard UHF transmitter with the non-directional deployable antenna system and the ground station UHF uplink receiver with a beam-tracking antenna system. Data rate up to 96 kbps.

The on-board VHF receiver and the on-board UHF transmitter have flight heritage in mission PolyItan-1. This system provides reliable communication but low data rate and uses a non-directional antenna with a low gain. The problem of transmitted data increasing due to the payload of the satellite (MiRA_ep) to the Ground Station in one communication session remains very relevant.

The antenna systems with a high gain should be installed onboard and at the Earth stations to provide enough microwave downlink power and also the power of the on-board transmitter should be increased. The last condition reduces the length of the communication session and it is not energy efficient. Besides, the Doppler shift and orientation errors and satellite coordinates must be taken into account. The development and testing of an adaptive microwave communication system of nanosatellite operating in a C (X) band with the ground station feedback through the VHF uplink are proposed. The developed system should automatically search and support the Ground Station by electronic control of the radiation pattern of an onboard adaptive active antenna array and the onboard C (X) band transmitter.

The adaptive communication system consists of:

1) On-board C (X) band transmitter with the adaptive active antenna array;

2) On-board local computer (to carry out the necessary calculations, to control the antenna array radiation pattern and operating mode of on-board microwave transmitter);

3) Ground Station VHF uplink transmitter with an antenna system;

4) Ground Station C (X) band receiver with an antenna system and turning mechanism.

In brief, the algorithm of the proposed system looks as follows:

The satellite appears in the visibility zone by the Ground Station command, transmitted through the VHF uplink. Based on orbit characteristics, ground station and satellite coordinates the On-board Microwave communication searches and refines the Ground Station antenna system position and precise guidance on a specific algorithm using an adaptive active antenna array.

The VHF uplink is used for feedback. This procedure is performed periodically, and On-board Computer traverses the results of previous search and adjustment sessions. The adaptive phased antenna array uses phasing of the common heterodyne signal at the input of T/R modules for the beamforming. The antenna area is about one decimeter square (for a Cubesat).

According to preliminary estimates, this system will improve Link Margin by a minimum of 10 dB. It will be achieved by using an adaptive active antenna array with a high gain comparing with the common patch antenna. It allows enlarging the duration of the communication session and data rate from the nanosatellite. UHF downlink remains as telemetry and a backup channel.

The Ground Station of Igor Sikorsky Kyiv Polytechnic Institute is equipped with the necessary hardware and software to provide communication with nanosatellites in the VHF and UHF bands. A C (X) band receiver with a beam-tracking antenna system will be installed at the ground station to ensure the operation of the adaptive microwave communication system.

Conclusions

1. A conception is developed to perform the space experiment for studying the origin and characteristics of the high energy charged particle microbursts in the inner magnetosphere with the MiRA_ep compact instrument installed on the 2U CubeSat platform.

2. A brief description, functional scheme, and principles of operation of the miniaturized registering analyzer of electrons and protons MiRA_ep built on the base of organic lightweight scintillator detector domestically produced are presented.

3. The upcoming facility for the production of the small-sized scintillators on the base of the *p*-terphenyl single crystal as well as some technical features is described.

4. Computer simulation of the light collection in the volumes of both *p*-terphenyl scintillators shown the best efficiency near the active areas of the silicon photodiodes to be planned to apply as photoreceivers of light splashes as results of charged particles interactions with crystallographic structure.

5. The rough structure, conception, and technical requirements to service systems of the nanosatellite such as electrical power system, attitude determination, and control system with attitude sensors and actuators, onboard computer, GPS/GLONASS receiver, communication system are presented.

REFERENCES

1. Oleynik P., Vainio R., Punkkinen A., Dudnik O., Gieseler J., Hedman H.-P., Hietala H., Haeggström E., Niemelä P., Peltonen J., Praks J., Punkkinen R., Säntti T., Valtonen E. Calibration of RADMON Radiation Monitor Onboard Aalto-1 CubeSat. *Advances in Space Research*.2020. Vol. 66, Iss. 1. P. 42–51. URL: https://doi.org/10.1016/j.asr.2019.11.020.

2. Dudnik O.V., Kurbatov E.V. The study of high energy particles' microbursts nature in the Earth magnetosphere with nanosatellites: a conception of space experiment. *Space Sci. & Technol.* 2018. Vol. 24, No. 2. P. 36–42. URL: https://doi.org/10.15407/knit2018.02.036 (*in Ukrainian*).

3. Tarasov V.O., Andryushchenko L.A., Dudnik O.V., Rybka E.A. Influence of surface treatment conditions for organic crystalline scintillators on their scintillation characteristics. *Functional Materials*. 2018. Vol. 25, Iss. 1. P. 144-150.

4. Dudnik O.V., Lazarev I.V., Kurbatov. E.V., Kowaliński M., Podgorski P., Ścisłowski D. Advisability of the axes orientation in p-terphenyl crystal of scintillation detector of the charged particle monitor in ChemiX solar X-ray spectrophotometer. *Space Sci.&Technol.* 2018. Vol. 24, No. 3. P. 33—39. URL: https://doi.org/10.15407/knit2018.03.033 (in Russian).

5. Dudnik O.V., Kurbatov E.V., Lazarev I. V., Sylwester. J., Kowaliński M., Gburek S. A method topile up the technical light output of organic scintillator in BPM particle detector of the ChemiX solar X-ray spectrophotometer. *Abstr. the 17th Ukr. Conference on Space Research,* Odesa, August 21–25, 2017. Kyiv, 2017. P. 75.

6. Dudnik O.V., Lazarev I.V., Sylwester. J., Siarkowski M., Kowaliński M. Feasibility of a usage of small-sized p-terphenyl scintillators with oriented crystalline axes in space measurements of high-energy charge radiation. *Abstracts 42nd COSPAR Scientific Assembly*, Pasadena, CA, USA, July 2018. P. 1954—1955.

7. Lazarev I.V., Dudnik O.V., Kowaliński M., Podgorski P. Evidence of the light yield anisotropy for small p-terphenyl single crystal. *Abstracts 6th International Conference "Engineering of scintillation materials and radiation technologies (ISMART 2018)*, Minsk, Belarus, 9–12 October, 2018. P. 66–67.

8. Barylak J., Dudnik O.V., Woźniczak T., Adamenko V.O., Antypenko R.V., Yezerskyi N.V., Kowaliński M., Lazarev I. V., Zielińska A., Sylwester J., Bąkała J., Podgórski P. Simulation of CubeSat caliber particle detector "MiRA_ep" response to energetic electrons and protons using GEANT4 package. *Proceedings SPIE, "Photonics Applications in Astronomy, Communications, Industry, and High-Energy Physics Experiments"*. 2019. Vol. 11176. 111763C-1–111763C-10; URL: https://doi.org/10.1117/12.2536748.

9. Movchaniuk A.V., Yezerskyi N.V., Adamenko V.O., Antypenko R.V., Dudnik O.V., Brichenko A. M. Concept of implementation the digital signal processing of the miniature particle detector MiRA_ep in the CubeSat format. *Abstracts International Conference «Radio-technical fields, signals, apparatus, and systems»*. Kyiv, Ukraine. 18–24 November 2019. P. 159–161.

A PROTOTYPE OPERATIONAL SERVICE FOR LOCAL GEOMAGNETIC FORECAST

A. Parnowski[1, 2], D. Vlasov[1]

[1] Space Research Institute of NAS of Ukraine and SSA of Ukraine
[2] Main Center of Special Monitoring

Introduction

Since the last decade space weather services worldwide are undergoing a gradual transition from predicting global, one-value-per-Earth, indices to more geographically nuanced products. This tendency reflects the customers' need for more precise and relevant space weather products [1].

There are several different approaches to building forecast models: statistical, empirical, semi-empirical, physics-base and data assimilation. While physics-based and, especially, data assimilation models, such as University of Michigan's Geospace model [2], which became operational in late 2016, potentially offer greater accuracy, they still did not reach maturity and require petascale computational clusters, which are not available in most countries. Thus, there is still a demand for empirical and semi-empirical models, which are generally more accurate than statistical models and can be run on a majority of personal computers.

One such approach based on machine learning [3, 4] was used to develop the AFFECTS geomagnetic forecast tool [5], which was operationally used to forecast Dst and Kp indices at DLR Neustrelitz since 2012, at SIDC since 2013, and in the "AFFECTS forecasts" app for Android since 2014 [6]. The same approach was used in 2015—2018 to develop predictive models for local geomagnetic variations, namely X, Y, and Z components at several magnetic observatories, as mentioned in 2018 Ukraine's biannual report to COSPAR [7].

In 2019 a prototype operational service built around these models was developed. It offers near-real time predictions of Dst and Kp indices, as well as X, Y, and Z geomagnetic elements at Boulder magnetic observatory (IAGA code: BOU). This service is now undergoing tests in operational environment at Main Center of Special Monitoring.

Models

The predictive models for BOU were trained using the NASA OMNI2 database [8, 9] and archived measurements of magnetic elements at BOU obtained from World Data Center for Geomagnetism (WDC-B) at Kyoto University. The rationale for choosing BOU

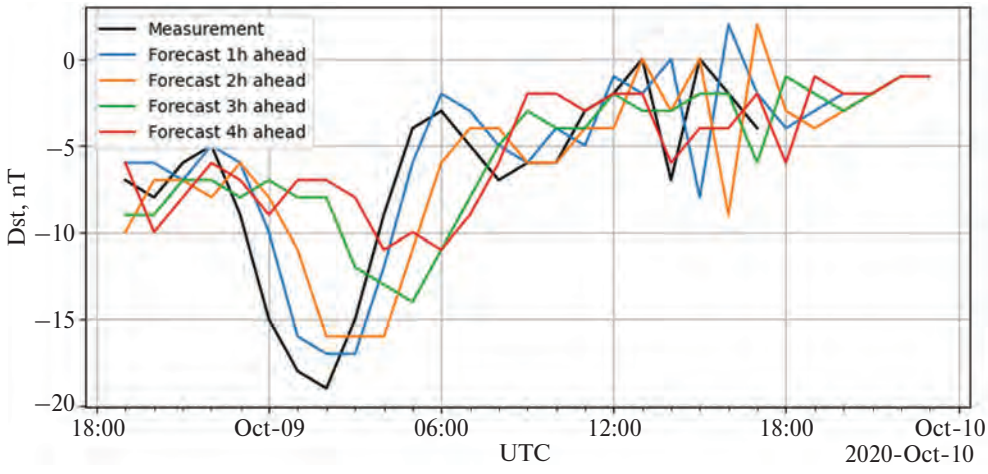

Fig. 1. A real-time forecast of Dst index, produced on October 9, 2020 18:03 UTC

Fig. 2. A real-time forecast of Kp index (as defined by GFZ Potsdam), produced on October 9, 2020 18:03 UTC

Fig. 3. A real-time forecast of X (top), Y (middle), and Z (bottom) geomagnetic elements at Boulder magnetic observatory (IAGA code: BOU), produced on October 9, 2020 18:03 UTC

over other magnetic observatories was that BOU is a recognised testbed for implementing novel geomagnetic data processing methods, and its data are always available in near-real time.

We found that the training sample should cover at least 11 years (one full sunspot cycle) to produce useful predictive models; taking any less leads to negative skill score values. Results are further improved when using longer training samples. Performance scores of the models are given in [7].

Service

The prototype service is based upon AFFECTS geomagnetic service [5, 6], which was refactored and optimized to provide local forecasts. The service is implemented as a Python 3 programme, which uses

the USGS *geomagio* library [10] to access BOU magnetic variation data from the USGS edge server, downloads ACE telemetry and quicklook Kp data over FTP, and quicklook Dst data over HTTP. Note that the Kp used is the official Kp from GFZ Potsdam (0_0 to 9_0 with a step of 1/3), rather than the estimated Kp from NOAA (0 to 9 with a step of 1). The L1 data are time-shifted to the Earth arrival using the technique described in [8] for compatibility with OMNI2 database. Thus, the prediction horizon depends on the solar wind velocity and typically lies between 4 and 5 hours.

Kp forecast is made if the UT hour is a multiple of 3, Dst and local forecasts are made upon each run. The service is set to be run on 12-th and 32-nd minutes of each hour by default. The output consists of fixed-width plain text files with prediction results, XML metadata and logs, and PNG plots of the predictions produced using *matplotlib* library. The structure of text and XML files is the same as in AFFECTS geomagnetic service.

Input and output data are stored in separate date-based directory trees with 3 levels (year/month/day-of-month). The root of both trees can be set, along with other parameters, in an XML Job Order File compliant with SWACI requirements. Latest output files are also placed in the root of the output tree.

The additional checks and optimizations introduced to the code made the service more stable and fast. The typical runtime on an average PC is now about 2 minutes, most of which are spent downloading L1 data over FTP.

Some examples of the forecast plots are provided in figures below (Fig. 1–3). We do not present quantitative performance scores due to small operational statistics and the lack of notable events since the beginning of operations.

Acknowledgements

The authors are grateful to the Space Physics Data Facility (SPDF) and the National Space Science Data Center (NSSDC) for the free online OMNI2 catalogue, the World Data Center for Geomagnetism (WDC-B) at Kyoto University for the free online catalogue of geomagnetic indices and observatories operated by the U.S. Geological Survey (USGS, geomag.usgs.gov). We also thank USGS for the free *geomagio* library, which was used in the prototype service.

REFERENCES

1. Space Weather Customer Requirements Document SSA-SWE-RS-CRD-1001 (28-07-2011). URL: http://swe.ssa.esa.int/DOCS/SSA-SWE/SSA-SWE-CRD-1001_i4r5a.pdf.

2. Cash M.D., Singer H.J., Millward G.H., Balch C.C., Toth G., Welling D.T. Space Weather Forecasting at NOAA with Michigan's Geospace Model: Results from the First Year in Real-Time Operations. *American Geophysical Union. Fall Meeting*. 2017. abstract #SM11E-07.

3. Parnowski A. Regression modeling method of space weather prediction. *Astrophysics & Space Science*. 2009. Vol. 323, Iss. 2. P. 169–180. DOI: 10.1007/s10509-009-0060-4. [arXiv: 0906.3271].

4. Parnowski A. Regression modelling of geomagnetic activity. *Journal of Physical Studies*. 2011. Vol. 15. Iss. 2. Ref. 2002. URL: http://physics.lnu.edu.ua/jps/2011/2/abs/a2002-8.html.

5. Parnowski A., Polonska A., Semeniv O., Yatsenko V., Cheremnykh O., Salnikov N., Kremenetsky I., Kuntsevich V. Provision of software tool for forecasting indices. *AFFECTS Deliverable 4.1*. 2012. URL: http://www.affects-fp7.eu/uploads/media/AFFECTS_Deliverable_Report_D4.1.pdf.

6. Semeniv O.V., Polonska A.Yu., Parnowski A.S. Operational geomagnetic forecast service. *Bulletin of Taras Shevchenko National University of Kyiv. Astronomy*. 2014. Vol. 51. P. 23–24.

7. Vlasov D., Parnowski A. Local geomagnetic forecast. *Space Research in Ukraine. Report to COSPAR 2016-2018*. P. 20–21.

8. OMNIWeb. URL: https://omniweb.gsfc.nasa.gov/html/ow_data.html.

9. King J.H., Papitashvili N.E. Solar Wind Spatial Scales in Comparisons of Hourly Wind and ACE Plasma and Magnetic Field Data. *J. Geophys. Res*. 2004. Vol. 110. A02209. DOI: 10.1029/2004JA010804.

10. Programmatic Access to Geomagnetism Data. URL: https://github.com/usgs/geomag-algorithms.

RESULTS OF EXPERIMENTAL AND THEORETICAL STUDIES OF PHYSICAL PROCESSES IN THE IONOSPHERE OVER UKRAINE IN 2018–2020

I. Domnin, L. Emelyanov, D. Kotov,
S. Panasenko, L. Chernogor, M. Lyashenko, O. Bogomaz
Institute of Ionosphere of NAS of Ukraine and MES of Ukraine

Ionospheric Observatory of the Institute of Ionosphere is located in 50 kilometers to the south-east from Kharkiv city (49.6° N, 36.3° E; Φ = 45.7°, Λ = = 117.8°). The Ionospheric Observatory facilities include the 158 MHz VHF incoherent scatter (IS) radar equipped with the zenith parabolic Cassegrain antenna of 100 m diameter; the 158 MHz VHF IS radar equipped with the fully steerable parabolic antenna of 25 m diameter and ionosonde VISRC-2.

Incoherent scatter radar with zenith-directed antenna allows measuring with high accuracy (usually error is 1–10 %) and acceptable altitude resolution (10–100 km) the following ionospheric parameters: electron density N, electron T_e and ion T_i temperatures, vertical component of the plasma drift velocity V_z, and ion composition. The investigated altitude range is usually 100–700 km, but can reach 100–1500 km in high solar activity period.

The aim of this paper is a brief overview of the investigation results of ionospheric processes over Ukraine, obtained in 2018–2020. During this period, we conducted monitoring of ionospheric processes in quiet and disturbed conditions, modernization of measuring systems, improving of geophysical data measurement and processing techniques [1–36].

Regular processes in the ionosphere over Ukraine

Variations of the main parameters of the ionospheric plasma [2, 3, 9, 10, 14, 28, 29, 32]. Observations of diurnal and seasonal variations of the electron density N, electron T_e and ion T_i temperatures over a wide range of altitudes (100–750 km) were carried out during the period of 2018–2019. The experimental data were obtained by means of Kharkiv IS radar for the specific geophysical periods: vernal and autumn equinoxes and summer and winter solstices in quiet heliogeophysical conditions.

Based on the data of Kharkiv IS radar, the patterns of altitude and diurnal variations in the vertical component of the ionospheric plasma motion velocity V_z and other parameters of the dynamic processes near the maximum phase of solar cycle 24 for the typical geophysical conditions (around the summer and winter solstices, the vernal and autumnal equinoxes) at low geomagnetic activity were studied and presented in [3]. The results of modeling of the dynamic processes in the ionospheric plasma under the conditions of the undisturbed ionosphere, including the determination of altitude-time variations in the thermospheric wind velocity, were presented too.

In order to study the dynamics of the ionosphere and, in particular, the V_z variations at the declining and minimum phases of the 24th solar activity cycle (2015–2019), regular measurements of V_z were carried out together with other ionospheric parameters. During these measurement periods, the error of V_z, depending on the altitude, time of day, and the state of the ionosphere, was 1–30 m/s for altitudes of 200–600 km at moderate solar activity (SA) and 200–400 km at low SA.

Altitude, temporal, and seasonal variations in the vertical plasma velocity were obtained in the same specific geophysical periods, mainly at low geomagnetic activity.

The main results of the analysis of V_z variations are as follows.

In the daytime, the value of the downward flow velocity was less in summer than in winter. The difference depends on the level of SA. At moderate levels of SA, this difference was less than at its low levels. The diurnal variations of V_z were close during the vernal and autumn equinoxes.

In some cases, the morning extremum of the diurnal V_z variation (a decrease in the magnitude of the velocity modulus of the downward ($V_z < 0$) plasma motion, a change in the direction of the plasma motion from downward to upward ($V_z > 0$), and an increase in the V_z modulus) was observed. Evening V_z extremum (increase in the velocity of downward movement) was less common. The amplitude of the extremum increased with increasing height. The appearance

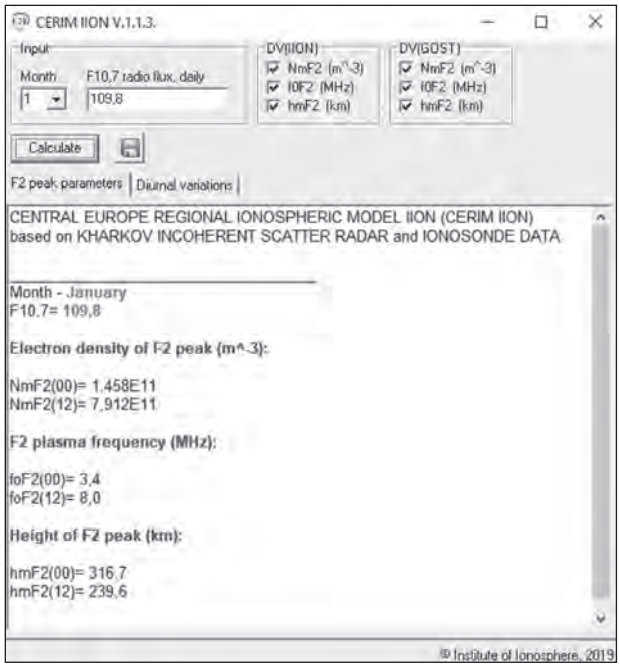

Fig. 1. The interface of the CERIM IION model and the calculation results of the main parameters of the ionospheric F2 layer

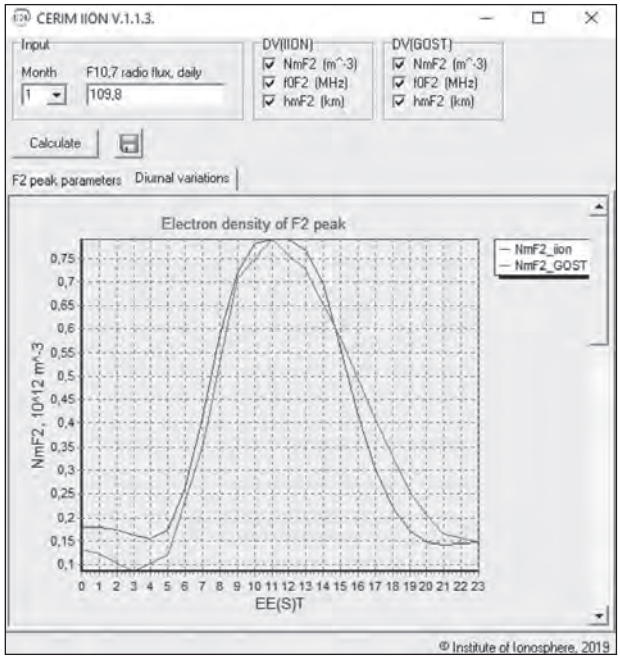

Fig. 2. The result of calculating the diurnal variation of the F2-peak electron density (*Nm*F2)

and end of these V_z variations was related to the time of sunrise and sunset at the corresponding heights.

At the beginning of the decline in SA, the winter and vernal morning extremums observed at altitudes of more than 300 km were more pronounced than at low SA. At low SA, morning V_z extremum was observed in summer at all altitudes, in autumn above 300 km, and in vernal and winter above 400 km.

An analysis of the altitude profiles of V_z showed that near local noon, the height of the change in the plasma motion from downward to upward was greater at the beginning of the decline in SA (compared with the period of low SA). For the vernal equinox and summer solstice, the absolute value of the downward plasma motion velocity was also greater at moderate SA.

Obtained results of observations of diurnal and seasonal variations of environmental parameters are used to verify and correct existing global ionospheric models, as well as to improve the regional ionospheric model CERIM IION, which developed in the Institute of Ionosphere and based on data from the Kharkiv IS radar [25, 32]. The results of experimental studies are presented in the database of the Institute of Ionosphere – http://database.iion.org.ua.

Modeling of variations of ionospheric plasma parameters over Ukraine

Regional model of the ionosphere CERIM IION [25]. The CERIM IION model is based on experimental data obtained using the IS radar and ionosonde in Kharkiv from 1986 to 2016.

During 2018–2019, the software implementation of model blocks for calculating the seasonal and diurnal variations of the ionospheric F2-region main parameters (F2-peak electron density *Nm*F2, critical frequency (*f*oF2) and maximum height of the F2 layer – *hm*F2) was performed. To calculate the diurnal dependences of *Nm*F2 (*f*oF2) and *hm*F2, the averaged (median) forms of diurnal moves were used:

1) based on experimental data of the Kharkiv IS radar and ionosonde;

2) based on the data from the model of the global distribution of concentration, temperature and effective electron collision frequency (GOST 25645.146-89) (https://internet-law.ru/gosts/gost/44354/).

The computer program is implemented in the programming language C++. The input parameters of the current version of the model are the values of the solar activity index $F_{10.7}$ (range of values from 60 to 250) and the month number (from 1 to 12).

The interface of the computer version of the CERIM IION model is presented in Fig. 1. The "F2 peak parameters" tab displays the results of the calculation of noon and midnight values of *Nm*F2, *f*oF2 and *hm*F2 (see Fig. 1). The "Diurnal variations" tab displays the results of calculating the diurnal dependences of the ionospheric F2 layer main parameters (see, for example, Fig. 2). For further use of the calculation results, it is possible to write them and save to a text file.

Irregular processes in the ionosphere over Ukraine

Irregular processes in the ionosphere are associated with ionospheric storms [16, 20, 23, 31], solar eclipses [7, 11, 12, 19], generation and propagation of wave disturbances [1, 19, 27, 30, 34], etc.

Strong response of the entire ionosphere-plasmasphere system to the weak magnetic disturbance of December 24, 2017. On the morning of December 25, 2017, Arase satellite registered the plasmaspheric electron density to be a factor of ~2 lower than on the morning of December 23 even though both the satellite passes were close in MLT, altitude, latitude, and longitude (Fig. 3) [5].

During the preceding night and evening of December 24, the Kharkiv IS radar observed high H^+ ion densities in the topside, and the Kharkiv ionosonde showed the development of a strong *Nm*F2 enhancement in excellent agreement with FLIP calculations with the NRLMSISE-00 H density doubled (Fig. 4). These ionosphere observations may be explained by the presence of strong downward plasmaspheric H^+ flux with the Kharkiv flux tube being full during the night of December 24–25 that is typical for magnetically quiet conditions. So, we concluded that the density in the Kharkiv flux tube was reduced sometime between ~2 UT and 5 UT of December 25. This conclusion is supported also by the vertical TEC data (Fig. 3) which shows that sharp TEC decrease (~33% at 50° N) was registered at ~4 UT of December 25 compared to the same time on preceding days. During the daytime and pre-evening hours of the next day (December 25), the FLIP model reproduced the observed *Nm*F2, topside O^+ density very well (Fig. 4). This means that the factor of 2 decrease of the topside H^+ density and F2-layer peak density observed by the Kharkiv IS radar and ionosonde during the night of December 25–26 (and the related changes seen in TEC data), but not reproduced by FLIP model (Fig. 4), may be the result of a depleted flux tube. The reduced plasmaspheric density would lead to a much weaker downward H^+ flux during the night of December 25–26 that could not support the higher densities of the night of December 24 to 25.

The likely cause of the flux tube depletion is the minor magnetic storm on the afternoon of December 24 (see Fig. 3). It is remarkable that the deep inner magnetosphere ($L \approx 2.1$) was strongly affected by such event (K_p=3+, $D_{st} > -22$ nT) which is not even classified as a storm in accordance with commonly used classifications. To our knowledge, this is the first time that such strong effects of such a weak geomagnetic disturbance were identified so deep into

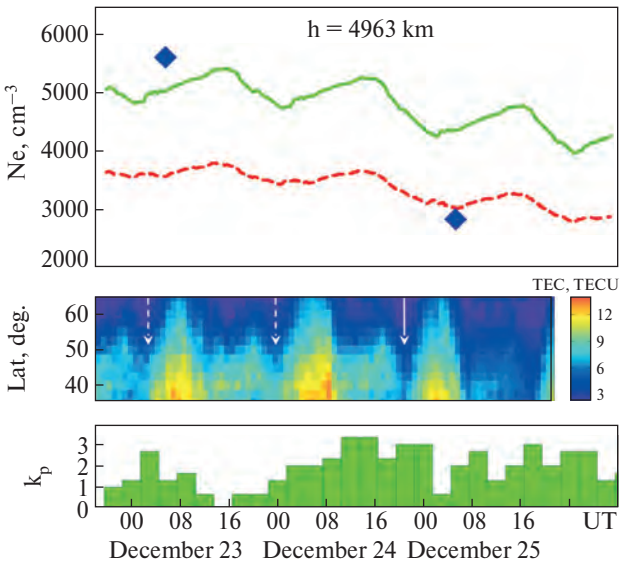

Fig. 3. Comparison of the electron density from the FLIP model for the Kharkiv flux tube ($L \approx 2.13$) at the altitude of Arase satellite orbit and the satellite density data (blue symbols) for the period of December 22–26, 2017 (top panel). The second panel shows vertical TEC at 35° E within the latitudes of 35°N–65°N. The solid white arrow indicates the time of sharp TEC decrease on the morning of December 25 while the dashed white arrows indicate the same times for the preceding days. The bottom panel shows variation of K_p index

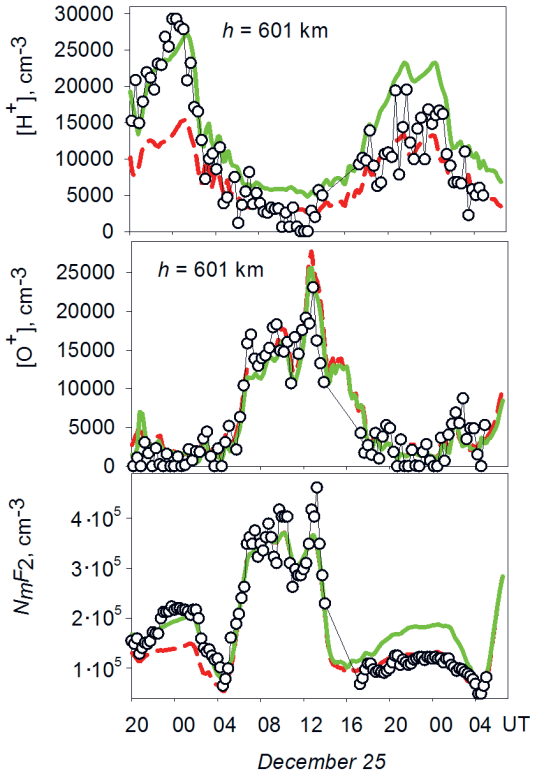

Fig. 4. Comparison of F2-layer peak density *Nm*F2, O^+ and H^+ ion densities observed by the Kharkiv IS radar (open circles) and simulated with FLIP model (lines). The dashed red lines show the results calculated using the standard NRLMSISE-00 H density while the solid green lines are for the case of doubled NRLMSISE-00 H density

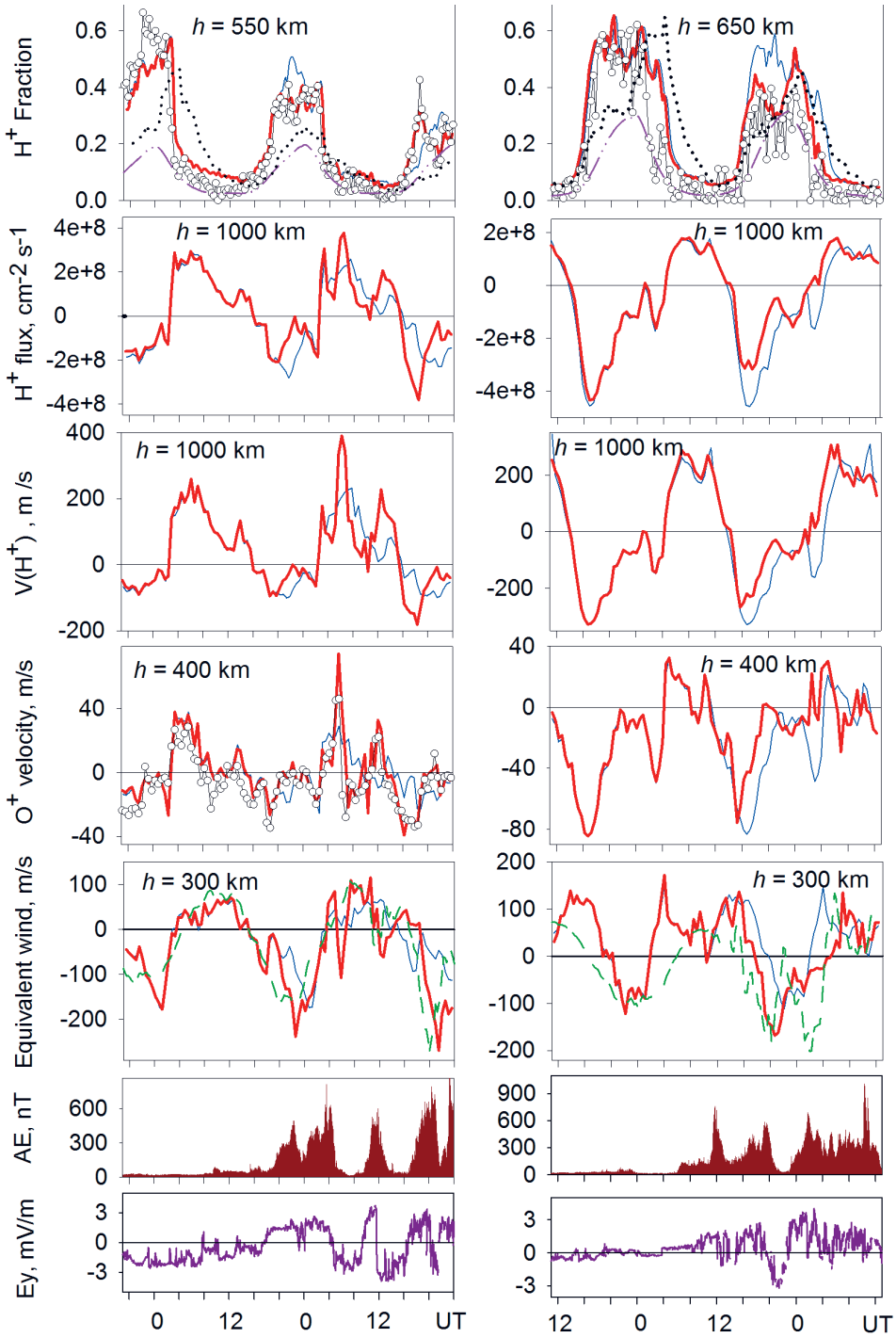

Fig. 5. Diurnal variations of zonal component of magnetospheric electric field *Ey*, *AE* index, equivalent meridional horizontal wind velocity at 300 km, O^+ ion velocity at 400 km, and H^+ ion velocity and flux at 1000 km for September 23–25, 2016 (left panels) and October 28–30, 2004 (right panels). Open circles show the observational results obtained with Kharkiv IS radar. The thick red line denotes the FLIP simulation when the IS *hm*F2 is used as input in the northern hemisphere and the digisonde *hm*F2 is used as input in the southern hemisphere. The thin blue line shows the FLIP simulation when the quiet first day equivalent winds deduced from the measured *hm*F2 in both hemispheres are used as input for all days. The dashed dark green line is the meridional horizontal wind velocity at 300 km from the CTIPe model. Black dots show the H^+ fraction calculated with the chemical equilibrium H^+ ion density. The dash-dotted pink lines show the H^+ fraction from the new TBT-15 empirical model of topside ion composition that is included in the International Reference Ionosphere model (IRI-2016)

the inner magnetosphere. As it is seen, related ionospheric manifestations of such storms may be significant too. One more important conclusion of this study is that other indices of storm-time activities like AE (see Fig. 5) are better for the determination of the magnetic disturbances which are effective in terms of their impact on plasmasphere-ionosphere system.

Significant modulation of ionosphere-plasmasphere system by the weak magnetic disturbances. A comprehensive study of the response of the ionosphere-plasmasphere system at mid-latitudes to weak ($D_{st\min} > -50$ nT) magnetic storms was made [20].

For the first time, we showed that weak magnetic disturbances can lead to significant modulation of ionosphere-plasmasphere interaction. Observations and observation-driven physical simulations revealed that even weak magnetic storms lead to significant modulation of ionosphere-plasmasphere H^+ ion fluxes (Fig. 5). This modulation is caused by variations in the topside O^+ ion density caused by the *hm*F2 motion most likely induced by changes of the thermospheric horizontal wind, but also possibly by magnetospheric penetrated electric fields (Fig. 5). Both mechanisms are closely related to the changes in the IMF *Bz* component.

Sharp prominent changes of the observed H^+ ion fraction in the topside ionosphere (Fig. 5) are a strong signature of the modulation of ionosphere-plasmasphere H^+ flux. Comparison of our H^+ ion fraction results with the calculations from the new empirical model of the topside ion composition TBT-15 reveals an interesting feature. The model H^+ fraction is underestimated by a factor of 2–3 (Fig. 5) during the quiet periods but it fits the observations very well during the disturbances. This indicates the need to include geomagnetic activity indices as input parameters to empirical topside ionosphere composition models.

Solar eclipse on March 20, 2015. The results of complex radiophysical observations of the effects of the partial solar eclipse on March 20, 2015 are presented. The eclipse effects in variations of the parameters of the geospace plasma are investigated and explained, wave disturbances in the ionosphere are revealed. It was shown that the solar eclipse led to a noticeable restructuring of the altitude structure of the ionosphere, changes in the dynamic and thermal regimes of the ionospheric plasma [7, 11, 12, 19].

Wave processes during the geospace storm on 1–3 September 2016. We have analyzed the parameters of traveling ionospheric disturbances (TIDs) which were obtained using Kharkiv incoherent scatter (IS) radar during the geospace storm on 1–3 September 2016 [23, 30]. This research aimed at determining the periods and relative amplitudes of predominant wave processes in the electron density, electron and ion temperatures observed at the latitudes of 100–400 km. The estimation of TID phase velocities and wavelengths were also done. We used the spectral analysis based on the adaptive Fourier transform. Further, the data passed through the digital band-pass filter to isolate the prevailing TIDs. The phase velocities were calculated performing the cross-correlation analysis of IS power temporal variations.

The observations were conducted at the decline phase of the solar activity. The values of $F_{10.7}$ index was slightly varied, ranging from 95 to 99 sfu. Three week X-ray flares (the maximum is C2.2) and weak optical ones were registered on 31.08.2016. The moderate magnetic storm occurred with such index maximum values as $AE = 1500$ nT, $D_{st} = -59$ nT and $K_p = 6$. During the first day of the observations, K_p does not exceed 3, $A_p \le 8$, that enabled considering it as magnetically quiet day. Staring from 01.09.2016, K_p went up to 4–6. This is accompanied by the drop of D_{st} from –12 to –59 nT. The peak values of *AE* were greater than 1500 nT in some cases.

It was shown that the periods of the predominant oscillations were 60–100 min, and their durations do not exceed two periods. We did not found the significant differences in these periods for the wave processes, occurring during the geospace storm and the previous day. The detected TIDs were demonstrated to be the signatures of the acoustic gravity waves (AGW) in the ionosphere. The relative amplitudes of quasi-harmonic variations in the electron density on 1 and 2 September exceeded their values during the adjacent days by a factor of about 2. They were both lesser and greater than the relative amplitudes of electron and ion temperature variations for the different TIDs. We estimated the vertical and horizontal components of the phase velocity and wavelength for the TIDs. It was shown that the vertical and horizontal phase velocities were 26–50 m/s and 210–455 m/s, respectively; the vertical and horizontal wavelengths fell into the ranges of 120–290 km and 1075–2450 km. We established the interrelation between a number of the observed TIDs and high-latitude magnetic field variations. The sources of such TIDs are likely to be Joule heating and Lorenz forcing due to auroral electrojet variations during the geospace storm. The precipitation of charged particles in the high and middle latitudes is probably an additional source of the observed wave processes.

Characteristics of traveling ionospheric disturbances during low solar and weak geomagnetic activities. This research aimed at the detection and parameter estimation of the TIDs observed using Kharkiv IS radar in the periods near the equinoxes and solstices during the low solar activity and magnetically quiet conditions [34]. We have also analyzed the potential sources generating the detected wave processes. To achieve the aim, we processed the temporal variations of IS power and passed them through the digital filters with different bandwidths. At first stage, the initial variations were filtered in the wide period range of 5–125 min to remove long-term variations (trend) as

well as rapid oscillations, which can be result of noise contamination. Further, the wide range was divided to the sub-ranges of 15–30 min, 30–60 min and 60–120 min. For each of the period intervals, the predominant TIDs were detected and their characteristics were estimated using the cross-correlation analysis and employing an elastic dispersion relation for AGWs.

We chose the measuring campaigns lasted 50–54 hours (over two days) during 2006–2018 to analyze the data. The solar radio flux value was $F_{10.7} \leq 85$ sfu that points to the low solar activity. Taking into account the K and K_p indexes to be not more than 3 and A, A_p – not more than 6, we can claim that the level of the magnetic activity was weak.

We detected TIDs in a wide range of periods from 5 to 125 min which had the relative amplitudes to reach 5–30 % from the background level. The TIDs with ranged from 60 to 120 min were shown to have the maximum energy. We have showed that the TIDs with the periods of 15–30 min and 30–60 min also occurred during all seasons. We established that 83% (49 events) of the detected TIDs were likely to be the signatures of the AGWs propagating from the lower altitudes. Both large-scale TIDs (LSTIDs) and medium-scale TIDs (MSTIDs) were revealed during all seasons. The most of TIDs and the maximum values of their relative amplitudes were demonstrated to be observed near the winter solstice and autumnal equinox periods. Such dependence on the season can be caused by seasonal changes in both the general circulation of the atmosphere and the vertical temperature gradient of neutral particles near the mesopause. The average values of LSTID parameters were shown to be 0.14 and 0.20 for maximum relative amplitudes of electron density variations; 105 and 56 m/s for vertical phase velocity; 495 and 473 m/s for horizontal phase velocity; 285 and 282 km for vertical wavelength; 1358 and 2322 km for horizontal phase velocity related to the sub-ranges of 30–60 min (with mean period of 45 min) and 60–120 min (82 min), respectively. The average values for those parameters but for MSTIDs are the following: 0.13 and 0.13; 127 and 64 m/s; 289 and 268 m/s; 166 and 157 km; 403 and 658 km related to the sub-ranges of 15–30 min (22 min) and 30–60 min (41 min), respectively.

We have analyzed the potential sources of TID generation. Both sunrise and sunset terminators was found to effectively generate the ionospheric disturbances during all seasons. Other AGW / TID sources are the wind structures in the lower atmosphere, the AGW dissipation in the lower atmosphere, which leads to the formation of secondary waves, and variations in geomagnetic activity. It was shown that 17% (10 events) of the detected TIDs were not the manifestations of AGWs. Such TIDs were mostly observed during the nighttime and were likely of electromagnetic nature. They occurred during all seasons with a slight increase in their number during solstice periods.

Modernization of measuring systems, improvement of measurement and processing methods

In 2018–2019, the modernization of measuring systems continued, as well as the further improvement of methods for measuring and processing ionospheric data [4, 6, 8, 13, 15, 17, 18, 21, 22, 24, 26, 33]. On key issues, Ukraine patents were obtained [35, 36].

Conclusions

1. Observations, analysis and physical interpretation of diurnal and seasonal variations of the electron density N, electron T_e and ion T_i temperatures, and plasma motion velocity V_z over a wide range of altitudes (100–750 km) were carried out during the period of 2018–2019.

2. The variations of vertical plasma motion velocity and other parameters of dynamic processes in the ionosphere at the maximum, declining and minimum phases of the 24th solar activity cycle (2015–2019) were studied.

3. In the frame of the development of the CERIM IION regional model of the ionosphere, a computer program for calculating the seasonal and diurnal variations in the electron density at the maximum of the ionospheric F2 layer and the height of the maximum F2 layer is presented.

4. For the first time, it was shown that very weak magnetic storms are able to modulate of ionosphere-plasmasphere interaction significantly. The modulation causes prominent manifestations above the F2-layer peak region. This new knowledge sheds light on the long-standing problems of the topside ionosphere modeling.

5. It was established that a geospace storm of 1–3 September 2016 with a maximum $Kp = 6$ contributed to the enhancement of TIDs at the altitudes of 150–400 km. The interrelation between a number of the observed TIDs and high-latitude magnetic field variations was found. Possible sources of such waves are Joule heating, Lorentz forcing and precipitation of energetic particles.

6. As a result of many years systematic monitoring of the ionosphere state using the Kharkiv IS radar, the regional TIDs characteristics of various temporal and spatial scales have been determined. The presence of large-scale TIDs even in magnetically quiet conditions is proved.

REFERENCES

1. Panasenko S.V., Goncharenko L.P., Erickson P.J., Aksonova K.D., Domnin I.F. Traveling ionospheric disturbances

observed by Kharkiv and Millstone Hill incoherent scatter radars near vernal equinox and summer solstice. *J. Atm. Sol.-Terr. Phys*. 2018. Vol. 172. P. 10–23. DOI: https://doi.org/10.1016/j.jastp.2018.03.001.

2. Themens D.R., Jayachandran P.T., Bilitza D., Erickson P.J., Häggström I., Lyashenko M.V., Reid B., Varney R. H., Pustovalova L. Topside electron density representations for mid and high latitudes: A new NeQuick and E-CHAIM topside parameterization. *J. Geoph. Res.: Space Phys*. 2018. Vol. 123. P. 1–15. DOI: https://doi.org/10.1002/2017JA024817.

3. Emel'yanov L.Ya., Lyashenko M.V., Chernogor L.F., Domnin I.F. Motion of ionospheric plasma: results of observation above Kharkiv in solar cycle 24. *Geomagnetism and Aeronomy*. 2018. Vol. 58, No. 4. P. 533–547. DOI: https://doi.org/10.1134/S001679321802007X.

4. Yemelyanov L.Ya. Development of principles and instrumentation for generation of test and control signals of the incoherent scatter radar. *Telecom. Rad. Eng*. 2017. Vol. 76, No. 14. P. 1259–1271. DOI: 10.1615/TelecomRadEng.v76.i14.50.

5. Kotov D.V., Richards P.G., Truhl k V., Bogomaz O.V., Shulha M.O., Maruyama N., Hairston M., Miyoshi Y., Kasahara Y., Kumamoto A., Tsuchiya F., Matsuoka A., Shinohara I., Hernández-Pajares M., Domnin I.F., Zhivolup T.G., Emelyanov L.Y., Chepurnyy Y.M. Coincident Observations by the Kharkiv IS Radar and Ionosonde, DMSP and Arase (ERG) Satellites, and FLIP Model Simulations: Implications for the NRLMSISE-00 Hydrogen Density, Plasmasphere, and Ionosphere. *Geophys. Res. Lett*. 2018. Vol. 45, No. 16. P. 8062–8071. DOI: https://doi.org/10.1029/2018GL079206.

6. Domnin I., Levon O., Kozlov S. Control system of the filter-compensating device with the second-order fuzzy regulator. *Tech. Electrodyn*. 2018. No. 6. P. 30–33. DOI: https://doi.org/10.15407/techned2018.06.030.

7. Chernogor L.F., Domnin I.F., Emel'yanov L.Ya., Lyashenko M.V. Physical processes in the ionosphere during the solar eclipse on March 20, 2015 over Kharkiv, Ukraine (49.6° N, 36.3° E). *J. Atm. Sol.-Terr. Phys*. 2019. Vol. 182. P. 1–9. DOI: https://doi.org/10.1016/j.jastp.2018.10.016.

8. Emelyanov L., Chepurnyy Y.,Bogomaz O. Simultaneous Sounding of the Ionosphere in the Vertical and Oblique Directions using Incoherent Scatter Radar. *2018 IEEE 38th International Conference on Electronics and Nanotechnology (ELNANO)*. 2018. P. 458–463. DOI: https://doi.org/10.1109/ELNANO.2018.8477456.

9. Shulha M., Aksonova K. , Shnitsar I., Pulyayev V. Calculation of the Height-Time Dependence of the Electron Density of the Ionospheric Plasma under Instability of the Incoherent Scatter Radar Constant. *2018 IEEE 38th International Conference on Electronics and Nanotechnology (ELNANO)*. 2018. P. 544–547. DOI: https://doi.org/10.1109/ELNANO.2018.8477544.

10. Grinchenko S.V. Some Inexactnesses of the European NeQuick Model and Possible Ways of their Correction. *International Conference on Mathematical Methods in Electromagnetic Theory, MMET 2018*. Kyiv, Ukraine, July 2–5, 2018. P. 95–98. DOI: https://doi.org/10.1109/MMET.2018.8460447.

11. Panasenko S.V., Chernogor L.F., Lazorenko O.V., Otsuka Y., M. van de Kamp. Observations of ultrawideband signals in GPS TEC variations over Europe during solar eclipse. *9th International Conference on Ultrawideband and Ultrashort Impulse Signals (UWBUSIS-2018)*. Odessa, 4–7 September 2018. Odessa, Ukraine. 2018. P. 115–118. DOI: https://doi.org/10.1109/UWBUSIS.2018.8520253.

12. Panasenko S.V., Chernogor L.F., Lazorenko O.V. Characteristics of wave processes in the ionosphere over Kharkiv during solar eclipse of 20 March 2015. *9th International Conference on Ultrawideband and Ultrashort Impulse Signals (UWBUSIS-2018)*. Odessa, 4–7 September 2018. Odessa, Ukraine. 2018. P. 119–122. DOI: https://doi.org/10.1109/UWBUSIS. 2018.8519995.

13. Emelyanov L.Ya., Pulayev V.A., Rogozhkin E.V. Correlation processing of incoherent scattering signal using multichannel device. *Radiotekhnika: All-Ukr. Sci. Interdep. Mag*. 2018. No. 192. P. 5–9 (*in Russian*).

14. Kotov D.V., Truhlik V., Richards P.G., Shulha M.O., Bogomaz O.V., Domnin I.F. Coordinated investigations of topside H+ ions: new results for inner magnetosphere. *VarSITI Newsletter*. Vol. 17. April 2018. P. 3–4. URL: http://newserver.stil.bas.bg/varsiti/newsL/VarSITI_Newsletter_ Vol17.pdf

15. Pulyayev V.A., Emelyanov L.Ya., Rogozhkin E.V. Improving the accuracy of calculation of the scatter signal ACF ordinates. *Bulletin of the National Technical University "KhPI". Series: Radiophysic and Ionosphere*. 2018. No. 43. P. 13–17 (*in Ukrainian*).

16. Shulha M.O., Kotov D.V., Bogomaz O.V. Investigation of the ionospheric F2-layer electron density peak reaction to weak geomagnetic storm of December 24, 2017 for different latitudes of the European region. *Bulletin of the National Technical University "KhPI". Series: Radiophysic and Ionosphere*. 2018. No. 43. P. 18–23 (*in Russian*).

17. Bogomaz O.V., Kotov D.V., Iskra D.O. Results of testing new hardware and software system for processing data obtained by incoherent scatter radar operating in the mode for middle ionosphere research. *Bulletin of the National Technical University "KhPI". Series: Radiophysic and Ionosphere*. 2018. No. 43. P. 24–32 (*in Russian*).

18. Emelyanov L.Ya., Miroshnikov A.E., Kolodiazhnyi V.V. Development of subsystem for reception of incoherent scatter signal, its recording and processing at the intermediate frequency. *Bulletin of the National Technical University "KhPI". Series: Radiophysic and Ionosphere*. 2018. No. 43. P. 33–42 (*in Russian*).

19. Panasenko S.V., Otsuka Y., M. van de Kamp, Chernogor L.F., Shinbori A., Tsugawa T., Nishioka M. Observation and characterization of traveling ionospheric disturbances induced by solar eclipse of 20 March 2015 using incoherent scatter radars and GPS networks. *J. Atm. Sol.-Terr. Phys*. 2019. Vol. 191. DOI: https://doi.org/10.1016/j.jastp.2019.05.015.

20. Kotov D.V., Richards P. G., Truhlík V., Maruyama N., Fedrizzi M., Shulha M.O., Bogomaz O.V., Lichtenberger J., Hernández-Pajares M., Chernogor L.F., Emelyanov L.Ya., Zhivolup T.G., Chepurnyy Ya.M., Domnin I.F. Weak magnetic storms can modulate ionosphere-plasmasphere interaction significantly: Mechanisms and manifestations at mid-latitudes. *J. Geophys. Res.: Space Phys*. 2019. Vol. 124. DOI: https://doi.org/10.1029/2019JA027076.

21. Miroshnikov A., Emelyanov L., Pulyaev V., Rogozhkin E. Determination of the incoherent scatter signal statistical characteristics. *2019 IEEE 39th International Conference on Electronics and Nanotechnology (ELNANO-2019)*: Proceedings. Kyiv, April 16–18, 2019. Kyiv, Ukraine. P. 774–777. DOI: https://doi.org/10.1109/ELNANO.2019.8783823.

22. Rogozhkin E.V., Podyachiy Yu.I., Emelyanov L.Ya. Modification of radar signals digital representation. *Radiotekhnika: All-Ukr. Sci. Interdep. Mag*. 2019. No. 196. P. 69–76. URL: http://nbuv.gov.ua/UJRN/rvmnts_2019_196_11.

23. Aksonova K.D., Panasenko S.V. Manifestations of wave processes in ionospheric plasma parameters during the geospace storm on 1–3 September, 2016. *Radio Phys. Radio Astr.* 2019. Vol. 24, No. 1. P. 55–67. DOI: https://doi.org/10.15407/rpra24.01.055 (*in Russian*).

24. Pulyayev V.A., Emelyanov L.Ya., Rogozhkin E.V., Gorbanenko R.V. Characteristics of the motion of space objects from coherent reflection signals in the method of incoherent scatter of radio waves. *Bulletin of the National Technical University "KhPI". Series: Radiophysic and Ionosphere*. 2019. No. 25. P. 3– 8 (*in Ukrainian*).

25. Lyashenko M.V., Iskra D.O. CERIM IION regional ionospheric model: calculating the seasonal and diurnal dependences of the main parameters of the ionospheric F2 layer. *Bulletin of the National Technical University "KhPI". Series: Radiophysic and Ionosphere*. 2019. No. 25. P. 24–30 (*in Russian*).

26. Emelyanov L.Ya., Chepurnyy Ya.M., Domnin I.F., Podyachiy Yu.I., Glaznev A.I. Development of methodology and hardware for research of the lower ionosphere at the Kharkiv incoherent scatter radar. *Bulletin of the National Technical University "KhPI". Series: Radiophysic and Ionosphere*. 2019. No. 25. P. 44–50 (*in Russian*).

27. Panasenko S.V. Improvement of method for detection of medium- and large-scale traveling ionospheric disturbances using data from dense networks of GPS receivers. *Bulletin of the National Technical University "KhPI". Series: Radiophysic and Ionosphere*. 2019. No. 25. P. 51–57 (*in Ukrainian*).

28. Bogomaz O.V., Kotov D.V., Shulha M.O., Gorobets M.V. Comparison of the F2 layer peak height variations obtained by ionosonde and incoherent scatter radar. *Bulletin of the National Technical University "KhPI". Series: Radiophysic and Ionosphere*. 2019. No. 25. P. 58–61.

29. Lyashenko M.V., Kolodyazhnyi V.V., Varvianska V.V. Variations of the main parameters of the ionospheric F2 layer during the descending phase of the 24th solar activity cycle according to the ionosonde and the incoherent scatter radar in Kharkov. *Bulletin of the National Technical University "KhPI". Series: Radiophysic and Ionosphere*. 2019. No. 25. P. 62–71 (*in Russian*).

30. Aksonova K.D., Panasenko S.V. Parameters of traveling ionospheric disturbances in ion and electron temperatures variations under quiet geomagnetic conditions obtained by Kharkiv incoherent scatter radar. *Bulletin of the National Technical University "KhPI". Series: Radiophysic and Ionosphere*. 2019. No. 25. P. 72–77 (*in Russian*).

31. Emelyanov L.Ya., Katsko S.V., Chernogor L.F. Ionospheric effects of geospace storms on December 21–24, 2016 and March 21–23, 2017. *Bulletin of the National Technical University "KhPI". Series: Radiophysic and Ionosphere*. 2019. No. 25. P. 78–85 (*in Russian*).

32. Bogomaz O.V., Lyashenko M.V., Barabash V.V., Reznychenko A.I. Long-term variations of the F2 layer peak electron density and the peak height obtained by ionosonde. *Bulletin of the National Technical University "KhPI". Series: Radiophysic and Ionosphere*. 2019. No. 25. P. 86–90.

33. Emelyanov L.Ya., Miroshnikov A.E. Experiments with subsystem for receiving, recording and processing the incoherent scatter signal extracted at intermediate frequency. *Bulletin of the National Technical University "KhPI". Series: Radiophysic and Ionosphere*. 2019. No. 25. P. 91–99 (*in Russian*).

34. Aksonova K.D., Panasenko S.V. Predominant traveling ionospheric disturbances over Eastern Europe during low levels of solar and geomagnetic activities using incoherent scatter radar data. *Radio Phys. Radio Astr.* 2020. Vol. 25, No. 2. P. 100–117. DOI: https://doi.org/10.15407/rpra25.02.100 (*in Ukrainian*).

35. *Patent of Ukraine No. 131859.* The method of determining height distribution of radial component of plasma velocity by method of incoherent scattering of radio waves / Pulyaev V.O., Emelyanov L.Ya., Rogozhkin E.V., Miroshnikov A.E.; published 11.02.19. Bull. No. 3 (in Ukrainian).

36. *Patent of Ukraine No. 140837.* The method to determine of radial component of artificial space objects velocity using incoherent scatter radar / Pulyaev V. O., Emelyanov L.Ya., Rogozhkin E. V.; published 26.12.19. Bull. No. 23 (in Ukrainian).

INFRASONIC, ATMOSPHERIC AND IONOSPHERIC EFFECTS OF NATURAL AND MAN-MADE ORIGIN

L. Chernogor [1], V. Koshovyy [2], O. Ivantyshyn [2], B. Rusyn [2]

[1] V.N. Karazin Kharkiv National University

[2] Karpenko Physico-Mechanical Institute of the NAS of Ukraine

Introduction

Investigations of infrasound-atmosphere coupling are of great scientific and practical importance. The infrasonic effects have been studied quite well, but the atmosphere-ionospheric effects have been studied significantly worse. The latter determines the urgency of the problem.

The aim of the study is the presentation of theoretical and experimental studies of atmospheric and atmosphere-ionospheric effects of infrasound.

Infrasound of Space Origin

Tunguska Meteoroid Infrasound. The Tunguska celestial body entered the terrestrial atmosphere at 00:13:59 UT ± 8 min on June 30, 1908. The geographic coordinates of the explosion epicenter are 60°53′09″ ± ± 6″ N, 101°53′40″ ± 13″ E [1, 2]. The initial mass of the body is estimated to be 1 Mt, the energy of the explosion 20–50 Mt TNT, the explosion altitude 6–10 km [1, 2]. The shock wave transformed into acoustic and atmospheric gravity waves, the infrasonic part of which contained periods, T, in the range from ~10 s to 3–5 min.

The study [1, 2] is concerned with the features of variations in the amplitude of infrasound wave propagating through the terrestrial atmosphere at global-scale distances. As a powerful source of infrasound, the passage and explosion of the Tunguska celestial body that occurred in the atmosphere over the Central Siberia have been chosen. The aim of this study is investigating the dependence of the amplitude on distance, developing simple approximating relations between the pressure in the infrasound wave and the distance between the infrasound source and the infrasound detector location.

The data acquired from the Europe-Asia array of 23 microbarographs located at distances of 0.49–35 Mm from the Tunguska catastrophe site are used to construct the correlation diagrams for the distance and amplitude, which are used to study the dependence of the infrasound amplitude on distance. In analyzing the dependence of the infrasound amplitude on the distance between the source generating infrasound and the location of the infrasound detector, the model for weakening the amplitude with distance, which best fits the observations, has being found. The relations approximating the dependence of the infrasound amplitude on distance have been developed for the different models of propagation of infrasound waves along the Earth's surface in the distance range of 0.49–35 Mm. For the base models of the global-scale propagation of infrasound waves, the following models have been chosen: (1) propagation of a spherical wavefront without attenuation, (2) propagation of a cylindrical wavefront without attenuation, (3) the combination of a spherical wavefront and a cylindrical wavefront without attenuation, (4) beam spreading loss described by an arbitrary power law without attenuation, (5) propagation of a cylindrical wavefront with attenuation, (6) propagation of a spherical wavefront with attenuation. The approximating relations obtained have been analyzed and compared. The rate of attenuation is estimated for a cylindrical and spherical wavefronts in the ground–stratosphere and the ground–thermosphere waveguides. It is equal to about 0.16 Mm^{-1} and 0.17 Mm^{-1}, respectively.

The following conclusions have been drawn from this study: (1) the dependence of the amplitude of the infrasound wave generated by the Tunguska celestial body on distance is determined to be complex and difficult to fit with simple mathematical relations based on reasonable physical models of the propagation of infrasound waves along the Earth's surface at global-scale distances, (2) the intercomparison of the approximating relations determined permitted the selection of preferable relations from their entire set. To these latter belong the relations based on the following models for propagation of infrasound waves in the waveguides formed by the ground and atmospheric layers (primarily, by the stratosphere, and, to a lesser

degree, by the thermosphere): (1) a spherical wavefront gradually becoming a cylindrical wavefront, and (2) a cylindrical wavefront with attenuation.

Indonesia Meteoroid Infrasound. The meteoroid entered the Earth's atmosphere at 02:57 UT and exploded over the point with the coordinates $\varphi = 4.9°S$, $\lambda = 122.0°E$ (average error of 2.9°) [3]. The initial kinetic energy of the meteoroid was 70 ± 20 kt TNT, 8...10 m in diameter, and mass of not more than 6000 t. The average time interval between two falls of such bodies is 10...22 years [3].

Using the observations of the infrasonic signals that have been registered at 17 stations, the statistical analysis has been performed of the basic signal parameters: time delay, celerity, duration, oscillation period, and amplitude vs. the great-circle distance between the Indonesian super-bolide flare and the site of an infrasonic station [3].

The delay time of the infrasound signal increased if the horizontal distance, r, from the epicenter of the meteoroid explosion to the stations increased linearly. The average signal celerity for all paths was close to 297 m/s. The average values of the celerities of the leading and trailing edges of the infrasound signal were approximately 299 and 281 m/s, respectively. They depended relatively weakly on the propagation path. The average duration of the infrasound signal for different paths was 18.44 ± 9.34 min. The dispersion spreading of the signal was insignificant at distances of 2...12 Mm. At the same time, there was a tendency to reduce the duration of the infrasound signal from 24...25 to 10...12 min if r increased from 2 to 17.5 Mm. The average values of the infrasound signal periods estimated by different methods were 10.6 ± 1.1, 13.4 ± 1.2, and 14.1 ± 1.4 s. The average value of the initial meteoroid kinetic energy obtained from infrasound observations of the oscillation period is 36.6 ± 6.0 kt TNT, which is insignificantly different from the independent NASA data (33 kt TNT). Approximation of the infrasound signal amplitude from a distance confirms that, at a distance of 2...12 Mm, there was a waveguide propagation of the signal with attenuation. The attenuation coefficient was close to 0.3 ± 0.1 Mm^{-1}. Approximation of the celerity of the infrasound signal from the sine of the azimuth angle showed that the corrected signal celerity was approximately 294 ± 2 m/s, and the average value of the troposphere-stratosphere wind for the Southern and Northern Hemispheres was approximately 16 and –4 m/s, respectively. The analysis of the correlation diagrams showed a stable statistical relationship between the observed and true values of the azimuth of the infrasound source, between the oscillation periods calculated by the two MatSeis methods, between the amplitudes of the infrasound signal estimated by two different methods (PMCC and MatSeis), and between the maximum and minimum values of the infrasound signal celerity.

Chelyabinsk Meteoroid Infrasound. The Chelyabinsk meteoroid entered the terrestrial atmosphere at 03:20:22 UT on February 15, 2013 [4–10].The celestial body traveled at the north-west direction at an inclination of the trajectory to the horizon of approximately 20°. The initial mass of the body was estimated to be $m_0 \approx 11$ kt, the initial velocity $v_0 \approx 18.5$ km/s, and the initial diameter $d_0 \approx 18$ m. The flyby of the celestial body was accompanied by a series of physical processes [4–10]. An important role among them played the generation and propagation of infrasonic signals.

The investigation subject in [4] is the statistical characteristics of the infrasound signal generated during the passage and airburst of the Chelyabinsk celestial body. The parameters under study include the time delay, amplitude, duration, period, celerity and its dependence on the distance to the epicenter of the airburst from the observation site and on the back-azimuth angle of arrival.

The study aims at constructing correlation diagrams for the signal celerity and the distance, the signal celerity and the sine of the back-azimuth angle of arrival, the signal duration and the distance, the signal amplitude and the distance, the period and the period for the periods determined by two techniques, and at fitting simple analytical relations to the diagrams obtained. Here, the distance refers to the distance between the infrasound source and the infrasound station where the infrasound is observed.

The data retrieved from the US Department of Defense, the Comprehensive Nuclear-Test-Ban Treaty Organization's International Monitoring System database are used to determine approximate relations for the basic characteristics of the infrasound signal generated by the passage and airburst of the Chelyabinsk celestial body.

The correlation diagrams for the infrasound signal celerity and the distance between the source and an observation station have been shown to exhibit a significant scatter with a mean of (286 ± 21.5) $m \cdot s^{-1}$. The model fits of the infrasound signal celerity to the signal duration, to the back-azimuth angle of arrival, and to the distance between the source and an observation station, as well as the model fit of the signal amplitude to distance, are determined. The correlation diagrams for the main oscillation periods obtained by two different techniques are constructed.

The infrasound signal time delay increases virtually linearly with the distance between the infrasound source and the station [4]. The infrasound signal celerity averaged over all paths is equal to 291 $m \cdot s^{-1}$.

The celerity dependence on distance is fit with a constant due to a large data scatter. The celerity dependence on the sine of the back-azimuth angle of arrival, both calculated and estimated, is fit with a straight line that gives mean values of the celerity (287–288 $m \cdot s^{-1}$) and troposphere-stratosphere winds (12–14 $m \cdot s^{-1}$) along all paths. The dependence of the infrasound signal duration on distance is fit with a straight line, and the signal duration near the source is found to be 10.7 min. The spectral components with a period within 17 to 85 s predominate in the infrasound signal spectrum, and the period mean values estimated by employing different techniques vary from 35 to 39 s.

Romanian Meteoroid Infrasound. The meteoroid entered the terrestrial atmosphere at 01:05:56 UT on January 7, 2015 [11–13]. The celestial body traveled in the north-east direction along the trajectory inclined from the horizon by 59.6°. The initial mass of the body was estimated to be 1.9 t, the initial speed 42.4 km/s, and the initial diameter 1 m [11–13]. The meteoroid explosion altitude and the meteoroid kinematical characteristics suggest that the meteoroid was, most likely, stony.

System spectral analysis of temporal variations in the level of signals recorded by a number of European infrasound stations during the flight and explosion of the Romanian meteoroid showed a marked increase in the amplitudes of the spectral components mainly in the range of 2–5 s [11–13]. The average value of the period was 3.68 ± 0.27 s. The delay times determined by means of the system spectral analysis made it possible to calculate the celerity of infrasonic signals, which varied 243–317 m/s. With allowance for wind correction, the actual celerity was about 280 m/s, and the average tropospheric–stratospheric wind velocity was about 20 m/s. The duration of infrasonic signals with increasing distance from the explosion area to the infrasonic station increased from about 0.1 min to several minutes. The initial kinetic energy of the meteoroid is estimated from the average period of acoustic oscillations (3.68 ± 0.27 s). Its value was 0.41 ± 0.10 kt, which is very close to an estimate of this energy by the luminosity energy (0.4 kt). According to pressure measurements at the microbarograph closest to the epicenter of the explosion (about 32 km), the acoustic energy of the explosion, $(2.0 \pm 0.4) \times 10^{11}$ J = 0.228 ± 0.013 kt TNT, was calculated, which was 12.0 ± 2.4 % of the meteoroid initial kinetic energy. The main parameters of a cylindrical shock wave were calculated: the radius of 100—140 m, the longitudinal dimension of about 42–46 km, and the characteristic period of 0.30–0.47 s. The pressure in the front of a cylindrical shock wave on the Earth's surface in the epicenter was about 0.6–12 Pa at a meteoroid altitude of 85–55 km, respectively. At altitudes of 50–40 km, there was an imposition of cylindrical and explosive shock waves. The main parameters of an explosive shock wave were calculated: the radius of 0.66 km, the characteristic period of 3.3 s, and the duration of 29 s. The pressure in the front of an explosive shock wave on the surface of the Earth in the epicenter of the explosion was close to 13 Pa. The both shock waves caused an overpressure from ~20 Pa to ~25 Pa on the surface of the Earth below the epicenter of the explosion, which is confirmed by measurements at the IPLOR station giving 21–28 Pa. It was confirmed that for the Romanian meteoroid, at distances of up to about 250 km from the explosion area, there was also ray propagation, and at larger distances there was mainly the waveguide propagation of acoustic waves. The dependence of the amplitude of the excess pressure on the distance traveled by the wave is calculated. Based on the experimental data, we estimated the dependence of the attenuation coefficient of the acoustic signal on the distance. This coefficient gradually increased from 1.4×10^{-4} to 1.8×10^{-3} km^{-1} with an increase in distance of ~300 km to ~1400 km.

Lipetsk meteoroid infrasound. The meteoroid entered the Earth's atmosphere on June 21, 2018, at 01:16:20 UT. The space body was moving at an angle of approximately 79° with respect to the horizon with an initial velocity of 14.4 km/s [14–20]. According to the calculations, the initial mass of the body was 113 t, and the initial diameter was approximately 4 m. The altitude of the meteoroid explosion, its kinematic characteristics, and discovered fragments indicate that it was a stony meteoroid or, more specifically, a chondrite.

Using the data acquired from 10 stations that are included in the International Monitoring System set up by Comprehensive Nuclear-Test-Ban Treaty Organization's International Monitoring System, the analysis of the temporal dependencies of the pressure in the infrasonic waves that were generated by the fall of the Lipetsk meteoroid on June 21, 2018, is presented, and the following important features have been established [19].

The infrasonic signal exhibits a linear dependence of the infrasonic signal time delay on the horizontal distance from the meteoroid explosion epicenter, and the signal celerity averaged over all propagation paths is estimated to be approximately 304–305 m/s. The infrasonic signal celerity first shows a rapid enough decrease with distance, but over the 4.5–8.66 Mm distance range exhibits fluctuations about the 302 m/s value. The duration of the infrasonic signal shows a linear decrease with distance, and the signal duration dispersion is insignificant in the 5–8 Mm distance range. The mean periods of the infrasonic signal, independent of distance and averaged over various

regression functions, are estimated to be 6.28 ±0.98 s and 6.14 ±0.76 s. The mean of the initial kinetic energy estimated using the oscillation period of the infrasonic signal is 2.26–2.43 kt TNT, which differs insignificantly from the NASA estimates (2.8 kt TNT). The approximation for the dependence of celerity vs. sine of the back-azimuth angle of arrival shows that the corrected value of the celerity is about 300 m/s, and the mean of the troposphere-stratosphere wind is approximately 25–31 m/s. Analysis of the scatter diagrams has shown that a steady statistical link exists between the true and observed back-azimuth angles of infrasound sources. It is noted that the level of fluctuations in the azimuth tends to increase with distance.

Infrasound of Seismic and Volcanic Origin

Infrasound of Seismic Origin [21, 22]. A mechanism for the generation of magnetic precursors was proposed. It is based on air heating over the earthquake preparation area, rising heated bubbles, AGW generation, AGW modulation in the ionospheric current jet, and the generation of quasi-periodic oscillations of the geomagnetic field. Depending on the degree of atmospheric heating over the earthquake preparation area and the size of the heated air formation, the characteristic rate of the rise of heated air formation can vary from 0.1 to 10 m/s. Here, the characteristic rising time varies from 5 min to days. Moving convective formations generate AGWs with relative amplitudes of $10^{-5}-10^{-4}$ at the Earth's surface and around $10^{-2}—10^{-1}$ at the heights of the ionospheric dynamo region. The magnetic precursor amplitude can be around 0.4–4 nT, and its duration can range from a few minutes to several hours.

Infrasound of Volcanic Origin [23]. A multiple linear regression analysis has been performed to fit the pressure amplitude in the shock wave from the megaton of TNT St. Helens volcano explosion on May 18, 1980 and the distance between the explosion epicenter and thirteen 0.9–39 Mm distant infrasound stations over altogether 15 propagation paths. Multiple linear regression fits are constructed for the cases of a spherical wave-front spreading, a cylindrical wave-front spreading, and a cylindrical wave front spreading taking into account the wave attenuation and the infrasonic radiation through the waveguide wall. The latter case has been shown to be preferable.

Infrasound of Man-Made Origin

Infrasound Generated by Multiple Explosions [24–34]. The military ammunition depot (arsenal No. 48, Ministry of Defense, Ukraine, military unit A-1119) near the Town of Kalyniwka, Vinnitsa Province, Ukraine, accommodated approximately 188×10^3 t of ammunition [25]. The geographic coordinates of the depot are 49°25′ N, 28°30′ E. The first series of massive blasts occurred at 19:59 UT on 26 September 2017, and the massive blasts ceased only at 08:03 UT on 27 September 2017. Overall, twenty six series of massive blasts occurred.

The Ukrainian network of infrasonic stations was used to study the basic parameters (spectral content, amplitudes, predominant oscillation periods, duration of the oscillation trains, celerity) of the infrasonic waves which propagated over long distances (~150 to 180 km) [25–34]. The signal processing technique in this study added up to the following. First, the time dependences of atmospheric pressure fluctuation acquired in relative units were converted into absolute units. Then, they were filtered within the period range of 0.2 to 10 s. Next, the filtered variations were subjected to the system spectral analysis that includes the short-time Fourier transform, the Fourier transform in a sliding window with a width adjusted to be equal to a fixed number of harmonic periods, and the wavelet transform. In the latter transform, the Morlet wavelet was used as the basis function.

Analysis of the infrasonic signals generated in the atmosphere by the chemical explosions at the depot near the City of Vinnitsa on September 26–27, 2017, has shown the following [25–34].

It was shown that an upward trend in the amplitude and period of the predominant oscillation were observed when the energy release increased from 3 to 53 tons of TNT, while the duration of the oscillation trains increased from ≈1.5 to 2 min. The infrasonic signal parameters were determined to change insignificantly when the distance between the explosion epicenter and an infrasonic station location changed a little (by 15 to 18 %). The differences in the wave forms are related to orientation of the propagation path. The analysis has revealed that the harmonics in the 3 to 5–6 s period range were predominant when the energy release was equal to 53 tons of TNT. The duration of the trains of oscillations with such periods amounted to 40 s. The average celerity was calculated to change within 300 to 309 m/s for different propagation paths with stratospheric wave reflections, which provides evidence for the influence of the wind in the upper atmosphere on the infrasound propagation. The thermospheric reflection resulted in the signal amplitude smaller by a factor of a few times and the celerity equal from 245 to 250 m/s.

The basic parameters of infrasonic signals generated during the recurrent explosions at the ammunition depot near Vinnytsia and propagating in the atmosphere have been studied.

Infrasound from Rocket Engines. The waves in a wide frequency range are generated during rocket launches. Infrasonic waves are part of this frequency range [35–37].

Facilities for Studying Atmosphere-Ionospheric Effects of Infrasound

Former Instrumentation [38]. In Ukraine, the different modifications of high-power Ground-Based Controllable Acoustic Transmitters (GBCAT) were designed in 1991, and are used at present, for conducting experiments in the acoustic modification of the near-Earth medium at the Lviv Centre of Institute of Space Research (LC ISR), NASU/NKAU with a contribution from the G. V. Karpenko Physics-Mechanical Institute (PMI). The modern data acquisition instruments and data processing techniques include the HF radio telescope (RT) URAN-3 (PMI), ionosondes and radars at the Institute for the Ionosphere, NASU and MESU, and at the V.N. Karazin Kharkiv National University, as well as different satellite systems.

To conduct these studies, a few modifications of the GBCAT have been developed: the stationary LF synchronously pumped parametric GBCAT, which generate infrasonic waves in the 1–10-Hz frequency range; the stationary HF GBCAT of the rotational type, which generate infrasound in the 10–30-Hz range; the portable HF GBCAT mounted in a lorry, which generates infrasound at frequencies greater than 10 Hz. The stationary GBCATs are located in the LC ISR's area, Lviv, and the portable ones are placed in different places: the LC ISR, Lviv, and the NASU/MESU Institute for the Ionosphere Observatory, Kharkiv.

To remotely probe the ionosphere in order to study artificial effects produced by the infrasonic emissions, the following instrumentation have been used. (i) The PMI RT URAN-3, at Shatsk, the facility for probing the ionosphere was used as a mini-interferometer with the baseline equal to the distance between two halves of the radio telescope antenna; (ii) The radio instrumentation of the NASU/MESU Institute for the Ionosphere and the V.N. Karazin Kharkiv National University, Kharkiv, which includes the incoherent scatter radar, the Doppler radar, the MF radar, the Basis ionosonde; (iii) The sensors for taking measurements infrasound parameters, atmospheric currents, very low frequency VLF radio signal parameters, climatic parameters at all observatories; (iv) Dedicated and broadcast radio stations in the HF range. The experiments were also conducted when the DEMETER (France) and CHIBIS (Russian Federation, Hungary) satellites passed nearby the GBCAT sites and were taking in situ satellite measurements in the ionosphere [38].

Modern Instrumentation [38]. The upgrades to the facility included the RT URAN-3 data acquisition systems in order to broaden the system passband, to increase the system sensitivity, and to optimize the data presentation and processing. At present, the system takes measurements of space radio emissions as dynamic spectra of the HF component in the 16.5–33 MHz range, with the 12-kHz frequency resolution and the 1-ms–1-min time resolution.

Facility and Techniques for Studying Atmosphere-Ionospheric Effects of Infrasound

The stationary GBCAT, which was developed employing parametric coupling effects, supersonic air stream modulation, and the creation of a shock wave train, and which has the following specifications: electrical drive power 150 kW, emitted acoustic energy 1.8×10^6 J during 60 s; predominantly emitted frequencies 100 Hz and 110 Hz or 600 Hz and 630 Hz; difference frequency 1–10 Hz or 30 Hz; atmospheric acoustic wave (AAW) pressure 165 dB at 1-m distance; mass 2 t; dimensions $2.5 \times 1.5 \times 1.5$ m^3 [38].

RT URAN-3. The main telescope characteristics: frequency band 4–32 MHz; 256 antenna elements, two linear polarizations; geometric area ~14400 m^2; effective area ~4320 m^2 at 25 MHz and ~5760 m^2 at 16.7 MHz; antenna efficiency ~0.3 at 25 MHz and ~0.4 at 16.7 MHz; antenna pattern width 3.5°×15° in the East-West and North-South direction, respectively, with phase system allowing ±70° deflection from the zenith; sensitivity 50 Jy = 50×10^{-26} W m^{-2} Hz^{-1}; when the signal-to-noise ratio is 1/10 providing 15 % flux measurement error in the band pass of 14 kHz; channels for receiving, registering, and signal processing, both are radio interferential and radiometer, for calibrating, computer processing, and imaging; the parameters that are registered include signal power for each polarization, the modulus of the signal autocorrelation function for each antenna half, the scanning of the antenna pattern vs. declination and azimuth, the amplitude of signal fading and The doppler shift of frequency. To conduct experiments, based on the RT URAN-3, a series of radio instrumentation has been created: the ionospheric diagnostic facility, the 100-m baseline mini-interferometer, the short baseline interferometer with a varying baseline employing the 16-element antenna with the repeater both mounted on the ZIL-151 lorry chassis, which provides the varying baseline.

Remote sounding. Techniques that were used for the remote sounding of the ionosphere during its acoustic modification using the GBCAT: (i) the radio astronomical technique, which utilized the reception of radio emissions from space radio sources, discrete ones and Galactic background; the weakly-inclined radio sounding of the ionosphere; (iii) the scattering of radio waves by ionospheric small-scale irregularities.

The methodology of radio sounding takes into account (i) the predicted relatively low-energy ionospheric response to the acoustic excitation generated by the GBCAT, and consequently, the low signal-to-noise magnitudes of the ionospheric signals; (ii) the informational

particularities of the ionospheric signals, arising from the acoustic-electromagnetic coupling, and the employment of different GBCAT techniques, which include the following: the transmission technique in the radio astronomical method, the reflective technique in the weakly-inclined radio sounding technique, the scattering technique in the scattering method; (iii) the necessity of employing different radio techniques for diagnosing the acoustic-ionospheric disturbances (AIDs); (iv) the necessity of employing a few GBCAT modes of operation: single, periodic (steady or unsteady one), single frequency, employing adjustable difference frequency, etc.

The following five techniques are used for studying ionospheric acoustic modifications. Techniques #1 and #2, which make use of the radio astronomy technique and the reception of radio emissions from the 3C10, 3C84, 3C123, 3C134, 3C144, 3C218 and other space radio sources, the effect of scintillation of radio signals, techniques for estimating statistical characteristics of the intensity, the ability of choosing the polarization. Technique #3, which employs the radio astronomical method and the reception of radio emissions from space radio sources, discrete ones and Galactic background, and radio interferometer measurements with the mini-interferometer. Technique #4, which employs the weakly-inclined radio sounding of the ionosphere, the URAN-3 ionospheric diagnostic facility, high-frequency (HF) radio stations, the recording of the traveling ionospheric disturbances (TIDs) along one-hop propagation paths between HF radio stations and the RT URAN-3, as well as the determination of TID parameters, based on the data on the fluctuations in the ray characteristics of the signals reflected from the ionosphere, specifically the angle of arrival and the Doppler shift of frequency. Technique #5, which makes use of scattering technique, high-frequency radio stations, the two halves of the RT URAN-3 antenna at two polarization, measurements of TID dependencies vs. amplitude, polarization, and time at frequencies greater than the maximum usable frequency.

Results of the Previous Studies

The sufficiency of the transmitter power for conducting man-made ground-based modifications of different layers in the near-Earth medium, the ionosphere in particular, has been confirmed experimentally for the first time, when using controllable acoustic ground-based radiators of the GBCAT type, created by LC ISR NASU/ NKAU. The qualitative and quantitative estimates of ionospheric radio signal informational characteristics, which are suitable for the realization of information technologies for detecting and identification of AID of ground-based acoustic origin, has been determined. The prevailing majority of ground-based experiments exhibit the ionospheric response to the acoustic action with characteristic time delays of 5 min and 40 min. The satellite observations have confirmed the adequacy of the model for the ionospheric transparency in the VLF radio wave range, as well as the adequacy of the hypothesis that the ionospheric responses to the acoustic excitation of both the seismic and man-made origin are similar. Based on the analysis of the propagation of AAW in the Earth–atmosphere–ionosphere system and of the frequency characteristics of wave-like processes in the ionosphere, the models for the excitation of the ionospheric Alfven resonator at ~30 Hz and the models for the modulation of the ionospheric transparency have been determined to be efficient, in particular for the VLF band, as well as the model for disturbing the ionospheric E and F layers to be efficient at frequencies less than 10 Hz.

Using the radio astronomical method during the man-made acoustic excitation and registering signals penetrating through the ionosphere, the following has been determined: (i) the first ionospheric response to the beginning of the excitation of the acoustic signal at the ground is detected in 5–6 min, which is accompanied by signal spectrum broadening. The model of the response is described by the change in the ionospheric transparency for radio waves from the cosmos when the AAW propagate in the ionosphere vertically. (ii) The repetitive ionospheric responses to the beginning of the excitation of the acoustic signal at the ground exhibit time delays of 10 min, 20 min, 30 min, 40 min, and 60 min, show broadened frequency spectrum and the greater amplitudes; moreover, the most stable and intense response occur with a time delay of 40 min, and the model of this response includes the propagation of acoustic and plasma waves with different velocities in the ionosphere. (iii) To detect the AID, the following information parameters, which were registered in the space radio signals, has been recommended: temporal relationships between the registered ionospheric disturbances, the relative phase differences registered over a fixed time interval, the cutoff frequency in the frequency spectrum broadening.

Using the weakly-inclined radio sounding of the ionosphere technique during the man-made acoustic excitation and registering signals reflected from the ionosphere, the following has been determined: (i) an increase in the signal amplitude with a time delay of 11–13 min after the beginning of the excitation at the ground; (ii) a change in the autocorrelation function (ACF) form 1-min in duration, namely, the ACF is smoothly decaying in the absence of the acoustic excitation, and in the presence of the acoustic excitation, the ACF is oscillating and rapidly decaying; (iii) the

Doppler shift exhibits changes, in particular, the parameters of the Doppler shift of frequency are observed to oscillate with a time delay of 32 min after the beginning of the acoustic excitation, with increasing amplitude in the 0.5–1.0 Hz frequency range and in the 15–16-min period range; (iv) the reflected signals show the appearance of two rays with the 0.2–0.4-Hz difference; (v) the acoustic-electromagnetic coupling, the oscillation of the ionospheric *E* and *F* layers, is modeled by the action of the low-frequency AAWs; (vi) the correlation between the dispersion of fluctuations in the polarization ellipse angle of the reflected signal and the beginning of the acoustic excitation, moreover, the acoustically modified ionosphere corresponds to a decrease in the fluctuations of the polarization ellipse angle; (vii) to detect the AID the following information parameters of the high-frequency radio signals emitted by radio stations and reflected from the ionosphere have been recommended: the slope of decay and oscillation periods of the normalized ACF of short-term, 1-min, signal realizations, the time of appearance, period, and the number of rays and their intensity in the Doppler shift of frequency, the variance in the polarization ellipse angle of the signal and the parameters of its temporal variations.

Using the weakly-inclined radio sounding of the ionosphere technique during the man-made acoustic excitation and registering signals scattered by the ionosphere, the following has been determined: (i) the correlation between the signal amplitude variations and the beginning of the acoustic excitation; (ii) the manifestation of the first response in 7 min as a insignificant, approximately by a factor of two times, a short-term, 10–15 min in duration, increase in the amplitude; (iii) a significantly greater, approximately by a factor of 5–6 times, long-term, ~1-hr in duration, increase in the signal amplitude and the amplitude oscillation with 10–12-min period; (iv) the structure of the fluctuations in the signal parameters, amplitude and period, when the ionosphere is in a disturbed and undisturbed state; this structure corresponds to the model of acoustic-ionospheric coupling suggesting changes in the spatial structure of the scattering small-scale ionospheric irregularities and experiencing an increase in its scales under conditions acoustically disturbed, which acts to give rise to the contribution from the reverberation processes in the ionosphere and to a respective increase in the amplitude of fluctuations in the scattered signal; (v) changes in the signal Doppler spectra suggesting that the AID have the vertical component traveling at speeds close to the speed of sound; this is supported by the following effects: the spectrum broadening by 1 Hz; the appearance in 7 min of an increase in the Doppler shift of frequency up to 7 Hz that persisted for less than 1 min; the appearance of two rays; the appearance of oscillations in the Doppler shift of frequency with amplitude of less than 1 Hz, with periods of ~ 10–11 min and of ~ 22–24 min, and over those temporal intervals where an increase in the signal amplitude occurs; the Doppler shift of frequency exhibits periodical, with a ~35-min period, broadening by ~7 Hz in the time–amplitude plane, which can be described by the following model: the low-frequency AAW propagates in the atmosphere and in 7 min traverses the scattering volume under study in the ionosphere and acts to vertically shift small-scale irregularities; (vi) to detect the AID, the following information parameters of the scattered radio signals of high frequency radio stations has been recommended: parameters of the signal power temporal dependences such as the mean level over the ~1-min time interval, the level of fluctuations, oscillation periods in the mean level; the 5–10-Hz Doppler shift of frequency; parameters of the Doppler shift of frequency in the scattered signal, in particular, the presence of oscillations and their parameters: the time of appearance, period, number of rays and their intensity, the Doppler shift of frequency.

Results of Recent Studies

Development of Information Technologies [38]. An example of a single generation at 30 Hz and the detection of man-made AIDs that arise in the ionospheric plasma under the action of AAWs demonstrates [38] the following: (i) the energy weakness of the ionospheric signals from AIDs that were generated by the GBCAT at 30 Hz under the current conditions; (ii) small efficiency of the used information technologies for revealing weak AIDs arising under the action of the GBCAT. Further, the effect of employing other signal processing techniques has been estimated in order to detect weak signals generated by the GBCAT at 30 Hz and penetrating through the ionosphere

Repetitiveness of the Effects of Man-Made Acoustic Modification. The intercomparison between the samples of the signals penetrating the ionosphere during ground-based acoustic transmissions and in their absence. The beginning of the GBCAT operation is marked by 0 s over the 0–1200-s and 500–800-s intervals. The results of the intercomparisons brought a conclusion that the formation of man-made AIDs in the ionosphere is accompanied by the appearance of ~400–800-s interval that contains periodic oscillations with a relatively steady period, and in the absence of the GBCAT generation, the ionospheric signals occur in a greater noise level and the range of oscillation amplitude period is significantly broader.

Information Conveyed by Amplitude Spectrum. The measured raw signals in the 500–800-s intervals and their amplitude spectra were acquired during GBCAT

operations on September 27–28, 2018, and in the absence of GBCAT operations on September 29, 2018. The records demonstrate the absence of a stable repetitiveness of the amplitude spectra under various conditions of acoustic excitation at ~30 Hz at the ground, and the amplitude spectra do not contain distinct information features that could be used to identify, without additional processing, the man-made AID generated by the GBCAT.

Band-Pass Filtering. The signals in the 0–1000-s intervals were measured on September 27–28, 2018, during GBCAT operations, and in the absence of GBCAT operations on September 29, 2018. The beginning of the GBCAT operation corresponds to 0 s. The 22-, 23-, and 24-MHz signals filtered in the 4-kHz band are also presented in [38]. Their analysis shows that the manifestations of the man-made acoustic ionospheric modification depend on the sounding frequency. This suggests that the sounding signal frequency influences the information that could be inferred with the radio astronomical technique, and consequently, the necessity of optimizing the receiver channel frequency parameters in such experiments.

Wavelet Transform of the Band-Pass Filtered Signals. The technique makes use of the signals that were measured on September 27–28, 2018, during GBCAT operations, and in the absence of GBCAT operations on September 29, 2018, the 22-, 23-, and 24-MHz signals filtered in the 4-kHz band, and their wavelet transform employing the Daubechies and Morlet wavelets as basis functions.

System Spectral Analysis. One of the modifications of augmented spectral analysis has been tested in order to reveal weak AIDs caused by the GBCAT action at frequencies close to 30 Hz. Following the spectral analysis applying the Daubechies basis function, the energy vs. period dependencies were obtained, which have confirmed that the main contribution to the effects from the applying this type of analysis consists in the localization of the spectral components on the time axis due to the wavelet transform, not due to the filtering.

Augmented System Spectral Analysis. The processing technique presented above has been supplemented by plotting scalograms that make use the number of LF oscillation periods calculated in the time interval of taking measurements. The use of scalogram plotting permitted the detection of the prevailing LF oscillation periods of the ionospheric signals that penetrated through the ionosphere over the 0–1000-s interval. The prevailing periods were stably detected on September 27, 2018, and September 28, 2018, during the acoustic excitation, they were observed to be 95 s and 190 s. In the absence of the acoustic excitation, March 29, 2019, these prevailing period values were not registered. The obtained result confirms the advisability of applying the information technologies of plotting scalograms for detecting weak AIDs created in the ionosphere under the GBCAT action in the ~30-Hz range.

Experimental Results. To test acoustics-electromagnetic facility for probing the ionosphere, a series of 15 experiments was conducted since September 25, 2018, to September 29, 2018 [38]. The current state of weather was taken into account, since it can significantly influence the propagation of the AAW at frequencies close to 30 Hz.

The man-made AID studies have been conducted with the cosmos radio emission technique using radio emissions from discrete sources and the Galactic background in the 20–25 MHz range. The temporal dependencies of radio waves that penetrated through the ionosphere were analyzed before, during, and after the GBCAT operation, as well as without the acoustic excitation when the direction of the RT URAN-3 antenna pattern was fixed. The geometry was chosen in such a way that the radio emissions could intercept the AAW at ionospheric altitudes of ~50–200 km, and the emission intensity correspond the RT URAN-3 sensitivity. These requirements at that time were met by the 3C274 and 3C348 radio sources at the climax angles of 51° and 44° and with the fluxes of 5300 Jy and 2300 Jy, respectively.

The changes due to the acoustic modification of the ionosphere at altitudes higher than 100 km have been detected. The detected ionospheric disturbances could be identified as the man-made AID caused by the GBCAT action by calculating the time delay needed for the AAWs to travel to the ionosphere. This result confirms the possibility of applying, in this case, the model of making the ionosphere resonantly transparent due to the traveling periodic structure in the ionospheric electron density with a period equal to the AAW duration. According to this model, the transparency of the ionosphere can increase under certain conditions; moreover, the transmission coefficient can increase by a factor of many times.

Conclusions

Analysis of measurements made with the upgraded facility and the employment of information techniques of the system spectral analysis of radio emissions of space radio sources using band-pass filtering, the wavelet transform, and scalogram plotting, has confirmed that the ground-based generation of infrasound at a frequency near the upper bound of the infrasonic range, 30 Hz, can bring about the physical realization of the effect of the man-made controllable acoustic modification of the ionosphere and the detection of weak man-made acoustics-ionospheric disturbances

under certain states of the near-ground and upper atmosphere, which determine the weather state and influence the propagation of the atmospheric acoustic waves, as well as under certain interference conditions. The further studies of the effects of the man-made acoustic modification of the ionosphere foresee the use of the ground-based controllable acoustic radiator in the 2–10-Hz range.

REFERENCES

1. Chernogor L.F., Shevelev M.B. Dependence of the infrasonic wave amplitude generated by the Tunguska celestial body on distance. *Radio Physics and Radio Astronomy*. 2018. Vol. 23, No. 2. P. 94–103.

2. Shevelev M.B., Chernogor L.F. Infrasonic effects from the Tunguska meteoroid: Global statistics. *Abstr. the 18th Ukr. Conference on Space Research,* Kyiv, September 17–20, 2018. Kyiv, 2018. P. 52.

3. Chernogor L.F., Shevelev M.B. Parameters of the infrasound signal generated by a meteoroid over Indonesia on October 8, 2009. *Kinematics and Physics of Celestial Bodies*. 2018. Vol. 34, No. 3. P. 147–160.

4. Chernogor L.F., Shevelev M.B. Characteristics of infrasonic signals generated by the Chelyabinsk celestial body: Global statistics. *Radio Physics and Radio Astronomy*. 2018. Vol. 23, No.1. P. 24–35.

5. Chernogor L.F., Qiang G., Rozumenko V.T., Shevelev M.B. The parameters of the infrasonic waves generated by the Chelyabinsk meteoroid. *Astronomy and Space Physics in the Kyiv University*: book of abstracts of International Conference, Kyiv, Ukraine, May 29 – June 01, 2018. P. 89–90.

6. Chernogor L.F., Lazorenko O.V., Onishchenko A.A. Multi-Fractal Analysis of the Acoustic Ultra-Wideband Signal Caused by the Chelyabinsk Meteoroid. *The 9th International Conference on Ultrawideband and Ultrashort Impulse Signals*: book of abstracts, September 4–7, 2018, Odessa, Ukraine. P. 27.

7. Chernogor L.F., Lazorenko O.V., Onishchenko A.A. Multi-Fractal Analysis of the Acoustic Ultra-Wideband Signal Caused by the Chelyabinsk Meteoroid. *Proceedings the 9th International Conference on Ultrawideband and Ultrashort Impulse Signals*. P. 123–126.

8. Chernogor L.F., Shevelev M.B. Dependence of infrasonic wave amplitude on distance: computer simulation. *Proceedings the 14th International Scientific Conference on Electronics and Applied Physics*. October 23–26, 2018, Kyiv, Ukraine. P. 136–137.

9. Guo Q., Zheng Y., Chernogor L.F., Rozumenko V.T., Shevelev M.B. The Parameters of the Infrasonic Waves Generated by the Chelyabinsk meteoroid: System Statistic Analysis Results. *Proceedings the IEEE 2nd Ukraine Conference on Electrical and Computer Engineering,* Lviv, Ukraine, July 2–6, 2019. P. 938–941.

10. Onishchenko A.A., Chernogor L.F., Lazorenko O.V. Dynamical fractal analysis of the acoustic ultra-wideband signal caused by the Chelyabinsk meteoroid. Eskişehir Technical University Journal of Science and Technology. *A– Applied Sciences and Engineering*. 2019. Vol. 20. P. 188–192.

11. Chernogor L.F. Physical effects of the Romanian meteoroid. 1. Space *Science and Technology*. 2018. Vol. 24, No. 1. P. 49–70.

12. Chernogor L.F. Physical effects of the Romanian meteoroid. 2. *Space Science and Technology*. 2018. Vol. 24, No. 2. P. 18–35.

13. Chernogor L.F. Parameters of Acoustic Signals Generated by the Atmospheric Meteoroid Explosion over Romania on January 7, 2015. *Solar System Research*. 2018. Vol. 52, No. 3. P. 206–222.

14. Chernogor L.F. Physical Effects of the Lipetsk Meteoroid: 1. *Kinematics and Physics of Celestial Bodies*. 2019. Vol. 35, No. 4. P. 174–188.

15. Chernogor L.F. Physical Effects of the Lipetsk Meteoroid: 2. *Kinematics and Physics of Celestial Bodies*. 2019. Vol. 35, No. 5. P. 217–230.

16. Chernogor L.F. Physical Effects of the Lipetsk Meteoroid: 3. *Kinematics and Physics of Celestial Bodies*. 2019. Vol. 35, No. 6. P. 271–285.

17. Chernogor L.F. Geomagnetic Variations Caused by the Lipetsk Meteoroid's Passage and Explosion: Measurement Results. *Kinematics and Physics of Celestial Bodies*. 2020. Vol. 36, No. 2. P. 79–93.

18. Chernogor L.F. Effects of the Lipetsk Meteoroid in the Geomagnetic Field. *Geomagnetism and Aeronomy*. 2020. V. 60, No. 3. P. 355–372.

19. Chernogor L.F., Shevelev M.B. Characteristics of the infrasonic signal generated by the Lipetsk meteoroid: Results of the statistical analysis. *Kinematics and Physics of Celestial Bodies*. 2020. *(in press)*.

20. Chernogor L F. Electrical, electromagnetic, acoustic, and plasma effects from the Lipetsk meteoroid. Global Electrical Circuit. *Proceedings of the 4th Russian Conference* / Borok Geophysical Observatory, O. Yu. Shmidt. Institute for Earth's Physics Branch, Yaroslavl: Filigran, 2019. P. 78–79.

21. Chernogor L.F. Geomagnetic Disturbances Accompanying the Great Japanese Earthquake of March 11, 2011. *Geomagnetism and Aeronomy*. 2019. Vol. 59, No. 1. P. 62–75.

22. Chernogor L.F. Possible Generation of Quasi-Periodic Magnetic Precursors of Earthquakes. *Geomagnetism and Aeronomy*. 2019. Vol. 59, No. 3. P. 374–382.

23. Chernogor L.F., Shevelev M.B. Dependence of infrasonic wave amplitude generated by the powerful volcano on distance. *Bulletin of Karazin Kharkov National University, Radiophysics and Electronics Ser*. 2017. Iss. 27. P. 57–60.

24. Chernogor L.F., Garmash K.P. Magnetospheric and Ionospheric Effects Accompanying the Strongest Technogenic Catastrophe. *Geomagnetism and Aeronomy*. 2018. Vol. 58, No. 5. P. 673–685.

25. Chernogor L.F., Liashchuk O.I., Rozumenko V.T., Shevelev M.B. Infrasonic Signals Generated by a Series of Chemical Explosions near Vinnytsia City. *Astronomy and Space Physics in the Kyiv University*: book of abstracts of International Conference, Kyiv, Ukraine, May 29 – June 01, 2018. P. 87–88.

26. Chernogor L.F., Liashchuk O.I., Shevelev M.B. Ultra-Wideband Infrasonic Signals Generated by Series of Chemical Explosions. *Abstr. the 9th International Conference on Ultrawideband and Ultrashort Impulse Signals,* Odessa, Ukraine, September 4–7, 2018. P. 39.

27. Chernogor L.F., Liashchuk O.I., Shevelev M. B. Ultra-Wideband Infrasonic Signals Generated by Series of Chemical Explosions. *The 9th International Conference on Ultrawideband and Ultrashort Impulse Signals*: conference proceedings. 2018. P. 318–321.

28. Shevelev M.B., Liashchuk O.I., Chernogor L.F. Infrasonic signals generated explosions at the military ammunition depot near the City of Vinnitsa. *Abstr. the 18th Ukrainian Conference on Space Research*, Kyiv, Ukraine, September 17–20, 2018. P. 51.

29. Chernogor L.F., Liashchuk O.I., Shevelev M.B. Parameters of the infrasonic signals generated in the atmosphere during man-made disaster near the City of Vinnitsa: Results of processing the data collected at the Ukrainian microbarograph network. Iss. 5. Numerical Techniques and Information Processing Systems*: proceedings of the 5th Science and Technology Conference*, Lviv, October 4–5, 2018. Lviv: PMI Institute NASU, 2018. P. 99–103.

30. Chernogor L.F., Liashchuk O.I., Shevelev M.B. Parameters of the infrasonic signals generated in the atmosphere by massive explosions at an ammunition depot. Radio *Physics and Radio Astronomy*. 2018. Vol. 23, No. 4. P. 280–293.

31. Chernogor L.F., Liashchuk O.I., Shevelev M.B. Parameters of infrasonic signals generated in the atmosphere by multiple explosions at an ammunition depot. *Proceedings of the 19th International Young Scientists' Conference on Applied Physics*. May 21–25, 2019, Kyiv, Ukraine. P. 100–101.

32. Chernogor L. F., Liashchuk O. I., Shevelev M. B. Parameters of infrasonic signals generated in the atmosphere by multiple explosions at an ammunition depot. *Astronomy and Space Physics in the Kyiv University*. book of abstracts of International Conference. May 28–31, 2019. P. 90–91.

33. Chernogor L.F. Electrical, magnetic, electromagnetic, and acoustic effects accompanying massive chemical explosions. Global Electrical Circuit: *Proceedings of the 4th Russian Conference* / Borok Geophysical Observatory, O. Yu. Shmidt. Institute for Earth's Physics Branch, Yaroslavl: Filigran, 2019. P. 80–81.

34. Chernogor L.F., Liashchuk O.I., Shevelev M.B. Systems spectral analysis of the infrasonic signals generated during a man-made disaster. International Baikal Youth Science School of Fundamental Physics. *Proceeding of the 16th Conference of Young Scientists*, Interaction of Fields and Radiation with Matter, Irkutsk, September 16–21, 2019. P. 178–180.

35. Vovk A.N., Voronkina V.O., Chernogor L.F. Effects from rocket launches: Results of Doppler radio sounding. *Abstr. the 18th Ukrainian Conference on Space Research*, Kyiv, Ukraine, September 17–20, 2018. P. 22.

36. Garmash K.P., Rozumenko V.T., Chernogor L.F. Geomagnetic effects accompanying rocket launches in 2017–2018 *Abstr. the 18th Ukrainian Conference on Space Research*, Kyiv, Ukraine, September 17–20, 2018. P. 25.

37. Chernogor L.F., Blaunstein N. Radiophysical and Geomagnetic Effects of Rocket Burn and Launch in the Near-the-Earth Environment. Boca Raton, London, New York: CRC Press. Taylor & Francis Group, 2018. 542 p.

38. Koshovyy V.V., Ivantyshyn O.L., Nogach R.T., Chernogor L.F., Nazarchuk Z.T., Melnyk M.O., Kalita B.I., Kharchenko B.C., Romanyshyn I.M., Lozynskyi A.B., Rusyn B.P., Karatayeva L.M., Lyubinetsky Z.I., Alyohina L.V., Lipsky V.K. Artificial acoustic modification of the near-earth environment. *Space Science and Technology*. 2020. Vol. 26, No. 2. P. 19–58. URL: https://doi.org/10.15407/knit2020. 02.000.

PHYSICAL EFFECTS IN THE ATMOSPHERE AND GEOSPACE ENVIRONMENT UNDER QUIET AND DISTURBED CONDITIONS

L. Chernogor, V. Rozumenko
V.N. Karazin Kharkiv National University

Introduction

During 2018–2020 Kharkiv V.N. Karazin National University has continued to conduct experimental and theoretical studies of physical processes operating in the atmosphere and geospace under quiet and disturbed conditions. The observations were made with the radio instrumentation located at the Kharkiv V.N. Karazin National University Radio Physical Observatory (49°38′N, 36°20′E) and with the magnetometer located at the Kharkiv V.N. Karazin National University Magnetometer Observatory (49°38′N, 36°56′E). Also, the multi-frequency multiple-path radio system located at the Harbin Engineering University campus, People's Republic of China, (45.78°N, 126.68°E) was used [1].

The purpose of this paper is to report the results of experimental, theoretical studies and simulations of physical processes acting in the atmosphere and the geospace environment, which were conducted at Kharkiv V.N. Karazin National University during 2018–2020. The study is based on systems science approach to understanding of the Earth–atmosphere–ionosphere–magnetosphere system and the Sun–interplanetary-medium–magnetosphere–ionosphere–atmosphere–Earth system [2, 3].

Solar Eclipse Effects

The solar eclipse (SE) over Kharkiv City commenced at 09:09 UT and ended at 11:09 UT on March 20, 2015. The eclipse magnitude equal to 0.55 was observed at 10:15 UT (12:15 LT), while the eclipse obscuration was equal to 0.45 [4, 5]. Observations of disturbances in the atmosphere, ionosphere, and the geomagnetic field have been taken from an middle frequency radar over 60–100 km altitude region, a Doppler radar at vertical incidence at 3.2 MHz and 4.2 MHz from 100 km altitude to the F2 peak, a digital ionosonde from 100 km altitude to the F2 peak, a navigation satellite system, a fluxgate magnetometer in the 0.001–1 Hz frequency range, and a standard thermometer system at the Kharkiv V.N. Karazin National University Radio Physical Observatory (near Kharkiv City). A decrease of approximately 0.5 MHz or 6.4 % in the critical F2-layer frequencies (f_oF2) occurred at approximately 10:00 UT with the corresponding decrease of 12 % in the electron number density N. The critical E-layer frequencies (f_oE) decreased by 11 % and N by 21 %. In the course of the eclipse, the Doppler shift of frequency f_D first sharply decreased approximately to –0.15 Hz, then gradually increased up to about +0.15 Hz at 11:00 UT, and subsequently decreased to 0.0 Hz. Quasi-periodic oscillations with periods of 10 to 60 min were superimposed on the slow variations in f_oF2 and f_D. The corresponding amplitude of 5–7 % was observed in the electron density. On the day of the SE and on reference days, quasi-periodic variations in the horizontal components of the geomagnetic field occurred with an amplitude of 0.5–1 nT. The cloudiness resulted in a maximum decrease in the air temperature by a mere 0.9–1 °C at an altitude of 3 m, with the minimum observed at 10:37 UT. The spatial distribution of disturbances near the F2 peak height is described in [2]. We confirmed that March 20, 2015, SE was accompanied by the intensification of wave processes at altitudes of the ionospheric $F2$ layer. The value of the response to the eclipse depended on the ionosonde geographic location.

The SE effects observed over the People's Republic of China on August 11, 2018, are described in [6, 7]. The solar eclipse was first accompanied by an increase in the number of rays, then by the generation of oscillatory processes in the atmospheric gravity wave (AGW) period range, as well as by the negative, and later by positive of lower value, Doppler shift of frequency.

The greatest reduction, 26 %, in the electron density is determined to occur in the ionospheric E region along the Hailar to Harbin propagation path where the eclipse magnitude, M, of 0.516 and the eclipse obscuration, A_m, of 0.415 occurred. The magnitude of this decrease determined from the observations virtually does not differ from the theoretical estimates, 24 %. The relative

amplitude of quasi-periodic oscillations in the electron density during the solar eclipse lies in the range of ~1–10 %.

Effects from Geospace Storms

In the 1980's, L. F. Chernogor ascertained that a geospace storm is comprised of inextricably linked geomagnetic, ionospheric, atmospheric, and electrical storms. Solar storm consequences are felt in all Sun–interplanetary medium–magnetosphere–ionosphere–atmosphere–Earth system subsystems [6, 8, 9]. All geospace storms, which occurred during the 2018–2020 have been analyzed.

Observations of radio wave characteristics in the ~6–10 MHz range and of ionospheric disturbances over the People's Republic of China during the strong (K_p = 7) geomagnetic storm of August 25–26, 2018, were performed by the coherent multiple-path radio probing of the ionosphere at oblique incidence. The observations have revealed aperiodic and quasi-periodic variations in the Doppler shift of frequency. The ionospheric storm caused an increase in the number of rays, Doppler spectrum broadening, and in a significant shift in the radio wave propagation paths. The value of aperiodic variations in f_D, changing sign, and in their oscillation amplitude have been shown to not exceed 0.6–0.7 Hz and 0.5–0.6 Hz, respectively. The magnetic storm was accompanied by a multiple-phase ionospheric storm that lasted for no less than 16 h, since 22:00 UT on 25 August 2018 till 14:00 UT on 26 August 2018. The reflection level rises and falls were caused by a decrease in N by a factor of 1.5–2 times and by an increase in N by a few times, respectively. The N exhibited a maximum increase of 1.5 times in the ionospheric E region and a factor of 3 times in the F region. The relative amplitude of oscillation in N attained many tens of percent.

The Large Celestial Bodies Falling Effects

Theoretical Studies and Simulation [10–13]. The results of studying the possibility of a meteoroid plume appearing at ionospheric heights and of estimating its basic parameters have shown the following [10]. A meteoroid plume that forms by even relatively small (meter-sized) celestial bodies can reach the altitudes of the lower ionosphere. The velocity of the plume motion exceeds 1 km/s; the time of its rise, depending on the size, ranges from several seconds to approximately two minutes. The supersonic motion of the plume leads to the generation of a ballistic shock wave with a radius of ~1–10 km. It corresponds to the characteristic period of 3–40 s. The shock propagating upward to the distances of tens of kilometers from the maximum altitude of the plume rise is able to cause relative disturbances in the N reaching ~10–100 % in the E and F1 ionospheric regions. The disturbances in N lead to variations in the ionospheric plasma conductivity, ionospheric currents, and geomagnetic field with an amplitude of ~1 nT. The meteoroid plume at stratospheric and mesospheric altitudes can cause the formation of nacreous and noctilucent clouds, respectively. The meteoroid plume at lower ionospheric altitudes can lead to the formation of the dust plasma, which significantly changes the electrodynamic properties of the medium. This leads to a significant decrease in the plasma conductivity and in the strength of ionospheric current, as well as to disturbances in the geomagnetic field and other processes.

Numerical simulations of one-dimensional movement of a thermal created by a meteoroid explosion in the terrestrial atmosphere and spanning scale sizes from decimeters to meters have shown the following [11]. The rise velocity varies nonmonotonically: it increases rapidly at first and its increase rate decreases with the increasing drag of the incoming air; for a long time (tens to thousands of seconds), this velocity remains close to the maximum (approximately 10...180 m/s), and then it decreases relatively slowly (for hundreds to thousands of seconds) to zero. The more heated is the thermal and the larger is its size, the faster and higher it rises, over longer time intervals. In the process of rising, the radius of the thermal increases by a factor of 6–25, depending on its initial size and initial temperature which is due to the entrained cold air. The greater the current radius value, the higher the increase rate of the thermal radius. A small thermal shows an increase in size by a factor of more times than a big thermal does. The thermal radius increases until it is completely stopped. Less heated thermals rise more slowly, entrain smaller amounts of cold air, and increase less in size. The cooling rate is proportional to the thermal rise velocity and is a maximum when the maximum value of this velocity is attained. The warmer thermal cools more rapidly than the less heated one. The thermal cooling rate depends relatively weakly on its initial size.

Third order splines provide the best fit to the Chelyabinsk meteoroid altitude and geographic coordinate regression time dependences. The temporal dependencies of the Chelyabinsk celestial body speed and deceleration have been calculated from the trajectory measurements. The equations of meteorite physics have been used to calculate mass, midsection, and meteoroid optical radiation intensity vs. time and vs. altitude dependences [12]. The air drag coefficients have been presented ($C_d \approx 0.8$).

The height-temporal balance of energy loss has been compiled and calculated for processes accompanying the fall of the Chelyabinsk meteoroid [13]. The temporal dependence of the mass loss rate is used for calculating

the temporal dependence of the Chelyabinsk celestial body midsection and the ratio C_h/Q has been estimated to be about $2.5 \cdot 10^{-8}$ kg/J. Based on the energy balance, the coefficient of the dynamic resistance, C_d, has been estimated to be about 0.76, the coefficient of heat transfer, C_h, to be about 0.4, and the ablation specific energy, Q, to be about 16.2 MJ/kg. The total energy loss transferred to the air amounts to 78 kt TNT (16.8 %), to the total radiated energy 37 kt TNT (8 %), to the ablation and disintegration 38 kt TNT (8.2 %), and to the mass loss involving fragment fall-away 311 kt TNT (67 %).

Tunguska Meteoroid. A statistical relation of the amplitude of the infrasonic signal generated by the celestial body vs. distance is presented in [14].

The Indonesian Superbolide. The Indonesian meteoroid entered the Earth's atmosphere on October 8, 2009 at 02:57 UT [15]. It exploded over the point with the coordinates 4.9°S, 122.0°E (average error of 2.9°). The initial kinetic energy of the meteoroid was 70 ± 20 kt TNT, 8...10 m in diameter, and mass of not more than 6000 t. The average time interval between two falls of such bodies is 10...22 years. Main parameters of infrasonic signal that generated by the Indonesian superbolide was studied [15].

The Chelyabinsk Superbolide. On the morning of February 15, 2013, a space object with diameter $d \approx$ ≈ 18 m, velocity $v \approx 18.5$ km/s and mass $m \approx 11$ kt entered the Earth's atmosphere at 03:20:22 UT (09:20:22 local time) near the city of Chelyabinsk. Most researchers conclude that the angle was approximately 18°. The azimuth was 283°. The initial kinetic energy was equal to ~440 kt TNT.

Chelyabinsk meteoroid effects that occurred in the magnetosphere on February 15, 2013, have been studied in [16]. Aperiodic variations with an amplitude of 1–6 nT and duration of approximately 25–30 min were discovered in the Earth's main magnetic field. The variations occurred 33–38 min prior to the explosion of the Chelyabinsk meteoroid and were associated with the passage of the meteoroid in the magnetosphere. Variations in the geomagnetic fluctuation level were discovered in the range of periods 1–1000 s, with an amplitude of 2–3 nT and duration of 27–35 min; they were observed 44–47 min before the explosion of the Chelyabinsk space body. A model of the generation of aperiodic, quasiperiodic, and noise-like geomagnetic disturbances caused by the approaching space body was proposed. According to this model, the asteroid's motion in the magnetosphere could create a zone of a decreased magnetic field with a induction of 0.7—28 μT, depending on the distance to the Earth's surface, which moved with the space body and persisted for approximately 23–29 min. The period of "lateral" oscillation of the magnetic field lines was 0.1—10 s. The disturbance in the geomagnetic field induction on the Earth's surface was approximately 0.4—1.8 nT. The estimated magnitude, durations, and periods of the disturbances are close to their observed values. The noise-like variations in the geomagnetic field were caused by the plasma turbulence generated by the space body.

The fractal and statistical characteristics of the infrasonic signals generated by the Chelyabinsk meteoroid are described in [17, 18].

Romanian Meteoroid. The meteoroid entered the terrestrial atmosphere at 01:05:56 UT on January 7, 2015 [19]. The celestial body traveled at north-west direction at about 211° azimuth with an inclination of the trajectory to the horizon, α, of approximately 59.6°. The initial mass, m_0, of the celestial body is estimated to be close to 2.6 tons, the initial velocity $v_0 \approx 35.7$ km/s, and the initial diameter $d_0 \approx 1.15$ m. The altitude of the meteoroid explosion, z_e, according to NASA, is estimated to be about 45.5 km, and the meteoroid kinematical characteristics suggest that it was stony.

The comprehensive analysis of the basic processes that accompanied the fall of the Romanian meteoroid through the Earth–atmosphere–ionosphere–magnetosphere system (EAIMS) has shown the following [19, 20]. The initial kinetic energy, E_k, of the meteoroid is estimated to be about 1.66 TJ or 0.4 kt TNT. Approximately 8 % of the E_k was transformed into the flash energy. The altitude of the Romanian body explosion is estimated to be about 43 km, and the length of the explosion region approximately 3.3 km. In the vicinity of this altitude, the meteoroid velocity reduced by 35 %, and the mass by a factor of almost 3. The excess pressure at the ground in the vicinity of the explosion epicenter has been estimated to be 20–30 Pa. The disturbances in the air pressure at ionospheric heights over the explosion epicenter attained tens or even hundreds of percent. The energy and power of the explosion-like process are estimated to be close to 1.3 TJ and 10 TW. The energy and power of the flare are estimated to be about 0.136 TJ and 1.6 TW, respectively. The meteoroid trail, which was heated to 3500 K, cooled mainly due to radiation, as well as owing to expansion and eddy mixing with the cold air. In the course of a few tenths of one second, an increase in the trail temperature amounted to mere a few degrees Kelvin. After the meteoroid fall and explosion, a heated and rarified trail appeared, and a plume traveled along it. Two simplified one-dimensional models have been suggested for the movement of the plume along the trail and in the vertical direction. The height of the plume ascension in both models was suggested to be approximately 10 km. The temporal and height dependences of the gas-dust cloud velocity, acceleration, and height of an uplift, which were caused by the

convection of heated explosion products have been found. The plume velocity, acceleration, and height of a vertical uplift have been estimated. The plume acceleration has been shown to increase from zero to a maximum value of 1500 m/s^2 in the course of 15 ms. During the following 250 ms, the acceleration magnitude decreased to 0 m/s^2. Then, a near-uniform cloud motion upwards took place. Within the 23–70-s interval after the explosion, the acceleration insignificantly increased due to a decrease in atmospheric pressure, while the uplift velocity did not increase appreciably. The model calculations suggest that this velocity was equal to approximately 90 m/s. The movement of the gas-dust cloud gradually ceased owing to its cooling and eddy mixing with the cold air. The maximum height of the plume uplift, attained in 23–70 s after the beginning of the uplifting, has been calculated to be 2.2–7.1 km, depending on the magnitude of the eddy diffusion coefficient. After the uplifting, the gas-dust cloud took part in the following three processes: a slow settling toward the Earth's surface, eddy mixing with the ambient air, and the transport around the globe by neutral winds. The time needed for the settling was controlled by eddy mixing and amounted to 10–30 days, depending on the size scale. The fall and explosion of a meteoroid of 1 m and greater in size act to give rise to appreciable (or large) disturbances in all geospheres. The fall of the celestial bodies mentioned above is accompanied by plasma, magnetic, electric, electromagnetic, and acoustic effects. The disturbance in the geomagnetic field at the ground in the vicinity of the meteoroid explosion can attain 0.5–1 nT. Appreciable disturbances from the explosion and secondary processes propagate at distances no less than a thousand kilometers. The acoustic and atmospheric gravity wave period is estimated to be a few tens of minutes, and the amplitude units of percent. The disturbances in N over the explosion epicenter attain tens to hundreds percent. The magnitude of the earthquake caused by the Romanian body did not exceed 1. The celestial bodies, similar to the Romanian meteoroid, fall at Earth at a rate of 1 per 43 days on average.

The main results of the study of the Romanian meteoroid infrasonic effect are described in [21].

Lipetsk meteoroid. The meteoroid entered the Earth's atmosphere on June 21, 2018, at 01:16:20 UT [22]. The space body was moving at an angle of approximately 79° with respect to the horizon with an initial velocity of $v_0 \approx 14.4$ km/s. According to the calculations, the initial mass of the body was $m_0 = 113$ t, and the initial diameter d_0 was approximately 4 m. The altitude of the meteoroid explosion, its kinematic characteristics, and discovered fragments indicate that it was a stony meteoroid or, more specifically, a chondrite.

The comprehensive analysis of the basic processes that accompanied the fall of the Lipetsk meteoroid in the EAIMS has ascertained the following [22–24]. The initial kinetic energy of the meteoroid was close to 11.7 TJ or 2.8 kt TNT [22]. Approximately 10.4 % of the initial kinetic energy of the space body was transformed into the energy of the light flare. The altitude of the explosion of the Lipetsk body was close to 27 km, and the length of the explosion region was approximately 3.75 km. At this altitude, the meteoroid velocity decreased by approximately 12 %, and the mass decreased by 16 %. The mass loss rate reached 130–140 t/s; the deceleration was approximately 21 km/s^2. The values of energy and power of the light flare were approximately 1.22 TJ and 2–3 TW, respectively. The excess pressure on the Earth's surface at the epicenter of the explosion was approximately 140 Pa. The relative perturbations of the air pressure at ionospheric altitudes above the explosion epicenter reached tens and even hundreds of percent. The energy and power of the explosive shock wave were close to 10 TJ and 0.8 TW, respectively. The meteoroid trail that was heated to approximately 5400 K cooled down mainly due to emission as well as due to thermodynamic expansion, cold air entrainment during the ascent of the thermal, and turbulent mixing with cold air [23]. Four stages of meteoroid-trail cooling have been revealed and considered. The lifetime of the heated thermal amounted to several hours. It was found that the first stage lasted for approximately 0.01 s; the temperature of the trail decreased by a factor of two due to emission. During the second stage (~1 s), the trail cooled down due to emission and expansion, and the temperature decreased by approximately 15 %. During the third stage with a duration of approximately 3 s, the explosion products and the heated gas (thermal), having an acceleration of 100–200 m/s^2, gained the ascent rate close to 200 m/s; the temperature decreased by 10 %. The fourth stage lasted for approximately 100 s; the thermal intensively entrained the cold air, gradually cooled down, and decelerated. The time and altitude dependences of the velocity, acceleration, and altitude of ascent of the gas-dust cloud due to convection of the heated explosion products have been found. The velocity, acceleration, and altitude for the vertical elevation of the plume have been estimated. It has been shown that the initial acceleration of the plume reached a maximum value of 240 m/s^2. Its velocity increased from 0 to approximately 200 m/s, then gradually decreased to 0 m/s. The time of ascent was approximately 100 s, and the altitude of ascent of the plume in this model was 15–20 km. Their settling time was limited by turbulent mixing and, depending on their size, did not exceed 10–30 days. It has been shown that the effect of turbulence in the meteoroid trail was well pronounced, while the effect of magnetic turbulence was weak. The main parameters of the plasma in the trail have been estimated:

the altitude dependences of the linear and volume electron concentrations, their relaxation times, the frequencies of particle collisions, plasma conductivity, and electron relaxation times [23]. It has been shown that the linear and volume electron concentration in the trail at the initial time point was $(2–40)\times10^{23}$ m^{-1} and $(1–4) \times 10^{21}$ m^{-3}; the plasma conductivity was approximately 1000 Ohm^{-1} m^{-1}. The role of the dust component of the plasma could be significant. The passage and explosion of the Lipetsk meteoroid caused noticeable (or strong) disturbances in all geospheres. The passage of the Lipetsk body was accompanied by plasma, magnetic, electrical, electromagnetic, and acoustic effects [24]. The perturbation of the geomagnetic field on the Earth's surface near the explosion of the meteoroid could reach ~1 nT. The magnetic effect of AGW, ionospheric currents, and current in the meteoroid trail could be significant (~1 nT). The effect of an external electric field could lead to a short-term current pulse with a strength of up to 10^4 A. The electrostatic effect could be accompanied by accumulation of a charge of 1 mC and electric field intensity of 0.01–1 MV/m. The flow of electric current in the trail could lead to the emission of an electromagnetic pulse in the frequency range on the order of 10 kHz with an intensity of 1–10 V/m. It was found that the electromagnetic effect of infrasound could be significant (1–10 V/m and 1–10 nT). The absorption of the shock wave at the altitudes of the ionospheric dynamo region (100–150 km) could be accompanied by the generation of secondary atmospheric gravity waves with a relative amplitude of 0.1–1. The passage of the meteoroid led to the formation of a plasma trail and to disturbance of not only the lower but also the upper atmosphere. Noticeable disturbances from the explosion and secondary processes propagated horizontally in the range of at least 1000 km. Based on the estimates, the period of secondary internal gravity waves was 7–14 min, and the relative amplitude was 1–10 %. The relative disturbances of the N above the epicenter of the explosion reached tens to hundreds of percent. The possibility of the occurrence of the electrophonic effect, the generation of ionic and magnetic sound by infrasound, as well as the generation of gradient-drift and drift-dissipative instabilities, are qualitatively evaluated. The magnitude of the earthquake caused by the explosion of the Lipetsk body did not exceed 1.7. Cosmic bodies like the Lipetsk meteoroid fall to the Earth every 248 days on average.

The Lipetsk meteoroid explosion led to two effects in the ionosphere: doppler shift (DS) decomposition and quasi-periodic variations in doppler frequency shift (DFS) [25]. The first effect had a delay time of ~11 min and a duration of 21 min. The effect was caused by propagation and dissipation of the shock wave at ionospheric heights. The second effect had a delay time of ~31–33 min, the duration of ~2 h, and a period of 10–20 min. This effect was caused by the generation and propagation along the ionosphere of the AGW formed by the dissipation of the shock-wave energy in the atmosphere above the site of the meteoroid explosion. The mechanisms for the generation of both effects have been proposed and validated. It is shown that meteoroids with a kinetic energy of $\sim10^{13}$ J are able to cause the effects that can be registered in the ionosphere at a distance of hundreds kilometers from the site of explosion.

Observational data from eight magnetic observatories were used to analyze the geomagnetic field variations before and after the Lipetsk meteoroid explosion and to determine the following. Bipolar (compression and rarefaction phases) disturbances of the magnetic field with an amplitude of ~0.5 nT and an average duration of ~25 min occurred 54–56 min before the meteoroid explosion. A model of this magnetic effect was proposed. This model is based on the geomagnetic field displacement from the region of the meteoroid flight in the magnetosphere ($L \approx 8–9$) and the generation of the magnetic effect by an equivalent magnetic dipole. The results of model estimates for the main parameters of magnetic disturbance are quite consistent with observational data. A bipolar disturbance of the geomagnetic field appeared with a delay time of 7–8 to 13–14 min upon an increase in the distance r between the explosion place and observatories from 0.584 to 4.324 Mm; this is typical for explosive processes with a length of 15–20 min and an amplitude of ~4 to ~1 nT for $r \approx 0.584–4.324$ Mm, respectively. A model of the magnetic effect was proposed. This model is based on the disturbance of the electron density and ionospheric current density at the heights of the dynamo region by a shock wave generated by the meteoroid flight and explosion. The agreement between the model and data indicates that the model is adequate and the magnetic effect is characteristic of meteoroid effects. Meteoroids with a kinetic energy of $\sim10^{13}$ J can cause a magnetic effect in the magnetosphere and ionosphere recordable by ground-based magnetometers.

Using a highly sensitive fluxgate magnetometer at the V.N. Karazin Kharkiv National University Magnetometer Observatory near the Kharkiv City, Ukraine, variations in the horizontal components of the geomagnetic field were observed on the day of the fall, June 21, 2018, of a 4-m meteoroid near Lipetsk (Russian Federation) and on reference days [27]. The distance between the epicenter of the explosion and the observatory was 360 km. A magnetic effect of the magnetosphere was discovered, which consists in the occurrence of specific (characteristic of explosive processes) variations in the level of the geomagnetic field 54–56 min before the explosion of the meteoroid in the Earth's atmosphere

(at an altitude of ~27 km). The amplitude of the perturbations was 0.5 nT, and the duration was 15–20 min. The physical mechanism of the magnetic effect of the magnetosphere is proposed, which consists in the generation of a magnetic disturbance by an equivalent magnetic dipole. A dipole is formed as a result of displacement of the magnetic field by an explosive intrusion of a meteoroid into the magnetosphere. The modeling results are in close agreement with the observations. A magnetic effect of the ionosphere is revealed. It consists in the occurrence of alternating variations in the level of the geomagnetic field approximately 6 min after the explosion of the meteoroid. The perturbation amplitude was approximately 1.2–1.5 nT, and the duration reached tens of minutes. The physical mechanism of the magnetic effect is proposed, which is based on the shock wave from the meteoroid. Upon reaching the ionospheric dynamo region in 4–5 min, the shock wave caused alternating (characteristic of explosive processes) variations in the atmospheric pressure and, as a result, variations in the electron concentration and ionospheric current density and, ultimately, observed variations in the level of the geomagnetic field. The modeling results are in close agreement with the observations. It has been demonstrated that celestial bodies with an initial kinetic energy on the order of 10^{13} J cause detectable perturbations of the magnetic field both during passage through the magnetosphere and their explosion in the lower atmosphere.

The Large Celestial Body Global Statistic. Using the NASA database collected during 1994–2016, the global statistics of large celestial bodies entering the terrestrial atmosphere has been studied. The main results of the meteoroid statistical characteristics are as follows [28]. On average, 30.1 ± 1.8 meter-sized cosmic bodies fall to the Earth every year. In some years, their number can decrease by approximately half or increase by approximately one and a half times. The average frequency of meteoroid falls over Ukraine is approximately 0.054 yr^{-1}. The average time interval between the two events is close to 18.6 yr. For a flash height of 30...40 km, the fall of the body can be observed at distances up to 600...700 km. The average frequency of falls of meteoroids with an energy of at least 3 kt TNT over Ukraine that are capable of causing destruction and injuring people is approximately 0.018...0.0333 yr^{-1}. The distribution of the number of events by longitudes is almost uniform. In this case, the calculated relative event density is $1/(2\pi)$ $rad^{-1} \approx 0.159$ rad^{-1} and the one obtained from the observational data is 0.159 ± 0.008 rad^{-1}. At the same time, a similar latitudinal distribution is proportional to the cosine of the geographical latitude. After excluding the latitudinal dependence, the calculated event density is 0.5 rad^{-1}. The determination of the density of events from observational data gave a close result of $0.46 \pm \pm 0.03$ rad^{-1}. The distribution of the number of falls of cosmic bodies to the Earth by initial kinetic energies in the range 0.1–440 kt TNT is described, on average, by a power law, which qualitatively confirmed the previously obtained regularities determined for a smaller data set. Quantitatively, the dependences vary significantly. The distribution of the number of falls of cosmic bodies on our planet by velocities in the interval 11...30 km/s was detected. In this case, the most probable value of the velocity was approximately 14.5 km/s and σ, 0.4 km/s. The distribution of the number of meteoroid entries into the Earth's atmosphere by mass can be approximated by normal and power law or by a polynomial of the third degree. The distribution of the heights of the maximum total radiated energy in the altitude range 22...55 km is described by the normal law with an average height of 36.7 ± 0.5 km and $\sigma \approx 7.2$ km. This law refers to the stone meteoroids of low and medium strength. Low-strength cosmic (cometary) bodies (approximately 7.0%) were shown in the altitude range 55...74 km. The height of the maximum total radiated energy for bodies with increased strength was 15...24 km. Their share was approximately 6.6 % of all observed bodies. Scatter diagrams "initial mass–initial kinetic energy" was concentrated near a straight line describing the linear dependence. Minor deviations from this dependence are associated with variations in the velocity of cosmic bodies. Scatter diagrams "maximum total radiated energy region height–initial kinetic energy", "maximum total radiated energy region height–initial velocity", and "maximum total radiated energy region height–square of the initial velocity" turned out to be very fuzzy. This is due to the different sizes of bodies, different density of matter, different angles of entry into the atmosphere, etc.

Earthquakes Effects

The effects arising in the geomagnetic field after earthquakes, similar to the great Japan earthquake of March 11, 2011, have been studied in detail, and the following has been determined [29]. The measurements of the level of the geomagnetic field fluctuations can, in principle, be used as a tool for the search of magnetic EQ precursors and the response of the geomagnetic field to a completed EQ. However, this requires a very thorough analysis of the variations in the geomagnetic field caused by other sources. The discovered wave trains in the geomagnetic field fluctuations with a period of 400–900 s following the EQ could be caused by the modulation of the *N* under the action of seismic and AGWs. The velocities of 2.2–3.5 km/s correspond to the former; the velocities of 250–800 m/s correspond to the latter. The amplitude of

the observed wavetrains reached 1.5–2.5 nT; their duration was 60–80 min. Long-period (20, 60, and 100–120 min), nearly synchronous variations in the level of the geomagnetic field with an amplitude of 4–8 nT were found following the earthquake. The fore front delay time of these disturbances increased with increasing distance between the epicenter and the observatory, while their amplitude decreased. The geomagnetic field disturbances were most likely transported by means of slow MHD waves.

Using as an example a series of earthquakes of July 7, 2018, and September 5, 2018, in Japan (magnitudes of 5.9 and 6.6, respectively), as well as September 27–October 1 2003 (Chuysk earthquakes, magnitude of the main earthquake shock of 7.3, and of the greatest aftershocks of 6.7, 7.0, and 4.5), the ionospheric effects and the effects in the geomagnetic field have been studied and the following has been established [30–32]. The system [1] has demonstrated the capability of observing the dynamical processes in the ionosphere associated with the earthquake of moderate magnitude ($M = 5.9$) at distances of ~$(1–2) \times 10^3$ km from the epicenter. The seismic activity in Japan on 7 July 2018 was accompanied by aperiodic processes in the ionosphere at distances no less than $(1–2) \times 10^3$ km from the epicenter, with an enhancement in multiple-mode propagation, and a significant Doppler spectrum broadening [30]. Wave disturbances have been detected in the infrasonic oscillation range (a 3- to 4-min period), which are generated by a surface Rayleigh wave launched by the earthquake. The relative amplitude of the quasi-periodic variations in the N is equal to 1.7–9 %. The temporal duration of the oscillation train falls in the range of 26–58 min. The wave disturbance speed of propagation is found to be equal to approximately 3 km/s, the speed of the Rayleigh wave. Wave disturbances exhibit periods in the 15–30-min range. They could have been generated in the vicinity of the epicentre and then propagated as AGW, which modulate the electron density in the ionosphere. The relative amplitude of the quasi-periodic disturbances in the electron density is equal to 14–34 %. The temporal duration of the wave train attains about 40–84 min, and the speed approximately 0.34–0.60 km/s. The retrospective analysis of the results of the multi-frequency multiple-path ionospheric sounding performed on September 5, 2018, the day when a moderate, $M \approx 6.6$, earthquake in Japan occurred, and on reference days [31]. The character of variations in the Doppler spectra, in the Doppler shift, f_D, of frequency, and in the signal amplitude on the day when the earthquake occurred has been revealed to differ appreciably from those on the reference days. Two characteristic apparent velocities, 3.3 km/s and approximately 500 m/s, of disturbances have been revealed. The first velocity is close to the velocity of seismic waves, and the second to the velocity of acoustic and gravity waves at ionospheric heights. The amplitude of disturbances in N on a relative scale is estimated to be ~0.15–0.31 % in the infrasonic wave field and 7–8 % in the atmospheric gravity wave field. Forty-three and one hundred sixty three minutes before the earthquake, quasi-periodic variations were detected in the geomagnetic field, which could be the precursors of the earthquake of Richter magnitude 7.3. The mechanism for such a precursor has been described. After earthquakes of Richter magnitude 7.3, 6.7, and 7, quasi-periodic variations in the geomagnetic field were detected. Such variations could be caused by disturbances transferred by seismic waves with velocities of from 1.9 to 5.3 km/s, and by AGWs traveling at velocities of 320 m/s to 670 m/s. On October 1, 2003, changes in the character of the variations took place with time delays from 0 to 5 min. If these variations are associated with the earthquakes, the disturbances could be transferred by MHD waves.

A mechanism for the generation of magnetic precursors was proposed [33]. It is based on air heating over the earthquake preparation area, rising heated bubbles, AGW generation, AGW modulation in the ionospheric current jet, and the generation of quasi-periodic oscillations of the geomagnetic field. Depending on the degree of atmospheric heating over the earthquake preparation area and the size of the heated air formation, the characteristic rate of the rise of heated air formation can vary from 0.1 to 10 m/s. Here, the characteristic rising time varies from 5 min to days. Moving convective formations generate AGWs with relative amplitudes of 10^{-5}—10^{-4} at the Earth's surface and around 10^{-2}—10^{-1} at the heights of the ionospheric dynamo region. The magnetic precursor amplitude can be around 0.4–4 nT, and its duration can range from a few minutes to several hours.

Effects from High-Power HF Radio Transmissions

The measuring campaigns of 2018—2020 involving a number of disturbance diagnosis methods confirmed that the heater switch-on/off under certain conditions of space weather could lead to stimulated aperiodic disturbances in the lower ionosphere [34]. The time of development of the disturbances was within 10—18 min and their duration, within 5—10 min. Aperiodic variations having a delay time of 15—20 min and a duration of about 20 min were detected for the first time according to the f_D on oblique paths. It was confirmed that disturbances in the middle ionosphere are quasi-periodic; they had a delay time of 45—60 min (propagation velocity 270—360 m/s), a duration of 2—2.5 h, and a period of 10—30 min. It was shown for the first time that in about 40—60 min after the start of the Sura emission on radio paths

located at distances of the order of 1000 km the Doppler spectra became much broader and multipathing manifested itself if the Sura heater has an effective power of no less than 40—60 MW. It was demonstrated that periodic heating of the ionosphere led to periodic variations in the signal amplitude A and f_D variations with the maximum deviation 0.1—0.2 Hz. The signal response time was 70—180 min. The relative amplitude of the N disturbances ranged from 3 % to 12 %. It was found that quasi-periodic variations in the f_D and A are due to the generation and propagation of waves with velocities of 0.2 to 1.6 km/s and periods of 15 and 30 min. The velocity 0.2—0.4 km/s, unlike the velocity about 1.6 km/s, was systematically observed and corresponded to the propagation velocity of the internal gravity waves at the ionospheric altitudes.

Rocket Engine Burn Effects

A special feature of this study is the search for the effects that rocket burns have at a significant (~1,000–10,000 km) distance from a space vehicle path [35]. The database contains disturbances observed in both the geomagnetic field and the ionosphere in association with rocket launches from Baikonur, Plesetsk, China, U.S., and the Guiana Space Center at Kourou launch sites. Of special interest are the magneto-ionospheric effects from launches of a few rockets from different launch sites and the features observed during geomagnetic storms. Approximately 5,000 observations taken over the 1970–2020 time interval during rocket launches have been analyzed and classified. The main results are as follows.

Rocket engine burns are shown to be associated with the generation and/or amplification of wave disturbances in the geomagnetic field and in the ionosphere in a wide period range of 5–10 min to 2–3 hr. It has been verified that the ionospheric response to a rocket launch significantly depends on the state of space weather. Perhaps the ionospheric storm effects can couple synergistically with the effects from rocket burns by enhancing each other. Ionospheric storms significantly complicate the detection of the effects from rocket burns. Two types of disturbance with speeds of 2–3 km s^{-1} and 400–800 m s^{-1} have been distinguished. These speeds, which were observed earlier in numerous studies, could belong to the slow MHD waves and to the internal gravity waves, respectively. The relative amplitude of disturbances δ_N in the electron density reached 0.05–0.07 and the value of its period approximately 0.5–3 hr.

The statistical and spectral analyses of the geomagnetic pulsations associated with 402 rocket launches from launches pads located at distances of 1500–9500 km from the observation site have performed.

The wave disturbances generated by rocket engine burns act to induce a partial rearrangement of coupling between the subsystems in the Earth–atmosphere–ionosphere–magnetosphere system. The coupling occurs via waves of different physical nature (acoustic gravity waves (AGWs), MHD waves, magneto-gradient waves, and others) and via energetic particle fluxes.

Effects from Natural and Great Man-Made Disasters in the Atmosphere and Geospace

In [36–43] papers has studied the physical effects and ecological consequences of natural and great man-made disasters. They include earthquakes, volcano eruptions, avalanches, tropic cyclones, potentially hazardous asteroids that can impact the Earth, as well as multiple explosions at ammunition dumps, accidents in gas and oil fields, disasters in gas pipelines, etc.

The disturbances from natural and man-made disasters are determined to encompass not only the Earth's surface and the atmosphere at the air-earth boundary, but also the upper atmosphere and even the magnetosphere, i.e., the entire Earth–atmosphere–ionosphere–magnetosphere system. The disturbances are transported by acoustic gravity waves, heat and aerosol fluxes, as well as variations in geophysical fields, and other processes. A technique has been developed for calculating physical effects and ecological consequences caused by natural and man-caused disasters in the Earth–atmosphere–ionosphere–magnetosphere system.

Geophysical Measurement and Information Processing Procedure

The study investigation results was used in study process, in radio- and TV discussions and for science and popular papers preparing [44, 45].

Conclusions

1. The experimental studies were conducted of the physical processes acting in the geospace environment during the 2018–2020 period of gradually increasing solar activity.

2. The experimental studies were conducted of the disturbances in geospace associated with an impact on the medium from high-energy sources (solar terminator, March, 20, 2015 and August 11, 2018 solar eclipses, geospace storms, HF high-power emissions, rocket engine burn great disasters, and others).

3. Theoretical models of physical processes arising from high-energy sources in geospace have been developed and advanced. Measurements are in good agreement with theoretical modeling.

4. The theoretical ideas and physical models of processes launched by natural and man-made disasters into the Earth–atmosphere–ionosphere–magnetosphere system have been developed.

5. Physical and mathematical models for processes associated with the passage and explosion of the Romanian and Lipetsk bolides have been developed. The processes include deceleration, heating, ablation, explosion, bolide fragment fallout, the generation of infrasound and AGW, the disturbances in the atmosphere, the ionosphere, and the geomagnetic field, the occurrence of electric and electromagnetic effects, the heating and relaxation of the meteorite trail, the generation of turbulence in the trail. The magnetospheric effect from the meteorites has been detected and modeled. The effect of the gas-aerosol plume and the acoustic and seismic effects arising from the meteorites have been studied and modeled in detail.

6. Indonesia, Chelyabinsk, Romania, and Lipetsk meteoroid physical effects was experimentally investigated. The main parameters of Earth–atmosphere–ionosphere–magnetosphere system disturbances were determined.

7. NASA satellite-based observations collected during 1994—2016 have been used to estimate the statistical characteristics of meteoroids in the 0.1–440 kilotons TNT kinetic energy range.

8. The basic parameters of aperiodic and quasi-periodic disturbances produced by radio emissions impacts from high-power heater in the ionosphere over the remote observation site, 1 thousand kilometers away, have been determined.

9. Based on data collected by the European ionosonde network, the basic parameters of wave disturbances generated by the March 20, 2015, solar eclipse have been determined over Europe. The features of ionospheric disturbances that accompanied the August 11, 2018, solar eclipse have been established.

10. The impact of high-energy sources on the Earth–atmosphere–ionosphere–magnetosphere system (EAIMS) was confirmed to be accompanied by the generation and/or the enhancement of wave disturbances. Generally, wave disturbances in the neutral atmosphere give rise to wave disturbances in the ionosphere and in the geomagnetic field. The wave disturbances are commonly observed to be nonlinear. The techniques for estimating their parameters have been developed.

The role of wave disturbances is great, for they are responsible for the EAIMS subsystem coupling.

11. The conclusion of the authors that an adequate description of the entire set of physical processes operating in the Earth–atmosphere–ionosphere–magnetosphere system and in the Sun–interplanetary-medium–magnetosphere–ionosphere–atmosphere–Earth system is possible only within a systems science paradigm has been confirmed.

REFERENCES

1. Chernogor L.F., Garmash K.P., Guo Qiang, Zheng Yu., Podnos V.A., Rozumenko V.T., Tyrnov O.F., Tsymbal A.M. Coherent multi-frequency multi-track complex for radiophysical monitoring of dynamic processes in the ionosphere. *Bulletin of V. N. Karazin Kharkiv National University, Radio Physics and Electronics Ser*. 2018. Vol. 28. P. 88–93 (*in Russian*).

2. Chernogor L., Rozumenko V. Results of the investigation of physical effects in the geospace environment under quiet and disturbed conditions. *Space Research in Ukraine 2016–2018. Report to COSPAR*. Kyiv, Akademperiodyka, 2018. P. 41–51.

3. Chernogor L., Domnin I., Emelyanov L., Kotov D., Lyashenko M., Panasenko S., Bogomaz A. Results of Observation of Ionospheric Processes over Ukraine in 2016–2018. *Space Research in Ukraine 2016–2018. Report to COSPAR*. Kyiv, Akademperiodyka, 2018. P. 33–40.

4. Chernogor L.F., Domnin I.F., Emelyanov L.Y., Lyashenko M.V. Physical processes in the ionosphere during the solar eclipse on March 20, 2015 over Kharkiv, Ukraine (49.6° N, 36.3° E). *Journal of Atmospheric and Solar-Terrestrial Physics*. 2019. Vol. 182. P. 1–9.

5. Panasenko S.V., Otsuka Y., van de Kamp M., Chernogor L.F., Shinbori A., Tsugawa T., Nishioka M. Observation and characterization of traveling ionospheric disturbances induced by solar eclipse of 20 March 2015 using incoherent scatter radars and GPS networks. *Journal of Atmospheric and Solar-Terrestrial Physics*. 2019. Vol. 191. P. 105051.

6. Guo Qiang, Zheng Yu, Chernogor L.F., Garmash K.P., Rozumenko V.T. Ionospheric processes observed with the passive oblique-incidence HF Doppler radar. *Bulletin of V. N. Karazin Kharkiv National University, Radio Physics and Electronics Ser.* 2019. Vol. 30. P. 3–15. URL: https://periodicals.karazin.ua/radiophysics/article/view/14938 (*in Russian*).

7. Guo Q., Chernogor L.F., Garmash K.P., Rozumenko V.T., Zheng Y. Radio Monitoring of Dynamic Processes in the Ionosphere Over China During the Partial Solar Eclipse of 11 August 2018. *Radio Science*. 2020. Vol. 55, No. 2. URL: https://doi.org/10.1029/2019RS006866.

8. Zakharov I.G., Chernogor L.F. Ionosphere as an Indicator of Processes in the Geospace, Troposphere, and Lithosphere. *Geomagnetism and Aeronomy*. 2018. Vol. 58, No. 3. P. 430–437.

9. Chernogor L.F., Garmash K.P., Lazorenko O.V., Onishchenko A.A. Multi-Fractal Analysis of the Earth's Electromagnetic Field Time Variations Caused by the Powerful Geospace Storm Occurred on September 7–8, 2017. *Problems an Atomic Science and Technology*. 2018. Vol. 116, Iss. 4. P. 118–121.

10. Chernogor L F. Magnetic and Ionospheric Effects of a Meteoroid Plume. *Geomagnetism and Aeronomy*. 2018. Vol. 58, No. 1. P. 119–126.

11. Chernogor L.F., Mylovanov Yu.B. Rise of a Meteoroid Thermal in the Earth's Atmosphere. *Kinematics and Physics of Celestial Bodies*. 2018. Vol. 34, No. 4. P. 198–206.

12. Chernogor L.F., Mylovanov Yu.B. The dynamics of the Chelyabinsk meteoroid fall: altitude and time dependences. *Radio Phys. Radio Astron*. 2018. Vol. 23, No. 2. P. 104–115 (*in Russian*).

13. Mylovanov Yu.B., Chernogor L.F. Dynamics of the Chelyabinsk meteoroid entering the atmosphere: mass-energy balance. *Radio Phys. Radio Astron*. 2018. Vol. 23, No. 3. P. 176–188 (*in Russian*).

14. Chernogor L.F., Shevelev N.B. Infrasound wave generated by the Tunguska celestial body: amplitude dependence on distance. *Radio Phys. Radio Astron*. 2018. Vol. 23, No. 2. P. 94–103 (*in Russian*).

15. Chernogor L F., Shevelev M.B. Parameters of the infrasound signal generated by a meteoroid over Indonesia on October 8, 2009. *Kinematics and Physics of Celestial Bodies*. 2018. Vol. 34, No. 3. P. 147–160.

16. Chernogor L.F. Magnetospheric Effects during the Approach of the Chelyabinsk Meteoroid. *Geomagnetism and Aeronomy*. 2018. Vol. 58, No. 2. P. 252–265.

17. Onishchenko A.A., Chernogor L.F., Lazorenko O.V. Dynamical fractal analysis of the acoustic ultra-wideband signal caused by the Chelyabinsk meteoroid. Eskişehir technical university journal of science and technology. *A– Applied sciences and engineering*. 2019. Vol. 20. P. 188–192.

18. Chernogor L.F., Shevelev M.B. Characteristics of the infrasound signal generated by Chelyabinsk celestial body: global statistics. *Radio Phys. Radio Astron*. 2018. Vol. 23, No. 1. P. 24–35 (*in Russian*).

19. Chernogor L.F. Physical effects of the Romanian meteoroid. 1. *Space Science and Technology*. 2018. Vol. 24, No. 1. P. 49–70 (*in Russian*).

20. Chernogor L.F. Physical effects of the Romanian meteoroid. 2. *Space Science and Technology*. 2018. Vol. 24, No. 2. P. 18–35 (*in Russian*).

21. Chernogor L.F. Parameters of Acoustic Signals Generated by the Atmospheric Meteoroid Explosion over Romania on January 7, 2015. *Solar System Research*. 2018. Vol. 52, No. 3. P. 206–222.

22. Chernogor L.F. Physical Effects of the Lipetsk Meteoroid: 1. *Kinematics and Physics of Celestial Bodies*. 2019. Vol. 35, No. 4. P. 174–188.

23. Chernogor L.F. Physical Effects of the Lipetsk Meteoroid: 2. *Kinematics and Physics of Celestial Bodies*. 2019. Vol. 35, No. 5. P. 217–230.

24. Chernogor L.F. Physical Effects of the Lipetsk Meteoroid: 3. *Kinematics and Physics of Celestial Bodies*. 2019. Vol. 35, No. 6. P. 271–285.

25. Chernogor L.F. Ionospheric Effects of the Lipetsk Meteoroid. *Geomagnetism and Aeronomy*. 2020. V. 60, No. 1. P. 80–89.

26. Chernogor L.F. Effects of the Lipetsk Meteoroid in the Geomagnetic Field. *Geomagnetism and Aeronomy*. 2020. Vol. 60, No. 3. P. 355–372.

27. Chernogor L.F. Geomagnetic Variations Caused by the Lipetsk Meteoroid's Passage and Explosion: Measurement Results. *Kinematics and Physics of Celestial Bodies*. 2020. Vol. 36, No. 2. P. 79–93.

28. Chernogor L.F. Statistical Characteristics of Meteoroid Parameters in the Earth's Atmosphere. *Kinematics and Physics of Celestial Bodies*. 2018. Vol. 34, No 3. P. 134–146.

29. Chernogor L.F. Geomagnetic Disturbances Accompanying the Great Japanese Earthquake of March 11, 2011. *Geomagnetism and Aeronomy*. 2019. Vol. 59, No. 1. P. 62–75.

30. Guo Q., Chernogor L.F., Garmash K.P., Rozumenko V.T., Zheng Y. Dynamical processes in the ionosphere following the moderate earthquake in Japan on 7 July 2018. *Journal of Atmospheric and Solar-Terrestrial Physics*. 2019. Vol. 186. P. 88–103.

31. Luo Y., Guo Q., Zheng Y., Garmash K.P., Chernogor L.F., Shulga S.M. HF radio-wave characteristic variations over China during moderate earthquake in Japan on September 5, 2018. *Bulletin of V. N. Karazin Kharkiv National University, Radio Physics and Electronics Ser*. 2019. Vol. 30. P. 16–26. URL: https://periodicals.karazin.ua/radiophysics/article/view/14939 (*in Russian*).

32. Luo Y., Garmash K.P., Chernogor L.F., Shulga S.M. Geomagnetic field fluctuations during Chuysk earthquakes on September October, 2003. *Bulletin of V. N. Karazin Kharkiv National University, Radio Physics and Electronics Ser*. 2019. Vol. 31. P. 87–104 (*in Russian*).

33. Chernogor L.F. Possible Generation of Quasi-Periodic Magnetic Precursors of Earthquakes. *Geomagnetism and Aeronomy*. 2019. Vol. 59, No. 3. P. 374–382.

34. Chernogor L.F., Garmash K.P., Frolov V.L. Large-scale disturbances in the lower and middle ionosphere accompanying its modification by the Sura heater. *Radiophysics and Quantum Electronics*. 2019. Vol. 62, No. 6. P. 395–411.

35. Chernogor L.F., Liashchuk O.I., Shevelev M.B. Parameters of infrasonic signals generated in the atmosphere by multiple explosions at an ammunition depot. *Radio Phys. Radio Astron*. 2018. Vol. 23, No. 4. P. 280–293. (*in Russian*).

36. Chernogor L.F., Blaunstein N., Radiophysical and Geomagnetic Effects of Rocket Burn and Launch in the Near-the-Earth Environment. Boca Raton, London, New York: CRC Press. Taylor & Francis Group, 2018. 542 p.

37. Chernogor L.F., Garmash K.P. Magnetospheric and Ionospheric Effects Accompanying the Strongest Technogenic Catastrophe. Geomagnetism and Aeronomy. 2018. Vol. 58, No. 5. P. 673–685.

38. Chernogor L.F. Dynamics of the Convective Rise of Thermals in the Atmosphere. Izvestiya, *Atmospheric and Ocean Physics*. 2018. Vol. 54, No. 6. P. 528–535.

39. Chernogor L.F. Dynamics of Convective Upwelling of Large-Scale Weakly Heated Atmospheric Aggregates. *Izvestiya, Atmospheric and Oceanic Physics*. 2019. Vol. 55, No. 3. P. 251–256.

40. Chernogor L.F. Effectiveness of monitoring the catastrophic processes of space and terrestrial origin. *Space Science and Technology*. 2019. Vol. 25, No. 1. P. 38–47 (*in Russian*).

41. Tiutiunyk V.V., Chernogor L.F., Kalugin V.D., Agazade T.Kh. The basic development of monitoring information system for emergency situations of tectonic source. *Applied Radio Electronics*. 2019. Vol. 18, No. 1—2. P. 52–65 (*in Russian*).

42. Tiutiunyk V.V., Chernogor L.F., Kalugin V.D., Agazade T.Kh. The trees of classification seismically active local territories of the Earth in the system of nonlinear energy interactions Sun-Earth-Moon. *Information Processing Systems*. 2019. Vol. 4 (159). P. 99–117. DOI: 10.30748/soi.2019.159.12 (*in Ukrainian*).

43. Tiutiunyk V.V., Chernogor L.F., Kalugin V.D., Agazade T.Kh. Influence estimation of rotation speed variation of the Earth on seismic activity level of local globe territory. *Geoinformatika*. 2018. No. 3 (67). P. 36–48 (*in Russian*).

44. Chernogor L.F. Cosmic final of dinosaur. *Svitoglyad (World View)*. 2018. No. 3 (71). P. 30–38 (*in Russian*).

45. Chernogor L.F. Sand particle in Universe. Newspaper «Vremya» (Time). 2018 (Electronic version from 17 September). URL: http://timeua.info/post/nauka-i-tehnika/peschinka-vo-vselennoj-12940.html (*in Russian*).

SPACE BIOLOGY: RESULTS AND PROSPECTS

E. Kordyum[1], T.Borisova[2], N. Krisanova[2], N. Pozdnyakova[2], G. Shevchenko[1], L. Kozeko[1], S. Romanchuk[1], O. Lobachevska[3], Ya. Charkavtsiv[3], N. Kyyak[3], N. Zaimenko[4], B. Ivanytska[4], V. Brykov[1], L. Mischenko[5]

[1] M.G. Cholodny Institute of Botany of NAS of Ukraine
[2] Palladin Institute of Biochemistry of NAS of Ukraine
[3] Institute of Ecology of the Carpathians of NAS of Ukraine
[4] M.M. Gryshko National Botanical Garden of NAS of Ukraine
[5] Educational and Scientific Center «Institute of Biology and Medicine» of Taras Shevchenko National University of Kyiv

During 2018–2020 years, the investigations in the field of space biology continued in the areas of plant biology at the cellular and molecular levels in simulated microgravity and astrobiology. The search for new approaches to testing the properties of substrates adequate to the requirements of space planting as well as selection of new edible plants for astronauts were conducted. Work is underway to create an autonomous life support system for plants on the CubeSat platform for realization of the PlantSat mission.

Effects of inorganic analogue of Martian dust on key characteristics of nerve signal transmission in brain nerve terminals

One of the possible causes of brain impairment under conditions of long-term flights may be influence of planetary and interstellar dust, the composition and properties of which, as well as the impact on human health, in particular, neurotoxicity, are not sufficiently investigated. It was suggested in our study that Martian dust particles due to interaction with albumin of blood plasma can own new properties and after reaching the central nervous system, influence the key characteristics of the neurotransmission that in turn can result in brain dysfunctions. An inorganic Martian dust analogue derived from volcanic ash (JSC, Mars-1A, Orbitec Orbital Technologies Corporation, Madison, Wisconsin, USA) was used. The obtained data showed the presence of nano-sized particles in Lunar and Martian dust analogues and their neuromodulatory properties [1].

As shown in Fig. 1, the extracellular level of L-[^{14}C] glutamate consisted of 0.217 ± 0.019 nmol mg^{-1} of protein in the control and 0.231 ± 0.020 nmol mg^{-1} of protein in the presence of albumin (0.25 mg/ml) [$F_{(1,16)}$ = 0.19; p = 0.67; n = 9]. The Martian dust particles (2.0 mg/ml) itself did not affected this parameter, which was equal to 0.234 ± 0.024 nmol mg^{-1} of protein [$F_{(1,16)}$ = 0.34; p = 0.56; n = 9]. Application of Martian dust particles and albumin at concentrations of 2.0 mg/ml and 0.25 mg/ml, respectively, did not significantly change the extracellular level of L-[^{14}C] glutamate that was 0.207 ± 0.030 nmol mg^{-1} protein [$F_{(1,16)}$ = 0.09; p = 0.75; n = 9]. Therefore, the addition albumin per se to the synaptosomal incubation media insignificantly increased the ambient level of L-[^{14}C] glutamate in nerve terminal preparations. Combined application of Martian dust and albumin did not influence properties of Martian dust particles in nerve terminal preparations.

Further studies have shown that (similarly with the experiments with L-[^{14}C]glutamate) Martian dust particles did not increased the extracellular level of [^{3}H]GABA in synaptosomal suspension, which was equal to 131.9 ± 7.98 pmol x mg^{-1} of protein in the control, 147.91 ± 5.92 pmol x mg^{-1} of protein in the presence albumin (0.25 mg/ml) [$F_{(1,16)}$ =2.96; p = = 0.10; n = 9], 139.46 ± 6.10 pmol x mg^{-1} of protein in the presence of Martian dust analogue (2.0 mg/ml) [$F_{(1,16)}$ = 0.65; p = 0.43; n=9] and 145.13 ± ± 7.12 pmol × mg^{-1} in the presence of Martian dust particles with albumin (MD + albumin) at concentrations of 2.0 mg/ml and 0.25 mg/ml, respectively [$F_{(1,16)}$ = 1.73; p = 0.20; n = 9] (Fig. 2).

The addition of albumin per se to the synaptosomal incubation media insignificantly increased the ambient level of [^{3}H]GABA in nerve terminal preparations. The results obtained in the experiments with synaptosomes by measuring the extracellular level of [^{3}H]GABA in the presence of Martian dust particles and albumin were very similar with those of L-[^{14}C]glutamate. Therefore, combined application of Martian dust particles and albumin did not influence properties of

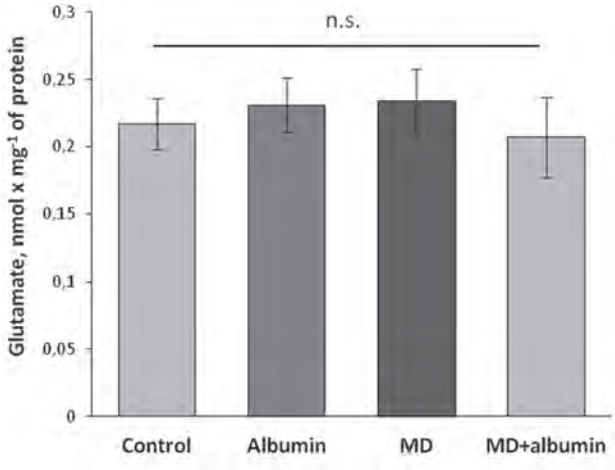

Fig. 1. The extracellular level of L-[^{14}C]glutamate in synaptosomal suspension after preliminary incubation with albumin (0.25 mg/ml); Martian dust analogue (MD) (2.0 mg/ml); Martian dust analogue with albumin (MD+albumin) at a concentrations of 2.0 mg/ml and 0.25 mg/ml, respectively; n.s., no significant differences n = 9

Fig. 2. The extracellular level of [^{3}H]GABA in synaptosomal suspension after preliminary incubation with albumin (0.25 mg/ml); Martian dust analogue (MD) (2.0 mg/ml), Martian dust analogue with albumin (MD+albumin) at concentrations of 2.0 mg/ml and 0.25 mg/ml;. n.s., no significant differences n = 9

Martian dust particles in nerve terminal preparations regarding modulation of the extracellular level of L-[^{14}C]glutamate and [^{3}H]GABA.

Continuation of comprehensive and detailed studies of the Martian dust analogue as well as other planetary dust particles allows developing strategies and discovering new means of elimination or reduction of neurotoxic risks under conditions of long-term space missions.

Role of microtubules and microfilaments in mechanical sensing in plant root cells

Crucial role in perceiving outer stimuli by plant root cell is attributed to cell wall-plasma membrane-cortical microtubule continuum (Baluška et al., 2003). Since cortical microtubules (cMTs) are connected to the plasma membrane (PM), they are good candidates for mechanical signal transduction caused by applied in our experiments 2D clinorotation. We have investigated expression of genes codding actin (*ACT2*) and tubulin (*TUA6*) (structural components for actin microfilaments' (AFs) and tubulin microtubules' (MTs) polimerization) in clinorotated *A. thaliana* plants treated with either inhibitor of tubulin polymerization (oryzalin (OR)) or inhibitor of actin polymerization (cytochalasin D (CD)). Our attention was focused on transcriptional regulation of *ACT2* and *TUA6* gene expression by mechanical stress. In our experiments, clinorotation alone down-regulated expression of *TUA6* (0.41 fold change versus 1) and this evidences direct impact of mechanical stimulation on tubulin expression also suggesting affection of cMT organization. Thus, observed during clinorotation down-regulated *TUA6* expression might result in distortion of tubulin polymerization and subsequent partial disorganization of cMT arrays.

In the control plants, OR and CD down-regulated expression of both *TUB6* and *ACT2* (Fig. 3, 4). This indicates a cross talk in regulation of *TUB6 and ACT2* expression by organization of MTs and AFs and certainly, proves MT-AF functional interconnection.

Another basic conclusion derived from the impact of mechanical perturbation on regulation of cytoskeleton gene expression is about possible involvement of AFs and MTs in mechanical signalling. Thus, OR treatment down regulated *ACT2* expression both in clinorotated and control plants (Fig. 3), evidencing independence of *ACT2* regulation by MT organization on mechanical stimulation. But, contrary to the control, *ACT2* expression was not changed in clinorotated plants treated by CD (Fig. 4) and this evidences different regulation of connection between AF organization and *ACT2* expression during mechanical stimulation.

The same is true for expression of *TUA6* in clinorotated plants happened to be not affected neither by OR nor CD treatment which is totally in contrast to the control (Fig. 3, 4).

Thus, our experiments have shown regulation of *ACT2* and *TUA6* expression by organization of cMTs and AFs and ability of mechanical stress to change such regulation. Analysis of *ACT2* and *TUA6* gene expression patterns during clinorotation suggested activation of special mechanism regulating cytoskeleton dynamics during mechanical stress. With the high probability, cMTs along with AFs role play a key role in plant cell mechanosensing [2].

Heat shock proteins 90 and 70 stabilize root gravitropic response in *Arabidopsis*

Evolving under 1 *g* force, plants acquired the ability to respond to gravistimulation, in particular by producing

a stable downward bending of roots. Plasticity of plant development is known to depend on function of heat shock proteins HSP90. This chaperone family is involved in many cellular processes through regulation of a diverse set of substrate proteins involved in hormonal signaling, cell cycle control, gravity responses etc. By supporting conformations of client proteins, HSP90 can stabilize the depending processes and thereby restrict stochastic development. Taking into account that HSP90s function in concert with HSP70s in many of their chaperone activities in plant cells, we evaluated the dependence of gravitropic root bending on cytosolic HSP90s and HSP70s. To study the gravitropic root response, we used *Arabidopsis thaliana* seedlings grown in the dark. Loss-of-function mutants *Athsp90-1*, *Athsp90-4*, *Athsp70-5* and *Athsp70-14* were compared with Col-0 ecotype. 4-day-old seedlings grown on vertical plates were turned 90 degrees, and the angles of root bending were measured after 48 hours. It was shown that deficiency of the HSP did not change the central tendency of the angle, but increased range of its variation (Fig. 5). In particular, *Athsp70-5* and *Athsp70-14* seedlings showed a slight increase in the angle variation (CV, 35% and 34% respectively) compared to the wild type (CV, 31%). In *Athsp90-1* and *Athsp90-4* seedlings, the trait varied markedly (CV, 63% and 54%), and several roots showed an upward turn (~11% and 3% of roots, respectively).

These results convincingly demonstrated the predominant role of HSP90 in stabilizing the gravitropic root response [3].

Ionizing radiation affects the formation of ER-bodies

Species of family Brassicaceae are considered as the most resistant to ionizing radiation exposure, in particular *Arabidopsis thaliana* model object. It is supposed that ER-bodies being inherent in Brassicaceae species, which are derivative of granular endoplasmic reticulum and selectively accumulate an enzyme β-glucosidase (PYK10), may be responsible for this resistance. We studied the effect of X-rays at doses of 0.5 Gy – 12 Gy, which includes a dose range, is to some extent equivalent to that in the cabin of manned spacecraft, on the ultrastructure of ER-bodies in root cells and *PYK10* gene expression in *A. thaliana* seedlings, to determine the participation of ER-bodies in plant tolerance to the effects of this factor.

The X-radiation effect was investigated on seedlings that grew under light conditions. 3-day-old seedlings were used for radiation. The studies were performed after 2 h (3-day-old seedlings) and 10 days (13-day-old seedlings) after the action of radiation. Transmission electron microscopy investigations were focused

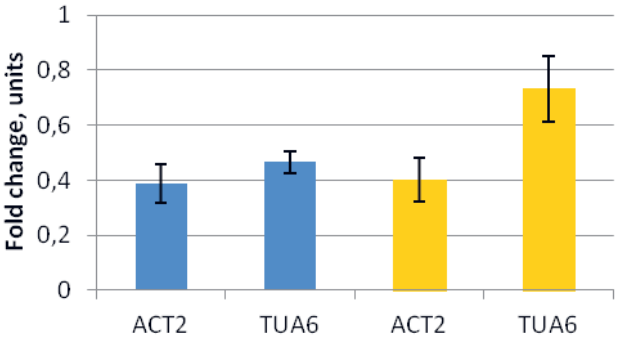

Fig. 3. Impact of oryzalin (OR) on *ACT2* and *TUA6* gene expression in control (black columns) and during clinorotation (gray columns)

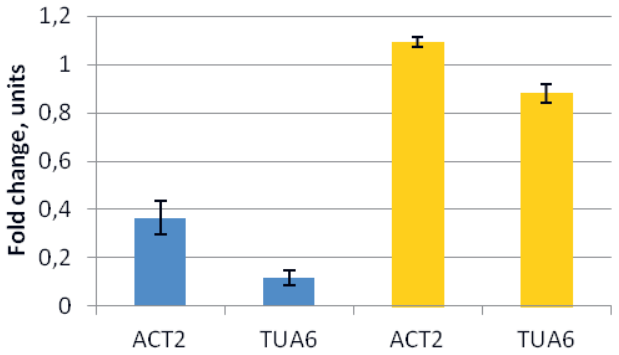

Fig. 4. Impact of cytochalazin D (CD) on *ACT2* and *TUA6* gene expression in control (black columns) and during clinorotation (gray columns)

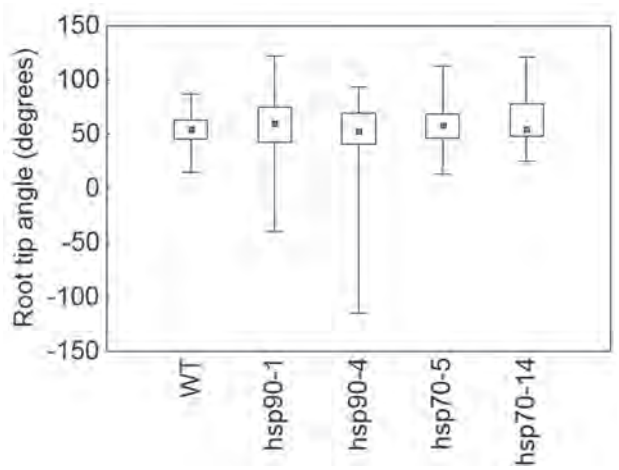

Fig. 5. The dependence of the root gravitropism response stability on molecular chaperones HSP90 and HSP70. Root tip angles in seedlings of loss-of-function mutants *Athsp90-1*, *Athsp90-4*, *Athsp70-5* and *Athsp70-14* after 48-hour gravistimulation by turning 90 degrees. Data are Me [25%, 75%], minimum and m aximum values

the root cap central statenchyma cells, as they are gravisensitive cells, and cells of the root distal elongation zone, since they are most sensitive to the influence of external factors (Fig. 6, *a*, *b*).

By real time RT-PCR detected that seedlings response that dose-dependent increase in induction of the *PYK10*

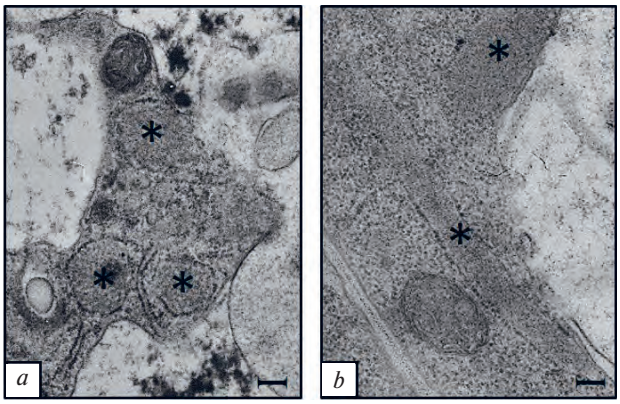

Fig. 6. ER-bodies in a root cap statocyte passed to secretion (*a*) and in an epidermal cell of the root distal elongation zone (*b*) of *A. thaliana* 13-day old seedlings. Asterisks marked ER-bodies. Bars: 500 nm

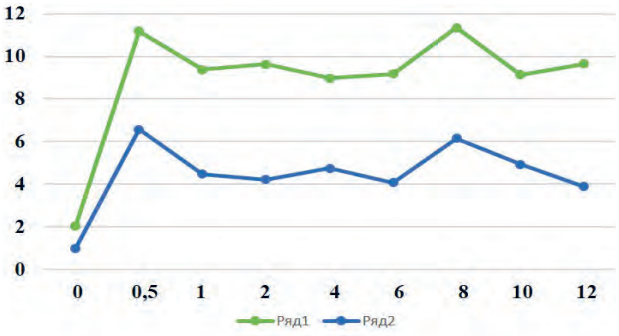

Fig. 7. *PYK10* expression in *A. thaliana* seedlings in 2 h and 10 days after irradiation by different doses (horizontally); conditional units (vertically)

gene in various quantities in response to irradiation, after 2 h (in 4.5–5.5 times depending on the dose), that had a tendency to decrease further, after 10 days, were established (Fig. 7). The highest stimulation was observed with a minimum radiation dose of 0.5 Gy and a dose of 8 Gy. According to the literary data, acute irradiation with a dose of 0.5 Gy caused DNA damages, amount of which reach certain thresholds in cells of 3-day-old seedlings. Cells perceive such damages as a signal to include adaptive responses, in which β-glucosidase apparently participates. High stimulation of *PYK10* gene expression at 8 Gy may be associated with the appearance of a certain asymmetry of a leaf rosette of leaves at 8 Gy – 12 Gy.

Thus, the data obtained for the first time by us demonstrate the involvement of ER-bodies and their highly specific component as the β-glucosidase enzyme in the cell responses to the action of X-irradiation, as well as in the seedling tolerance to these factors. The absence of deviations in seedling morphology and growth is evidence of this assumption. A significant increase in the number and mean area of ER-bodies and their variability in shape and size at the sections of cells of the root distal elongation zone may indicate an increase in the accumulation of β-glucosidase in them, under the influence of X-rays. Enhanced *PYK10* gene expression under irradiation, taking into account the activity of other genes of the DDR system (DNA damage response), may be used to develop a molecular marker of the ionizing radiation impact [4–6].

Gravimorphoses of the mosses in extreme environment

Gravisensitivity of mosses at the different stages of ontogenesis has the adaptive importance and promotes the gametophyte functional activity and stability in the extreme habitations. Gravity is an inducer of not only tropism, but also it is an important factor in plant morphogenesis. The various aspects of the morphogenetic action of gravity are combined in a term "gravimorphosis" (Sabovljević et al., 2014; Braun et al., 2018). Gravimorphoses are species-specific, change depending on the stages of moss development and environmental pessures, and it is a widespread adaptive form of growth in the life strategy of bryophytes. The subject of our work was to determine the participation of gravimorphoses in the adaptive plasticity of two moss species to impact of the unfavorable environmental conditions in Antarctica.

Samples of mosses *Bryum caespiticium* and *Polytrichum arcticum* were collected in 2019 on the west coast of the Antarctica (Galindez Island) during the 24th Ukrainian Antarctic Expedition organized by the National Antarctic Science Center of Ukraine. Samples of *B. caespiticium* growing in the Roztochia Nature Reserve (Ivano-Frankove village, Yavorivskyy district, Lviv region, Ukraine) on sandy moist soil were collected to compare with the Antarctic samples.

To understand how moss gravisensitivity manifests in extreme conditions the gravi-reactions of *B. caespiticium* and *P. arcticum* species common in Antarctica have been analyzed. In *B. caespiticium*, gametophores and the secondary caulonema are gravisensitive. Gravitropic growth of the secondary protonemata from moss shoots from Antarctica was slower than in control (moss from Ukraine). A number of amyloplasts in the top of an apical cell of the protonema stolon was a characteristic feature of Antarctic *B. caespiticium* that is not typical for gravisensitive moss species. This may be one of the reasons for the slower gravitropic reaction of *B. caespiticium* from Antarctica and it may be important in extreme habitat conditions, but requires researches.

Apical cells of gravitropic stolons of both *B. caespiticium* and *Polytrichum arcticum* (Fig. 8, *a*, *b*) intensively branched on the light resulting in the formation of protonemata from short chloronema stolons on their tops, which could disintegrate into numerous

2–3-celled fragments. Fragmentation, as a form of asexual reproduction, enables one moss plant to produce genetically identical offspring most adapted to the habitation and quick colonization of a large area. Bud primordia, which developed in gravisensitive gametophores, also initiated on the branches.

In *P. arcticum* from Antarctica, only the secondary caulonema stolons were gravisensitive. Stolons formed as a result of shoot regeneration, which is one of the methods of moss rapid vegetative propagation in nature. Chloronemal stolons, which were obtained from isolated young leaves or their small fragments, did not respond to gravity (Fig. 8, *c*, *d*). Buds of gametophores initiated rather on the gravitropic protonemata of *P. arcticum*, than on the non-gravistimulated one, also developed the larger protonemata. In natural conditions, morphological variations of protonema stolons promote to form more vigorous protonemata and then the moss cover to occupy the area of distribution. It is important to note that 30% branches of the *P. arcticum* gravitropic protonemata initiated at right angles to the main stolon (Fig. 9, *a*) and grew plagiotropically without showing gravitropism (Fig. 9, *b*).

Such type of branching facilitates the horizontal overgrowth of the underground caulonema, which secures protonemata in the substrate, stores nutrients and provides water retention in terrestrial gametophytes. So, on the same stolon of the caulonema there are gravisensitive apical cells and lateral branches that do not respond to gravity. In general, a life form of the moss gametophyte, adapted to the ecological factors of habitation, was formed with the involvement of the gravitational signaling system and the morphological heterogeneity of stolons [7]. Gravity-dependent morphoses and formation cells branched on the tops of gravitropic stolons of antarctic mosses *Polytrichum arcticum* and *Bryum caespiticium* as well the rapid development of shoots on it are a manifestation of the participation of gravimorphogenesis in the moss adaptation to stressful enviromental conditions.

The gravisensitivity and gravimorphogenesis are determinative features of the secondary caulonema which is the most stable and plastic stage of the protonemata development of the investigated mosses under ecological stress. Gravimorphoses enrich the phenotypic plasticity of mosses that ensures their viability and formation of the moss cover in the extreme environment.

Biochemical and physiological aspects of plants cultivation in the hermetic plastic vessels under simulated microgravity conditions

Creation of plant-based Bioregenerative Life Support Systems is crucial for future long-duration space exploring missions. Such systems are expected to provide astronaut`s habitat with food, CO_2 reduction, O_2 production, waste recycling and water management. The effects of altered gravity and closed environment on the higher plant basic physiological processes such as growth, development, reproduction, photosynthesis, primary and secondary metabolism etc. were demonstrated in many studies. Inducing production of phytotoxic phenolic compounds, which could inhibit further growth and development of plants, was not excluded. Experiments with selected crop species were focused on the possibilities of plants to adjust to the environment in space greenhouses in order to optimize the growth and productivity of higher plants.

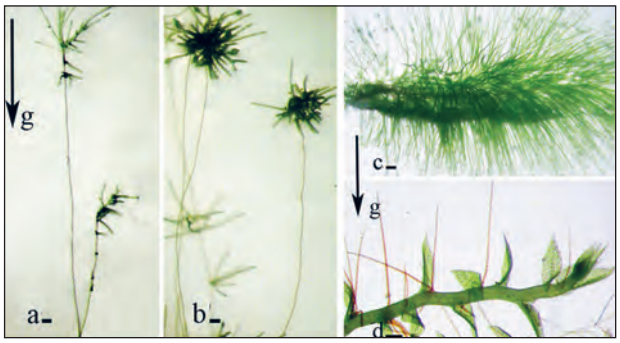

Fig. 8. Branching of apical cells of gravitropic stolons of *Bryum caespiticium* (*a*) and *Polytrichum arcticum* (*b*). Regenerative protonemata of *Polytrichum arcticum*: intensitive to gravity chloronemata developed from cells of isolated leaves (*c*), gravitropic caulonemal stolons growing from shoot cells (*d*). Vertical arrow shows the direction of gravity. Scale bar: 100 μm

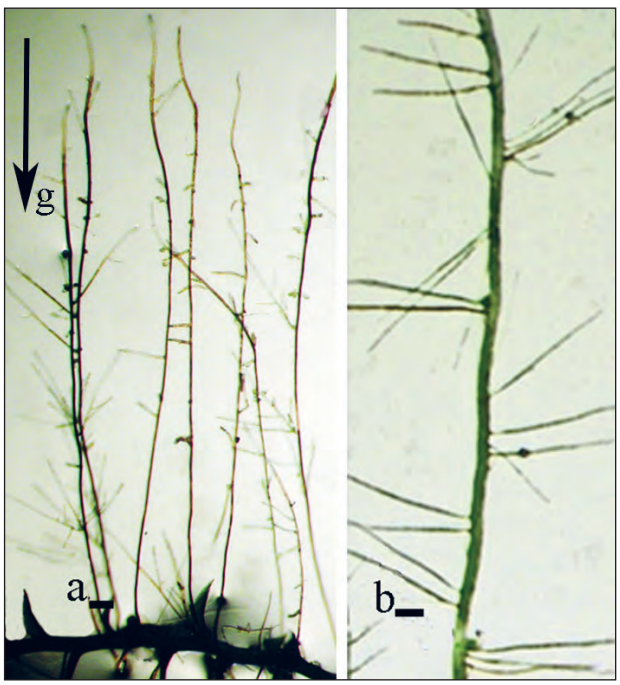

Fig. 9. Gravitropic stolons from branched *Polytrichum arcticum* shoots (*a*), a separate stolon with lateral branches predominantly formed at right angles to the main stolon (*b*). Vertical arrow shows the direction of gravity. Scale bar: 50 μm

Fig. 10. Plant species grown on different substrates in closed vessels, *a* – Grodan substrate and *b* – sphagnum moss: *Chlorophytum comosum variegatum*, *Cryptanthus acaulis*, *Phalaenopsis pulcherrima,* (syn. *Doritis pulcherrima*), *Tradescsntia fluminensis*, *Mammilaria prolifera*

The purpose of our experiments was to study the physiological and biochemical changes in plants which grew in hermetical plastic container under simulated microgravity conditions during 6 months (Fig. 10). The results will make it possible to delimit the effect of microgravity and hermetic conditions on plant development.

The data obtained indicate the CO_2 significant increased concentration in plastic vessels, that affects the content of photosynthetic pigments and free amino acids as well as the concentration of biogenic elements in the investigated plants. An increase in the content of nitrogen, potassium, manganese, chlorophyll and a decrease in the level of free amino acids were characteristic for plants in hermetic conditions. The RNA content in leaves decreased under the CO_2 level increased 5-fold.

Significant differences were also detected in the allelopathic activity of sphagnum moss, which was used as a substrate for growing plants in hermetic containers. Our studies have shown no manifestation of phytotoxicity of moss in sealed conditions. During the study of water-soluble secretions of the roots of experimental plants, stimulation of the development of test plants was indicated. In contrast to the standard Grodan substrate, a decrease in both the number of micromycetes and stress of mineralization processes was observed. The obtained data demonstrate the feasibility of using plastic chambers for the study of greenhouse gas emissions, determining the participation of plants with different morphological structures in the processes associated with the regulation of carbon metabolism and optimization of the mineral nutrition system.

Simple closed ecosystem development for PlantSat nanosatellite mission

It is generally accepted that plants are irreplaceable components of Bioregenerative Life-Support Systems (BLSS) for astronauts' in the future long-term flights in deep space, visiting Mars, building Moon bases, as the sources of oxygen, food, and recycled water. So, investigations of plant responses and adaptation to microgravity are necessary for the further human space exploration. Unfortunately, the opportunities for the implementation of experiments with plants on board the ISS are very limited.

In our opinion, closed man-made ecological system is a perspective model for biological experiments on nanosatelites. It is known that plants are capable to be in a closed hermetic habitat for a sufficient long time. Isolation of living organisms from the ambient atmosphere is called closed man-made ecological system (CMES). The ability of an orchid *Phalaenopsis pulcherrima* to grow in CMES in 3 dm^2 over 13 years was demonstrated in the M.M. Gryshko National Botanical Garden of the National Academy of Sciences of Ukraine. In order to maintain the viability of plants in CMES, it is only necessary to provide temperature and light conditions and any more manipulations are not required, so they are suitable to use in biological experiments on nanosatellites.

Now we are working on the design of a hermetic growth chamber and the creation of an autonomous life support system for plants on the CubeSat platform for realization of the PlantSat mission. The primary scientific purpose of the PlantSat mission is to investigate the influence of microgravity on plant growth and development, its respiration and photosynthetic activity and plant-microbial interactions. To simplify a problem of plant growth support, we propose to develop the miniature CMES using of which requires only corresponding temperature and light regimes. PolyITAN-4-PlantSat will be equipped with sensors of temperature, light, carbon dioxide and oxygen concentration as well as an optical system to detect the plant growth and telemetry. It is planned to test the growth and

physiological state of certain plant species selected for space planting in CMES in monoculture (one crop) or polyculture (multiple crops). Currently, we are providing experiments to select plant species suitable for growth in closed system [8, 9].

The results of the PolyITAN-4-PlantSat mission will answer one of the key questions of plant space biology, namely how long higher plants can exist in an active physiological state in the spaceflight conditions and whether a simple closed ecosystem will be functioning in microgravity

Prospects for using tomatoes (*Solanum lycopersicum*) and yacon (*Polymnia sonchifolia*) as food for astronauts

A list of plants recommended for space agriculture includes, except cereals and grain legumes, a sufficiently wide range of vegetable crops. Tomatoes is one of the most common vegetable crops in Ukraine, they are a valuable product of medicinal and dietary nutrition, as they contain a significant amount of nutrients and minerals and vitamins necessary for the human body, and due to the content of carotenoids – lycopene and β-carotene – are powerful antioxidants. That is why tomato plants can be successfully used by astronauts in long space flights.

We study tomato cultures since 2011 depending on the set purpose and constantly observed earlier fruit ripening in "space" variants (Fig. 11, *a*, *b*), in comparison with the control. Our data indicate the absence of harmful effects of long-term orbital spaceflight factors on tomato seeds and thus the possibility of obtaining quality crops of tomatoes in the Bioregenerative Life

Fig. 11. Tomato plants grown from seeds that were on board the Mir space station for 1992–1998 (*a*). Harvesting in the experimental field (*b*)

Fig. 12. Yacon plants in the experimental field (*a*, *b*). Harvesting root tubers (*c*)

Fig. 13. Dry slices of yacon root tubers (*a*, *b*). Drying in a convective electric dryer (*c*)

Support System in space flight. In addition, grown from "space" seeds tomato plants in terrestrial conditions are characterized by their increased resistance to phytopathogens, including viruses [10].

Yacon is a new non-traditional vegetable plant. It is a perennial herb of the Asteraceae family. The middle latitudes of South America is the native habitat of this species and it has been introduced in Ukraine by us in 2011-2012 (Fig. 12, *a–c*).

Yacon leaves have strong antioxidant properties, as they contain the high concentrations of chlorogenic, caffeic acid, and selenium. Yacon root tubers contain the high content of sugars, most of which are fructosans (over 60%). Such biochemical properties of yacon plants make them promising as nutritional and vitamin food for human. In Ukraine, juices and dried slices of root tubers successfully used for food (Fig. 13).

Based on the data obtained, we propose the use of this culture in the form of juices and dry slices in food for astronauts. The conducted researches deserve further continuation to clear the possibility of yacon vegetative reproduction in microgravity in space flight.

REFERENCES

1. Borisova, T. Perspective express assessment of neurotoxicity of particles of planetary and interstellar dust. NPJ Microgravity. 2019. Vol. 5, 2. https://doi.org/10.1038/s41526-019-0062.

2. Shevchenko G.V. Impact of clinorotation on microtubule regulation by tubulin–associated proteins in plants. Book of Abstracts. 26th ELGRA Biennial Symposium and General Assembly, 24–27 September 2019, Granada, Spain. 2019. P. 140.

3. Kozeko L. The role of HSP90 chaperones in canalized and non–canalized growth responses of Arabidopsis seedlings to altered gravity. Book of Abstracts. 26th ELGRA Biennial Symposium and General Assembly, 24–27 September 2019, Granada, Spain. 2019. P. 292.

4. Romanchuk S.M. PYK β-glucosidase gene expression in Arabidopsis thaliana (L.) Heynh. seedlings under clinorotation and X-irradiation. Factors of Experimental Evolution of Organisms. 2019. Vol. 22, № 2. P. 166–171. doi: https://doi.org/10. 7124/FEEO.v25.1159 (in Ukrainian).

5. Romanchuk S.M. Ultrastructure of ER-bodies in statocytes and cells of the distal elongation zone of Arabidopsis thaliana (L.) Heynh. root apices under X-radiation. Visnyk of Taras Shevchenko Kyiv National University. Biology. 2019. № 1. C. 61–67. URL: http://www.library.univ.kiev. ua/ukr/host/10.23.10.100/db/ftp/visnyk/biolog (*in Ukrainian*).

6. Romanchuk S.M. The effect of X-irradiation on -glucosidase PYK 10 gene expression in Arabidopsis thaliana (L.) Heynh. Seedlings. Reports of the National Academy of Sciences of Ukraine. 2019. № 5. P. 91–96. doi: https://doi.org/10.15407/dopovidi2019.05.091 (*in Ukrainian*).

7. Lobachevska O.V., Kyyak N.Ya., Khorkavtsiv Ya.D. Morpho-functional peculiarities of the moss Weissia tortilis Spreng. protonemata cells with different gravisensitivity. Space Science and Technology. 2019. Vol. 25, № 2. P. 60–70. doi: 10.15407/knit2019.02.060 (in Ukrainian).

8. Brykov V., Rassamakin B., Zaimenko N. Design of the first Ukrainian PlantSat nanosatellite. Proceedings of 12th IAA Symposium on Small Satellites for Earth Observation, 06–10 May, 2019. Berlin, Germany. 2019. https://web.tresorit.com/l#x b50seCuu9albxLzoVQdA&viewer=yYtM9D6h25xVzEHVF9 1Nx0Nr1TZoSQbY.

9. Brykov V., Ivanitskaya B., Zaplatnikov Y. Simple closed ecosystem development for PlantSat nanosatellite mission. Book of Abstracts. 26th ELGRA Biennial Symposium and General Assembly, 24–27 September 2019, Granada, Spain. 2019. P. 123.

10. Dunich A., Mishchenko L., Dashchenko A. PVYN-Wi isolate from tomato plants in Ukraine. Arch. Phytopath. Plant Protect. 2020. Vol. 53, № 3–4. P. 112–126. https://doi.org/10.1 080/03235408.2020.1730021.

DEVELOPMENT OF AUTOPHAGY IN PLANT CELLS UNDER MICROGRAVITY: THE ROLE OF MICROTUBULES AND ATG8 PROTEINS IN AUTOPHAGOSOME FORMATION

A. Yemets, R. Shadrina, I. Horyunova, S. Plokhovska, O. Kravets, Y. Blume

Institute of Food Biotechnology and Genomics of NAS of Ukraine

Various abiotic stressors, such as starvation, osmotic and salt stress, and UV-B irradiation have recently been reported to induce the development of autophagy in plant cells with involving microtubules, an important structural and functional element of the cytoskeleton [1–3]. Autophagy, being an intracellular adaptive process, is a highly conservative and evolutionarily established way of maintaining cellular homeostasis and survival under a stress induced by either a lack of essential living resources (e.g. caused by starvation) or by accumulation of damaged organelles or proteins in the cell. This catabolic process is characterized by the formation of autophagosomes that deliver cytoplasmic components to the vacuoles for subsequent decomposition and reutilization. The autophagy processes mediate plant development and play an important role in many stages of ontogenesis (namely, seed formation and germination, reproductive stage, formation of conductive xylem tissues, immune response, etc.). Whilst the realization of autophagy in animal cells has been studied in details, in plants, despite the extremely important physiological role of this process, the mechanisms of autophagy regulation are still insufficiently explored [4, 5].

Earlier, we established a functional relationship between α-tubulin acetylation and the development of induced autophagy in plants [3]. Besides, the patterns of expression of α-tubulin and *atg8* protein genes, genes of the enzymes involved in α-tubulin acetylation, as well as kinesin genes (microtubule motor proteins), which may play a part in the mediation of autophagy processes involving microtubules, have also been characterized [6, 7]. Inhibition of the autophagy by cysteine protease inhibitor, E-64, under the influence of the above mentioned abiotic factors leads to a more significant inhibition of growth. Such reaction affirms the adaptive function of the autophagy in response of plants to the stress [3]. However, the influence of such a factor as microgravity on the development of autophagy and the importance of this process for the adaptation of plants under weightlessness still remain unexplored [4, 5].

The influence of clinorotation on the seedling development and the autophagy progression in different parts of *A. thaliana* root

Although no experimental data suggesting the possible influence of microgravity on the development of autophagy in plant cells has been available until recently, it was known that under space flight or simulated microgravity, plants may undergo more or less significant morpho-physiological changes. So, significant differences in the proliferative activity of cells, the growth rate of roots and seedlings, reproduction processes, aging of plant organs, etc. under such experimental conditions were previously revealed [4, 5, 8]. Earlier we also reported that microgravity induced a reorientation of the direction of export of assimilates with weakening of their inflow to the stem and root apexes took place [8]. Since under different stress conditions the main factors that trigger autophagy are lack of living resources (e.g., lowering the levels of amino acids, energy, growth factors, etc.), it seems logical to assume that microgravity can lead to the development of autophagy for survival and adaptation of plants under such stress conditions. Building up on that, the aim of the first stage of our research in this topic was to identify the first signs of growth inhibition in *Arabidopsis thaliana* seedlings and cytological analysis of the appearance of autophagosomes in the root cells under the conditions of clinorotation. The main results of these studies are presented in [9].

To conduct this series of experiments the seeds of *A. thaliana* (Columbia Col-0 ecotype) germinated on a horizontal clinostat (4 rpm) or under stationary conditions (control) for 10–12 days at 22 °C, with a photoperiod of 14/10 h (day/night) and lighting of 4000 lx. Autophagosome imaging was performed with monodansylcadaverine (MDC) (Sigma, USA) [7].

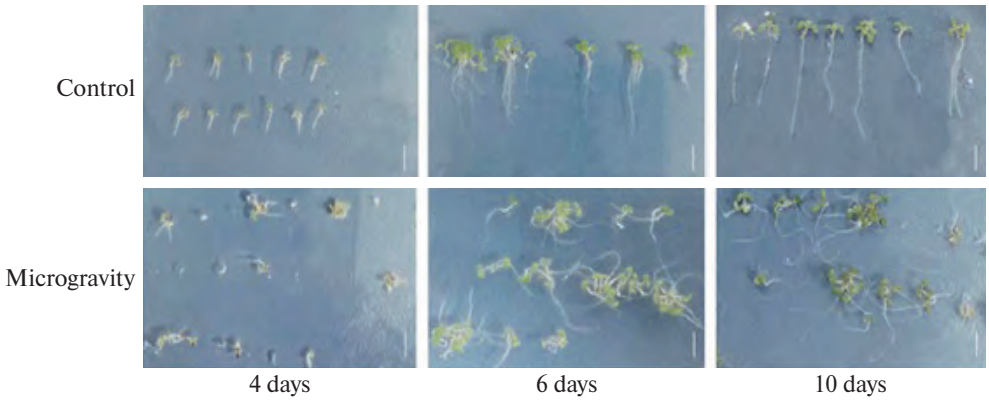

Fig. 1. Changes in the phenotype of *A. thaliana* seedlings grown under clinorotating conditions. *Scale bars*: 0.5 cm [9]

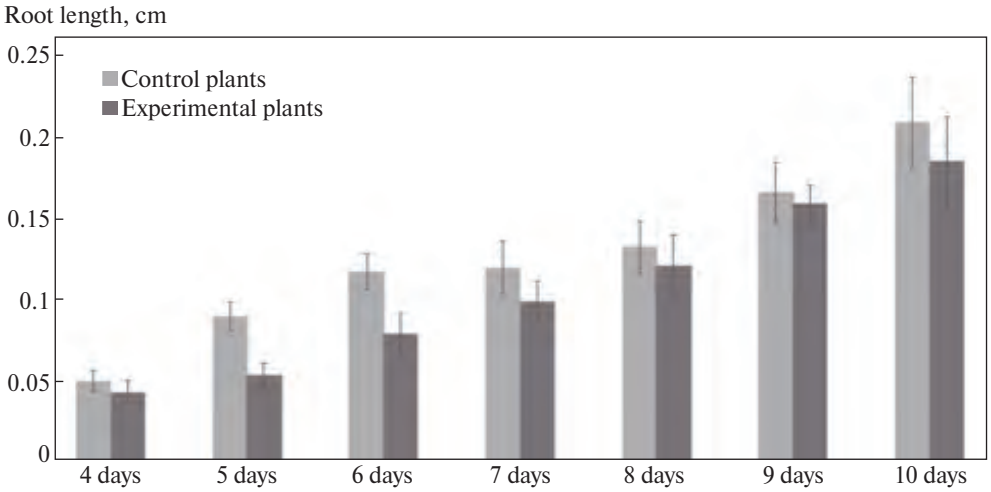

Fig. 2. The effect of clinorotation on the growth of seedlings' roots of *A. thaliana* [9]

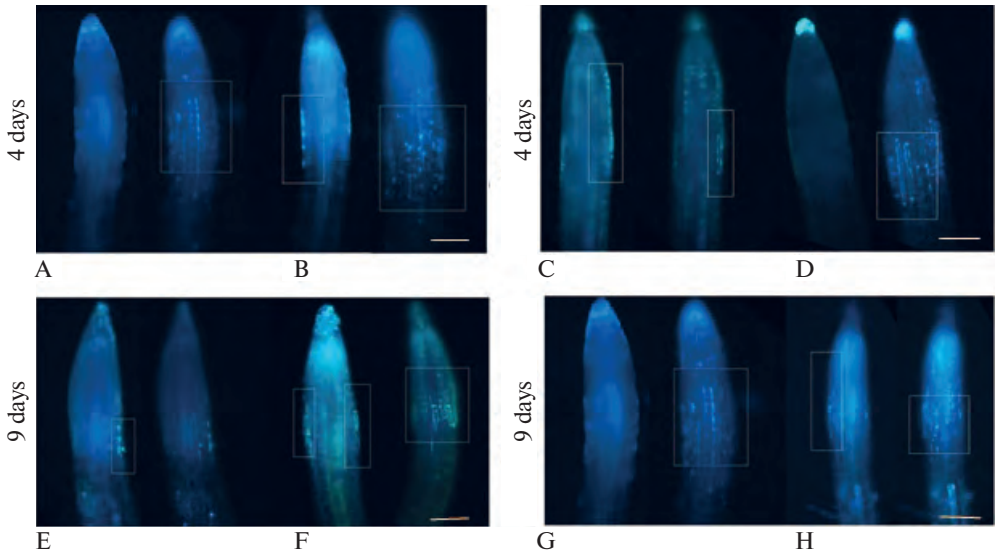

Fig. 3. Morphological features s of autophagy in the root cells of *A. thaliana* seedlings exposed to 10 days clinorotation. *Staining*: MDC – monodansylcadaverine (A, C, E, G – control plants, B, D, F, H – experimental plants). *Scale bars*: 50 μm [9]

The samples were analyzed using a fluorescence microscope (Axioscope 40, Carl Zeiss).

The clinorotation increased the degree of variation of seedling sizes and changed the orientation of their growth (Fig. 1). The difference between experimental and control plants in the length of the main root was observed the greatest in 5–6-day-old seedlings. In time, this difference was leveled and by 8–10 days of

the experiment the size variations were within the range of an error (Fig. 2). Given the small size of the seedlings and their variation, we decided to conduct microscopic analysis of the roots, starting from the 6th day of the experiment.

The first morphological signs of autophagy development were detected in 6-day-old seedlings, these were MDC-stained structures ranging in size from 3 to 20 μm. Under the conditions of clinorotation, the maximum compactness of autophagosomes in the cells of root cap was observed on the 8th–9th day, but their number rapidly decreased by the 10th day of the experiment (Fig. 3, A–H). The appearance of autophagosomes in the stretching zone of root was recorded on the 7th day of the experiment. Later, the number of autophagosomes increased significantly and peaked on the 10th day of clinorotation (Fig. 3, B–H).

Using PI (propidium iodide) to visualize the DNA of apoptotic cells, it was found that the root cells of 6–10 days seedlings under clinorotation demonstrated high survival rates. Within this clinostating period the percentage of cells in the PCD state remained within 5 %, which is the physiological norm for *A. thaliana* seedling cells. Accordingly, this data suggests that the development of autophagy did not facilitate apoptosis.

Thus, the study of the effect of microgravity on the early development of *A. thaliana* seedlings has shown clear signs of growth inhibition on 4 th–6th day of their cultivation. Autophagosomes appeared in the 6-day-old seedlings, their cellular and tissue localization and density in the tissues of the root apex were recorded. The highest density of autophagosomes was observed in the root cap cells on the 8th–9th day of clinostating, and in the stretching zone cells autophagosomes were found on the 10th day of clinorotation. We believe that the rapid decrease in the number of autophagosomes in the cells of the root cap on the 10th day of clinostating can be associated either with the mechanisms of self-regulation of autophagy or due to the peculiarities of the functioning of this tissue.

The effect of clinostating on the formation of autophagosomes and transcriptional activity of atg8 genes in root cells of *A. thaliana* seedlings

The above primary results of the study of the autophagy development under microgravity, described above, allowed us to analyze the dynamics of this process over time. In this part of the experiments we have studied not only changes in autophagy activity over 12 days period of early ontogenesis (by the density of autophagosoms in cells), but also analyzed their relationship with the transcriptional activity of *atg8* genes involved in the formation of autophagosomes. This was aimed to investigate the relationship between the initial stages of autophagy and the transcriptional activity of the *atg8* genes involved in the formation of autophagosomes under simulated microgravity. The obtained results were presented in [10].

The *in vivo* localization of autophagosomes was investigated using LysoTracker™ Red DND-99 (Thermo Fisher Scientific, USA), 1 mM. The images were obtained using a laser scanning confocal microscope LSM 510 META (Carl Zeiss, Germany). The gene expression levels of ATG8 family proteins were determined as described earlier in [1–3].

Membrane structures ranging in size from 3 to 20 μm corresponding to autophagosomes were visualized in the epidermal root cells of 6-day-old seedlings by staining with LysoTracker ™ Red DND-99. For epidermal cells of the transitional zone of seedling roots cultured under clinostating, the number of autophagosomes per cell was higher than in the control (Fig. 4, *a–f*), The density of autophagosomes in these cells decreased on the 9th and 12th days of clinostating in comparison with 6-day-old seedlings (Fig. 4, *b, d, f*). This may indicate the self-regulatory nature of the autophagy, when the peak of its activity is followed with an attenuation due to the creation at that point of time of a certain regulatory optimal level of living resources for further normal growth and development of cells.

In the root cap cells, activation of autophagy was observed on the 6th–9th days of the experiment and attenuation on 12th day of clinostating (Fig. 5, *b–f*). In control plants, the activation of autophagy occured a bit later – on the 9th day of the experiment (Fig. 5, *c*). However, no significant difference between the development of autophagy in the cells of control and experimental plants was observed.

The ATG8 protein is known to be the key ubiquitin-like protein of one of the two conjugation systems required for realization of autophagy in plants, yeast and animals. Located on both the outer and inner membranes of the autophagosome, ATG8 protein is responsible for the detachment and expansion of the preautophagosome structure. In *A. thaliana*, the family of *atg8* genes is represented by 9 genes, which are assigned to three subfamilies. The presence of many *atg8* genes suggests that their protein products may be involved in various stages of autophagosome formation.

The molecular genetic analysis of the expression profiles of 9 genes of the *atg8* family has revealed that the levels of their expression differed depending on the duration of clinostating (Fig. 6).

In particular, the expression levels of the *atg8e, atg8f and atg8i* genes increased on the 6th, 9th and 12th days of clinostating. Changes in the expression levels of the *atg8i* gene under the conditions of clinostating were the largest (1.5–1.75 times higher than the control) in comparison with other genes of the *atg8* family (Fig. 6).

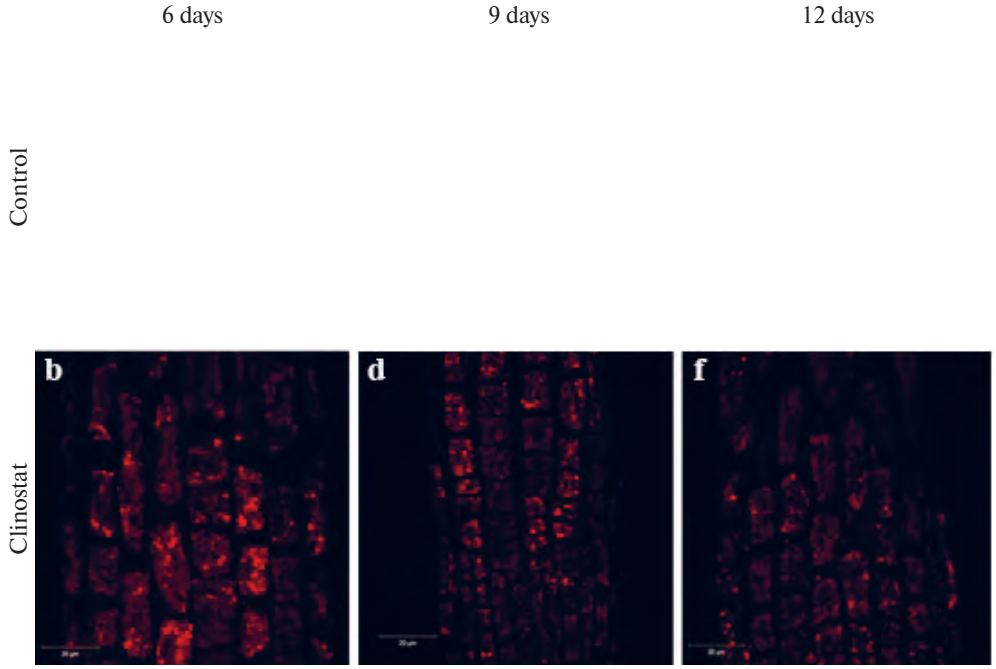

Fig. 4. Visualization of autophagosomes in epidermal cells of the transitional zone of *A. thaliana* root on the 6th, 9th, 12th day of cultivation in the conditions of control (*a, c, e*) and under clinostating (*b, d, f*). *Staining*: LysoTracker ™ Red DND-99. *Scale bars*: 20 μm [10]

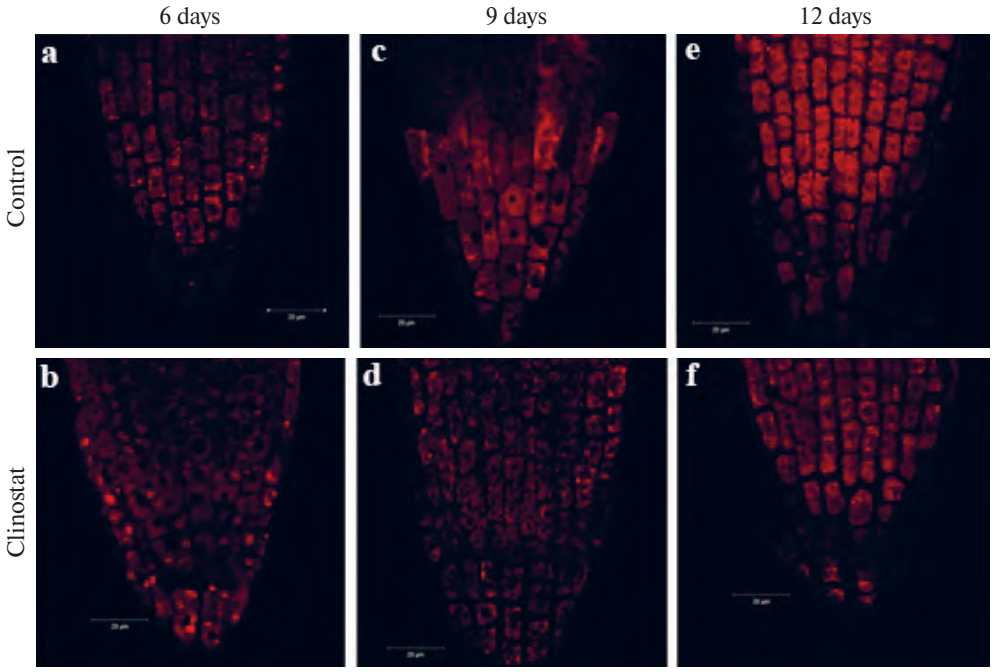

Fig. 5. Visualization of autophagosomes in the cells of the root cap of *A. thaliana* on the 6th, 9th, 12th day of cultivation under control conditions (*a, c, e*) and at clinostating (*b, d, f*). *Staining*: LysoTracker ™ Red DND-99. *Scale bars*: 20 μm [10]

In the case of the *atg8a, atg8b, atg8c and atg8d* genes, other regularity of expression change were observed. On the 6th day of clinostating the level of their expression increased, but later, on the 9th and especially the 12th day of cultivation there was a sharp decrease in their level of expression (Fig. 6). The *atg8h* gene was the most sensitive to the conditions of clinostating. Its expression underwent the sharpest changes during this short period of early ontogenesis: from complete blockade on the 6th day of the experiment to a rapid increase on the 9th day and subsequent attenuation on the 12th day of clinostating (Fig. 6).

Comparison of this data with the expression levels of *atg8* genes under conditions of starvation, salt and

osmotic stresses and UV-B irradiation [1, 2] demonstrated an increase in the expression levels of *atg8e* genes (1.5–2 times) under the influence of all these stressors, and the *atg8f* gene – under the action of all stresses, except UV-B. For the *atg8i* gene, higher expression levels were observed only under starvation and clinostating. For the *atg8g* gene, no increase in expression levels was detected during clinostating (Fig. 6), while under conditions of salt and UV-B stress, its expression increased [1, 2]. The *atg8h* gene appeared to be particularly sensitive to clinostating, the expression of which showed the most dramatic changes. These data may indicate that the *atg8g* and *atg8h* genes are not directly involved in the initial stages of autophagy, although they respond to the influence of clinostating.

Given the fact the ATG8 protein is a structural unit of autophagosoms, and is directly involved in the development of stress-induced autophagy, these results also suggest that some genes of the atg8 family (*atg8e* and *atg8i*) can be more involved in the full development of autophagy under microgravity. This assumption is supported by an increase in the expression of these genes under starvation [2].

Cell microtubules and microfilaments play an important role in regulating the development of autophagy. Previous studies of autophagy in plant objects have shown [3, 6] that microtubules are involved in the maturation and active transport of mature autophagosomes for fusion with lytic organelles, as well as in the mediation of cellular signals that regulate autophagy. The dynamic state of the microtubules changes involving posttranslational modification (acetylation) of tubulin. We have registered a significant increase in acetylated α-tubulin levels under the influence of abiotic stressors and, in addition, we have shown that this posttranslational modification of α-tubulin provides a stronger interaction of tubulin with ATG8 protein [3, 6]. The latter confirms the functional role of microtubules in realization of autophagy. Using the (atg8h)-GFP line of *A. thaliana*, Western blot analysis of ATG8 lipid protein and determination of synchronous GFP release, it has been shown that metabolic, salt, osmotic stresses and UV-B irradiation led to the development/activation of autophagy, mainly in root tissues.

Pre-treatment of seedlings with E-64, an autophagy inhibitor, enhanced the growth inhibition caused by stressors, provoked a decrease in the ratio of free GFP/Atg8-eGFP, as well as the level of tubulin acetylation [3]. This provides a reason to expect that under microgravity stress-induced autophagy is also accompanied by hyperacetylation of α-tubulin. Immunohistochemical analysis of tissue-specific acetylation of α-tubulin also confirms the involvement of α-tubulin acetylation in the implementation of autophagy

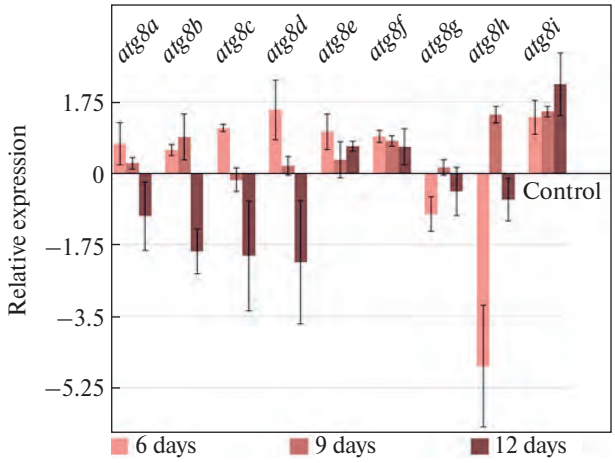

Fig. 6. Expression levels of *A. thaliana* atg8 genes on 6, 9, 12 days of clinorotation [10]

mechanisms in plants. Under various stressors, it has been shown that acetylation of α-tubulin is most pronounced in the tissues of root apexes (root cap, epidermis and pericycle) and the meristem of young leaves (under the action of UV-B) [6].

Notably, it should also be expected that under the action of abiotic stressors microtubule motor proteins such as kinesins (tubulin-dependent ATPases) may be involved in the mediation of autophagy processes involving microtubules. Previously, we characterized the patterns of expression of kinesin genes concerned in vesicular transport at the transcriptional level [6]. There was a significant increase in the transcriptional activity of the kinesin genes *KIN5B, KIN12B, KIN12F* after UV-B irradiation, genes *KIN6, KIN7O, KIN7D, KIN12B* under an osmotic stress and genes *KIN6* and *KIN12B* – under a salt stress, indicating the peculiarity of the involvement of these genes products in the implementation of the adaptive response of plants to the action of various abiotic factors [7]. At present, we are carrying out similar experiments using induced microgravity as a model.

Apart from starvation, autophagy can be induced by oxidative stress and/or by accumulation in the cytoplasm of partially denatured proteins and their aggregates belonging to the chaperone type of autophagy, unique to mammals. This type of autophagy is characterized by mediation of chaperones of the HSP70 family. In cooperation with colleagues from the M.G. Kholodny Institute of Botany of NAS of Ukraine, we have found that clinostating stimulates the response to heat shock (synthesized by AtHSP70s and AtHSP90-1) in *A. thaliana* seedlings, which is confirmed both at the level of transcription and translation [11]. The obtained results indicate that the seedlings, grown under prolonged clinostating, are able to withstand the effects of high, close to lethal, temperature better than seedlings grown under normal conditions. These facts support the

hypothesis that clinorotation may provide cross-adaptation of plants to fluctuations in environmental conditions, which correlates with data on HSP expression [11].

Conclusion

The results obtained at the morphological and transcriptional levels confirm for the first time activation of autophagy in the cells of the root cap and the epidermis of the root apexes of *A. thaliana* seedlings under the conditions of clinostating. Development of stress-induced autophagy is characterized by the appearance of autophagosomes in root tissues without an increase in the PCD index. It has been shown that activation of autophagy at the morphological level correlates with an increase of expression levels of *atg8* genes, some of which (in particular, *atg8e* and *atg8i*) can be involved in the full realization of autophagy just under microgravity conditions. In contrast, the *atg8g* and *atg8h* genes are apparently not directly involved in autophagy, although they are sensitive to clinostating. After the phase of autophagy activation, its regulatory attenuation follows in response to an increase of the level of living resources. This indicates adaptive changes to the conditions of clinostating. The obtained data deepen the understanding of the molecular mechanisms of development of stress-induced autophagy, in particular the involvement of different isotypes of Atg8 proteins and their interaction with other molecular components involved in the induction of autophagy under microgravity. Thus, exploration of the influence of microgravity on the expression of genes of proteins involved in the implementation of autophagy, deepens the understanding of molecular genetic mechanisms of autophagy activation. This knowledge may find its practical application for developing effective ways to adapt plants to the conditions of weightlessness during prolonged space flights in the future.

Acknowledgements

This research has been financially supported by the project "Development of the concept of regulation of development and stress resistance of plants for their adaptation to space flight conditions by attracting cellular and biological resources" of the Target Comprehensive Program of NAS of Ukraine for Space Research for 2018–2022 (№ 01118U003742).

We acknowledge the suggestions by Dr. V. Kyrylenko (Institute of Food Biotechnology and Genomics, NAS of Ukraine, Kyiv), aimed to improve the manuscript language.

REFERENCES

1. Olenieva V.D., Lytvyn D.I., Yemets A.I., Blume Ya.B. Influence of UV-B on expression profiles of genes involved in the development of autophagy by means of microtubules. *Reports of Natl. Acad. Sci. Ukraine*. 2018. No. 1. P. 100–108. DOI: https://doi.org/10.15407/dopovidi2018.01.100 (*in Ukrainian*).

2. Olenieva V.D., Lytvyn D.I., Yemets A.I., Blume Ya.B. Influence of sucrose starvation, osmotic and salt stresses on expression profiles genes involved in the development of autophagy by means of microtubules. *Visnik ukrains'kogo tovaristva genetikiv i selekcioneriv*. 2017. Vol. 15, No. 2. P. 174–180. DOI: https://doi.org/10.7124/visnyk.utgis.15.2.876 (*in Ukrainian*).

3. Olenieva V., Lytvyn D., Yemets A., Bergounioux C., Blume Ya. Tubulin acetylation accompanies autophagy development induced by different abiotic stimuli in *Arabidopsis thaliana*. *Cell Biol. Intl.* 2017. Vol. 43, Iss. 9. P. 1056–1064. DOI: 10.1002/cbin.10843.

4. Kravets O.A., Horyunova I.I., Plokhovskaya S.G., Olenieva V.D., Spivak S.I., Blume Ya.B., Yemets A. I. Development of adaptive processes to conditions of modified gravitation at tissue and cellular levels in plants. *Abstr. the 17th Ukr. Conference on Space Research,* Odesa, August 21–25, 2017. Kyiv, 2017. P. 60.

5. Kravets O.A., Yemets A.I., Horyunova I.I., Plokhovska S.G, Olenieva V.D., Lytvyn D.I., Spivak S.I., Blume Ya.B. Investigation of plant cell and tissue adaptive mechanisms to modified microgravity. *Space Research in Ukraine. Report to COSPAR 2016-2018*. P. 66–72.

6. Lytvyn D.I., Olenieva V.D., Yemets A.I., Blume Ya.B. Histochemical analysis of tissue-specific acetylation of α-tubulin as a response for autophagy development in *Arabidopsis thaliana* induced by different stress factors. *Cytol. Genet*. 2018. Vol. 52, No. 4. P. 245–252. DOI:10.3103/S0095452718040 059.

7. Olenieva V.D., Lytvyn D.I., Yemets A.I., Blume Ya.B. Expression of kinesins, involved in the development of autophagy in *Arabidopsis thaliana*, and the role of tubulin acetylation in the interaction of ATG8 protein with microtubules. *Factors Exp. Evolution Organisms*. 2018. Vol. 22. P. 162–168 (*in Ukrainian*).

8. Kravets O.A., Berezhna V.V., Sakada V.I., Ovsyannikova L.G., Rashydov N.M., Yemets A.I., Blume Ya.B., Grodzinsky D.M. Influence clinostating on structure, growth activity and attracting of apical meristem of bean plants. *Abstr. the 16th Ukr. Conference on Space Research,* Odesa, August 22–27, 2016. Kyiv, 2016. P. 66.

9. Shadrina R.Yu., Yemets A.I., Blume Ya.B. Development of autophagy as an adaptive response of *Arabidopsis thaliana* plants to microgravity conditions. *Factors Exp. Evolution Organisms*. 2019. Vol. 25. P. 327–332. URL:https://doi.org/10.7124/FEEO.v25.1186 (*in Ukrainian*).

10. Shadrina R.Y., Horyunova I.I., Blume Ya.B., Yemets A.I. Autophagosome formation and transcriptional activity of *atg8* genes in Arabidopsis root cells during the development of autophagy under microgravity conditions. *Reports of the NAS of Ukraine*. 2020. No. 9. P. 77–85. URL: https://doi.org/10.15407/dopovidi2020.09.077 (*in Ukrainian*).

11. Kozeko L.Ye., Buy D.D., Pirko Ya.V., Blume Ya.B., Kordyum E.L. Clinorotation affects induction of the heat shock response in *Arabidopsis thaliana* seedlings. *Gravit. Space Res.* 2018. Vol. 6, Iss. 1. P. 2–9. DOI: 10.2478/gsr-2018-0001.

ASSESSMENT OF SUSTAINABLE DEVELOPMENT GOALS WITHIN THE EUROPEAN NETWORK FOR OBSERVING OUR CHANGING PLANET (ERA-PLANET)

N. Kussul[1, 2], A. Shelestov[2, 1], M. Lavreniuk[1, 2], B. Yailymov[1], O. Fedorov[1], A. Kolotii[1, 2], H. Yailymova[1, 3], S. Skakun[4], L. Shumilo[1, 2], Y. Bilokonska[1], L. Kolos[1]

[1] Space Research Institute of NAS of Ukraine and SSA of Ukraine
[2] National Technical University of Ukraine "Igor Sikorsky Kyiv Polytechnic Institute"
[3] Taras Shevchenko National University of Kyiv
[4] University of Maryland, College Park, MD, USA

Introduction

The ERA-PLANET Horizon 2020 project "The European Network for Observing our Changing Planet" is a contribution of the European Community for addressing the objectives of international agreements such as the Sustainable Development Goals (SDGs), the Paris Agreement on Climate and the Sendai Framework for Disaster Risk Reduction. One of the four strands, GEOEssential [1], of the project is focusing on Resource Efficiency and Environmental Management. Within this strand, Earth observation (EO) data are used for monitoring resource efficiency utilization, as well as for assessing the progress towards achieving SDGs. The main task of our research in this project is to contribute to SDG on agriculture aiming at: end hunger, achieve food security and improved nutrition, promote sustainable agriculture aimed at ensuring sustainable food production systems and implementing resilient agricultural practices. To reach these goals, specific targets have been set: ensuring the conservation, restoration and sustainable use of inland freshwater ecosystems and their services. In this paper, we focus on three particular indicators, namely:

- 2.4.1. Proportion of agricultural area under productive and sustainable agriculture;
- 15.1.1 Forest area as proportion of total land area; and
- 15.3.1 Proportion of land that is degraded over total land area.

Within the Global Support Program, a pilot project was setup by the UN Committee on Combating Desertification and the Security Assistance Program with the aim of reaching Land Degradation Neutrality (LDN). The goal of LDN is to maintain or enhance the natural capital of the land and associated land-based ecosystem services. Land cover change, land productivity dynamics (LPD) and organic carbon stock are selected as sub-indicators for the indicator 15.3.1. Land cover changes evaluated based on ESA's Climate Change Initiative (CCI) Land Cover dataset and EC Joint Research Centre's (JRC) LPD dataset are used as default sources for land productivity assessment [2]. The main problems associated with these datasets are coarse spatial resolution and lower accuracy compared to regional based products [3, 4].

Therefore, this study aims to fill the above-mentioned gap by improving the calculation of the SDG indicators through the use of moderate and high spatial resolution data [5, 6]. The main goal is to apply and improve the methodologies, which were used for generating global products with coarse spatial resolution data, to higher spatial resolution data, which will be better suited for regional products and applications. For calculating the selected SDG indicators, we use a food-water-energy nexus approach based on satellite data [7], in-situ data, vegetation indices (VIs) and meteorological data. Since global land cover products have lower accuracy for Ukraine compared to regional products [8], we use regional land cover maps with high spatial resolution based on Landsat 8, Sentinel-2 and Sentinel-1 data [9]. These regional land cover maps were produced using the state-of-the-art methodology based on deep learning approach [10–12]. We also propose a new improved methodology for calculating a land productivity map based on high spatial resolution satellite data.

Methodology

Workflows for calculating SDG indicators. From the list of 232 SDG indicators, we present a general workflow [13] for calculating three selected SDGs indicators as shown in Fig. 1.

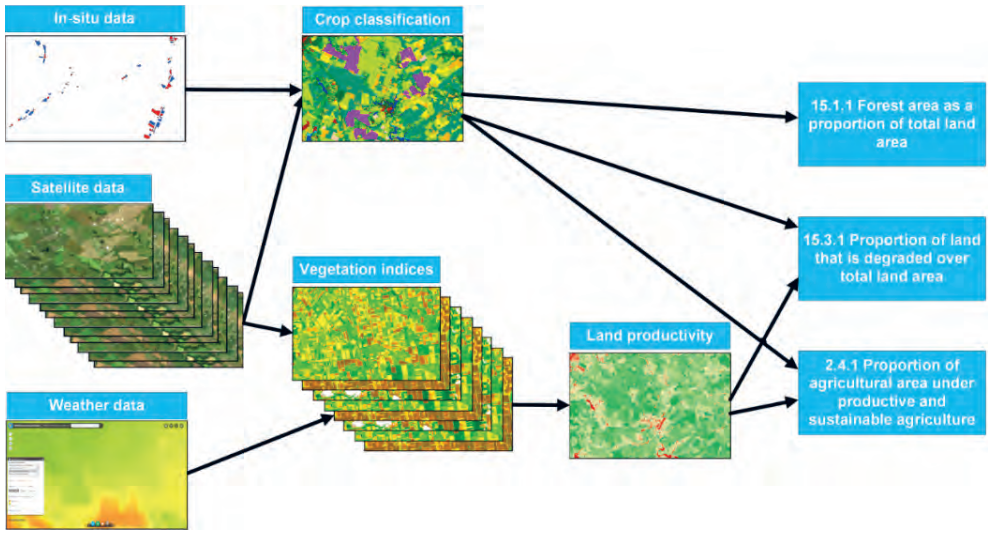

Fig. 1. Workflow for calculating Sustainable Development Goals indicators 15.1.1, 15.3.1 and 2.4.1

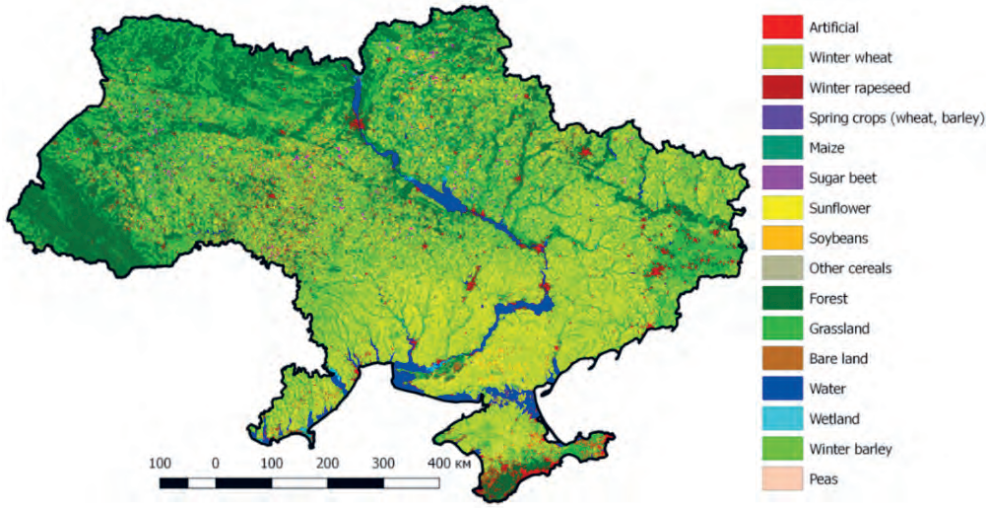

Fig. 2. Crop classification map at 10 m spatial resolution for Ukraine for 2017

GEOEssential ERA-Planet project is focused on development of workflows for Essential Variables (EVs) monitoring and SDG estimation using remote sensing (RS) data within nexus approach. This nexus approach is considering environmental system as model constructed from food, water and energy components and relationships between them. Thus, EVs can often belong to more than one nexus approach component. Within the project the list of EVs for food-water-energy nexus approach was created and described in deliverable 6.1 "Description of Food Water Energy EVs" [14]. Workflows for indicators 15.1.1, 15.3.1 and 2.4.1 based on EVs related to food, water, energy nexus approach was developed.

EVs from the food security domain include crop area and crop type represented by crop classification map, crop condition assessment and crop phenology characterized by vegetation indices (VIs) as such as NDVI, DVI, EVI [15], and biophysical parameters [16] such as leaf area index (LAI) [17]. For better estimation of crop condition and crop phenology with the use of VI, weather data that relate to Water and Energy Essential Variables are valuable. Water and Energy Essential Variables include precipitation, evaporation, surface air temperature, solar surface irradiation, humidity, and wind speed. These agrometeorological parameters are essential for VI modelling and enhancement of satellite-based estimation of crop productivity [18].

Workflow for calculating indicator 15.3.1. The indicator "15.3.1 Proportion of land that is degraded over total land area" is a binary, degraded/not degraded, quantification based on the analysis of available data for sub-indicators to be validated and reported by national authorities (namely, Trends in Land Cover, Land Productivity and Carbon Stocks) [13, 19]. This indicator is based on

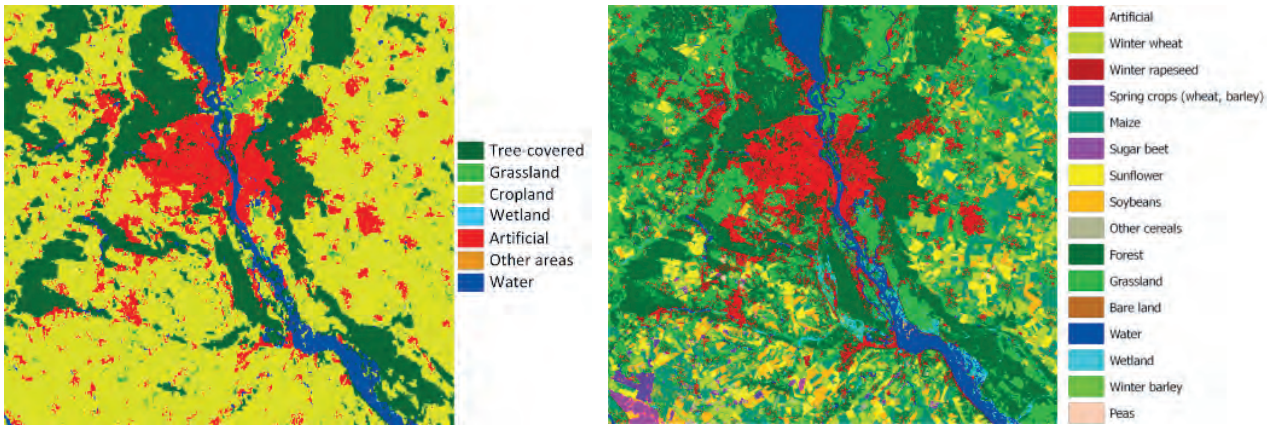

a *b*

Fig. 3. Visual comparison of the (*a*) 300m landcover ESA CCI-LC and with the (*b*) 10m crop classification map for Kyiv

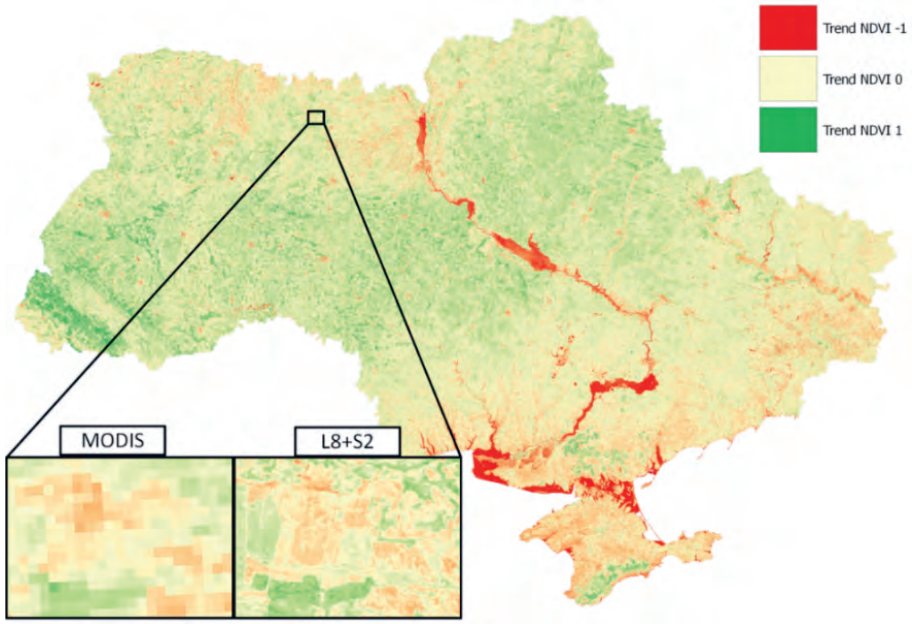

Fig. 4. Comparison coarse resolution productivity map based on MODIS data and our high-resolution productivity map for Ukraine territory for the year 2017

statistical principal "One Out, All Out" on evaluation of changes in the sub-indicator. This principle means that we have three types of changes in the sub-indicators, which are depicted as positive or improving, negative or declining and sustainable or unchanging. If one of the sub-indicators has negative changes for some area, then this area has negative productivity.

Our proposed methodology is based on a deep learning approach, in particular an ensemble of neural networks [12]. At the core of the architecture are multilayer perceptrons (MLP), which are trained using different parameters and architectures (number of hidden layers), and form an ensemble, which outperforms any of the individual MLPs. The rectified linear unit (ReLU) function is used as the activation function for neurons in the hidden layers,

Table 1

Forest area as a proportion of total land area by statistics and our classification maps in 2000, 2010 and 2016 years

	2000	2010	2016
Statistics	0.172	0.172	0.176
Classification maps	0.176	0.179	0.189

Table 2

Indicators 15.3.1 and 2.4.1 for territory of Ukraine for 2016 and 2017 years

	2016	2017
Indicator 15.3.1	46.19%	48.24%
Indicator 2.4.1	37.6%	42.8%

and training of the MLPs is performed using a stochastic gradient-based optimizer. In order to avoid overfitting, an L2 regularization was used with regularization coefficient set to 0.1, and learning rate was set to 10^{-3}. A committee of neural networks is used for providing crop classification and land cover maps for Ukraine using high spatial resolution Landsat 8, Sentinel-1 and Sentinel-2 imagery [20–23] and appropriate in-situ data for 2000, 2010, 2016 and 2017 [24–26]. The spatial resolution of the resulting maps is 30m for 2000 and 2010, and 10m for 2016 and 2017 (Fig. 2).

The overall accuracy is improved by more than 10 % compared to ESA's Climate Change Initiative Land Cover dataset; the kappa coefficient for ESA's Climate Change Initiative Land Cover dataset is 0.75, while the kappa coefficient for our map is 0.9 [8]. Fig. 3 shows the difference between coarse-resolution ESA's Climate Change Initiative Land Cover for 2015 and our high-resolution classification map for 2016 year in Kyiv region.

Workflow for calculating indicator 2.4.1. The indicator "2.4.1: Proportion of agricultural area under productive and sustainable agriculture" can be calculated using the same methodology as proposed for indicator 15.3.1 calculation. This indicator is a ratio of agricultural area that has a positive productivity value to the total agricultural area by the rule "One Out, All Out". For this indicator, we use the same sub-indicators as for indicator 15.3.1, but the area of interest is not the whole land area, but rather the agricultural (cultivated) land. For this indicator, the use of high spatial resolution satellite images is particularly important, since mixed pixels greatly affect the value of sub-indicator changes.

Workflow for calculating indicator 15.1.1. The indicator "15.1.1 Forest area as proportion of total land area" is a ratio of all land area to forest area. We estimate total land area, removing water and wetland areas, using classification map, and then calculate this indicator as proportion of forest area to total land area.

Implementation of the SDG Indicator's workflows in the Virtual Laboratory. In the ECOPotential project (http://www.ecopotential-project.eu), several partners are responsible for generating heterogeneous resources such as satellite data, in-situ data, services, analysis and modelling tools, processing algorithms, models/workflows and models results. To address these requirements, an interoperability framework, that was developed as a Virtual Laboratory (VLab: https://vlab.geodab.eu/), provides a web service-based access to the resources. Using cloud computing resources [27], with direct access to data of the GEOSS Portal, VLab has the ability to introduce workflows to calculate and monitor essential variables of water, food and energy and, accordingly, to calculate SDGs indicators for different countries around the world. We use the VLab tool to calculate the indicators 2.4.1 and 15.3.1. The benefits of using VLab are an opportunity to implement complex workflows in a cloud platform [28] with an easy access to data from GEOSS and other major data providers and the possibility of knowledge generation for ECOPotential storylines. The workflow for indicator 2.4.1 calculation in VLab takes as an input a classification map with agricultural classes of land cover and a time series of satellite images [29] for several years. For indicator 15.3.1 VLab takes land cover change map and land productivity map as inputs, calculates area of productive land and total area of land, and outputs their ratio.

Results

Using the proposed workflow shown in Fig. 1, we calculated indicators 15.1.1, 15.3.1 and 2.4.1 for the territory of Ukraine. Forest and total land area values were derived from land cover maps for 2000, 2010 and 2016. Thus, indicator 15.1.1 was calculated as a proportion of forest and total land area for these years (Table 1). We could see the positive trend when using statistics data as well as with satellite data. It means that in Ukraine, forest plantations dominate deforestation.

A land productivity map has been obtained using NDVI based on high resolution Sentinel-2 and Landsat-8 satellite images for 2013–2017 years. In Fig. 4, a comparison of coarse resolution productivity map based on MODIS data and our high-resolution productivity map is shown for Ukraine territory for 2017. Using our high-resolution productivity map and crop classification map we calculated indicators 15.3.1 and 2.4.1 for territory of Ukraine for 2016 and 2017. Combined values of indicators 15.3.1 and 2.4.1 for 2016 and 2017 are shown in Table 2.

We can observe a positive dynamic in productivity growth for all land from 46.19 % to 48.24 % and for agricultural land from 37.6 % to 42.8 %, but the area with negative trend of vegetation index is still more than 29.046 thousand ha. The growth can be explained by the introduction of effective agricultural practices, the establishment of harvesting systems, but usually these actions are carried out in large agricultural lands or in fields belonging to large agricultural enterprises, so this large part of the land with a negative trend still exists. Particularly highlighted with the negative value of productivity, we find: Eastern Ukraine [30] and Crimea due to the deterioration of the situation and problems with access to water; and Western Ukraine through deforestation. If we consider general growth, then, in addition to improving the conditions of agricultural land in Ukraine, there is a restoration of cut down forests, which provide improve-

ment each year with a significant trend of vegetation. According to the State Agency for Forest Resources of Ukraine, 52.6 thousand hectares of forest was restored in 2016, and 53.2 thousand ha in 2017.

Conclusions

In this paper, we proposed an improved workflow based on satellite data, in-situ data, Essential Variables, vegetation indexes and meteorological data for calculating three SDG indicators "2.4.1 Proportion of agricultural area under productive and sustainable agriculture", "15.1.1 Forest area as proportion of total land area" and "15.3.1 Proportion of land that is degraded over total land area and indicator". Within a pilot project of the UN Committee on Combating Desertification and the Security Assistance Program, a methodology for calculating index 15.3.1 was developed. It is based on ESA's Climate Change Initiative Land Cover dataset and JRC LPD dataset. These datasets are global and therefore have course spatial resolution and not perfectly accurate. Thus, we used land covers provided by our deep learning methodology based on high spatial resolution imagery from Landsat, Sentinel-2 and Sentinel-1 for Ukraine territory. Quality and accuracy of such land covers are much higher than global ones (gain is approximately 10%). Also, in this study, we proposed a new methodology for generating a land productivity map using high spatial resolution Sentinel-2 and Landsat-8 data that allow us to calculate indicator 15.3.1 and other derivatives indicators 15.1.1 and 2.4.1 more precisely. We conclude that newly available high-resolution RS products can significantly improve our capacity to assess several SDGs indicators through dedicated workflows from data to indicators and through essential variables.

REFERENCES

1. Kussul N., Lavreniuk M., Shumilo L., Kolotii A., Rakoid O., Yailymov B., Shelestov A., Vasiliev V. Assessment of Sustainable Development Goals Achieving with Use of NEXUS Approach in the Framework of GEOEssential ERA-PLANET Project. *Recent Developments in Data Science and Intelligent Analysis of Information*. 2018.

2. Gallego J., Kussul N., Skakun S., Kravchenko O., Shelestov A., Kussul O. Efficiency assessment of using satellite data for crop area estimation in Ukraine. *International Journal of Applied Earth Observation and Geoinformation*. 2014. Vol. 29. P. 22–30.

3. Kussul N., Shelestov A., Basarab R., Skakun S., Kussul O., Lavreniuk M. Geospatial intelligence and data fusion techniques for sustainable development problems. *11th International Conference on ICT in Education, Research and Industrial Applications: Integration, Harmonization and Knowledge Transfer*, ICTERI 2015 (14–16 May 2015, Lviv, Ukraine). 2015. Vol. 1356. P. 196–203.

4. Lavreniuk M., Kussul N., Skakun S., Shelestov A., Yailymov B. Regional Retrospective High Resolution Land Cover For Ukraine: Methodology And Results. *International Geoscience and Remote Sensing Symposium 2015* (IGARSS 2015), № 15599383, P. 3965–3968.

5. Kussul N., Skakun S., Shelestov A., Lavreniuk M., Yailymov B., Kussul O. Regional scale crop mapping using multi-temporal satellite imagery. *International Archives of the Photogrammetry, Remote Sensing & Spatial Information Sciences*. 2015. P. 45–52.

6. Lavreniuk M., Skakun S., Shelestov A., Yalimov B., Yanchevskii S., Yaschuk D., Kosteckiy A. Large-Scale Classification of Land Cover Using Retrospective Satellite Data. *Cybernetics and Systems Analysis*. 2016. Vol. 52, No. 1. P. 127–138.

7. Kussul N., Lavreniuk M., Shumilo L., Kolotii, A. Nexus Approach for Calculating SDG Indicator 2.4.1 Using Remote Sensing and Biophysical Modeling. *IGARSS 2019-2019 IEEE International Geoscience and Remote Sensing Symposium*. 2019. P. 6425–6428.

8. Kussul N., Kolotii A., Shelestov A., Yailymov B., Lavreniuk M. Land degradation estimation from global and national satellite based datasets within UN program. *Intelligent Data Acquisition and Advanced Computing Systems: Technology and Applications (IDAACS), 9th IEEE International Conference*. 2017. Vol. 1. P. 383–386.

9. Kussul N., Shelestov A., Skakun S. Flood Monitoring from SAR Data. *NATO Science for Peace and Security Series C: Environmental Security*. 2011. P. 19–29.

10. Kussul, N, Skakun S., Shelestov A., Kussul O. The Use of Satellite SAR Imagery to Crop Classification in Ukraine within JECAM Project. *IEEE Geoscience and Remote Sensing Symposium*. 2014. P. 1497–1500.

11. Kussul N., Skakun S., Shelestov A., Kravchenko O., Gallego F., Kussul O. Crop Area Estimation in Ukraine Using Satellite Data within the MARS Project. *IEEE International Geoscience and Remote Sensing Symposium*. 2012. P. 3756–3759.

12. Kussul N., Lavreniuk M., Skakun S., Shelestov A. Deep learning classification of land cover and crop types using remote sensing data. *IEEE Geoscience and Remote Sensing Letters*. 2017. Vol. 14(5). P. 778–782.

13. Kussul N., Lavreniuk M., Kolotii A., Skakun S., Rakoid O., Shumilo L. A workflow for sustainable development goals indicators assessment based on high-resolution satellite data. *International Journal of Digital Earth*. 2019.

14. McCallum I., Montzka C., Bayat B., Kollet S., Kolotii A., Kussul N., Mosnier A. Developing food, water and energy nexus workflows. *International Journal of Digital Earth*. 2020. Vol. 13(2). P. 299–308.

15. Kogan F., Kussul N., Adamenko T., Skakun S., Kravchenko O., Kryvobok O., Shelestov A., Kolotii A., Kussul O., Lavrenyuk M. Winter wheat yield forecasting in Ukraine based on Earth observation, meteorological data and biophysical models. *International Journal of Applied Earth Observation and Geoinformation*. 2013. Vol. 23. P. 192–203.

16. Kogan F., Kussul N., Adamenko T., Skakun S., Kravchenko O., Kryvobok O., Shelestov A., Kolotii A., Kussul O., Lavrenyuk A. Winter wheat yield forecasting: A comparative analysis of results of regression and biophysical models. *Journal of Automation and Information Sciences*. 2013. Vol. 45, No. 6. P. 68–81.

17. Shelestov A., Kolotii A., Skakun S., Baruth B., R. Lopez Lozano, Yailymov B. Biophysical parameters mapping within the SPOT-5 Take 5 initiative. *European Journal of Remote Sensing*. 2017. Vol. 50(1). P. 300–309.

18. Kussul N., Kolotii A., Shelestov A., Lavreniuk M., Bellemans N., Bontemps S., Defourny P., Koetz B. Sentinel-2

for agriculture national demonstration in Ukraine: Results and further steps. *IEEE International Geoscience and Remote Sensing Symposium (IGARSS)*. 2017. P. 5842–5845.

19. Yailymov B., Lavreniuk M., Shelestov A., Kolotii A., Yailymova H., Fedorov O. Methods for determining significant variables to assess the land cover state. *Space Science and Technology*. 2018. Vol. 24, No. 4. P. 24– 37 (*in Ukrainian*).

20. Skakun S., Kussul N., Shelestov A., Kussul O. The Use of Satellite Data for Agriculture Drought Risk Quantification in Ukraine. *Geomatics, Natural Hazards and Risk*. 2015. Vol. 7(3). P. 901–917.

21. Kussul N, Lemoine G., Gallego F., Skakun S., Lavreniuk M., Shelestov A. Parcel-Based Crop Classification in Ukraine Using Landsat-8 Data and Sentinel-1A Data. *IEEE Journal of Selected Topics in Applied Earth Observations and Remote Sensing*. 2016. Vol. 9(6). P. 2500–2508.

22. Kussul N., Lavreniuk M., Shelestov A., Skakun S. Crop inventory at regional scale in Ukraine: developing in season and end of season crop maps with multi-temporal optical and SAR satellite imagery. *European Journal of Remote Sensing*. 2018. Vol. 51(1). P. 527–636.

23. Ghazaryan G., Dubovyk O., Löw F., Lavreniuk M., Kolotii A., Schellberg J., Kussul N. A rule-based approach for crop identification using multi-temporal and multi-sensor phenological metrics. *European Journal of Remote Sensing*. 2018. Vol. 51(1). P. 511–524.

24. Shelestov A., Lavreniuk M., Kussul N., Novikov A., Skakun S. Exploring Google Earth Engine Platform for Big Data Processing: Classification of Multi-Temporal Satellite Imagery for Crop Mapping. *Frontiers in Earth Science*. 2017. Vol. 5. P. 17.

25. Skakun S., Kussul N., Shelestov A., Lavreniuk M., Kussul O. Efficiency Assessment of Multitemporal C-Band Radarsat-2 Intensity and Landsat-8 Surface Reflectance Satellite Imagery for Crop Classification in Ukraine. *IEEE Journal of Selected Topics in Applied Earth Observations and Remote Sensing*. 2016. Vol. 9(8). P. 3712–719.

26. Waldner F., Abelleyra D., Verón S., Zhang M., Wu B., Plotnikov D., Bartalev S., Lavreniuk M., Skakun S., Kussul N., Maire G., Dupuy S., Jarvis I., Defourny P. Towards a Set of Agrosystem-specific Cropland Mapping Methods to Address the Global Cropland Diversity. *International Journal of Remote Sensing*. 2016. Vol. 37(14). P. 3196–231.

27. Kravchenko A., Kussul N., Lupian E., Savorsky V., Hluchy L., Shelestov A. Water resource quality monitoring using heterogeneous data and high-performance computations. *Cybernetics and Systems Analysis*. 2008. Vol. 44, No. 4. P. 616–624.

28. Shelestov A., Lavreniuk M., Vasiliev V., Shumilo L., Kolotii A., Yailymov B., Yailymova H. Cloud approach to automated crop classification using Sentinel-1 imagery. *IEEE Transactions on Big Data*. 2019.

29. Kussul N., Shelestov A., Yailymov B., Yailymova H., Lavreniuk M., Shumilo L., Bilokonska Y. Crop monitoring technology based on time series of satellite imagery. *IEEE 11th International Conference on Dependable Systems, Services and Technologies (DESSERT)*. 2020. P. 346–350.

30. Skakun S., Justice C., Kussul N., Shelestov A., Lavreniuk M. Satellite data reveal cropland losses in South-Eastern Ukraine under military conflict. *Frontiers in Earth Science*. 2019. Vol. 7. P. 305.

SDG INDICATOR 11.3.1 WITHIN HORIZON-2020 SMURBS

N. Kussul[1, 2], A. Shelestov[2, 1], M. Lavreniuk[1, 2], B. Yailymov[1], A. Kolotii[1, 2], H. Yailymova[1, 3], S. Skakun[4], L. Shumilo[1, 2], Y. Bilokonska[1]

[1] Space Research Institute of NAS of Ukraine and SSA of Ukraine
[2] National Technical University of Ukraine "Igor Sikorsky Kyiv Polytechnic Institute"
[3] Taras Shevchenko National University of Kyiv
[4] University of Maryland, College Park, MD, USA

Introduction

Sustainable Development Goals (SDGs) indicators assessment is a very important task for today's global scientific communities [1]. Remote sensing data has been used to solve many problems in the process of ensuring sustainable land use and city's management [2]. One such example is assessment of SDG indicator 11.3.1: "Ratio of land consumption rate to population growth rate". It is tier 2 indicator, which has methodology for calculation, but data sources for estimation are still uncoordinated.

This work proposes several simplifications that give possibility to calculate land consumption [3, 4], using built-up area maps and demonstrate how this methodology works on the world cities. As a result, generation of high quality local or global land cover maps on regular basis, can solve the task of accurate indicator 11.3.1 estimation.

The indicator 11.3.1 is proposed two ways for this indicator calculation [5]. The first one is for the country level for goal monitoring and comparison of countries. For this purpose, indicator better to build on such quality global products as GHSL. The second one is for the local city level and it is better to use the local data that can be obtained and more applicable for these communities.

Google Earth Engine (GEE) platform provides the great opportunities for this task – possibility to use large satellite data sets with implemented classification approaches [6, 7] and implementation of local data. Within Horizon-2020 SMURBS project, Space Research Institute developed approach [8] for 10 meters land cover maps classification for urban growth assessment [9] in GEE platform that can be used for each city in the world.

Data

Satellite data. The time series of SAR Sentinel-1 acquired from 01-04-2016 to 25-10-2016 [10, 11] and cloud free images of optical Sentinel-2 satellite [18] were used for built-up area maps building for Kyiv in 2016, and cloud free images of optical Landsat-5,7 were used for built-up area maps building for Kyiv in 2000. In particular, for Kyiv city in 2016 were available 8 images of Sentinel-2, and 3 and 5 images of Landsat-5,7 respectively, which are presented in the Table 1.

The following pre-processing steps are used for Sentinel-1 data: apply orbit file, border noise removal, thermal noise removal, radiometric calibration, orthorectification and filtration with window 3×3. The L1C optical Sentinel-2 data were used for composites creation. The free cloud platform Google Earth Engine was used for the Random Forest (RF) algorithm implementation. All of satellite data are available in this platform.

Train and test data. Train and test data were generated by photointerpretation [13], using optical Sentinel-2 data for 2016 and Landast-5,7 for 2000. The artificial objects are the main type of land cover which must to be identified [14], so the test and training data contain two classes, which are presented in Table 2.

Auxiliary data. As additional data sets were used the Global Human Settlement Layer (GHSL) for the products comparison and Global Forest Change layer for products validation.

Table 1

Satellite images for Kyiv city in 2000 and 2016

	Sentinel-2 (2016)	Landsat-5 (2000)	Landsat-7 (2000)
Dates of images	28.04, 17.06, 17.07, 06.08, 09.08, 26.08, 29.08, 08.09	28.04, 24.07, 09.08	06.05, 07.06, 14.06, 25.07, 17.08

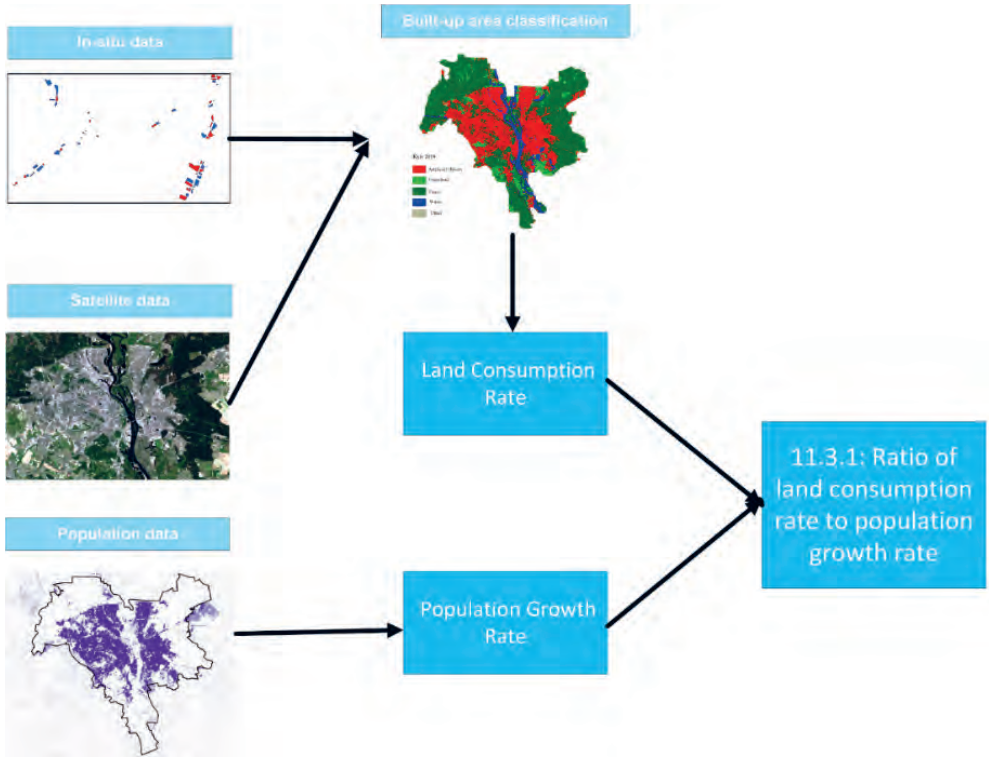

Fig. 1. Methodology for indicator 11.3.1 estimation using satellite data and population statistics

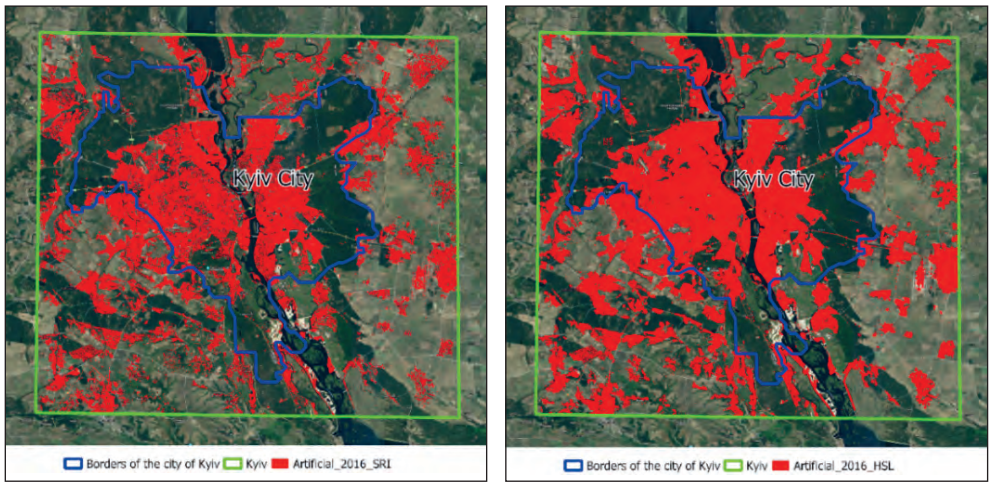

Fig. 2. The map of artificial objects for Kyiv in 2016, (*a*) – RF algorithm, (*b*) – GHSL product)

Methodology

Global human settlement layer validation and comparison with local land cover map. It is proposed to use two approaches for the built-up area validation [15, 16]. The first one needs the calculation of the confusion matrix for each of the set years using the independent test samples, and thus estimate the overall accuracy of the artificial objects. The second approach involves the use of an additional independent layer of green areas to estimate the artificial objects that intersects with it and measure this type of errors. Such an independent layer is the Global Forest Change layer (created at the University of Maryland). As a result, the intersection of artificial and green areas will be calculated and their percentage relative to the total area of the forest estimated.

Table 2

Train and test data distribution

	2000		2016	
	Train	Test	Train	Test
Artificial	30	29	57	57
Non artificial	95	96	160	161
Total	125	125	217	218

Indicator 11.3.1 estimation. Fig. 1 shows the methodology for SDG indicator 11.3.1 calculation with two included sub-indicators.

First sub-indicator is population growth rate and to estimate it, there is a need for reliable statistics with high update rate. In this reason, the best data source is statistics provided by government city administrations. For indicator estimation on country level it is possible to use UN statistics [17] and global products as GHSL population layer.

Population growth rate (PGR) is logarithm of two years' population numbers ration

$$\mathrm{PGR} = \mathrm{In}(Popt_{(t+n)} / Popt_t) / (y),$$

where $Popt_t$ is population for year t, $Popt_{(t+n)}$ is population for year $(t + n)$, (y) is a numbers of years between measurements.

Land consumption rate (LCR) estimation [11] is more complex, for this reason built-up area map is required. Built-up area map can be received from land cover classification maps or artificial surface maps. The best way to estimate LCR for city scale is build land cover map using local training data and free available satellite data as Sentinel-2 and Sentinel-1 fused in one-time series. On country or region level it is possible to use global products such as GHSL built-up area layer.

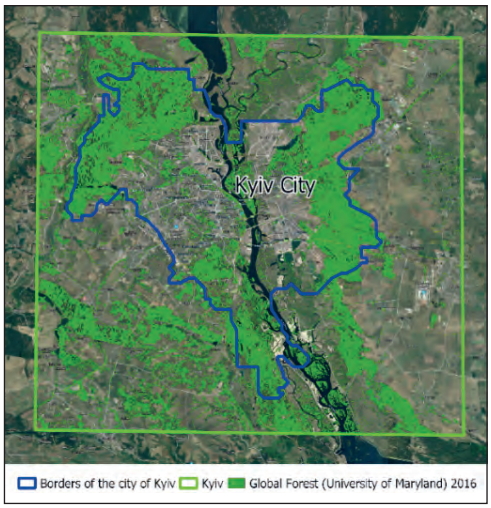

Fig. 3. Forest mask for the Kyiv city of 2016 (based on the Global Forest Change layers)

LCR calculation is similar to PGR. LCR is equal to logarithm of two years built-up area ratio

$$\mathrm{LCR} = \mathrm{In}(Urb_{(t+n)} / Urb_t) / (y),$$

where Urb_t is built-up area for year t, $Urb_{(t+n)}$ is built-up area for year $(t + n)$, (y) is a numbers of years between measurements.

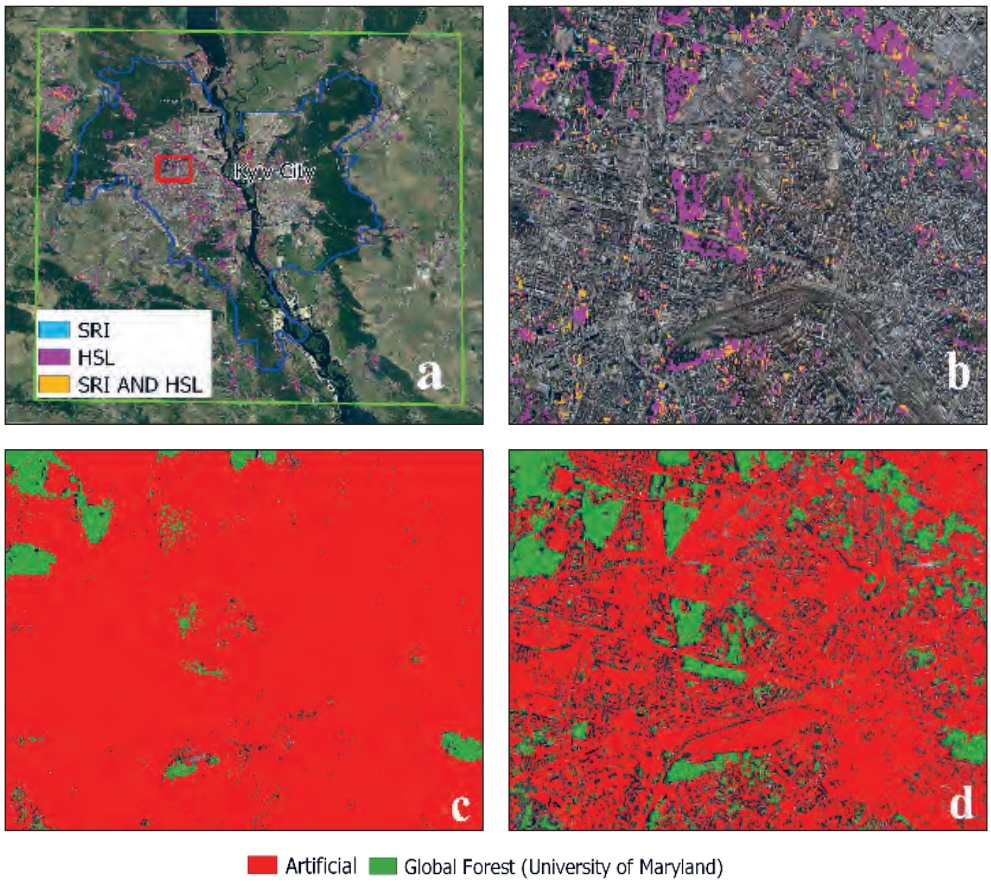

Fig. 4. Intersection of a forest mask from the Forest Mask for Kyiv City 2016 (based on the Global Forest Change layers). Artificial Object Mask: *c* – GHSL, *d* – RF

Table 3

The results of intersection green space with artificial object masks

The intersection layer	Area, ha	%, relative to the forest
SRI	58.93	0.75
GHSL	582.61	7.41
SRI and GHSL	165.26	2.10

Table 4

Land consumption rate and SDG indicators 11.3.1 based on local SRI maps and GHSL

Land Consumption Rate by SRI map	0.074
Land Consumption Rate by GHSL	0.044
SDG 11.3.1 by SRI map	4.758
SDG 11.3.1 by GHSL	2.845

SDG indicator 11.3.1 or ratio of land consumption rate and population growth rate (LCRPGR) can be calculated by formula:

$$LCRPGR = LCR / PGR.$$

Results

Validation and comparison of local land cover map and GHSL. The city is constantly expanding relative to its official boundaries. That is why the map was built with a buffer around the city (on the Fig. 2 it is marked in green). The Fig. 2, *a* presented the artificial object map (SRI maps) based on RF algorithm made on local data in GEE. The confusion matrix based on the independent test samples was calculated to validate the generated map. The overall accuracy is 85,2%. The product of the GHSL based on SAR Sentinel-1 data with spatial resolution 20 meters was used for another way to validate the classification map. This product contains the artificial objects for all world for 2016. The Fig. 2, *b* presented the part of the GHSL for Kyiv city. The overall accuracy based on independent test samples is 72.6 % which is a good result for the global product with spatial resolution up to 20 m. The main problem of this product is the presence of other objects that fall into the mask. In particular, it can be forest strips, trees, forests, parks, gardens etc. The reason is spatial resolution that causes effect of mixed pixels. But, due to that all cities in the world built on one model and have similar characteristics, usage of this global dataset is the best way for global indicator 11.3.1 assessment.

During experiment decided to use the Global Forest Change layer (created by the University of Maryland) for further validation. Granule data with top-left corner at 60°N, 30°E for Kyiv was used for this purpose. Based on the treecover2000 layer, the operations were performed to obtain a forest mask for 2016 (taking into account the layers lossyear_60N_030E1 and gain_60N_030E1). Given that the forest values were encoded as a percentage per output grid cell, in the range 0–100, a threshold of values greater than 30 was selected after the final forest cover was formed. As according to the visual estimation based on high resolution satellite data, such a threshold provides the best coverage of green area. The result is presented on the Fig. 3.

Using the resulting layer, an intersection of the green spaces and artificial objects was carried out (Fig. 4, *a*, *b*). Blue indicates the intersection of the forest layer with the result based on SMURBS approach, pink color is with GHSL, and orange is with two maps together. As can be seen in the figure, most pixels are pink (Fig. 4, *b*).

An area which was obtained is presented in the Table 3. Colors in the Table 3 correspond to colors on the Fig. 4, *a*. This area can be interpreted as the area of tree cover that was misclassified as artificial surface for both maps.

The obtained results confirm the accuracy of the constructed maps of artificial objects in Kyiv. The best performance based on RF algorithm map is provided by the spatial resolution 10 meters and usage of local data. In the future, it is planned to create maps of the same type for other set years (including 2020) and it further using within the HORIZON 2020 program, in particular the SMURBS / ERA-PLANET project [18, 19].

SDG indicator 11.3.1 built on local and global data comparison. Built-up area map for Kyiv 2000 was built using in-situ training samples [20], Landsat-5 and Landsat-7 satellite data with 83.4 % accuracy. This map used for initial year built-up area calculation for LCR. Cover map was used for 2016-year built-up area estimation. The similar year's maps were chosen from GHSL and on both data sources, land consumption rate was calculated. The local statistics provided by municipal statistical service was used to estimate population growth rate. Table 4 shows result of this experiment. As shown, difference strongly affect land consumption rate and in cases for city level indicator assessment it is better to use local data.

Conclusions

The results show that GHSL have high accuracy for country or regional level SDG indicator assessment. Due to this indicator informative and useful on high scale (city scale). For this purpose, it is better to use local data and satellite data with higher spatial resolution. That can improve accuracy of indicator calculation. Land cover classification approach in GEE developed

in SMURBS project provide good results with 10 m resolution and can be used in different cities to build similar built-up area maps with implementation of local data.

REFERENCES

1. Kussul N. Formation of the Ukrainian segment of the European research space in the Earth observation sphere (According to the materials of scientific report at the meeting of the Presidium of NAS of Ukraine, January 29, 2020). *Visn. Nac. Akad. Nauk Ukr.* 2020. No. 3. P. 39–45.

2. Shumilo L., Yailymov B., Lavreniuk M., Shelestov A., Korsunska Y. Land Surface Temperature Analysis and Trends for Rivne Using Remote Sensing Data. *2019 IEEE 2nd Ukraine Conference on Electrical and Computer Engineering (UKRCON)* 2–6 July 2019, Lviv, Ukraine. 2019. P. 1107–1111.

3. Shelestov A., Sumilo L., Lavreniuk M., Vasiliev V., Bulanaya T., Gomilko I., Kolotii A, Medianovskyi K, Skakun S. Indoor and outdoor air quality monitoring on the base of intelligent sensors for smart city. *XVIII International Conference on Data Science and Intelligent Analysis of Information*. 2018. Vol. 836. P. 134–145.

4. Lavreniuk M., Shelestov A., Kolotii A., Vasiliev V., Bulanaya T., Gomilko I. Air Quality Monitoring in Smart City Using Intelligent Sensors. *EGU General Assembly Conference Abstracts*. 2018. Vol. 20. P. 17087.

5. Kussul N., Lavreniuk M., Kolotii A., Skakun S., Rakoid O., Shumilo L. A workflow for sustainable development goals indicators assessment based on high-resolution satellite data. *International Journal of Digital Earth*. 2019. Vol 13, No. 2. P. 309–321.

6. Kussul N., Lavreniuk M., Skakun S., Shelestov A. Deep learning classification of land cover and crop types using remote sensing data. *IEEE Geoscience and Remote Sensing Letters*. 2017. Vol. 14(5). P. 778–782.

7. Shelestov A., Lavreniuk M., Kussul N., Novikov A., Skakun S. Exploring Google Earth Engine platform for big data processing: Classification of multi-temporal satellite imagery for crop mapping. *Frontiers in Earth Science*. 2017. Vol. 5. P. 17.

8. Shelestov A., Kolotii A., Lavreniuk M., Yailymov B., Shumilo L., Korsunska Y. Smart City Services for Kiev City Within ERA-PLANET SMURBS Project. *IEEE 39th International Conference on Electronics and Nanotechnology (ELNANO)*. 2019. P. 784–788.

9. Shelestov A., Raudner A., Kolotii A., Marinosci I., Attanasio A., Munafò M., Lavreniuk M., Speyer O., Yailymov B., Kussul N. Urban Growth Services Within ERA-PLANET SMURBS Project. *2019 Living Planet Symposium*, 13–17 May 2019, MiCo – Milano Congressi – Milan, Italy.

10. Kussul, N, Skakun S., Shelestov A., Kussul O. The Use of Satellite SAR Imagery to Crop Classification in Ukraine within JECAM Project. *IEEE Geoscience and Remote Sensing Symposium*. 2014. P. 1497–1500.

11. Shelestov A., Lavreniuk M., Vasiliev V., Shumilo L., Kolotii A., Yailymov B., Yailymova H. Cloud approach to automated crop classification using Sentinel-1 imagery. *IEEE Transactions on Big Data*. 2019.

12. Kussul N., Kolotii A., Shelestov A., Lavreniuk M., Bellemans N., Bontemps S., Defourny P., Koetz B. Sentinel-2 for agriculture national demonstration in Ukraine: Results and further steps. *IEEE International Geoscience and Remote Sensing Symposium (IGARSS)*. 2017. P. 5842–5845.

13. Shumilo L., Kussul N., Shelestov A., Korsunska Y., Yailymov B. Sentinel-3 Urban Heat Island Monitoring and analysis for Kyiv Based on Vector Data. *2019 10th International Conference on Dependable Systems, Services and Technologies (DESSERT)*, Leeds, United Kingdom. 2019. P. 131–135.

14. Shumilo L., Yailymov B., Kussul N., Lavreniuk M., Shelestov A., Korsunska Y. Rivne City Land Cover and Land Surface Temperature Analysis Using Remote Sensing Data. *2019 IEEE 39th International Conference on Electronics and Nanotechnology (ELNANO)*, 16—18 April 2019, Kyiv, Ukraine. 2019. P. 813—816.

15. Shumilo L., Shelestov A., Yailymov B., Korsunska Y., Kussul N. Land Surface Temperature estimation for Smart City. *2019 Living Planet Symposium,* 13–17 May 2019, MiCo – Milano Congressi – Milan, Italy.

16. Shelestov A., Kolotii A., Borisova T., Turos O., Milinevsky G., Gomilko I., ... & Kolos L. Essential variables for air quality estimation. *International Journal of Digital Earth*. 2019. Vol. 13, No. 2. P. 278—298.

17. Kussul N., Kolotii A., Shelestov A., Yailymov B., Lavreniuk M. Land degradation estimation from global and national satellite based datasets within UN program. *Intelligent Data Acquisition and Advanced Computing Systems: Technology and Applications (IDAACS), 9th IEEE International Conference*. 2017. Vol. 1. P. 383–386.

18. Korsunska Y., Shumilo L., Kolotii A., Shelestov A. Air Quality Estimation Using Satellite and In-situ Data for Kyiv City within ERA-PLANET Project. *2019 IEEE 2nd Ukraine Conference on Electrical and Computer Engineering (UKRCON)*, 2–6 July 2019, Lviv, Ukraine. 2019. P. 1032–1036.

19. Shelestov A., Shumilo L., Kolotii A., Korsunska Y. Air Quality Estimation for the Kyiv City Within ERA-PLANET Project . *Earth Observation Phi-Week,* 9-13 September 2019, Rome, Italy.

20. Shelestov A., Kolotii A., Lavreniuk M., Medyanovskyi K., Vasiliev V., Bulanaya T., & Gomilko I. Air Quality Monitoring in Urban Areas Using in-Situ and Satellite Data Within Era-Planet Project. *IGARSS*, Valencia, Spain. 2018. P. 1668–1671.

AUTOMATION IN REMOTE SENSING DATA PRE-PROCESSING

V. Lukin, M. Uss, S. Abramov, I. Vasilyeva, G. Proskura, O. Ieremeiev, V. Abramova, O. Rubel, N. Kozhemiakina, V. Naumenko

National Aerospace University "Kharkiv Aviation Institute"

The goal of our studies in 2018–2020 has been design of approaches and methods for automated processing of remote sensing (RS) and other types of data acquired by different existing imaging systems most of which are multichannel. With application to RS, examples of multichannel systems are multispectral, hyperspectral, multi-polarization ones [1, 2]. Images provided by them are of different quality [3–5]. Some of them are characterized by input peak signal-to-noise ratio (PSNR) exceeding 40 dB, then noise cannot be observed by visual inspection and its influence on classification results is negligible. However, there are also component images (or types of RS data) for which noise is clearly seen (see examples in Fig. 1) and, then, its removal is desirable. These are some component images in multispectral (Fig. 1) and hyperspectral data as well as radar images, even if they are multilook (see one example in Fig. 1, *b*). Pre-processing of such images is highly desired.

Pre-processing of multichannel RS data includes not only pre-filtering [2] but a certain set of operations (stages) where some of them can be mutually dependent and some are optional. In general, pre-processing might include different operations (stages) as, e.g., blind estimation of noise characteristics and/or peak signal-to-noise ratio (PSNR) [3, 4], multimodal co-registration [5], denoising and enhancement [6–10], lossless or lossy compression [11–15], object detection and image classification [16–19]. Necessity to perform some operations as, e.g., denoising (filtering) depends upon many factors like input PSNR and/or visual quality, noise properties (its intensity, is noise spatially correlated or uncorrelated), image content (simple structure, textural, a lot of fine details), filter properties and parameters. This means that it is desired to have automatic methods and tools for fast and reliable estimation of quality of original (acquired) RS images as well as techniques and tools for prediction of filtering efficiency. Such tools can be based on different theoretical and practical platforms including neural networks, support vector machines, multi-parameter regression, etc. The advantages of these tools are that they all able to solve complex approximation tasks, to combine input parameters of different origin in an optimal (proper) manner.

Multichannel RS data are useful only under condition that all component images are presented in the same coordinate system. This means that co-registration should be either provided at image acquisition stage, as this is, e.g., done in hyperspectral imaging, or after collecting a desired set of component images [5]. Automation of co-registration is needed if images are of large size and if component images are not highly correlated. Then, the task of finding similar patches (blocks) arises [5, 16, 20]. This task becomes more complicated if co-registered images are noisy and/or noise is spatially correlated. We have put forward the approach [5] based on deep learning. We have proposed to unify the patch discrimination and localization problems by assuming that the more accurately two patches can be aligned, the more similar they are. A two-channel patch matching convolutional neural network (CNN), called deep learning similarity measure (DLSM), has been trained to solve a regression problem with uncertainty. The designed CNN uses two multimodal patches as inputs. It predicts a normal two-dimensional distribution of the translation vector. The determinant of the covariance matrix can be employed as a measure of uncertainty in patch matching. Experiments have been performed on a large base of real-life RS images. It has been demonstrated that the proposed DLSM provides both a higher discriminative power and a more precise localization in comparison to existing hand-crafted SMs and SMs trained with conventional losses. The DLSM is able to correctly predict translation error distribution ellipse for different modalities, both isotropic, and anisotropic structures, different noise types and levels.

After co-registration, one gets a set of component images with either known characteristics of the noise or unknown characteristics. The characteristics are known if they have been analyzed before and imaging

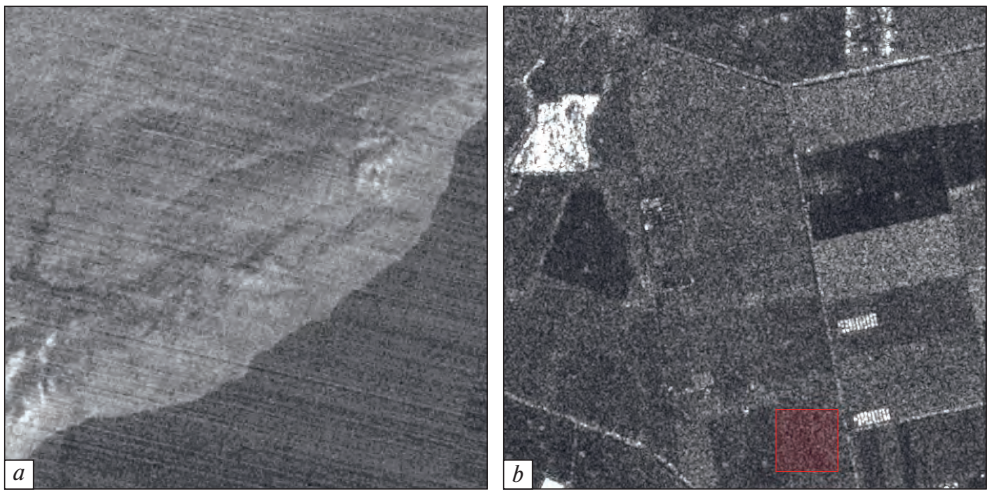

Fig. 1. Examples of component image in Sentinel-2 multispectral data (*a*) and Sentinel-1 radar data with marked homogeneous area (*b*) for which noise and speckle are clearly seen

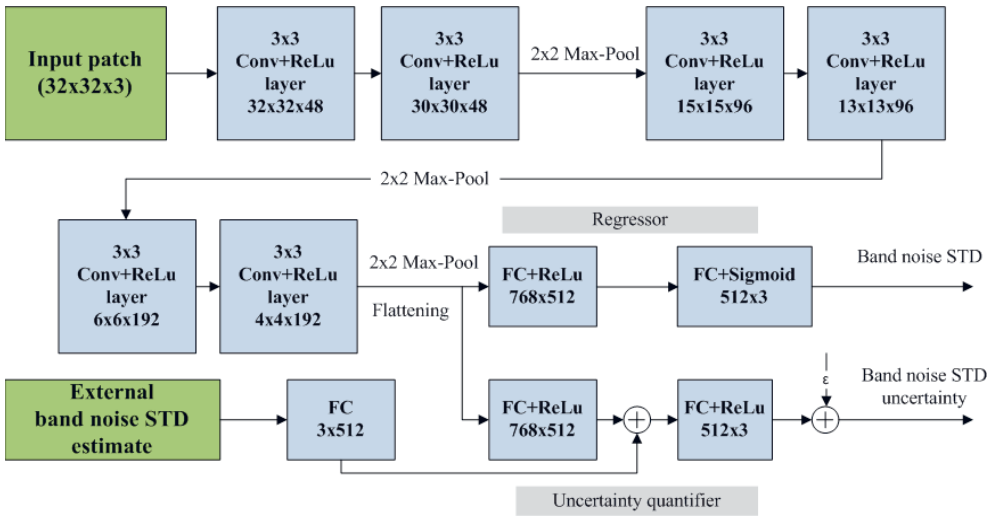

Fig. 2. The block-diagram of blind estimator of noise characteristics in three component images of multichannel RS data

system parameters are stable. The noise characteristics, both statistical and spectral, are unknown if imaging system parameters can change from one mission to another and/or component image interpolation has been done at co-registration stage. Then, to improve efficiency of further processing [6], noise characteristics have to be estimated [3, 4]. It is often desired to carry out noise characteristic estimation in a blind manner in order to save time of image processing and to be able to cope with big data (multichannel RS images can be treated as a specific type of big data).

In design of blind methods for noise characteristic estimation for multichannel RS images, we have taken into account a modern tendency to apply convolution neural networks (CNNs). We have also taken into consideration an important and inherent property of multichannel RS data that component images (at least, some of them) are sufficiently correlated. This has resulted in design of deep learning CNN-based estimator [3] that jointly process three component images (the estimator structure is shown in Fig. 2). The proposed CNN called vNoiseNet can be applied to both RGB images from digital cameras and three-component subsets of multispectral and hyperspectral bands.

Training data for this CNN were obtained from three different sources: calibrated images captured by Nikon D80 camera, AVIRIS hyperspectral data with accurately estimated noise parameters, and Sentinel-2 multispectral data with synthetic noise. An important advantage of the vNoiseNet is that it estimates not only sub-band (component) image noise variance but also uncertainty of this estimate from 32 × 32 × 3 image patches. Based on such estimates, signal-independent and signal-dependent noise component parameters can

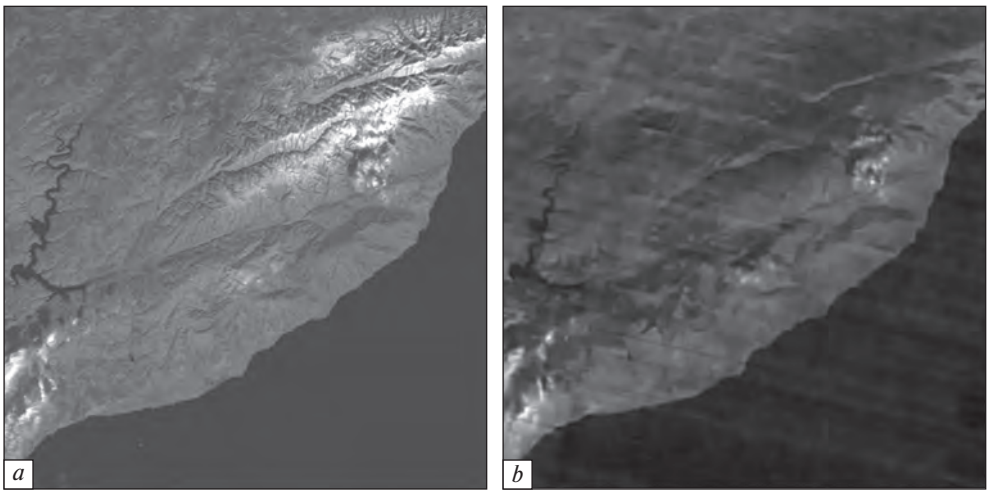

Fig. 3. Example of component image denoising with reference: component image in sub-band with high input PSNR used as reference (*a*) and the denoised image (original image with low input PSNR is presented in Fig. 1, *a* (*b*)

be estimated. Experiments on NED2012 database, AVIRIS sensor data and Sentinel-2 imager data have demonstrated high accuracy of the designed CNN based automatic estimator.

Knowledge obtained in design of blind estimators of noise in images has been successfully exploited is estimation of input PSNR for Sentinel-1 radar images [4] and in blind estimation of variance and spatial correlation width for fine-scale measurement errors in digital elevation models (DEMs) [21]. Such information about sensed terrain can be useful at RS data classification stage if radiophysical models of signal backscattering are employed for estimation of object parameters and characteristics.

Due to estimation of noise characteristics, it becomes possible to evaluate quality of original images acquired (formed) by RS sensors. For some multichannel images, quality of all or almost all component images can be appropriate and no preliminary filtering is needed [2, 4]. However, there can be component images for which pre-filtering is strongly desired. Fig. 1, *a* gives one example of noisy component image in multispectral Sentinel-2 RS data. For such multichannel images, there is a good opportunity to employ component images with high input PSNR as references in denoising the components with low input PSNR. Fig. 3, *a* gives an example of the component image fragment that is practically noise-free and has high correlation with the component image fragment in Fig. 1, *a*. Processing procedure proposed in [2] leads to very effective noise removal – Fig. 3, *b* shows the obtained output image for the image in Fig. 1, *a*.

In multispectral and hyperspectral imaging, pre-filtering can be needed in a certain percentage of sub-band images [2]. The situation is principally different for multichannel radar imaging. On one hand, recent advances in synthetic aperture radar (SAR) imaging have led to creation and wide use of modern SAR systems as TerraSAR-X, Sentinel-1 and others [4, 7, 17, 18]. Despite basic characteristics of aforementioned imaging systems are almost perfect, images acquired by any SAR suffer from noise-like phenomenon called speckle characteristics of which depend upon several factors [7]: number of looks, data sampling used that has impact on spatial correlation of the speckle. Thus, there are several parameters (criteria) that describe quality of original and filtered SAR images [4, 7, 17]. Note that a considered quality metric has to be application oriented [17, 18]. Alongside with traditional metrics (MSE, PSNR), probability of correct classification is widely used [17, 18]. There is a tendency to apply visual quality metrics for characterization of RS images [20] as well including radar images [7]. This tendency can be partly explained by the fact that visual inspection is still widely used in analysis of SAR images [7].

It is still unknown what visual quality metrics have to be used in analysis of radar images. As it follows from analysis for optical images, SSIM and SSIM modified metrics are not the best. Besides, reference (noise-free) image in characterizing acquired SAR images is not available. Then, there can be two ways out – either to apply no-reference metrics or to use prediction of full reference metrics without having the reference image itself. The latter approach has been recently proposed by us [4] for characterizing the visual quality of noisy images. This method implies using a trained neural network (its block-diagram is shown in Fig. 4).

The following aspects have been taken into account. First, speckle is a specific type of multiplicative noise

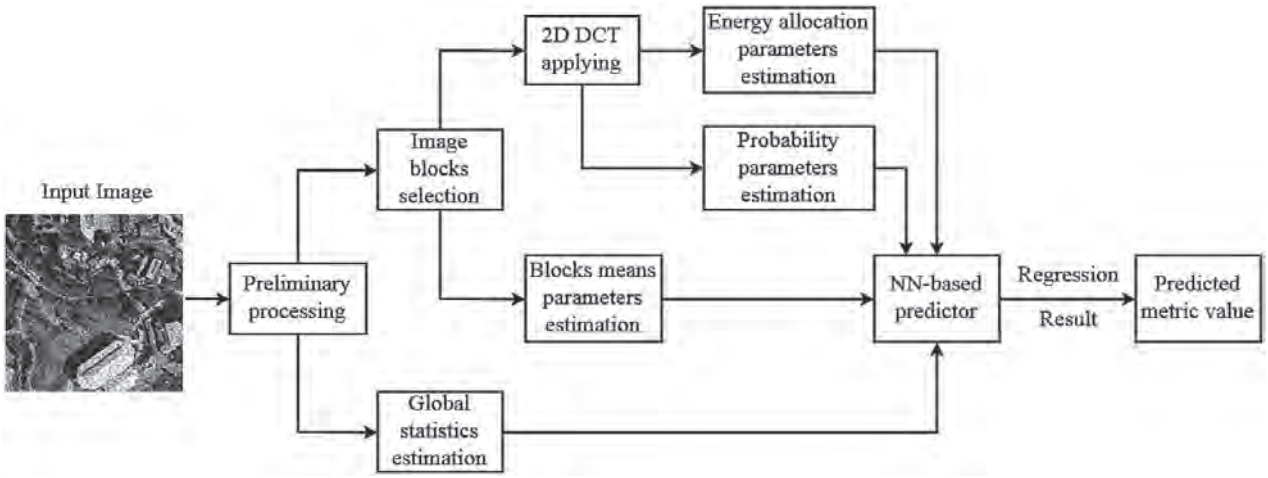

Fig. 4. Flowchart of the proposed approach proposed in [7]

that is spatially correlated [7]. Second, since SAR images acquired by Sentinel-1 are multilook, speckle probability density function is close to Gaussian with relative variance close to 0.05. Third, speckle is spatially correlated where the corresponding properties are spatially invariant and stable [7]. We have demonstrated that a lot of full-reference quality metric can be accurately predicted for original SAR images including standard PSNR, modification of PSNR taking into account masking effect and different sensitivity of human vision system to distortions in different spatial frequencies (PSNR-HVS-M), feature similarity index (FSIM), multi-scale structural similarity index (MS-SSIM), gradient magnitude similarity deviation (GMSD), Haar wavelet-based perceptual similarity index (HaarPSI), gradient similarity (GSM), modified four-component structural similarity index (SSIM4) [20], most apparent distortion index (MAD) and many others.

It has been decided to analyze four groups of parameters used as NN inputs. The first group is related to peculiarities of human vision system. The second one takes into account multiplicative nature of the noise. The third one deals with pure noise components estimates in the discrete cosine transform (DCT) domain. The last one takes global statistics of entire image.

To evaluate prediction performance of the proposed approach, root mean square error (RMSE) and adjusted coefficient of determination R^2 (as measure of goodness of fit) have been used. Recall that larger (closer to unity) values of R^2 indicate better prediction accuracy. Smaller values of RMSE relate to better prediction performance. For many metrics (PSNR, PSNR-HVS-M, FSIM, MS-SSIM, HaarPSI, GSM, SSIM4), adjusted R^2 exceeds 0.98, RMSE values for PSNR and PSNR-HVS-M are equal to 0.045 dB and 0.062 dB, respectively (for single dataset evaluation) which show that prediction accuracy is excellent. The results are slightly worse for cross-dataset but, anyway, adjusted R^2 and RMSE values are very good [4].

Quality of original image (or its accurate estimate) is one pre-requisite for undertaking the decision has one to apply preliminary filtering or not (if quality is high, there is no reason for denoising since it spends time and resources without obvious benefits). Another pre-requisite in decision undertaking for denoising applying or skipping is efficiency of denoising. It is known [6–10] that denoising efficiency (in terms of different metrics) depends on several factors including image complexity, noise type and intensity, filter type and parameters. Denoising can be not efficient if: 1) a considered image is highly textural [9]; 2) noise intensity is not high [9]; 3) noise is spatially correlated [6]; 4) a filter is not properly chosen or its parameters are not adjusted properly [9]. Even if a filter is chosen correctly and its parameters are set in a good manner, the problem of efficient denoising of highly textural images corrupted by middle and low intensity noise (especially if it is spatially correlated) remains. Moreover, the task of providing considerable improvement of visual quality due to filtering is more problematic than image enhancement according to conventional metrics (criteria) [7, 9, 10].

Similarly to the way the metrics' values have been predicted for original images [4], filter performance can be predicted in different ways [6–10]. In recent years, we have considered prediction of metric improvement (difference between the values of a given metric after and before denoising) using one or several input parameters and a predetermined dependence of output parameter (predicted metric improvement) [8, 9] as well as prediction using a set of input parameters and a trained neural network [7, 10]. Each approach has its advantages and drawbacks. The former one is simpler since less input parameters and prediction can be obtained faster. Meanwhile,

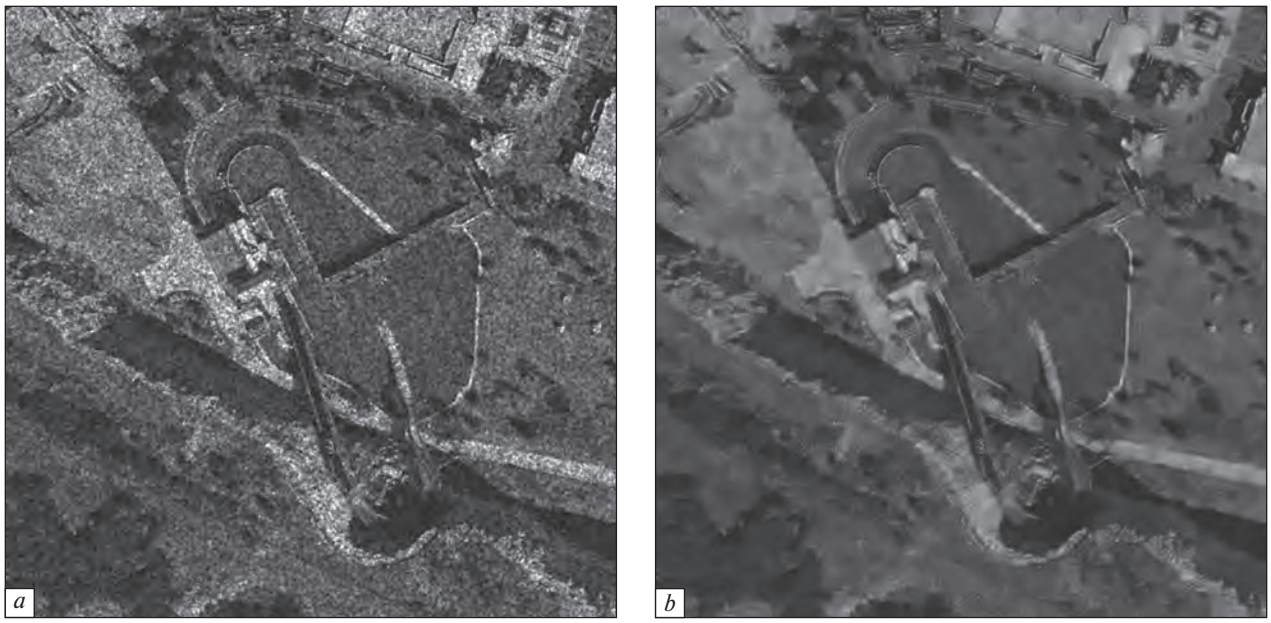

Fig. 5. Original noisy test image (*a*) and the filter output (*b*)

the latter approach requires more calculations but results in a sufficiently better accuracy of prediction. In particular, the method [7] produces prediction of improvement of PSNR with RMSE of the order 0.25...0.3 dB, i.e. with accuracy that can be considered appropriate for practical applications (decision undertaking). One example for the test image corrupted by speckle with the same characteristics as for Sentinel-1 SAR is shown in Fig. 5, *a*. As one can see, speckle is clearly visible although 5 looks are used at the stage of image obtaining. The values of some metrics for the input noisy image are the following: PSNR = 24.842 dB, PSNR-HVS-M = 22.353 dB. The denoising results expressed by improvements of these two metrics are 4.414 dB and 3.722 dB, respectively. The predicted values of these improvements are equal to 4.303 dB and 3.697 dB, respectively. As one can see, the differences are very small. This means that prediction is very accurate.

The image processed by DCT-based filter (see [7] for details) that takes into account the speckle properties is represented in Fig. 5, *b*. Speckle is effectively suppressed whilst fine details are preserved well.

One more typical stage of multichannel image processing is data compression. We have considered lossy compression since it potentially allows satisfying requirements to data size reduction [11–15]. The main problem in lossy compression is to find and provide a reasonable threshold between introduced distortions (losses) and attained compression ratio (CR). This general problem leads to necessity to save several particular problems: 1) how to improve performance of compression techniques? 2) how to provide a desired quality, what metrics have to be used to characterize compressed image quality, what quality has to be considered appropriate for a given application? 3) how to provide a desired CR if this task is of prime importance?

In our studies, we have paid attention to all these sub-problems. In particular, lossy compression of multichannel images in sub-band groups has been considered [12]. As it can be expected, three-dimensional (3D) compression of hyperspectral data has certain advantages and peculiarities. First, 3D compression is beneficial compared to component-wise one both in senses of a smaller MSE of introduced distortions and a larger CR attained (it can be larger by 1.5...2.5 times). Second, benefits of 3D compression start to appear themselves for quantization step (QS) starting from 1/50 of image dynamic range (usually, the recommended QS is larger). Third, additional errors can appear due to normalization and we propose to use preliminary normalization of component images to 10 bit range. Fourth, we have proposed automatic approach for providing acceptable distortions. We assume that PSNR should be larger than 36...38 dB to make distortions' influence on further processing of hyperspectral data small enough. Then, acceptable distortions occur to be larger than equivalent noise variance in many sub-band images and this leads to considerably larger CR values in such sub-bands (or groups of sub-bands).

In other words, there are some threshold values for the metric PSNR that have to be provided to make introduced distortions appropriate. Analogous thresholds can be recommended for other metrics including visual quality ones as PSNR-HVS-M (42... 45 dB) or FSIM (0.995). Then, a question arises how

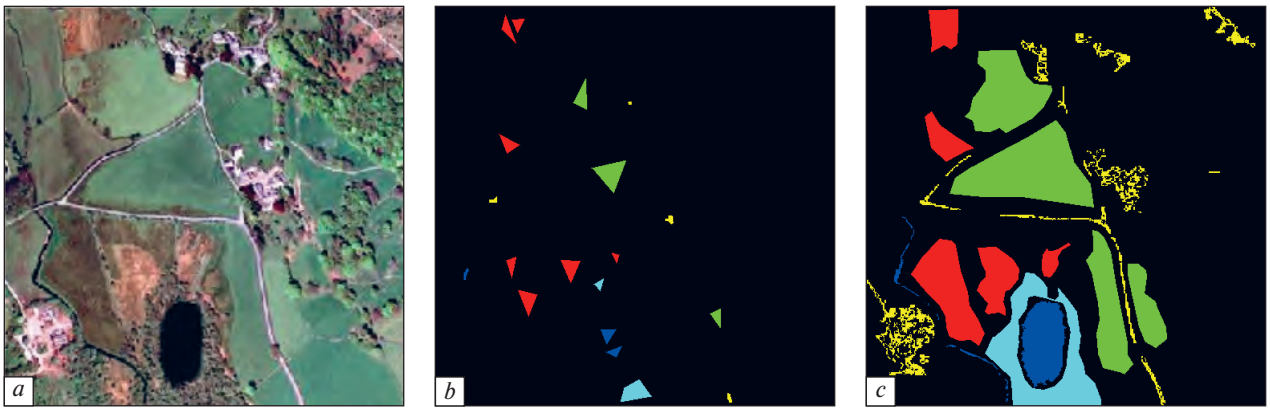

Fig. 6. Test image (Landsat TM image) (*a*), three-channel fragments used for classifier training (*b*) and ground truth map (*c*)

to provide this quality accurately and quickly enough? This question has been partly answered in our recent papers [11, 13–15]. It has been shown that MSE, PSNR, and PSNR-HVS-M can be predicted and then provided by a proper setting of QS or another parameter that controls compression quickly and with appropriate accuracy. This can be done by obtaining dependences of a considered output (predicted) parameter on one or several input parameters. Peculiarities of this approach are the following. First, dependences are obtained off-line for a set of test images compressed by a given coder in a wide range of compression ratios. Fitting of curves (dependences) into scatter-plots is used at this stage. These dependences are then used online for an image subject to lossy compression with calculating input parameter(s) and substituting it (them) as arguments.

It has been demonstrated [13–15] that quality of compressed images characterized by PSNR or PSNR-HVS-M can be provided with RMSE less than 1 dB and this is accuracy acceptable for practice. Moreover, such accuracy can be provided in one step – without iterations, i.e. multiple compression, decompression and metric estimation. Furthermore, in prediction, it is enough to get and analyze image statistics of a limited size – to analyze DCT coefficients determined in 300...1000 blocks of size 8 × 8 pixels randomly placed in an image to be compressed. Then, calculation of parameters needed for prediction (e.g., percentage of DCT coefficients that are assigned zero values after quantization with a given QS) and execution of prediction and final determination of QS in aggregate require considerably less time than execution of image compression.

One more problem studied by us in recent years is multichannel image classification. This problem has been analyzed from different viewpoints [17–19]: 1) "how to provide a better classification (higher probability of correct classification in aggregate and for particular classes)?"; 2) "what are the best classifiers, can their outputs be combined to improve classification performance [19]?"; 3) "what is the influence of pre-filtering and lossy compression on classification?".

As it is known, all existing classifiers are not perfect and it is not an easy task to discriminate classes if feature distributions are not Gaussian, class description is not full, if a given pixel (resolution element) contains elements that belong to different classes, etc. Methodology and peculiarities of training (for classifiers trained in a supervised manner) also have impact. To improve classification accuracy, we have proposes an integrated (combined) approach that includes the stage of image segmentation into homogeneous areas by elementary classifiers and the stage of post-classification processing in pseudocolors that realizes a certain local spatial filtering algorithm, which allows taking into account the topological properties of objects [19]. As the basis for the synthesis of this post-classification procedure, the following three elementary classifiers have been chosen: support vector machine (SVM), logistic regression (LGR), and multilayer perceptron (MLP).

To analyze the efficiency of the methods for pixel-wise classification of multichannel images, a three-channel image has been used in our simulations. This test image has been formed using three optical bands of Landsat TM image that relate to central wavelengths 0.66 μm, 0.56 μm, and 0.49 μm. These images have been associated with R, G and B of colour images represented below (Fig. 6, *a*). Five classes have been selected for this image, namely, "Soil" (class 1, red), "Grass" (class 2, green), "Water" (class 3, dark blue), "Urban (Roads and Buildings)" (class 4, yellow), and "Bushes" (class 5, azure).

To form the training set (fragments of the original image containing objects of each class), color masks have been used (Fig. 6, *b*). To analyse the classification efficiency of elementary and combined classifiers, the ground truth map has been employed (Fig. 6, *c*). The results of class recognition (discrimination) for the considered image using two aforementioned elementary

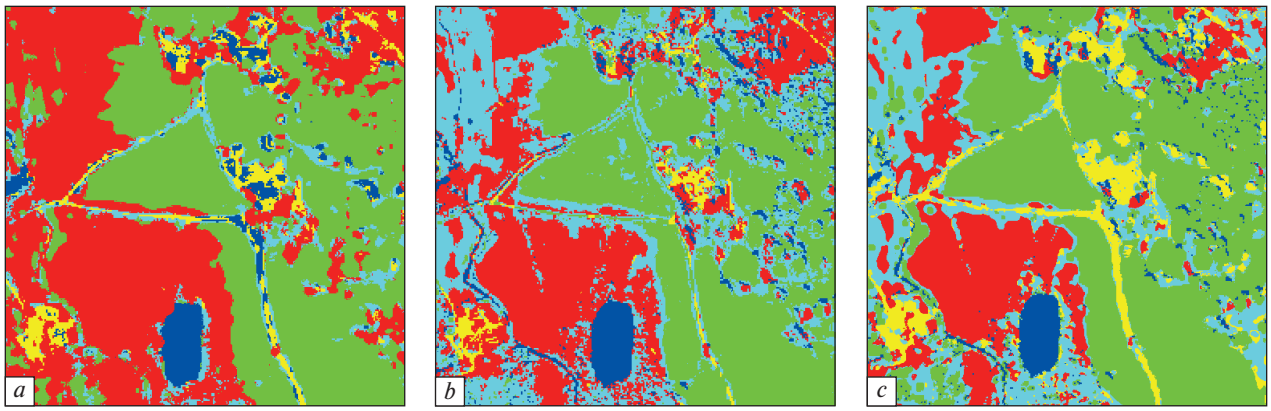

Fig. 7. Classification results by SVM (*a*), MLP (*b*) and combined method (*c*)

methods (classifiers) are shown in Fig. 5, *a, b*. As one can see, the "homogeneous" classes as Water and Grass are recognized quite well whilst "heterogeneous" classes are recognized poorly especially the classes Urban and Bushes by linear SVM (Fig. 7, *a*). The general tendencies for elementary classifiers are similar whilst there are differences in classification results. The use of the combined method [19] has led to better classification (Fig. 7, *c*) with providing the following probabilities of correct recognition: 0.97 for "Soil", 0.99 for "Water" and "Grass", 0.70 for "Buildings" and 0.74 for "Bushes". They have occurred to be considerably better than for any elementary classifier.

The influence of pre-filtering on classification accuracy of multichannel radar images have been studied as well [17, 18]. It has been demonstrated that both a filter and a classifier applied have impact on classification results for determining the types of plants in agricultural region of Ukraine using multitemporal observations from Sentinel-1. In particular, it has been shown that the modification of the known BM3D (block matching three-dimensional) filter adapted to multiplicative nature of speckle and its spatial correlation is able to provide essential improvement of classification accuracy compared to speckle filters available in standard tools of radar image processing. It has been also shown that CNNs can be effective for both radar image filtering and classification.

Finally, the influence of lossy compression on classification accuracy of multichannel RS data has been analyzed. For three-channel Landsat image (Fig. 6, *a*), different compression ratios and, respectively, image qualities have been studied. It has been demonstrated that if PSNR-HVS-M is about 43...45 dB (PSNR is about 40 dB) the classification accuracy for compressed data is practically the same as for original (uncompressed) image. CR provided in this case is about 6 for component-wise compression and about 10 for 3D compression. Two more tendencies are worth stressing. First, it is better to carry out training of a classifier for compressed data if it is presumed that compressed RS data will be classified. Second, post-processing of elementary classifier outputs can sufficiently increase probability of correct classification.

REFERENCES

1. Vozel B., Lukin V., Bazi Y. Editorial to Special Issue "Multispectral Image Acquisition, Processing, and Analysis". *Remote Sensing*. 2019. Vol. 11, Iss. 19. 4 p.

2. Abramov S., Uss M., Lukin V., Vozel B., Chehdi K., Egiazarian K. Enhancement of Component Images of Multispectral Data by Denoising with Reference. *Remote Sensing*. 2019. Vol. 11, Iss. 6. 16 p.

3. Uss M., Vozel B., Lukin V., Chehdi K. Blind noise parameters estimation for multichannel images using deep convolutional neural networks. *Proceedings SPIE, 11155, Image and Signal Processing for Remote Sensing XXV*, Strasbourg, France, 7 October 2019. 11 p.

4. Rubel O., Lukin V., Rubel A., Carli M., Egiazarian K. Blind DCT-based prediction of original image quality for Sentinel SAR data. *Proceedings of EUVIP*, October 2019, Rome, Italy. 6 p.

5. Uss M. L., Vozel B., Lukin V., Chehdi K. Efficient Discrimination and Localization of Multimodal Remote Sensing Images Using CNN-Based Prediction of Localization Uncertainty. *Remote Sensing*. 2020. Vol. 12, Iss. 4. 22 p.

6. Rubel O., Lukin V., Egiazarian K. Additive spatially correlated noise suppression by robust block matching and adaptive 3D filtering. *Electronic Imaging, Society for Imaging Science and Technology*. 2019. Vol. 2019, No. 11. P. 60401-1–60401-11.

7. Rubel O., Lukin V., Rubel A., Egiazarian K. NN-Based Prediction of Sentinel-1 SAR Image Filtering Efficiency. *Geosciences*. 2019. Vol. 9, No. 7. 22 p.

8. Rubel O., Lukin V., Rubel A., Egiazarian K. Prediction of Lee filter performance for Sentinel-1 SAR images. *IS & T International Symposium on Electronic Imaging 2020, Image Quality and System Performance*, USA, January 2020. P. 371-1–371-6.

9. Rubel O., Lukin V., Abramov S., Vozel B., Pogrebnyak O., Egiazarian K. Is Texture Denoising Efficiency Predictable? *International Journal of Pattern Recognition and Artificial Intelligence*. 2018. Vol. 32, No. 01. 32 p.

10. Rubel A., Rubel O., Lukin V. Blind DCT-based prediction of image denoising efficiency using neural networks. *Proceedings of EUVIP*, November 2018, Tampere, Finland. 6 p.

11. Krivenko S., Zriakhov M., Kussul N., Lukin V. Prediction of Visual Quality for Lossy Compressed Images. *Proceedings of CADSM*, Svalyava, Ukraine, February 2019. 5 p.

12. Zemliachenko A., Lukin V., Ieremeiev O., Vozel B. Peculiarities of Hyperspectral Image Lossy Compression for Sub-band Groups. *Proceedings of UkrCon 2019*, Lviv, Ukraine, July 2019. P. 918–923.

13. Abramov S.K., Krivenko S.K., Lukin V.V., Vozel B., Chehdi K. Lossy DCT-based compression of remote sensing images with providing a desired visual quality. *Proceedings SPIE, 11155, Image and Signal Processing for Remote Sensing XXV*, Strasbourg, France, 7 October 2019.

14. Alhihi M., Zemliachenko A., Abramov S., Vozel B., Egiazarian K., Lukin V. Pre-requisites for Smart Lossy Compression of Noisy Remote Sensing Images. *Telecommunications and Radio Engineering*. 2018. Vol. 77, No. 3. P. 225–241.

15. Lukin V., Zemliachenko A., Krivenko S., Vozel B., Chehdi K. Lossy compression of remote sensing images with controllable distortions. *Book chapter in "Satellite Information Classification and Interpretation"*, IntechOpen, 2018. P. 1–17.

16. Rubel O., Abramov S., Abramova V., Lukin V. Use of similarity metrics in template-based detection of objects in images. *Telecommunications and Radio Engineering*. 2019. Vol. 78, No. 14. P. 1249–1261.

17. Lukin V., Rubel O., Kozhemiakin R., Abramov S., Shelestov A., Lavreniuk M., Meretsky M., Vozel B., Chehdi K. Despeckling of Multitemporal Sentinel SAR Images and Its Impact on Agricultural Area Classification, *Book chapter in "Recent Advances and Applications in Remote Sensing*" / edited by Dr. Ming-Chih Hung, InTech, 2018. P. 21–40.

18. Lavreniuk M., Shelestov A., Kussul N., Rubel O., Lukin V., Egiazarian K. Use of modified BM3D filter and CNN classifier for SAR data to improve crop classification accuracy. *Proceedings of UkrCon 2019*, Lviv, Ukraine, July 2019. P. 1071–1076.

19. Lukin V., Proskura G., Vasilyeva I. Improvement of Multichannel Image Classification by Combining Elementary Classifiers. *Proceedings of PIC S&T*, Kyiv, Ukraine, October 2019. P. 666–670.

20. Ponomarenko M., Egiazarian K., Lukin V., Abramova V. Structural Similarity Index with Predictability of Image Blocks. *Proceedings of Intern. Conf. MMET*, 2018, 4 p.

21. Uss M.L., Vozel B., Lukin V.V., Chehdi K. Estimation of Variance and Spatial Correlation Width for Fine-Scale Measurement Error in Digital Elevation Model. *IEEE Transactions on Geoscience and Remote Sensing*, November 2019, 16 p. DOI: 10.1109/TGRS.2019.2951178.

APPLICATION OF SPACE ENVIRONMENTAL MONITORING TO IDENTIFY DESERT LOCATIONS IN UKRAINE

V. Lyalko, L. Elistratova, A. Apostolov, I. Romanciuc

State Institution "Scientific Centre for Aerospace Research of the Earth of Institute of Geological Sciences of NAS of Ukraine"

One of the most threatening global and transient processes of modern climate is the expansion of desertification and loss of biological potential of the Earth. Such processes correspond to similar conditions of the natural desert. The problem of desertification is now becoming relevant for the territory of Ukraine. Ukraine, like any other country, is vulnerable to climate change. Every year our economy suffers considerable losses from natural disasters. Measures should be taken to estimate the negative consequences of this process. Increasing average temperature of air and uneven distribution of precipitation caused by global climate change can lead to a significant transformation of climatic and agricultural zones. The most noticeable consequence will be an increase in the number and intensity of extreme weather events: severe droughts, extremely hot days. Therefore, there is an urgent need to increase adaptation to climate change in some sectors of the national economy of Ukraine. The urgency of this problem was confirmed by the Resolution of the Cabinet of Ministers of Ukraine of August 18, 2017 No. 20. As a result, the Coordinating Council for Combating Land Degradation and Desertification was organized. The Council is a temporary advisory body of the Cabinet of Ministers of Ukraine until 2021 coordinating the formation and implementation of state policy on sustainable land use and protection, combating land degradation and desertification, drought mitigation.

At present, it is important for Ukraine to define the boundaries of arid lands and the centers of territories that may become arid over time, in accordance with the recommendations of the UN Convention to Combat Desertification. With modern climate change, a special attention should be paid to droughts as a powerful factor in the development of desertification. For this purpose it is necessary to reveal the features of spatial distribution of humidification of Ukraine.

Water indices were used to calculate the moisture content of the surface. This allowed us to assess the susceptibility of areas subjected to desertification in the context of climate change and to provide appropriate quantitative information about the moisture content of the territory of Ukraine. The indices were obtained by calculations, quantitative estimates of the intensity and duration of the process of moisture exchange of the earth's surface. The selection of optimal water indices is consigned to reflect the processes of desertification. The Normalized Difference Infrared Index (NDII) was chosen through analysis of the most effective water indices. It can be calculated from the data of MOD13C2 product with spatial resolution 5600 m and used for the regional level of research for all the territory of Ukraine.

Normalized Difference Infrared Index (NDII) was previously used in (Hardinsky et al., 1983; Abdullah et al., 2018; Gao, 1996). This index operates with data from infrared channels to monitor the water content of vegetation. The change in the projective vegetation cover is used to detect the period of plant stress caused by drought. On the example of the model years 2007 (very arid) and 2015 (arid) the spatial features of drought as a powerful factor of desertification are revealed (Fig. 1).

With further climate change in Ukraine, there will be a change in natural zonation. The main factor in the formation of natural areas is the balance of heat and moisture. While maintaining the existing trends of increasing aridity, a gradual shift of the semi-desert zone to the territory of the modern steppe zone is possible. The steppe zone can be transformed into a forest-steppe. The zone of deciduous forests can turn into a forest-steppe zone. The territory of the forest-steppe zone will decrease accordingly. Only the rate of such changes remains a debatable issue [1].

Moisture supply of a certain area is a significant factor influencing crop yields in any climatic zone. Relevant calculations of the moisture supply of Ukraine were performed for the administrative regions of the country according to the water index NDII using the product MOD13C2 (Fig. 2). The territory of administrative regions of Ukraine was ranked according to the values

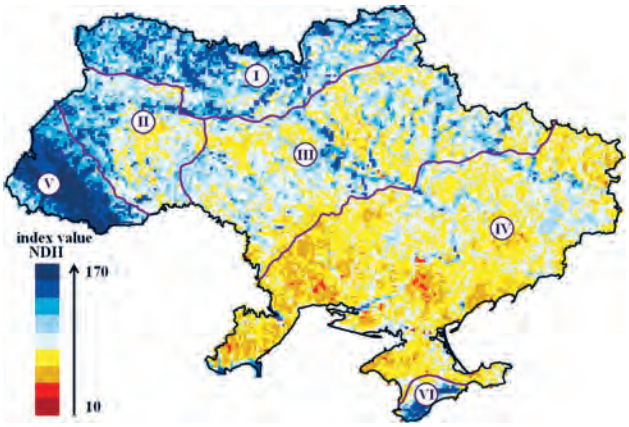

NDII 2007		NDII 2015	
No.	Humidification	NDII	
		Color	Indice values
1	Excessively moisturized		> 160
2	Highly moisturized		150...160
3	Enough moisturized		140...150
4	Humidified		130...140
5	Slightly moisturized		120...130
6	Arid		110...120
7	Very arid		100...110
8	Excessively arid		90...100
9	Catastrophically arid		< 90

Fig. 1. Map of the NDII water index on the territory of Ukraine (scale 1 : 3700000) for typical landscape and climatic zones of Ukraine: I – zone of mixed (coniferous-deciduous) forests, II – zone of deciduous forests, III – forest-steppe zone, IV – steppe zone, V – Ukrainian Carpathians, VI – Mountain Crimea

NDII, 2007		NDII,2015	
Conditional values:			
	Excessive humidity (> 150) Very high humidity (140–150) Strong humidity (130–140) Moderate humidity (125–130)		Low aridity (120–125) Severe drought (110–120) Catastrophic drought (< 110)

Fig. 2. The ranking of administrative regions of Ukraine according to NDII index of moisture supply for 2007 and 2015

of the NDII for 2007 and 2015 – from excessively humid (>150) to catastrophically arid (<110). Analysis of the territory of Ukraine using this index shows that the southern steppe regions of Ukraine characterizing by lack of moisture are under the greatest threat. This trend is intensifying over the years [2, 3].

The use of multispectral space images is effective in studying the processes of desertification. In this study for regional level we used product MOD13C2.

Our results of the calculation of the NDII water index from the data of multispectral space survey from the MODIS satellite allow us to conclude that in the future we should expect significant losses in biodiversity due to the effects of high temperature and water stress. This effect is unfavorable from an environmental point of view, as it will lead to the extinction of certain species of natural systems sensitive to climate change. It is strictly necessary to develop adaptation measures estimating negative consequences of nature management at the state level.

REFERENCES

1. Lyalko V., Romanciuc I., Elistratova L., Apostolov A., Chekhniy V. Detection of Changes in Terrestrial Ecosystems of Ukraine Using Remote Sensing Data. *Journal of Geology, Geography and Geoecology*. 2020. Vol. 29, No. 1. P. 102—110. DOI:10.15421/112010.

2. Apostolov A.A., Elistratova L.O., Romanciuc I.F., Chekhniy V.M. Assessment of Desertification Areas in Ukraine by Estimation of Water Indexes Using Remote Sensing Data. *Ukrainian Geographical Journal*. 2020. No. 1(109). P. 16–25. URL:https://doi.org/10.15407/ugz2020.01.016.

3. Lyalko V.I., Elistratova L.O., Apostolov A.A., Romanciuc I.F. Experience in assessing changes in the natural environment in Ukraine with the use of space imagery. *Environmental Safety and Balanced Nature-Used in Agroindustrial Production*: Proceeds of International Scientific Conference, Kyiv, July 3–5, 2019. P. 164–168.

ANTI-PANDEMIC MEASURES HELP TO REDUCE THE IMPACT OF THE GREENHOUSE EFFECT ON CLIMATE

V. Lyalko, A. Apostolov, E. Dorofey

State Institution "Scientific Centre for Aerospace Research of the Earth of Institute of Geological Sciences of NAS of Ukraine"

The COVID-19 pandemic situation, rapid increasing of global warming and negative climate change could be considered as natural response to the consumer strategy of human development. This is a signal that requires a prompt response and returning to the UN strategy of "sustainable development" of society and nature.

At the same time, according to the information published around the world it is observed that the introduction of quarantine measures on a global scale significantly reduced the intensity of industrial production and transport exploitation that correspondingly diminished the CO_2 emissions. This fact looks like a global experiment that confirms the crucial role of anthropogenic impact on the formation of the greenhouse effect and negative climate change impact.

The usage of monitoring surveys based on specialized spacecraft ENVISAT, GOSAT, OCO-2 made it possible to record the peculiarity of CO_2 content changes in the atmosphere in time and space and their correlation in dependence of air temperature. Studies performed during the first – second quarter of 2020, analysis of the monthly changes of CO_2 average in the atmosphere over the Ukraine and the surface air temperature corresponding changes confirm above assumption.

The research was realized on the basis of the air temperatures measures over the city of Kyiv by the Kyiv Geophysical Observatory during 2019–2020 in the regular mode. The average monthly temperature for April and May of 2020 is characterized by decreasing of these values compared to respective period of 2019 (Table 1). This coincides with the introduction of quarantine restrictions in February – March 2020 both in Ukraine and in other countries.

The difference between the years ΔT (T2020–T2019): negative values in April – 0.7 °C, negative values in May – 4.6 °C.

On Fig. 1 is a graph of CO_2 concentration changes in the atmosphere over the Ukraine, obtained from remote sensing data for the 2003–2019. During the observation period from spacecraft (2003–2019), the concentration of CO_2 in the atmosphere over the Ukraine increased annually by approximately 1.5–2.2 ppmV per year (from 377 to 407 ppmV).

In terms of CO_2 values content, the 2020 quarantine period was compared with the corresponding 2019 period. According to the State Statistics and data determined by space observations the values of CO_2 emissions into the atmosphere decreased in 2020 by about 17% in comparison to 2019.

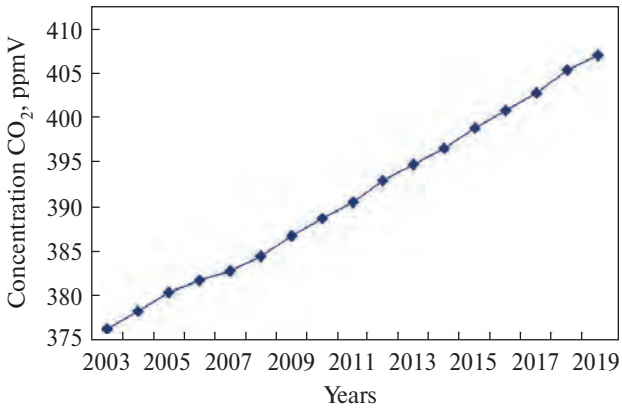

Fig. 1. Graph of changes in the CO_2 concentration in atmosphere over Ukraine, obtained from space survey materials for the 2003–2020 period

Table 1

Average monthly air temperature (°C) over the Kyiv in 2019–2020

Years	Months				
	January	February	March	April	May
2019	–4.5	0.6	5.1	10.6	17
2020	0.8	2.5	6.5	9.9	12.4
T 2020 – T 2019	5.3	1.9	1.4	**–0.7**	**–4.6**

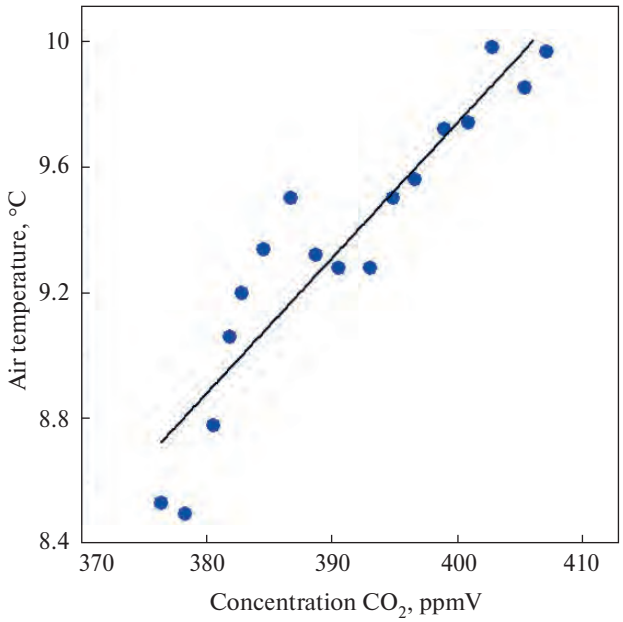

Fig. 2. The annual trend of air temperature and CO_2 concentration comparison in Kyiv for the 2003–2019 period

According to the Kyiv Geophysical Observatory named after B. Sreznevsky, the annual average of air temperature in Kyiv increased by 0.14 °C each year during the same period.

The dependences of the air temperature and CO_2 content changes in the atmosphere over the city of Kyiv indicated a high degree of their correlation ($R^2 = 0.86$). These data can be used to mutually predict their changes in time and space, as well as to develop measures to minimize the negative impact of actual climate change (Fig. 2).

Considering the observed tendencies of the content of carbon dioxide changing in the atmosphere over the territory of Ukraine, based on dependence provided in [1, 2] and specified for these conditions, the forecast of air temperature change (T) as a function of the CO_2 content in the atmosphere for the period in 30 years is made:

$$\Delta T(t) = -0.1 + 7 \cdot \ln {}^{C(t)}/_{C_0(t_0)}, \quad (1)$$

where t – is time, C_0 – initial concentration, $C(t)$ – predicted concentration of CO_2 (440 ppmV) at time t(2030).

An example of temperature rise forecast from 2003 to 2030 is presented below:

$$\Delta T = -0.1 + 0.7 \cdot \ln^{440\text{ppmv}} /_{375\text{ppmv}} = \\ = -0.1 + 1.12 = 1.02\ ^\circ\text{C},$$

where $C(t2003) = 375$ ppmv, $C(t2030) = 440$ ppmv.

Due to the pandemic conditions, a modeling of global experiment was set up, which confirms the anthropogenic impact of greenhouse gas emissions on the temperature of the Earth's atmosphere.

The protective reaction of the society to counteract these negative effects should include the prompt implementation of measures defined in the UN resolutions and in the legislation of Ukraine on sustainable development.

An effective means of counteracting these negative tendencies is the revival of natural forest and swamp ecosystems as effective absorbers of excess CO_2 from the atmosphere. The rational technology for these projects' implementation has to be based on the remote sensing data and materials involvement, as well as monitoring and computer modeling of energy and mass transfer processes in geosystems.

REFERENCES

1. Greenhouse Effect and Climate Changes in Ukraine: assessments and consequences / Editor-in-Chef Academician of NAS of Ukraine V.I. Lyalko. Kyiv: Naukova Dumka, 2015. 283 p.

2. Lyalko V., Apostolov A., Yelistratova L., Artemenko I. Analysis of the relationship between the concentration of CO2 in the atmosphere and temperature of the air for research and forecasting of climate change in Ukraine. *Ukrainian Journal of Remote Sensing*. 2016. No. 10. P. 17–20. URL: https://ujrs.org.ua/ujrs/article/view/84 (*in Ukrainian*).

MONITORING OF SOLID DOMESTIC AND INDUSTRIAL WASTE LANDFILLS BY SPACE SURVEY MATERIALS IN THE LONG-WAVE IR RANGE (ON EXAMPLE OF GRIBOVICHY LANDFILL AND SPOIL TIP OF CHERVONOGRAD COAL PREPARATION PLANT)

V. Filipovych, A. Mychak, R. Shevchuk

State Institution "Scientific Centre for Aerospace Research of the Earth of Institute of Geological Sciences of NAS of Ukraine"

The utilization problem of household and industrial waste in Ukraine has been extremely relevant for many decades, which, unfortunately, has no system solution. Despite the development of waste-free technologies, recycling processes, the main way to eliminate waste is to store them in landfills using outdated technologies and methods.

This paper considers the opportunities of satellite data application for assessing the fire hazard of domestic and industrial waste landfills on example of Gribovichy solid waste landfill near Lviv, and the spoil tip of Chervonohrad coal preparation plant of the same name geological and industrial area.

In general, the operation of existing landfills is carried out mainly in violation of sanitary regulations and the lack of effective control over compliance with their requirements. As waste accumulates, hazardous pollutants are formed in landfills under the influence of precipitation infiltration and the development of physicochemical processes, and, as a result, environmentally harmful processes are occurring. In particular, the liquid phase of highly toxic effluents is formed in large volumes – the filtrate, which flows down thalwegs and ravines from the landfill, polluting the soil and vegetation, infiltrates into aquifers. Particularly dangerous phenomenon at landfills and coal dumps is a significant emission of heat and methane gas, appearance of surface and underground conflagrations. As a result, nearby ecosystems are destroyed, catastrophic environmental pollution occur (especially of soil and vegetation cover, aquifers, atmosphere), which leads to deterioration of population health of the surrounding areas. The causes of fires are mainly spontaneous combustion due to the methane accumulation in the body and subsurface of landfills, lack of its active degassing (gas continues emitting to the surface decades after landfill closure), careless handling of fire, arsons, lightning cause ignition. A frequent source of fire is air-pockets, which are formed in the body of the landfill as a result of storage of bulk trash, which is primarily filled with methane. The situation with fire extinguishing of landfills is complicated by excessive overflow of landfills with household waste, their untimely processing and storage.

According to the sanitary regulations, the incineration of household waste is prohibited and all the necessary actions must be undertaken to prevent spontaneous combustion. In practice, these measures are not implemented and landfills conflagrations are often recorded. Only in 2019, several large fires broke out around the landfills of a number of Ukrainian cities, which is one of the current topical urban problems. In the event of a fire, the pungent smell of burning household waste spreads to residential areas; its influence on the human body is instantaneous, because even a single pollutants release from a fire many times exceeds sanitary and hygienic standards. Toxins formed during low-temperature combustion of plastics get into the air: from nitrogen dioxide, which causes respiratory tract irritation, to dioxin, which when ingested, even in microscopic doses, leads to gene mutations.

Thus, the problem solution of preventing spontaneous combustion and fires in landfills is an extremely important task for urban and rural communities that exploit them.

One of the methods of control over the landfills, control over its thermal regime is the use of satellite multispectral imagery, in particular, in long-wave infrared (thermal) range of the electromagnetic spectrum. The results of the satellite images analysis of can provide valuable information, not only on the state of the landfill thermal field, but also for analyzing the dynamics of thermal processes in the landfills surface over the years, months, for providing forecast of possible areas of spontaneous combustion.

Fig. 1. Satellite image of Gribovichy domestic waste landfill as of 09.04.2016 spatial resolution is 2.5 meter per pixel)

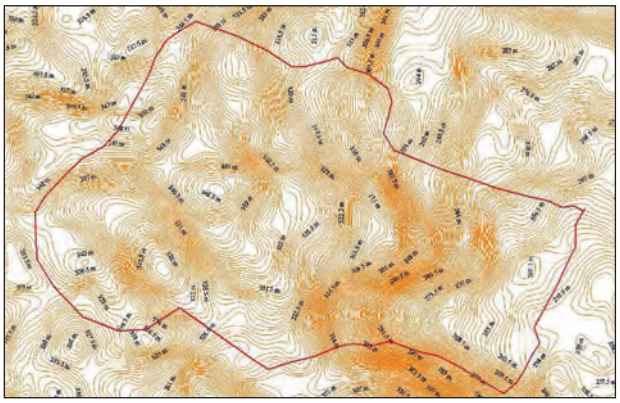

Fig. 2. Hypsometric surface (relief) of Gribovichy household waste landfill based on radar survey data Aster DEM v.2. The red line is the contour of the landfill

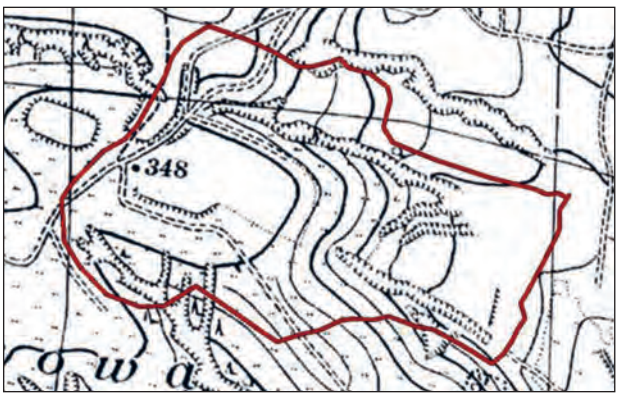

Fig. 3. Fragment of a topographic map (scale 1:25 000) of the territory of the future landfill (based on the materials of the Geographical Military Institute, Warsaw, 1930). The red line is the contour of the landfill

Assessing the surface temperature distribution of the land surface is one of the important opportunities of modern space imagery data. The Earth's surface is composed of different materials that have actual physical properties, which is reflected in the difference in thermal emission value of each satellite image pixel. Obtaining thermodynamic data requires computer processing of long-wave infrared remote sensing data. The source data for the study of the land surface thermal field are space images obtained by satellites of the Landsat (5, 7 and 8), Terra Aster, Sentinel (1, 2). This technique details are highlighted in authors' article [1].

For calculating of the land surface temperature distribution, two images are required: the thermal band with radiometric correction done and emissivity image. The spatial resolution of the calculated temperature image will be the same as the input image with a higher resolution, thus visible and near-infrared data necessary for emissivity calculation and long-wave infrared data can be taken from different sources in order to enhance resulting image resolution.

Thermal regime analysis of the domestic waste landfill based on remote sensing data

Satellite images have been selected for the last six years: 24.05.2014, 20.05.2015, 27.05.2016, 29.05.2016, 01.06.2017, 28.05.2018, 20.05.2019. The selection of annual data took into account the similarity of weather conditions in the region of the Gribovichy landfill, in particular the background temperature characteristics of May. The main reason for the selection of acquisition time in May was the date of May 30, 2016, when tragic events occurred at this landfill with the death of people in the fire that broke out on May 28.

Gribovichy landfill is located 6–7 km north of Lviv and 0.5 km south of the village Velyki Gribovichy. The general view of the landfill, as of 09.04.2016, is shown in Fig. 1.

In geomorphological aspect the landfill territory is confined to the slope of the watershed with absolute marks, in the most elevated part of it – 340–348 m and in the lowered southeastern part of the slope – 270 m. Hypsometric data for map was extracted from ASTER_DEM v.2. as of 2013 (Fig. 2).

By the time the landfill was established, it's surface was turfed, occasionally covered with low shrubs, and complicated by gullies. Perpendicular to the slope were 3–4 deep ravines, with a width of 3 on the slope top to about 6 m at the foot of the slope (Fig. 3).

On May 28, 2016, a large-scale fire broke out in the landfill. The fire extinguishing took three days. On May 30, firefighters have quenched the last meters of the fire. May 30, approximately at 3:30 p.m. garbage slide occurred and three firefighters and an ecologist from a utility company were buried under the trash mass. On May 31, a tailings dam with harmful toxins (filtrate) cracked at the Gribovichy landfill.

The results of the landfill thermal field study based on satellite imagery in May 2014, 2015, has shown that the surface temperature of the landfill was in the range from 22–26 °C (periphery) to 36–38 °C (center) (Fig. 4).

In 2016, on May 29 at 11:20 a.m. the maximum temperature values in all waste dump area were fixed. It was in the range of 31–38 °C on the periphery, and reached +42 °C in the southern part of the landfill. At the same time, outside the landfill, the temperature corresponded to the background values and was in the range of 22–26 °C.

Obviously, such a temperature level of +42 °C reflected the most active phase of underground combustion in the body of landfill. The horizontal

Fig. 4. Isolines of surface temperatures of Gribovichy landfill on 24.05.2014, 20.05.2015, 27.05.2016, 29.05.2016, 01.06.2017, 28.05.2018, 20.05.2019 as of 11 hours 20 minutes, obtained using space imagery data

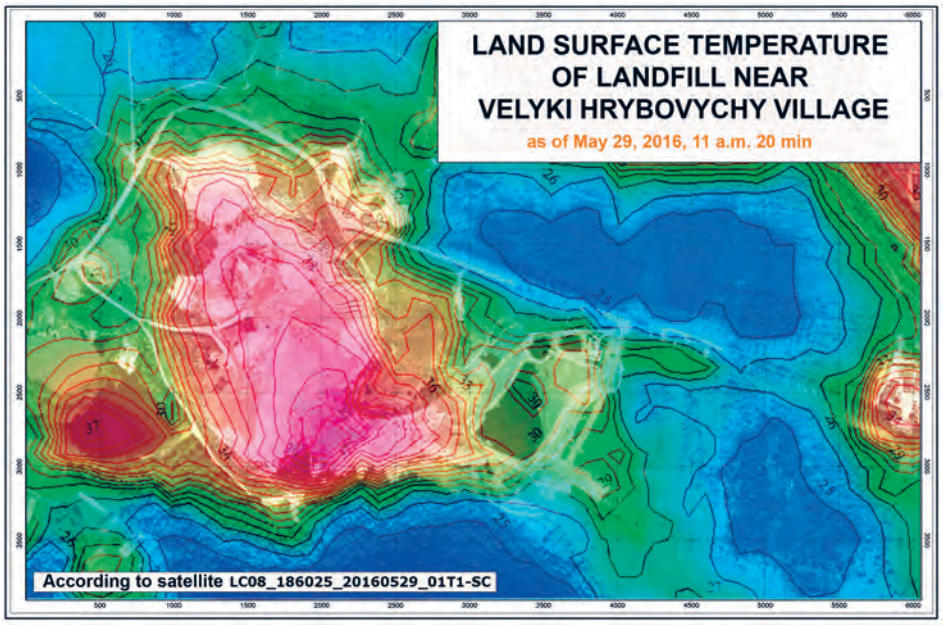

Fig. 5. The nature of the land surface temperature distribution of the Gribovichy landfill on May 29, 2016 at 11:20 am

Fig. 6. Spoil tip of Chervonohrad coal preparation plant

Fig. 7. Extinguishing the next spontaneous combustion in the spoil tip of the Chervonohrad coal preparation plant. September 2016 (photo: Lviv portal https://portal.lviv.ua/)

location of the most "heated" landfill areas on a space image is shown in Fig. 5.

In 2017 and 2019, the May surface temperatures of the Gribovichy landfill were in the range of 19–24 °C on the periphery and 25–30 °C in some parts. May 2018 is marked by a slightly high temperature level, in some parts of the landfill the temperature reached 34–36 °C. On the periphery 31–33 °C and outside the landfill 29–30 °C. Thus, taking into account the shown brief analysis of the landfill thermal field on May before 2016 and until 2019, it can be stated that the catastrophic fire on May 29, 2016 was the result of spontaneous combustion in landfill. Probably, with proper control over the temperature of the landfill surface, the catastrophe could have been prevented.

Analysis of the thermal field of mining waste (heaps) according to satellite monitoring

Coal mining in the Lviv-Volyn coal basin (LVVB) is carried out in two geological and industrial districts: Novovolynsk and Chervonohrad.

The coal shipment from LVVB mines has begun in 1954 and continues to this day. During this period, a total number of spoil tips formed of mines and coal preparation plants is 55 waste, 26 of which are burning. They cover an area of over 200 hectares. The volume of garbage mass is about 40 million m^3.

Negative environmental effect of spoil tips is manifested primarily in changes in the hydrogeological regime and chemical composition of groundwater, surface and subsurface waters, the development of flooding, atmospheric pollution, changes in terrain morphological characteristics, soil withdrawal from agriculture, etc.

A significant factor of negative environmental impact and a threat to human health are the processes of ignition, decay and combustion of waste, which leads to temperature increasing, acid rains, changes in the atmosphere gasses composition etc. Within the Novovolynsk coal-mining district, 28 waste heaps appeared, which contain more than 32 million tons of waste. Every year about 200 thousand tons of waste comes to the surface.

To prevent (mitigate) the occurrence of negative phenomena and processes associated with spoil tips, it is necessary to conduct geo-ecological monitoring, intensification of reclamation within their boundaries and adjoin areas. Problems solving of the coal mining industry, in particular the tips fires, can be effectively carried out on the basis of modern satellite imagery. The monitoring technique of coal mine dumps temperatures, allows prompt obtaining quantitative information on any spoil tip surface temperature. Thus, not only time and place of fire is determined, but the most probable spontaneous combustion are predicted. Remote research allows quenching the fires, and using financial, material and human resources more effectively.

The main environmental risk of the Chervonohrad mining and industrial region is the periodic burning of coal mine heaps. It was proposed to study this phenomenon with the aid of satellite imagery in the thermal IR range at the test site – the Chervonohrad coal preparation plant spoil tips.

Several internal combustion centres of spoil tips were found in a very limited area. The exception is the spoil tip of the Chervonohrad coal preparation plant, which have stable and significant thermal anomalies. It is the largest spoil tip in Western Ukraine with an area of 70 hectares and a height of 120 m (Fig. 6) was formed along with the commissioning of the Central coal preparation plant "Chervonogradskaya" in 1970. Since then, it has processed millions of tons of "black gold" from the Lviv-Volyn coal basin, but over the decades, a mountain of waste has grown near the plant, which has become a constantly smoldering heap. (Fig. 6–7).

The cause of this fire is self-ignition due to biochemical processes occurring inside the heap. Year-round

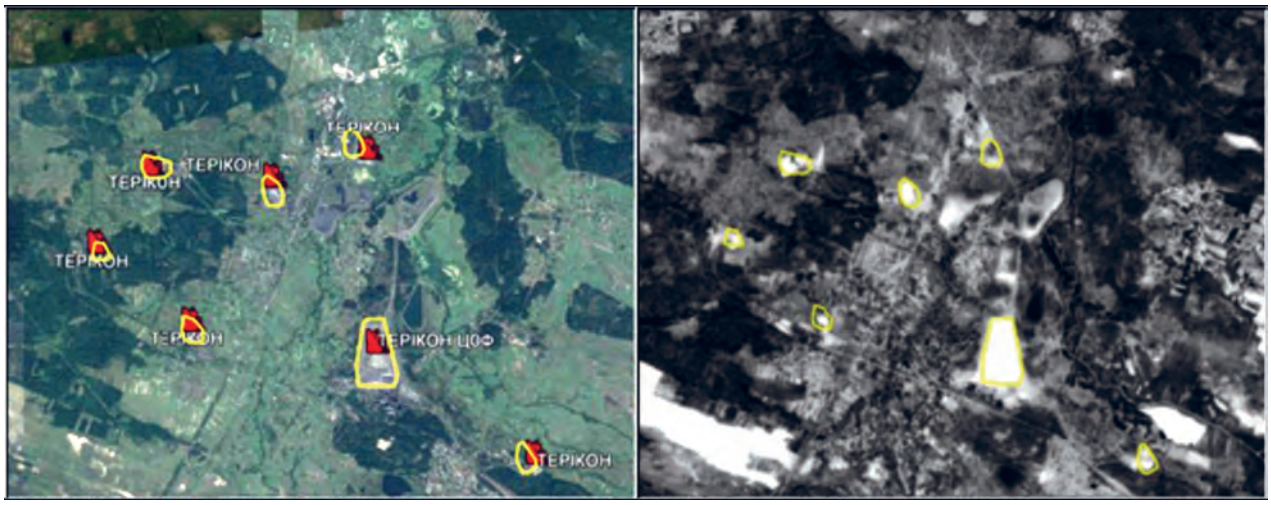

Fig. 8. Spoil tips detection in visible (left) and thermal (right) satellite data ranges

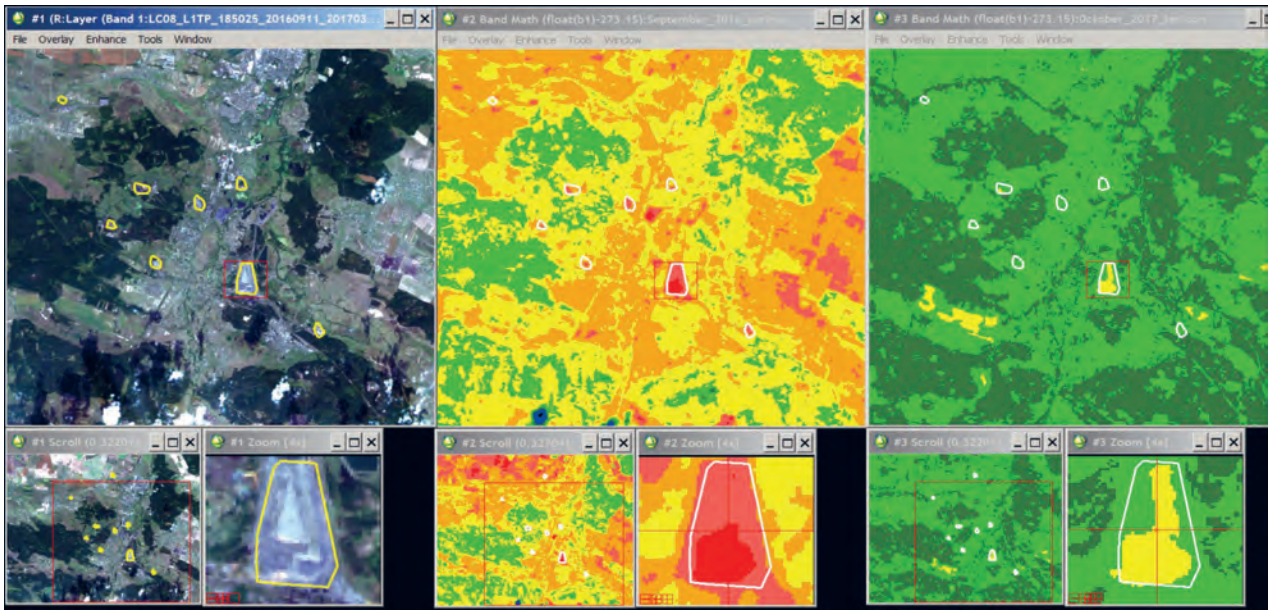

Fig. 9. Interpretation of spoil tips in southern part of Lviv-Volyn coal basin in visible (left) and thermal (right, centre) satellite data ranges (Landsat 8, acquisition dates 11.09.2016 and 16.10.2017)

combustion (Fig. 7) causes the release of significant amounts of carbon dioxide and sulfur dioxide, which are dangerous to human life and health. Therefore, the ecological situation in the surrounding villages and towns, such as Silets, Girnyk, Sosnivka, Mezhyrichchya, Chervonohrad, is always tense and depends on wind direction.

Therefore, satellite monitoring can provide constant control on the thermal regime of the heap and prevent the risks of spontaneous combustion in time. These also applies to other dumps and spoil tips of the Lviv-Volyn coal basin.

Because of Insufficient amount of archival satellite imagery, a successful algorithm for processing primary data and detecting thermal anomalies associated with the internal spontaneous combustion of heaps has not yet developed. Thus in Fig. 8 within thermal field of heaps alongside with the increased temperature values other similar anomalies are found, which is hard to explain without ground truth data. Obviously, further field research in this region, the same as availability of additional space information, will help to solve these problems. (Fig. 8–9).

Thus, the opportunities of satellite data for environmental monitoring of industrial waste dumps allow recognizing the development of dangerous processes associated with the fire hazard of spoil tips in early stages.

In general, the estimation of landfills surface temperature on the basis of remote sensing data allows obtaining immediate information on:

• state of the thermal field (surface temperature) of the landfill in the monitoring mode, which provides the ability to predict the fire occurrence, identify priority areas for fire protection activities;

• state of air, soil and vegetation cover, surface and groundwater pollution located near landfills;

• location of unlawful, spontaneous landfills, due to the contrasts of surface temperatures.

REFERENCES

1. Mychak A., Filipovych V., Shevchuk R. Satellite monitoring and thermal inspection over domestic waste landfills (on example of Gribovichy landfill). *Reclamation of landfills and waste dumps: problematic issues and best practices: proceeds of National forum "Handling of waste in Ukraine: legislation, economics, technologies"*, Sviatohirsk, Donetsk region, November 7–8, 2019. Kyiv: Environmental education and information centre, 2019. P. 53–57.

RESULTS OF DEVELOPMENT, MODELING, TESTING AND OPERATION OF THE POLYITAN SERIES NANOSATELLITES

B. Rassamakin[1], M. Ducheiko[1], N. Bayskov[1], S. Ostapchuk[1], A. Lauch[2], E. Lanevsky[3], V. Hominich[1], A. Tsybenko[1], V. Brykov[4], O. Padun[1]

[1] National Technical University of Ukraine "Igor Sikorsky Kyiv Polytechnic Institute"
[2] CB "Centr"
[3] Diona LLC
[4] M.G. Cholodny Institute of Botany of NAS of Ukraine

This article gives general information about the goals, requirements of missions and describe show these requirements are expressed in the development of nanosatellites (NS) of the PolyITAN series of CubeSat standard. The report also discusses the integration of electronics with the design and payload, provides information on the applied manufacturing methods and tests of NS of various modifications for performing tasks in orbit. The analysis of the results of flight tests of the NS (PolyITAN-1 and PolyITAN-2)and potential capabilities of the developed NS "PolyITAN-3" (assessment of the quality of shooting when sensing the Earth from an altitude of 400...350 km) and "PolyITAN-4-Plant" (features of simulating the environment and plant growth under microgravity and cosmic radiation).

Leading universities of the world are now actively encouraging students to create nanosatellites – small spacecraft, the so-called international standard "CubeSat" (U1 format (single unit) corresponds to a mass of about 1 kg and dimensions of 10 × 10 × 10 cm). In addition to solving purely educational purposes, such spacecraft in the future may be used in the implementation of a number of scientific, technical and social projects for different purposes. Standard "CubeSat" makes it possible to create miniature satellites weighing 1–10 kg in a short period of time (1–3 years) and with relatively small means. Such work is carried out in dozens of scientific centers around the world. The rapid development of the element base gives hope for the commercial application of these spacecraft. The establishment of such satellites allows the space research at relatively low financial cost and it is actual for Ukrainian conditions with its high potential in the field of designing and developing of space technology [1–6].

Restrictions on mass, volume and surface area, in particular solar cells, require the development of extremely efficient design of CubeSat standard nanosatellites (NS). According to it, National Technical University of Ukraine "Igor Sikorsky Kyiv Polytechnic Institute" (KPI) has created the NS series named PolyITAN. Launched in 2009, the NS "PolyITAN-1" project is a joint activity of researchers, teachers and students of a number of faculties of the KPI, who first created the space electronic platform of the NS.

Model of "PolyITAN-2-SAU nanosatellite"

At present, the PolyITAN-2-SAU launched into the near-Earth orbit is part of the scientific space network of the QB50 project intended for studying the thermosphere. The main task of the QB50 project is to study the Earth's climate change. The NS carries a payload on board – an experimental sensor for analyzing the oncoming gas flow FIPEX, capable of distinguishing and measuring the characteristics of atomic and molecular oxygen, which is the main element at altitudes of 90–420 km from the Earth's surface. This is important for the assessment of thermosphere models.

Object of Study. Structurally, NS "PolyITAN-2-SAU" is the successor of the previous model (NS "PolyITAN-1") designed at NTUU "KPI" and launched into Earth orbit in 2017 (finished mission in 2019 when was burned in the Earth's atmosphere). The results of the first run and participation in QB50 mission allowed significant changes in the NS design. Thus, "PolyITAN-2-SAU" is a 2U (2-Unit) format, with a payload, which is a thermosphere composition analyzer FIPEX. This is the main difference compared to the first model (PolyITAN-1 is a 1U), which is caused by a special range of tasks to be carried out of the NS.

The key to finding innovative solutions is the need to comply with the requirements of the NS QB50 project, under which the payload is ready to be installed on

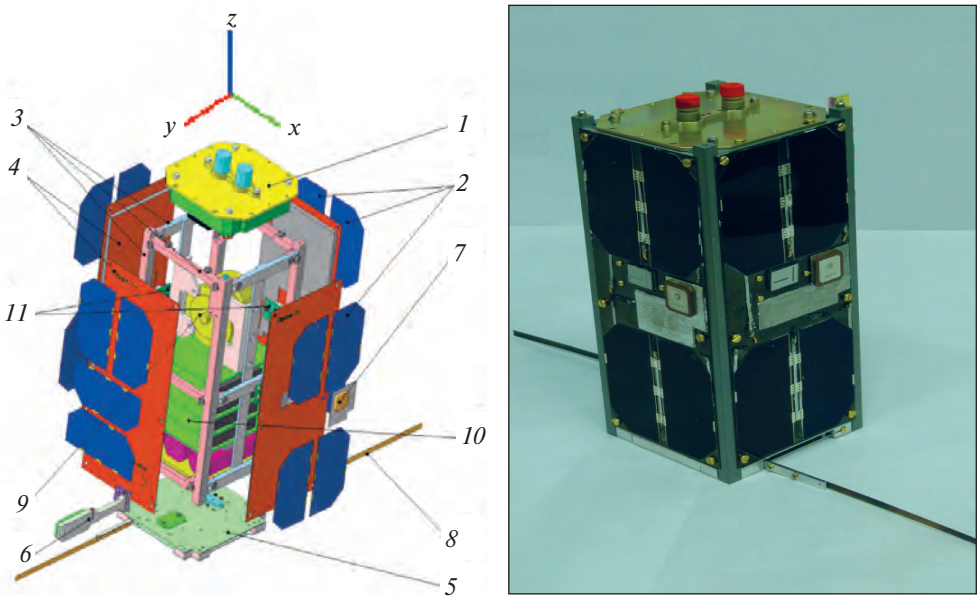

Fig. 1. Engineered (*a*) and real (*b*) view of "PolyITAN-2-SAU": *1* – payload (FIPEX); *2* – solar battery; *3* – satellite case; *4* – honeycomb panel; *5* – aerial module; *6* – magnetometer with deployment mechanism; *7* – GPS/GLONASS aerial; *8* – radio aerial; *9* – flywheel; *10* – electronic platform; *11* – Sun direction sensor

the projected satellite. Thus, these are size, layout, set of subsystems, which should provide integration, and the ability to manage the already developed FIPEX (Fig. 1).

Payload is FIPEX (Flux-Probe-Experiment) – parser of the thermosphere composition, developed at Dresden Technical University, which is able to distinguish and measure the behavior of atomic oxygen, as a key element in the lower thermosphere, in the time domain [7].

Thermal vacuum testing. Thermal vacuum testing, during which was simulated the effect of space factors on the NS and its parts, is one of the important stages in the development of "PolyITAN-2-SAU". Significant factors of space for the thermal vacuum test are low temperature, vacuum, space blackness, Sunlight and reflected radiation from the Earth [3, 6–8].

During its orbital motion, NS continuously falls under various influences – Sun radiation, Earth radiation etc., which significantly affect the thermal state and thermal mode of the NS systems, and thus the reliability and efficiency of the NS elements in flight.

At various intervals, the impact of these factors will vary: depending on the NS position in orbit and on the functioning conditions of its systems the carcasses surfaces will be exposed to variable heat flows of different intensity, which will determine the thermal state of subsystems and elements of NS, including its electronic equipment [6, 7].

One of the main characteristics that determine the readiness of the NS PolyITAN-2-SAU to start is conformity of the temperature conditions of the electronic platform and equipment of the NS to their operating temperature range. Thus, the result of thermal vacuum test should conclude that during the imitation of external and internal heat evolution, temperatures of NS elements do not exceed their permissible limits. Also, during the test there was made the checkup of the functional ability of the satellite subsystems to perform their tasks at the orbit, and confirmation of the correct thermal regulation of NS systems. Also, tests are needed to fulfill international QB50 project requirements. This includes checking performance and capability to control the payload under the impact of space factors.

To carry out the necessary tests simulating thermal vacuum chamber TVC-0.2 [7] was used, which is the single set of tools and equipment that provides the necessary space conditions simulation. This camera is designed specifically for the NS research, elements of space technology and small-sized spacecraft. This camera is located in the NTUU "KPI". The diameter of the cylindrical part of the chamber is 0.5 m, height is 0.6 m. The pumping system consists of the oil diffusion pump H-2 T-3 and two fore-vacuum pumps. Pumping speed equals to 1500 l/s, and the ultimate pressure test is 10^{-5} Pa. Imitation of solar flux is carried out by solar radiation simulator (SRS), a xenon lamp.

The optical system in the working zone of the chamber provides a radiant heat flux, the power and spectral characteristics of which are close to the solar radiation of the open space. Solar radiation imitator is

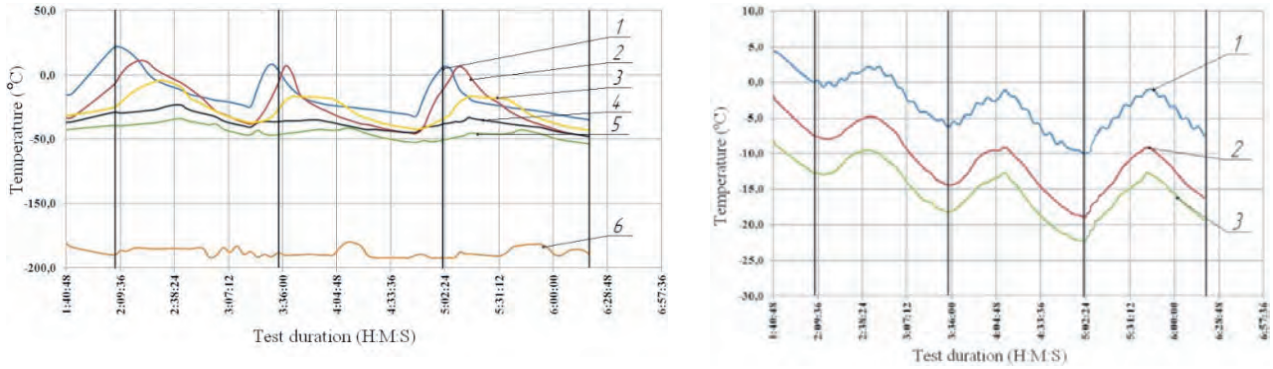

a *b*

Fig. 2. Distribution of temperatures on the inner sides of the NS honeycombs (*a*): *1* – side Z+; *2* – side Y–; *3* – side X–; *4* – side X+; *5* – side Y+; *6* – cryo shields; Distribution of temperature on the electronics boards of NS (*b*): *1* – radio channel board; 2 – CPU board; *3* – FIPEX board

located outside the chamber and let the beam of light pass through the inspection hole. Earth radiation simulator (ERS) (4) is copper heater formed as a plate which is fixed directly under the NS. The measuring system is designed to measure temperature dependences and uses copper-constantan thermocouple and copper resistance thermometers as sensors, which are attached to the NS, as well as temperature sensors, which are structurally a part of the NS, and are located on the electronic platform and the battery unit.

As a result of the test, rotation of NS around the Earth was simulated and the temperature dependence of its components, on which temperature sensors were placed, was received. The Fig. 2, *a* shows the temperature dependence of the inner sides of honeycombed structure which serves as frame, i.e. the temperature distribution on its planes.

The graph is divided into 3 parts, which correspond to three different simulation cycles of NS turnover in its orbit. Also, the graph shows the temperature of TVC-0.2 cryoscreens, i.e. the temperature of the surrounding space of the NS. It can be seen that the maximum temperature corresponds to the temperature of the parts and Z+ and Y+ in the beginning of the cycle, as solar radiation falls on these faces at a small angle relative to the normal line. At the same time the coldest face of X+, as in the process of rotation NS Sun's rays almost do not fall on it. It can be stated repeatability of values from cycle to cycle, what is a necessary condition for thermal vacuum tests. Temperature limits varies (–55...+20 °C), which corresponds to the capabilities of the normal operation of the NS, as well as correlate with previously conducted mathematical modeling.

Fig. 2, *b* is a graph showing changes in temperature values on the control board of the payload, on the radio board and the CPU board. As can be seen from the chart, board temperature does not significantly dependent on external factors and changed slightly from the Sun to the shadow mode (2...3°). The maximum temperature is presented on radio board (+3...–10°), then the CPU board (–5...–20°) and the control board of payload (–10...–23°). Based on the data it can be stated that the electronic system of NS is within acceptable temperature limits. Also worth noting the practical independence of temperature between the NS of orbital position, and fluctuations in the radio card, which can be observed in the course of the experiment – those are the results of the performance of this NS element. As a result, thermal vacuum tests:

- studied the temperature distribution on the modules, assemblies and construction elements of the NS, electronic board surfaces, depending on the external radiant heat fluxes corresponding to movement of NS by the proposed orbit;
- revealed the limits of temperature fluctuations of the NS elements caused by modeling of changes in its orbital position;
- confirmed the performance of the NS equipment under conditions consistent with the orbital.

According to test results, it can be concluded that the engineering model of the NS sustains thermal loads and can operate in space in normal mode.

Strength and dynamic analysis. "PolyITAN-2-SAU" is made according to the non-hermetic scheme in the CubeSat satellite bus. One of the most important stages in the design and ground testing is the task of ensuring the strength of the NS at various stages of its life cycle, including a comprehensive calculation and experimental analysis of the dynamics and strength of the NS.

The main and most responsible from the point of view of the mechanical loads acting on the NN is the stage of launching into orbit. At this stage, the NS experiences maximum quasistatic overloads, harmonic and random vibrations, impulse and acoustic effects. At the launch stage, NS is located in the launch container ISIS-POD. The NS lower end faces are

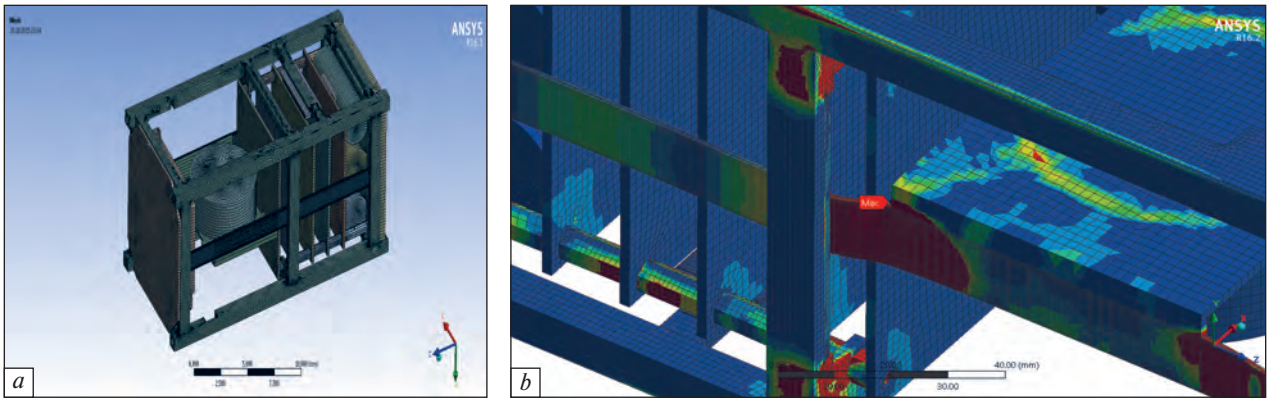

Fig. 3. "PolyITAN-2-SAU" Finite Element Model (*a*) and distribution of stresses in the bridge of the support frame in the section of fastening of the SOS bracket for the X-axis overload option (*b*)

Fig. 4. General view of the stand with a satellite

supported by a spring pusher, the upper ones on the cover of the launch container.

The dynamic and strength cycle of work implies:

- Static analysis;
- Modal analysis;
- Harmonic and random vibration analysis.

According to the requirements of QB50 and ECSS-E-HB-32-26A, for nanosatellite there is no need to check the strength of acoustic and impulse actions due to small overall dimensions of the NS and the conditions for placing the ISIS-POD on the carrier rocket adapter.

The finite-element model (FEM) of the NS generated in the ANSYS and shown in Fig.3, *a*. For approximation of the framework, scientific module (FIPEX), stacking racks of the EP, batteries and antenna module we used 20 hexagonal finite elements (FE) SOLID186. To approximate the SOS brackets and electronic circuit boards we used FE SHELL181 with 4 layers in thickness. The articulation of plate and volumetric FE was carried out by means of massless absolutely rigid bonds based on two-node beam elements BEAM188. Conjugating fragments of FEM with different partition densities, contact elements of CONTA174 were used with the same type of FE. The obtained rational FEM NS, consisting of 326,300 elements with 1,221,504 nodes (Fig. 3, *a*), was used for static, modal, harmonic and random vibration analysis.

In quasi-static analysis, the conditions for placing the NS in the shipping container were taken into account by setting zero displacements ($u_x = u_y = u_z$) of the frame supporting surfaces, with the exception of longitudinal ($u_z \neq 0$) for the side ribs (Fig. 3, *b*). It was found that the largest Mises stresses occur in the frame bridge (material – D16) near the attachment points to the SOS brackets (Fig. 3, *b*). In turn, in the stacking rack of the EP (material – L63), the stress is realized during overload in the vicinity of the contacts with the central board. Among the electronic circuit boards of the EP, the lower one is the most loaded, for which in case of an overload at the points of contact with the stacking racks.

The strength of NS is determined from the following conditions:

a) The absence of plastic deformation under the action of limit loads;

b) The absence of destruction in the structural elements of the NS under the action of design loads.

As a result, it was established that the maximum total von Mises stresses (179.06 MPa) occur in the frame bridge near the mounting locations of the SOS brackets when the NS is loaded in the direction of the X axis. In this case, the factor of safety for the limit η_L = 1.12 and ultimate loads η_U = 1.30. For the developed design of the NA PolyItan-2-SAU, a rational combined ECM is constructed, containing volumetric,

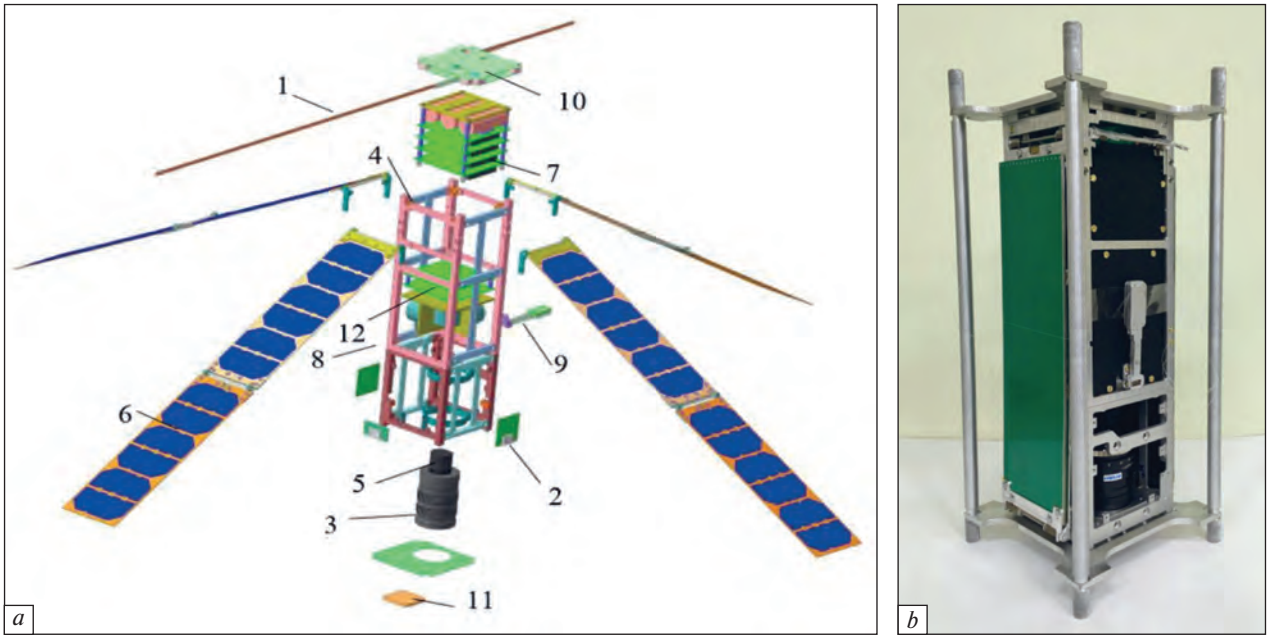

Fig. 5. "PolyITAN-3" engineering model (*a*): 1 – antenna 144/435 MHz, 2 – solar sensor, 3 – camera lens, 4 – frame, 5 – camera, 6 – solar panels, 7 – electronic platform, 8 – flywheel, 9 – magnetometer, 10 – antenna module, 11 – high-speed antenna, 12 – electromagnet board; and real photo (b)

shell, beam and contact EC. Calculated way, amplitude-frequency characteristics and parameters of VAT in PolyItan-2-SAU structural elements are determined on the basis of a single CEM under the action of quasi-static overloads, harmonic and random vibrations corresponding to the elimination stage. It is established that, in accordance with the requirements, the considered PolyItan-2-SAU design is rational in terms of strength.

Studies on the functionality of the system of orientation and navigation in the development of "PolyITAN-2-SAU". The role of the orientation system is extremely important for the success of any mission, so calibration and testing are performed on specialized simulator stands. The stand creates a magnetic field that corresponds to a certain mode of flight, and the onboard system of the nanosatellite determines its position and/or the characteristics of rotation and performs the rotation of the nanosatellite at a given angle or stops the conditional rotation.

The stand creates a magnetic field of a given value of magnetic induction, direction and the in the required volume, where the nanosatellite will be located. After comparing the layout options of the stands, a scheme was chosen using three pairs of square Helmholtz coils with a size of 1.5 by 1.5 meters.

Electrical part of the stand consists of:

1) coil drivers, which are H-bridges and with the help of pulse-width modulation can smoothly change the current and, as a result, the magnitude of the magnetic field;

2) magnetometer used for feedback;

3) Circuit board with STM32F103 microcontroller, which provides control of drivers according to feedback signals;

4) UART to WIFI / Ethernet adapter, which allows you to connect the stand to a computer network and control it remotely.

General view of the stand is provided on the Fig. 4. The stand is controlled completely remotely; feedback is provided by a magnetometer connected through Arduino. The control system allows to use any program of changing the magnetic field as input and to receive an instant response from the magnetometer.

Depending on the resulting accuracy it will be possible to also begin tests of system of orientation and stabilization of the PolyITAN-3 nanosatellite in the laboratories of the National Technical University of Ukraine "Igor Sikorsky Kyiv Polytechnic Institute".

Future projects of PolyITAN series

The mission of the project "PolyITAN-3" (for Earth sensing) is creation of 3U CubeSat nanosatellite by developing, modeling and researching effective service subsystems to provide a payload – an optoelectronic scanner with a capability of shooting in the range of up to 30 m when operating in orbit at altitudes up to 700 km.

"PolyITAN-3" (Fig. 5) is 3U CubeSat satellite with camera for remote sensing. This feature is associated with new challenges in the thermal control system and the power supply of the satellite. Solar panels have the form of 4 wings, each wing consists of two modules

of six elements. The modules are connected in the wing by the mechanism of opening and connected in series. In addition, a high-speed radio link module is used. It has the following properties: 5.7 GHz 800 kB, 2 W; and will be used for transfer of images to the earth station.

All previous work has been carried out, such as selection and development of equipment, electric and thermal calculations, etc. A thermal model of the nanosatellite was created, and a numerical calculation was also carried out in the ESATAN-TMS program. Now the satellite is being assembled and scheduled to produce thermal-vacuum test.

The feature of the "PolyITAN-4-PLANT" mission. Plants are an indispensable component of bioregenerative life support systems for long-term space missions (long-haul flights and extraterrestrial bases), as the plants act as oxygen and water regenerators, a source of food and utilization of vital products. Summarizing the numerous biological experiments conducted on different spacecraft, we can conclude that microgravity is not a factor that limits the growth, development and reproduction of plants. An important condition for the successful cultivation of plants in space is the use of elite seeds and maintaining certain conditions for plants cultivation. It is impossible to predict the stability of plants in life support systems to space flight conditions over long flights, since almost all plant objects grown on space platforms are annual plants with a short life cycle (up to 6 months), and the duration of most experiments on board The International Space System (ISS) did not exceed 30 days. It is advisable to conduct long experiments with plants in simplified, compared with those used on the ISS, growth chambers, in order to establish a record for the duration of stay of higher plants in the active physiological state in space flight (up to 3 years). Such an experiment can be carried out on the platform of a small satellite CubeSat, using the technology created and successfully tested in space conditions created by National Technical University of Ukraine "Igor Sikorsky Kyiv Polytechnic Institute" and microcosm technology – growing plants in a closed gas environment, which was developed in M.M. Gryshko National Botanical Garden of NAS of Ukraine. In a unique experiment at this institution, the plants show the ability to grow in a closed gas environment for a long time (currently the duration of the experiment is 12 years).

Carrying out the experiment and promoting it in the media has a powerful image component and will promote the promotion of cosmonautics and the attraction of young people to pre-scientific space exploration.

The technology of the developed unit for long-term cultivation of plants in microgravity can be applied for the implementation of space experiments in the future, as well as being a tested basis for the creation of new cultivation chambers for growing plants aboard spacecraft. With plant life support system (temperature and lighting) from on-board telemetry and model experiments on plant growing is created in a stationary unit under stationary conditions with observation of the condition of plants growing in a stationary unit. Creating such a system will allow for various biological experiments on the CubeSat platform.

The proposed space experiment is unparalleled and will be the first attempt at long-term exposure of several species of plants in space flight in a power unit. Information on the resilience of such an artificial ecosystem to the long-term impact of microgravity is a prerequisite for the creation of bioregenerative life support systems and the implementation of their long-term space missions.

The feature of the "PolyITAN-4-PLANT" mission is current impossibility to give a positive forecast for the stability of higher plants in the conditions of space flight during long flights; since almost all vegetable objects that have been grown on space platforms are annual plants with a short life cycle, and the duration of most of the experiments aboard the ISS did not exceed 30 days. Plants are considered as a source of food and oxygen in bioregenerative life support systems of long space missions. The satellite design includes a hermoblock with a system for maintaining the viability of plants: fibrous substrate, grating for a substrate, NIR-camera for shooting (observing the state of plants), fan with protection, LED lighting, a system for monitoring the environment inside (Fig. 6).

Hermetically sealed block potentials an technical data

- Led light with regulation of brightness and emission band; Top-light with intensity 300 W/m^2 (white 225 W/m^2, red 75 W/m^2). Light period is equal to Earth light period (16 hours day and 8 hours night).
- Opaque coating provides isolation from sunlight.
- Supporting of the predetermined temperature 18±10 °C.
- Humidity sensors, 4 humidity probes during the day.
- CO_2 quantity control (2 probes per minute).
- Fan with guard group for gases convection providing inside the block.
- Camera with possibility of monitoring in IR spectrum, taking of pictures from one and more pictures per day.
- Block dimensions are less than 80 × 80 × 160 mm, it weights less than 2 kg.

Expected results: selection the optimal plant composition with the best growth characteristics and

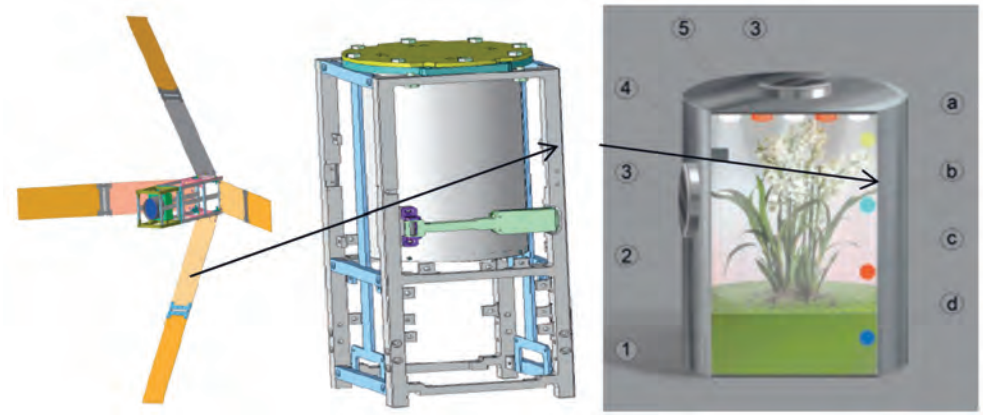

a *b* *c*

Fig. 6. General view *"PolyITAN-4-PLANT"* (*a*); Placing of hermoblock in the case of *"PolyITAN-4-PLANT"* (*b*); hermoblock composition (*c*) include plant's life support systems:1 – fibrous substrate, 2 – holding mesh for the substrate, 3 – NIR-camera (to monitor the state of the plant) 4 – fan with protection, 5 – LED light; and the environmental monitoring system inside the unit: *a* – light sensor, b – CO_2 sensor, *c* – temperature sensor, *d* – substrate humidity sensor

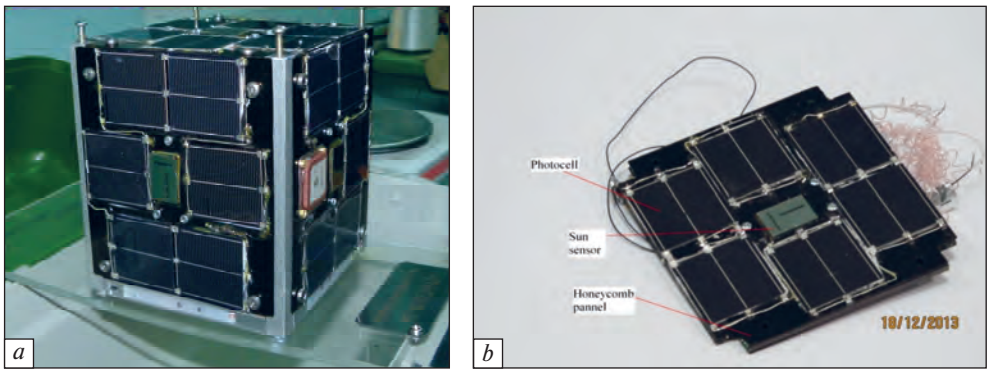

a *b*

Fig. 7. General view of the university nanosatellite "PolyITAN-1" (*a*) endSolar battery on honeycomb carbon fiber frame and the coordinates of the Sun Sensor (*b*)

the value of the minimum-sufficient level of water with the mineral component for plant nutrition.

Operation in orbit of nanosatellite "PolyITAN-1" models

Objectives of KPI "PolyITAN-1" nanosatellite launch: the development and research of solar sensors for small satellites; check of the power circuitry between the solar panels and batteries, developed at the University; improvement and adaptation of digital radio information and control commands transmission to the space environment; exploration of space influence to the operation of electronic subsystems; study the functioning of the navigation subsystem of global signal receiver GPS / GLONASS.

Nanosatellite was launched into orbit 19.06.2014 with the carrier rocket "Dnepr" as a part of the cluster starts. Beacon EM0UKRI of "PolyITAN-1" satellite has been heard in the early hours after the launch at the telemetry control and collection center of the university NTUU KPI, it also was recorded by radio amateurs of Japan, Germany, Britain and others. Today, nanosatellite is operating in low-Earth Sun-synchronous orbit at a distance about 620 km from the Earth, duration of its circulation is 97.8 minutes. At every 5th out of 16 daily turns around the Earth in a short time (2–9 minutes) it is possible to communicate with the spacecraft from the ground station established in KPI. During these moments developers get information about the functioning of the nanosatellite subsystems, required for future work.

"PolyITAN-1" is a typical single block CubeSat 1U format Nanosatellite. It is a cubic frame carcass, which houses electronic circuits (Fig. 7, *a*). The side faces of the cube are ultra-light multilayer honeycomb panels frames of carbon fiber and aluminum honeycomb, the so-called "sandwich panels" (Fig. 7, *b*).

The university nanosatellite "PolyITAN-1" version of the radio and control subsystem includes two radio link: a radio link "up" (ground control and receive station – satellite ("uplink")), which is used to transfer command information; and a radio link "down"

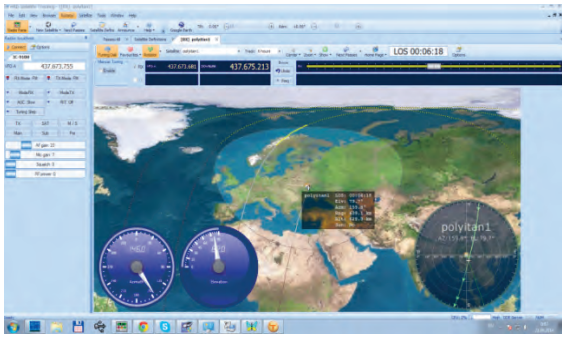

a

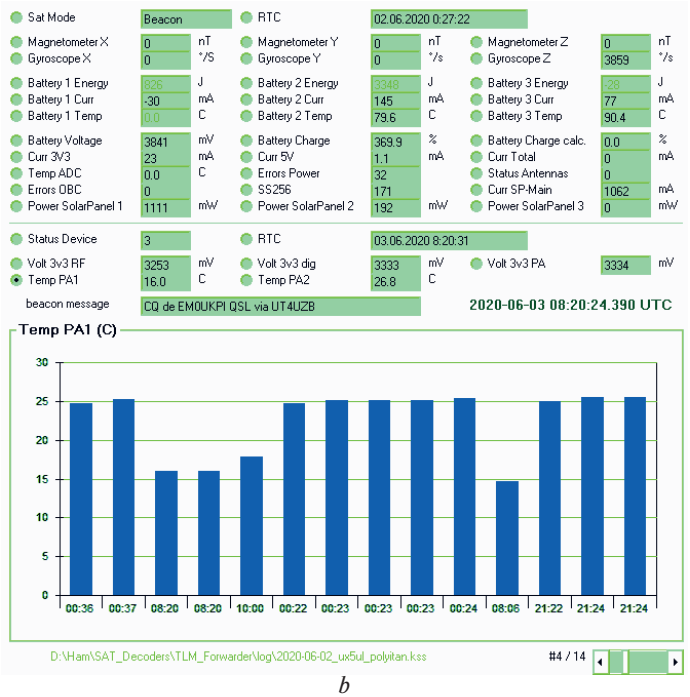

b

Fig. 8. The ground control station of nanosatellite specialized program view (*a*) during a radio communication session and (*b*) telemetry from the PolyITAN-1 satellite on 03.06.2020 (the radio module temperature)

(satellite – ground control and receive station ("downlink")), used for the transmission of telemetry and other information.

The composition of ground segment of nanosatellite control (Fig. 8) including: radio transmitter (RT) of command information, radio receiver (RR) for receiving information from the on-board systems, radio modem for the primary message processing, separate antenna systems of RT and RR, antennas tracking guidance and display control system, personal computer, tachometer with software for RT and RR control, software for antennas tracking guidance and display control system. The composition of the board includes radio transmission device for transmitting information from the on-board systems, radio receiver for command information, radio modem for primary messages processing, separate antenna systems of RT and RR.

Where as it is necessary to provide at the frequency 437 MHz the reception of data from the ground station, and their transfer to it, it was considered possible variants of transceivers, minimizing weight and size.

The PolyITAN-1 nanosatellite is active in the Earth's orbit at a height of 602...607 km to the present time (https://www.n2yo.com/?s=40042). Telemetry from the PolyITAN-1 satellite as of 03.06.2020 (the radio module temperature) is shown in Fig. 8, *b*.

Summary and conclusions

Aerospace technology and manufacturing techniques were used in the design and manufacturing of nanosatellites series "PolyITAN". Architecture of "PolyITAN" nanosatellite allowed to avoid problems that occur with a reduction in scale structures of satellite systems for their use in small and nanosatellites. This was made possible thanks to realization of the key differences between large satellites and satellites CubeSat, the development of new sub-systems and systems specially designed for use in CubeSat format nanosatellites.

"PolyITAN" nanosatellites provides high-performance electronic platform for testing new materials in space, carrying out scientific experiments and testing of technologies.

Benefits of "PolyITAN" Platform:

- High precision positioning using GPS + GLONASS (Galileo optional).
- The cost of mass production is lower by 40–60 % than in the US and European counterparts.
- The presence of a complete set of satellite system at University (satellite into orbit and ground station).
- Start services, support and maintenance.
- The possibility of supply of separate components and subsystems.
- Scalable platform in accordance with the Cubesat standard.
- Using for a wide range of applications (radio communication, Earth sensing, scientific experiments, etc.).
- Use of carbon fiber honeycombs for heat control and radiation protection.
- The full nanosatellite development cycle.

Analysis of the functional characteristics of "PolyITAN-1" subsystems and test of the impact of external damaging factors are still going on in the orbit. However, all tests up to this day have been successful and the results are compared with the design.

Acknowledgements

This work was supported by participants and sponsors of the project "PolyITAN-2-SAU": Academician Mikhalevich Foundation, Kalinin Foundation (Ukraine), Boeing-Ukraine Ltd.

REFERENCES

1. Rassamakin B.M., Baiskov N.F., Ostapchuk S.V., Khairnasov S.M., Menzhega A.S., Rassamakin A.B., Pershin N.A., Smakovsky D.S. Development and research of subsystems of the nanosatellite NTUU "KPI" "PolyITAN-1" with carbon fiber honeycomb panels. *Abstr. the 12th Ukr. Conference on Space Research,* Eupatoriya, September 3–7, 2012. Kyiv, 2013. P. 109 (*in Russian*).

2. Laush A.G., Rassamakin B.M., Baiskov N.F., Ostapchuk S V. Testing of orbital flight parameters of nanosatellite using GNSS simulator. *Abstr. the 13th Ukr. Conference on Space Research,* Eupatoriya, October 2–6, 2013. Kyiv, 2013. P. 127 (*in Russian*).

3. Rassamakin B M., Baiskov N.F., Ostapchuk S.V., Khairnasov S.M., Budenny A.V., Rassamakin A.B., Menzhega A.S., Pershin N.A., Antipenko R.V., Kovalenko E.Y., Smakovsky D.S., Martynyuk S.E., Khominich V.I. University nanosatellite PolyITAN-1. *Abstr. the 14th Ukr. Conference on Space Research,* Uzhgorod, September 8–11, 2014. Kyiv, 2014. (*in Russian*).

4. Rassamakin B. The First Ukrainian Nanosatellite – PolyItan-1: Development, Simulation, Flight Tests. *Abstr. the 5-th International Space Conference SEMW*. October 21—23, 2014. P. 26 (*in Russian*).

5. Rassamakin B.M., Baiskov N.F., Ostapchuk S.V., Khairnasov S.M., Rassamakin A.B., Menzhega A.S., Pershin N.A., Antipenko R.V., Kovalenko E.Y., Smakovsky D.S., Martynyuk S.E., Khominich V.I., Dusheiko M.G. University nanosatellite POLITAN-1: Flight test results. *Abstr. the 15th Ukr. Conference on Space Research,* Odesa, August 24–28, 2015. Kyiv, 2015. P. 117 (*in Russian*).

6. Kovalenko E.Yu., Rassamakin B.M., Baiskov N.F. Electrical power system of POLYTAN series CUBESAT nanosats. 7th European CubeSat Symposium, 9–11 September, 2015, Liège, Belgium. P. 29.

7. Rassamakin B.M., Baiskov N.F., Ostapchuk S.V., Pinchuk A.V., Kovalenko E.Y., Lanevsky E.V., Khairnasov S.M., Rassamakin A.B., Khominich V.I., Bendasyuk N.M. Engineering model of the POLYITAN-2-SAU nanosatellite for studying the atmosphere at altitudes of 380-90 km. *Abstr. the 15th Ukr. Conference on Space Research,* Odesa, August 24–28, 2015. Kyiv, 2015. P. 118 (*in Russian*).

8. Rassamakin B.M., Rogachev V.A., Khairnasov S.M., Zavadskaja E.S, Khominich V.I. Experimental modeling of thermal modes of nanosatellites. *Technology and design in electronic equipment*. 2013. No. 4. P. 27–30 (*in Russian*).

ROCKET SOUNDING SYSTEM FOR LOWER IONOSPHERE RESEARCH

S. Larkov[1], V. Prisiagnii[1], G. Lizunov[2], K. Volokh[1], S. Moskalenko[1], O. Piskun[1], O. Piankova[2], S. Pipko[3]

[1] National Space Facilities Control and Test Center
[2] Space Research Institute of NAS of Ukraine and SSA of Ukraine
[3] National Aviation University

Processes in the ionosphere provide a wide range of research fields, addressing questions from technology applications (such as satellite communication, navigation systems, space weather effects on space and ground assets) to fundamental physics (space particles energization, wave – particle interaction, non-linear processes and turbulence, etc.). Multiscale complex plasma environment of the Earth is the accessible "laboratory" where processes of astrophysical importance can be studied *in situ*.

Physics of the ionosphere is one of priorities of the Ukrainian scientific school. The availability of various scientific instruments (ionosondes, incoherent scatter radar, and system for scanning the ionosphere with signals from navigation satellites) and research teams developing methods for processing and interpreting measurement data is a significant contribution of Ukrainian science to the World fund of knowledge.

Traditional methods for studying the ionosphere are remote radio-physical methods providing tracking of the most important ionosphere parameter – the electron density distribution. However, the data obtained in this way are insufficient for understanding the inner meaning of the ionosphere's behavior, especially for the purpose of modeling and forecasting the space weather. In fact, it is required to provide the measurement of complete set of gas and plasma parameters (temperature and concentration of neutral and charged particles, chemical and ionic compound, concentration and type of impurities, mainly metallic, etc.) and electrodynamic parameters (in wide frequency range – from quasi-static to high frequencies), that can only be achieved with *in situ* measurements. Thus, the relevance of the development of contact techniques for studying the ionosphere is undoubtedly.

In terms of the physics of the ionosphere, its lower layers (*D* and *E*) stand somewhat apart, both in terms of accessibility (for spacecraft – too low, for classical atmosphere sounding with balloons – too high) and in terms of the set of control processes. Along with photoionization and recombination, an important role is played by chemical reactions, the interaction of the charged and neutral plasma species, which complicates the study on laboratory models and, thus, direct measurements are the most adequate way to obtain required data.

The study of the ionosphere in all its variety is constrained by the extremely large scatter of the spatial and temporal scales of the ionospheric disturbances (from fractions of millimeters to thousands of kilometers and from microseconds to tens of years). Moreover, "one-point" measurements (both terrestrial and space) do not provide any integral reflection of actual ionospheric state. Also noteworthy is the relative scarcity of data: spacecraft carry out measurements in a limited altitude layer, ionosondes give a vertical distribution at one geographical point, and only the study of radio wave propagation provides coverage of large spatial zones, but only for one plasma parameter (total electron content). In this sense, the combination of various measuring techniques in order to obtain "slices" of the ionosphere within a single space-time window (geophysical rocket + flying spacecraft + + ionosonde + navigation and meteorological network) seems to be very expedient.

Progress in microelectronics and computing technology has created the prerequisites for a sharp decrease in the mass and power consumption of ionospheric probe payload. We assume that the mass of necessary equipment will be up to 2 kg at a cost comparable with the cost of the meteorological balloon equipment. Such payload can be delivered to an altitude of 120–150 km using a tiny solid-propellant geophysical rocket with a launch mass of about 50 kg and, accordingly, at a cost level one to two orders of magnitude lower than the cost of launching "conventional"

geophysical rockets. It is opens up opportunities for conducting regular sounding of the ionosphere similar to balloon sounding of the troposphere and stratosphere for meteorological weather predictions. Obtained data can become the basis for the refinement of ionosphere models (both semi-empirical models and, in the future, complete electrodynamic models). As a further development of the system, we can propose its use in obtaining the initial conditions for a complete numerical simulation of the ionosphere. Such a theoretical model, taking boundary conditions from atmospheric weather models and solar activity models, promises to provide proper forecast of space weather, similar to the weather forecast today.

Special Department of the National Space Facilities Control and Test Center – the Main Center for Special Control, monitors the state of the Earth's geophysical shells, including the ionosphere. The next step in the Department development was the deployment of the Center for Forecasting the Space Weather. In 2020 National Space Facilities Control and Test Center together with the Space Research Institute carried out research "Scientific and technical substantiation of the creation of lower ionosphere rocket sounding system", which main purpose was to justify the list of measured parameters, measurement techniques and requirements for scientific payload. During the research, the following tasks were solved:

• promising spheres of ionospheric research have been identified, tasks and objectives of experiment have been formulated;

• a list of measured parameters was determined and technical requirements for sensors were formulated;

• the types of sensors, secondary converters were selected, the requirements for the telemetry system were estimated;

• the composition and weight and size characteristics of a set of scientific equipment were determined;

• the requirements for the rocket sensing system as a whole have been formed in the form of the Terms of Reference for R&D.

The following tasks were identified as priority:

• study of the structure of D and E layers – parameters of the charged and neutral particles plus the level of Solar radiation (mass spectrometer, Langmuir probe, UV spectrometer, Pitot tube with ionization manometer);

• study of the electrodynamics' structure of the D-, E- and F1- regions – electron concentration and DC magnetic field (mass spectrometer, Langmuir probe, fluxgate magnetometer);

• study of the conditions of wave propagation in the low frequency range – concentration of charged particles (ions and electrons) plus waveforms of magnetic and electric fields (mass spectrometer, Langmuir probe, electric field sensors, fluxgate and search-coil magnetometer).

Model composition of the proposed instrumentation is described in Table. Specifically, full set of scientific equipment must include six instruments partially designed and manufactured in Ukraine. Lviv Center of Institute for Space Research has developed miniaturized versions of fluxgate and search-coil magnetometers, as well as electric field sensors. The sensors are made in the CubeSat form-factor and are successfully used in international projects under the ESA and NASA programs. Langmuir probe developed by Institute of Technical Mechanics of NAS of Ukraine and SSA of Ukraine can be used practically unchanged with newly developed electronics unit.

The fanciest instruments (mass spectrometer and UV spectrometer) are to be developed. As analogs, it is possible to consider:

Table

Model composition of the payload

Unit	Parameters to measure	Brief data
	Electromagnetic measurement set	
Search-coil magnetometer	3 components of magnetic field 0–40 Hz	Sensor: 30 × 30 × 30 mm /40 g Electronic unit: 50g / 0.4 W
Fluxgate magnetometer	3 components of magnetic field 40–10 000 Hz	20 × 20 × 20 mm / 11g / 0,1 W
Electric probes 2 pcs	1 component of electric field 0–10 000 Hz	Sensor 30 mm / 0.1 W
	Plasma measurement set	
Langmuir probe	Electron temperature and concentration	Sensor 45 mm / 40 g Electronic unit: 350 g / 2.5 W
Mass spectrometer (ion trap)	Temperature, concentration and type of ions	77 × 77 × 58.2mm / 500 g / 0.5 W
	Photonic measurement set	
EUV spectrometer	Energy in 180–4000 Å	Sensor 80 mm. 500 g / 3 W
	Electronic unit with flash memory	
TOTAL	Weight up to 2 kg, power consumption up to 6 W	

• a miniaturized version of the magnetic sector mass analyzer in the CubeSat form factor (Mullard Space Science Laboratory, University College, UK);

• spherical UV spectrometer/plasma analyzer (Fraunhofer Institute, Germany).

The project could be divided in two stages. At the first stage of the project implementation, it is planned to launch a limited set of scientific equipment using the ILR-33 rocket, created at Instytut Łotnictwa (Poland). The set of scientific equipment includes instruments that are already available in the form of prototypes, preproduction or production samples (magnetic and electric field sensors, Langmuir probe, ionization manometer). The head fairing of the launch vehicle should be dropped at an altitude of about 45...50 km with simultaneous opening of the rods with magnetometers and electric field sensors placed on them. The transmission of scientific information is supposed to be carried out using a telemetric radio link built in the CubeSat form factor.

At the second stage of the project development, it is planned to create a full system for sounding the ionosphere, consisting of:

• solid-propellant rocket with a rescue system;

• mobile launcher;

• stations for receiving telemetry information;

• data processing/storage center.

In 2020, as a part of student project of creating a suborbital rocket, the National Aviation University (Kyiv) developed a small-sized reusable solid-propellant rocket motor. A prototype of a modular propellant grain pellet was made and tested from a composite propellant based on ammonium perchlorate/polybutadiene with the addition of aluminum fuel, which was tested in the bench version of a micro-solid propellant motor. The results obtained (specific impulse at the level of 205–210 s) open up opportunities for the creation in Ukraine of a rocket sounding system of the ionosphere, the key features of which will be:

• tiny reusable sounding rocket;

• set of scientific equipment;

• operation together with radio-physical remote sensing means.

COMPUTER VISION SYSTEM FOR SPACECRAFT RELATIVE POSE DETERMINATION DURING RENDEZVOUS AND DOCKING

V. Gubarev[1], V. Vasylyev[2], V. Volosov[1], L. Maksymyuk[1], S. Melnychuk[1], N. Salnikov[1], V. Shevchenko[1], L. Godunok[3], S. Derkach[3]

[1] Space Research Institute of NAS of Ukraine and SSA of Ukraine
[2] Private Joint Stock Company "ELMIZ"
[3] Private Joint Stock Company "Research and Production Complex "KURS"

Development a reliable and efficient vision-based method for relative pose estimation of non-cooperative spacecraft (NCS) during rendezvous and docking is an urgent problem. The main difficulties consist in meeting strict requirements for performance and accuracy of determining the relative position of spacecraft in unfavorable lighting conditions and limited computing resources.

Here we present some general issues of developing an on-board computer vision system (CVS) designed to measure the relative pose of a target NCS in real time. Aspects of creation mathematical and algorithmic ground, software development and bench testing are considered.

The overall work plan included architecture development, mutual approach dynamics model selection, development of solid body pose estimation methods, image processing and recognition methods, modelling orbital dynamics and ellipsoidal filtration, usage of computer graphics and graph theory, and other issues, details of which are not described in this article.

Purpose of the computer vision system

CVS is designed for mounting on the spacecraft, which is called service or active, in contrast to NCS, which is passive and can't be controlled. The aim of CVS is to determine the relative position and attitude of two spacecraft by a video on the final stages of rendezvous. The proposed CVS operates in visible spectrum which provides sufficiently high resolution images to solve the pose estimation problem with required accuracy. The input data for CVS [1–4] includes a three-dimensional graphic model of target NCS and current images of NCS captured by an active camera.

The CVS consists of a sensor subsystem represented by two calibrated cameras with different focus length, a computing unit, and a lighting subsystem (Fig. 1).

In the proposed CVS scheme cameras are rigidly fixed relative to carrier spacecraft in known position and its lenses have fixed focal length due to the requirement not to use moving parts. The choice of a dual-camera scheme is justified by the need to obtain high quality images over a wide range of distances. The resulting images are processed in the Computing unit to calculate the parameters of the spacecraft relative position using 3D model of NCS from Database. In case of need for additional lighting the use of Backlight system is provided.

Camera parameters determination

In view of the above, when choosing the cameras optical scheme, the following requirements were additionally set, namely: focal length and view angle of the camera are unchanged; at long distances the NCS image should occupy the largest possible area on the picture; at the nearest distances the docking or connecting surface must extend the camera vision field as small as possible.

One camera with a fixed angle of view cannot cover the entire specified range of distances. That's why two cameras are used. Each one provides an image acquisition on its own range: far mode camera with narrow field of view and near mode camera with a wider field of view. Using the formula for determining the boundaries of sharply depicted space the following camera parameters were determined: focal length, view angle, aperture, number of pixels and the matrix size. It will ensure the implementation of the CVS technical requirements. Also the analysis of the image sensitivity to the change in relative position and attitude of the NCS have been kept.

Mathematical and algorithmic support

The CVS operation cycle consists of several phases. The first is pre-flight camera calibration. The second is the target NCS data initialization when all necessary information on the chosen NCS is prepared and then

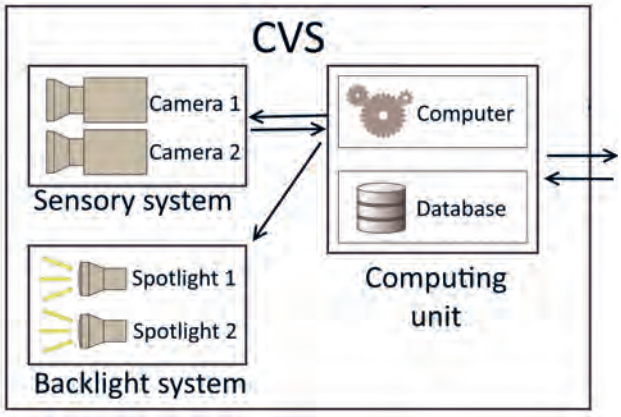

Fig. 1. CVS structure

loaded in CVS memory. Next CVS switches to sleep mode. The third phase is an active work at the latest stage of approaching to NCS. It starts with the inclusion of the CVS by the external input signal. CVS should turn on and run continuously when approaching the target NCS in the distance range of 1.5–30 m from the NCS surface.

The informative data extraction from the captured image is performed by a sequence of stages, which differs by complexity of the analyzed data and the size scale: from the whole image to fragments.

We will identify 3 possible cases, which determine available data and the approach used. The first one corresponds to a situation when the whole NCS is in the field of view. The second corresponds to a situation when the docking surface of NCS occupies almost the entire image. The third case occurs when the image is completely formed by a part of docking surface of NCS.

These three cases correspond to the stages of rapprochement. Each of them determines classes of informative features, which are possible to obtain from captured images. These features are recognized and positioned, making up sets of input data for pose estimation problem. At large distances to the NCS, its observed angular size are too small. Therefore, here the external contour of the object is used, visible mostly or completely. At medium distances, large details of the structure become visible, which give additional information. Since this, the solution is reduced to the recognition of individual elements and their use as reference objects. At close range, the number of recognizable objects increases.

Implementation of approach used requires solving a number of common and particular problems. Common problems are:

1) Management of operating modes, consisting in the selection of the most meaningful, reliable and accurate set of available source data.

2) A method for pose estimation by an outer contour of NCS using a database with pre-calculated contours.

3) A method for pose estimation by reference points with outliers in the source data.

Particular problems include methods for finding, recognizing and positioning various classes of reference elements, frame-by-frame tracking and others. Specific problems are determined by the classes of reference objects used: contours, lines, circles, spots, angles, singular points, etc.

Software implementation is represented by the set of specialized modules that interact through certain application programming interfaces. It includes:

- The control program which performs monitoring and control of all units. It also provides an external programming interface of CVS which is used by a spacecraft control system.
- The driver program that performs a physical exchange of information through external programming interface of CVS. It provides downloading into the CVS memory the NCS data, output captured video data, and exchange of service data and signals.
- The program which performs capturing and primary processing images from cameras.
- The preprocessing engine that performs extraction an informative data from 3D models.
- The library for detecting, recognizing and positioning features on image.
- The service programs for internal data management providing storage and deployment.
- The program of relative pose (rotation matrix and position vector) estimation using database of the NCS image features and special calculation algorithm.
- The program which estimates relative angular velocity and relative velocity between the active spacecraft and the NCS using kinematical and dynamical model of the NCS.
- The program that calculates predicted areas of disposition of the feature point at the frame which will be obtained at the next time step.

Spacecraft motion parameters estimation

The NCS dynamic model and ellipsoidal estimation algorithm are used to define the approaching velocity and the NCS angular velocity, which are necessary for rendezvous and docking with the NCS. The dynamics of orbital motion and rotation around center of mass can be considered separately. When docking the estimation accuracy of rotation parameters is more important, so using of estimation algorithm of rotational motion parameters is considered. One of the modifications [5, 6] of ellipsoidal estimation algorithms [7, 8] is chosen for this purpose in this work. The main advantages of the used modification are high convergence speed, ease of realization, applicability to nonlinear systems and robustness to possible violations of a priori hypotheses about the properties of uncertain variables.

The dynamics equations of the NCS rotational motion in the body frame rigidly fixed to the NCS are used. The numerical simulation results showed the viability and effectiveness of the ellipsoidal filter [4] use in solving the problem of parameter estimation of relative rotational movement of two spacecrafts, when the angular coordinates sensor is the CVS. The quaternion of the NCS attitude relative to inertial coordinate system and the NCS angular velocity vector are restored by ellipsoidal estimation algorithm. These parameters are required for docking and their estimation accuracy is significantly increased in comparison with the CVS direct measurements.

The filtration problem was solved using some simplifications, which does not significantly affect the research results. In particular, one of these simplifications was the assumption that the camera is installed in the center of mass of the active spacecraft, which is not true. Accounting the real situation complicates the transformation formulas in the part of the equations associated with the measurements to some extend but it is not an obstacle to the implementation of the proposed algorithms. The small force moments constantly acting on the NCS were not taken into account too. All these and other insignificant details necessarily require careful attention in the proposed algorithms implementation when used in real devices and prototypes. It is this direction that the authors intend to develop further.

It should be stressed on exceptionally important application of the proposed algorithms. According to the authors, these algorithms are indispensable in the automatic docking of a spacecraft and the NCS, which are in the rotational motion. Only knowledge of high-accuracy values of orientation parameters and angular speed will allow to calculate and to perform a maneuver of approaching and docking to tumbling NCS.

Mathematical modeling of spacecraft docking

The mathematical modeling of spacecraft relative motion and control at rendezvous process is performed. For simplicity sake, perturbations of Earth's gravity field caused by its oblateness, and also other disturbing factors of higher order of smallness were neglected. The movement parameters of active and passive spacecraft are marked by indexes *a* and *p*, respectively. Differential equations of spacecraft motion relative to the basic inertial coordinate system is expressed as

$$\frac{d^2r_p}{dt^2} + \mu\frac{r_p}{\|r_p\|^3} = 0,\ \frac{d^2r_a}{dt^2} + \mu\frac{r_a}{\|r_a\|^3} = a_a,$$

where r_p and r_a are current position radius-vectors of passive and active spacecraft in the inertial coordinate system, respectively, $\|r_p\|$ and $\|r_a\|$ are lengths (Euclidean norms) of the vectors (the distance from the spacecraft to the Earth's center),

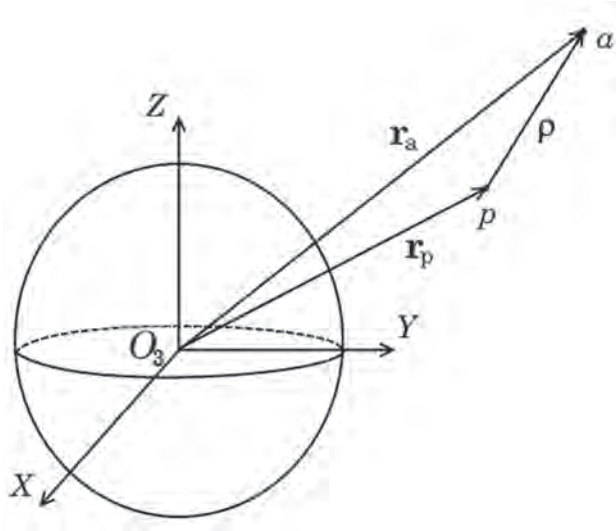

Fig. 2. Satellites configuration in inertial space

a_a – the active spacecraft control acceleration, m = 398 600,4 km^3/sec^2 is the Earth's gravitational constant. The relative position $\rho = r_a - r_p$ is defined, as shown in Fig. 2 (vector ρ is a line of vision), point O_3 – Earth's gravitational center.

Relative motion equations of these two spacecraft are as follows:

$$\frac{d^2\rho}{dt^2} + \mu\left(\frac{r_a}{\|r_a\|^3} - \frac{r_p}{\|r_p\|^3}\right) = u,\ \rho = r_a - r_p,\ u = a_a.$$

The equations describing the spacecraft motion [9] relatively to the NCS in the inertial coordinate system were obtained by successive mathematical transformations. The active spacecraft rotational motion is described with dynamic Euler equation as:

$$J\dot{\omega} + \breve{\omega}J\omega = M,$$

where $J = J^T > 0$ is a positively definition symmetric matrix of the spacecraft inertia tensor in its body fixed frame; $\omega = (\omega_1, \omega_2, \omega_3)^T$ is a vector of absolute angular velocity of spacecraft given by its projections on coordinate axes of the body frame $O_a x_a y_a z_a$

$$\breve{\omega} = \begin{pmatrix} 0 & -\omega_3 & \omega_2 \\ \omega_3 & 0 & -\omega_1 \\ -\omega_2 & \omega_1 & 0 \end{pmatrix};$$

$M = (M_1, M_2, M_3)^T$ is a control moments vector. The orientation of the active satellite relative to passive spacecraft are described by equation:

$$2\dot{\Lambda} = B(\Lambda)(\omega - S(\Lambda)\omega_*),\ S(\Lambda) = I_3 - 2\lambda_0\breve{\lambda} + 2\breve{\lambda}\breve{\lambda},$$

where $\Lambda^T = (\lambda_0, \lambda^T)$ is a union quaternion, $\lambda^T = (\lambda_1, \lambda_2, \lambda_3)$ is the quaternion vector part, $S(\Lambda)$ is a rotation matrix, $B(\Lambda) = \begin{pmatrix} -\lambda^T \\ \lambda_0 I_3 + \breve{\lambda} \end{pmatrix}$, I_3 is a unit 3 × 3 matrix, ω_* is an angular velocity of passive spacecraft.

The docking problem statement at final stages is formulated as the general synthesis problem of control

accelerations $u = u_c$ and control moments $M = M_c$ for the dynamic Euler equation of the spacecraft motion at conditions that in a given time moment $t = t_E$ the following relations $d(t_E) = \|\rho(t_E)\| = 0$, $\|\dot{\rho}(t_E)\| = 0$, $S(t_E) = I_3$, $\|\omega(t_E)\| = 0$ are hold. These conditions are common for any docking control system with arbitrary measuring equipment. The solution of this control problem can be obtained by solving optimal synthesis problems with some typical criteria in a form of some functions $u_c^* = u_c(Z,t)$, $M_c^* = M_c(Z,t)$ of time t and full state vector $Z = (\rho, \dot{\rho}, \Lambda, \omega)^T$. But in this work it is assumed that the single measuring device of the control system is the CVS only. Therefore, the actual problem is restoration and estimation of other parameters of the state vector. These problems are planned to be considered in future investigations.

The experimental stand description

The CVS experimental stand was used for the on-ground testing of methods and algorithms. The stand was created in special research chamber designed to test equipment for space purposes in the PrJSC "ELMIZ" [10]. The equipment allows precise orientation of a camera at yaw and roll angles and horizontal translation of the NCS model (Fig. 3).

The CVS camera (Fig. 4) is mounted on a rotating plate controlled remotely. The stand provides high precision angular rotation around two perpendicular axes simulating the change of the relative attitude of the CVS and the NCS with yaw and roll angles. The NCS model (Fig. 5) has the shape of a parallelepiped with some test elements of the front. It can be moved along the horizontal axis. Two spotlights are mounted at this plate. The experimental chamber has two pairs of floodlights simulating front and back (behind the docking surface) bright lighting, respectively.

The parameters characterizing the stand geometrical configuration, yaw and roll angles do not coincide with parameters measured by the CVS. The transform formulas for geometrical parameters of the stand

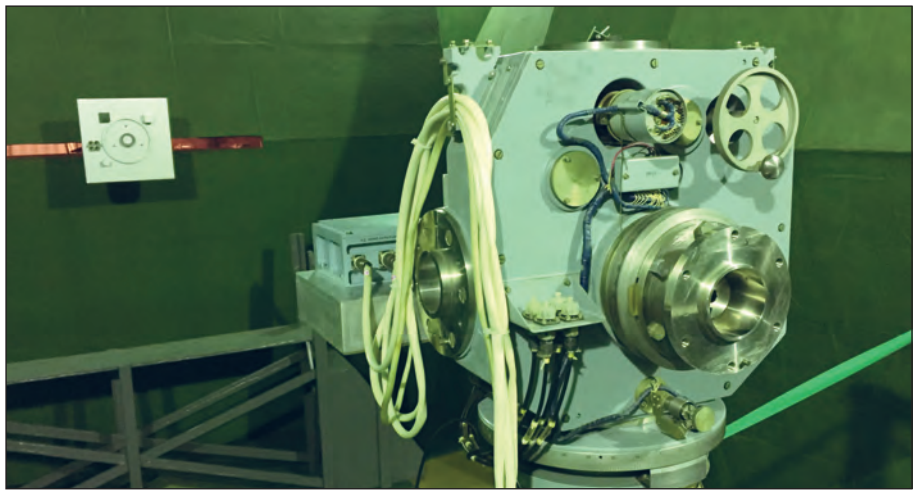

Fig. 3. The CVS experimental site

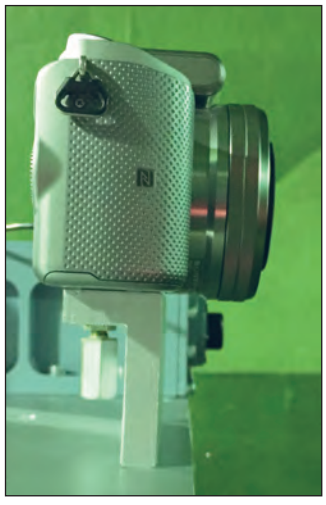

Fig. 4. Camera

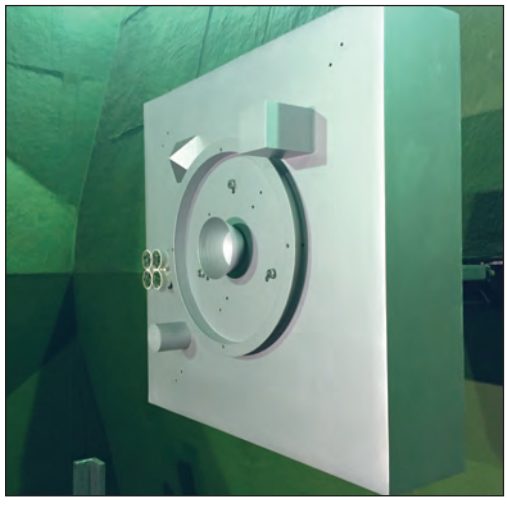

Fig. 5. NCS model

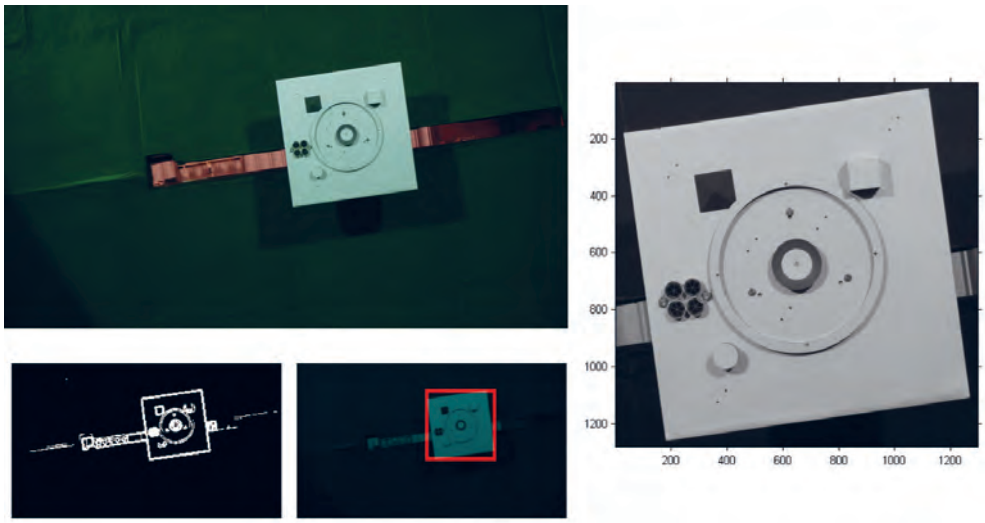

Fig. 6. ROI detection

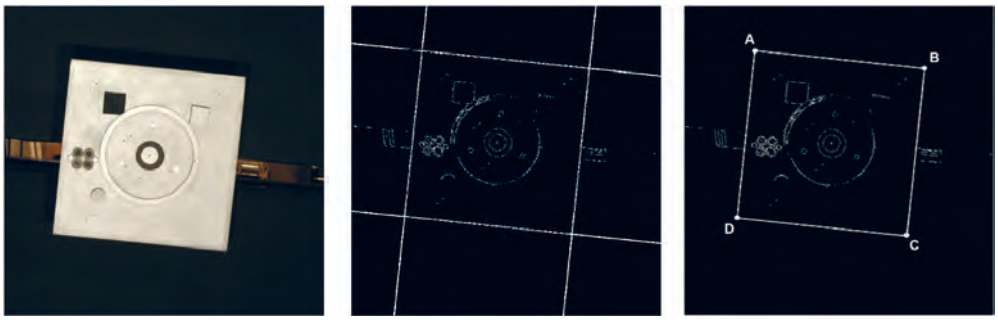

Fig. 7. Definition of reference points

and corresponding parameters measured by the CVS were obtained. These formulas are needed for obtaining the CVS accuracy characteristics during bench testing.

Bench testing

Verification the practical applicability of proposed mathematical, algorithm and software solutions were conducted in the series of bench test experiments. Several main and auxiliary problems were solved. Some of them are listed below.

Searching for the NCS image on the frame and defining the region of interest (ROI) for further analysis. The special search function over the image allows to find docking surface as a solid area with sharp boundaries. The input data for the program is a full frame. An output is a bounded rectangle. The result of the program work is shown in Fig. 6.

An original frame is shown on the top left of Fig. 6, the gradient of the image and the found area are depicted below. ROI, which will be used for further analysis, is depicted on the right.

Estimation position and attitude parameters of the NCS model relative to the camera. The docking surface corners were selected as reference points. They

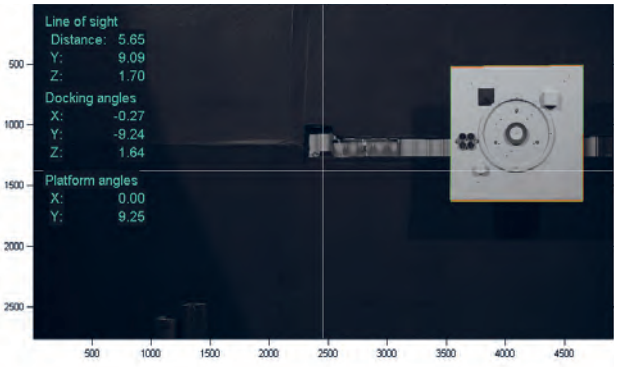

Fig. 8. Determining the position and attitude using obtained reference points

were defined and then recognized through Hough transform as points of border lines intersection.

The result of docking surface borders selection is shows in Fig. 7. The resulting binary image is used to determine straight border. The intersection of the obtained lines were used to determine the spatial positions of the docking surface with high accuracy.

The parameters of position and attitude of the NCS docking surface relative to the camera has been converted into the stand platform rotation angles. Estimations obtained were compared with the preset

stand rotation angles fixed with the stand control panel. The result of the comparison is shows in Fig. 8.

The estimated parameters are shown in Fig. 8 on the left at the image. Parameters 1–3 (under the heading Line of sight) define relative location: direction to the center of the NCS coordinate system and the distance to it. The first (Distance) corresponds to the Euclidean norm of vector position $\left\| t_1^1 \right\|$ and it is expressed in meters. The second and third parameters determine the sight line angles: the NCS model offset to the right and above the horizon. Their values are given in degrees. Parameters 4-6 (Docking angles) are Euler angles determining the attitude of the NCS relative to the camera. The last 2 parameters are calculated based on the parameters 1-6 and known camera position on platform. They denote estimates of the platform rotation angles. Here first value is the platform roll angle, the second one is the platform yaw angle. These values are measured from the coordinate system associated with the NCS model, so as it can be seen, the value of the roll angle of the platform will be almost equal to the roll angle of the NCS model relative to the camera, but with a sign minus. The same is with the platform yaw angle.

The CVS bench tests have confirmed the possibility of applying the proposed methods and technical solutions to meet the technical requirements.

Analysis, findings and conclusions

General schemes of the CVS formation and operation was proposed. An analysis of the potential opportunities to meet the requirements was conducted. A general solution scheme combines the flexible selection of a suitable algorithm based on the informative data that is extracted from each received image.

The proposed approach and methods constitute the main frame of the mathematical support and software of the CVS. General software architecture of the CVS is developed. The main challenges are identified and decomposed into separate tasks which are implemented in corresponding software modules. A number of critical places have been identified that require further research, development of methods, algorithms or software implementations.

The results of analysis, modeling and testing showed that realization of the proposed architecture, methods and procedures can ensure the functioning of the CVS with the required characteristics.

The ellipsoidal filtering algorithm which allows obtaining high-accuracy estimates of the attitude quaternion and the NCS angular velocity have been proposed. Additionally, some problems of motion control during rendezvous and docking have been considered. In particular, on the basis of Lyapunov method the method of control synthesis of translational and angular motion for docking stage was developed.

The bench testing showed an efficiency of software implementation and a perspective of the chosen approach to the solution.

REFERENCES

1. Gubarev V.F., Boyun V.P., Melnichuk S.V., Salnikov N.N., Simakov V.A., Godunok L.A., Komisarenko V.I., Dobrovolskyy V.Yu., Derkach S.V., Matviyenko S.A. Using Vision Systems for Determining the Parameters of Relative Motion of Spacecrafts. *Journal of Automation and Information Sciences*. 2016. Vol. 48, No. 11. P. 23–39. DOI: doi.org/10.1615/JAutomatInfScien.v48.i11.30.

2. Melnychuk S.V., Gubarev V.F., Salnikov N.N. Using information features in computer vision for 3D pose estimation in space. *Cybernetics and Computer Engineering*. 2017. No. 4. P.32–54. DOI: doi.org/10.15407/kvt.

3. Simakov V.A., Gubarev V.F., Melnichuk S.V., Salnikov N.N. Using videoimages for determining relative disposition of two spacecrafts. *Cybernetics and Computer Engineering*. 2016. Iss. 185. P. 35–47. DOI: doi.org/10.15407/kvt.

4. Gubarev V.F., Melnychuk S.V., Salnikov N.N. Ellipsoidal Pose Estimation of an Uncooperative Spacecraft from Video Image Data // in Control Systems: Theory and Applications. River Publishers Series in Automation, Control and Robotics, 2018. P. 169–195.

5. Salnikov N.N. On One Modification of Linear Regression Estimation Algorithm Using Ellipsoids. *Journal of Automation and Information Sciences*. 2012. Vol. 44, No. 3. P. 15–32.

6. Salnikov N.N. Estimation of State and Parameters of Dynamic System with the Use of Ellipsoids at the Lack of a Priori Information on Estimated Quantities. *Journal of Automation and Information Sciences*. 2014. Vol. 46, No. 4. P. 60–75.

7. Volosov V.V., Tyutyunnik L.I. Development and Analysis of Robust Algorithms for Guaranteed Ellipsoidal Estimation of a State of Multidimensional Linear Dynamical Systems. Part 1. *Problemy upravlenia i informatiki*. 1997. No. 4. P. 31–43 (*in Russian*).

8. Volosov V.V., Tyutyunnik L.I. Development and Analysis of Robust Algorithms for Guaranteed Ellipsoidal Estimation of a State of Multidimensional Linear Dynamical Systems/ Part 2. *Problemy upravlenia i informatiki*. 1997. No. 6. P. 52–65. (in Russian).

9. Volosov V.V., Tyutyunnik L.I. Synthesis of spacecraft attitude control algorithms using quaternions. *Space Science and Technology*. 1999. Vol.5, No. 4. P. 61–69 (*in Russian*).

10. Vasylyev V.V., Godunok L.A., Derkach S.V., Matviienko S.A. A stand for working out and testing of mutual measurement systems for the position of two spacecraft. *Space Sci. & Technol*. 2019. Vol. 25, No. 1. P. 3–13. DOI: doi.org/10.15407/knit2019.01.003(*in Russian*).

DESIGN FEATURES OF THE STEP-F PARTICLE DETECTOR AND THE SPHINX SOLAR X-RAY SPECTROPHOTOMETER AS SEEDS FOR REVEALING SOME PECULIAR PROPERTIES OF THE EARTH RADIATION BELTS

O. Dudnik[1], J. Sylwester[2], M. Kowaliński[2], P. Podgórski[2], H. Didenko[3], I. Zajtsevskiy[4], O. Perevertaylo[5]

[1] Institute of Radio Astronomy of NAS of Ukraine
[2] Space Research Centre of Polish Academy of Sciences
[3] Institute for Scintillation Materials of NAS of Ukraine
[4] Institute for Safety Problems of Nuclear Power Plants of NAS of Ukraine
[5] Scientific Production Company "Alex Detector" Limited Liability Company

The radiation belts of the Earth and the variations of high energy electron and proton fluxes in the magnetosphere are the targets for intensive exploration by the scientific community. Quickly grown number of artificial Earth satellites around the Earth supports the continuous improvement of the space weather forecast quality. As the charged space environment affects the wide aspects of human civilization, the sustained monitoring of energized elementary particles is an important current task. Different methods and sensors are developed to provide measurements of particle fluxes at Low Earth Orbits (LEOs), geostationary orbits, and in the interplanetary space [1]. Silicon PIN, solid-state, surface barrier detectors, organic and inorganic scintillation detectors, large area photodiodes, multi-pixelated silicon photomultipliers are among them. The gamma- and X-ray detectors are often used to study non-steady variations in magnetospheric particle fluxes because of a bremsstrahlung generation by precipitating of subrelativistic electrons present in the upper layers of the atmosphere. We present in this work an example of simultaneous registration of particle streams by direct method and via bremsstrahlung of magnetospheric electrons aboard the CORONAS-Photon LEO satellite.

The CORONAS-Photon satellite was launched in January 2009 to the circular orbit with an inclination ~83° and an altitude of about 550 km. Most of the payload was aimed at the study of a different manifestation of solar activity. The Satellite Telescope of Electrons and Protons STEP-F was intended to monitor the high energy charged particle fluxes. We present specific features in STEP-F constructing and in SphinX solar photometer in X-ray range that had been installed aboard the CORONAS-Photon satellite too [2]. The SphinX instrument in its last ADC channels was capable to detect the low and intermediate energy particle fluxes both directly and through bremsstrahlung of the primary electrons. The axes of the directivity of the STEP-F and SphinX were mutually orthogonal.

Specific features in the construction of both instruments allowed revealing some interesting phenomena in radiation belts during one year of a minimum of 11 year's cycle of solar activity [3]. We present some results of data processing such as detection of the three-belt spatial structure of electron fluxes, lower limits of the energies for particle registration by the SphinX X-ray spectrophotometer, new ideas about contours of the South Atlantic Anomaly according to STEP-F particle detector measurements.

Brief description of the STEP-F particle detector

Space experiment with the STEP-F instrument was aimed to study variations of high-energy electrons, protons, and α-particles in the radiation belts, in the South Atlantic magnetic Anomaly and outside of them during magnetospheric storms, and to study the connection between trapped and precipitating particles of magnetospheric origin with the solar proton events and solar cosmic rays [4].

STEP-F consists of the detector unit STEP-FD, mounted outside the pressurized section of the spacecraft, and the digital signal processing unit STEP-FE, located inside the pressurized compartment. The STEP-FD

a *b* *c* *d*

Fig. 1. A structural scheme of the detector head (*a*); the flight (*b*) and the breadboard (*c*) models of the STEP-F; the STEP-FD unit is among external detectors of the CORONAS-Photon satellite, as seen during vacuum tests (*d*)

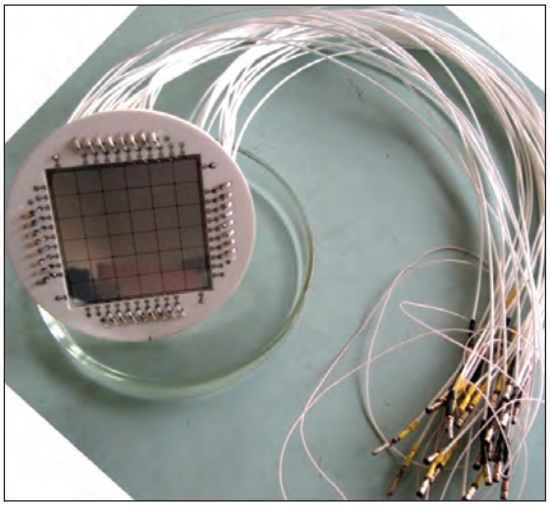

a

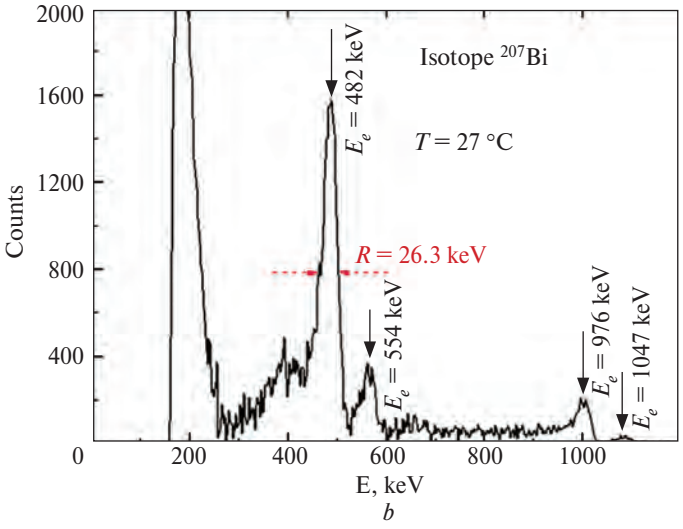

b

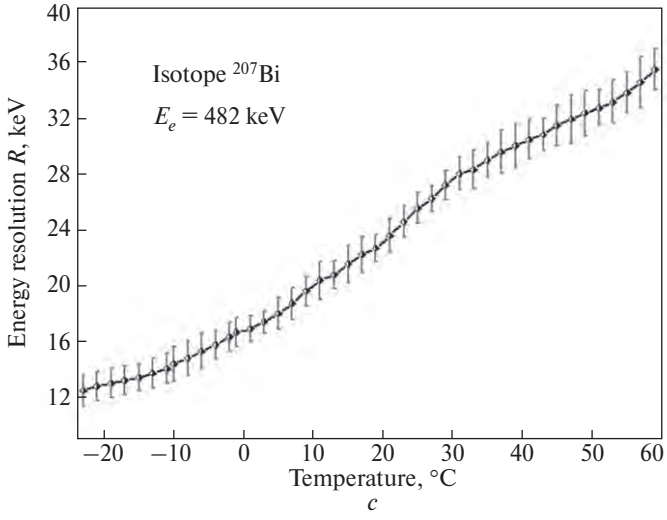

c

Fig. 2. The position-sensitive silicon matrix detector connected by soldering with thin coaxial cables outgoing from each matrix element (*a*); an example of the energy spectrum of conversion electron isotope source ^{207}Bi obtained from one matrix element at a fixed temperature (*b*); the energy resolution R of matrix element for the energetic line E_e = 482 keV of ^{207}Bi's β-particles vs temperature (*c*)

unit consists of the detector head and 69 channels of analog signal processing. Each of the channels comprises charge-sensitive preamplifiers (CSA) and shaping amplifiers. The detector head of STEP-FD is designed as a telescopic system. Fig. 1 represents a structural scheme, different models of the STEP-F instrument, and placement of the STEP-FD unit among other external units of the payload of CORONAS-Photon satellite during ground-based vacuum tests.

The detector head contains two identical silicon position-sensitive matrix detectors D1 and D2, each of them has an area of 45 × 45 mm^2 and a thickness of 380 micrometers, and two scintillation detectors based on a CsI(T1) single crystals viewed by the large area photodiodes in detector layer D3 and a vacuum

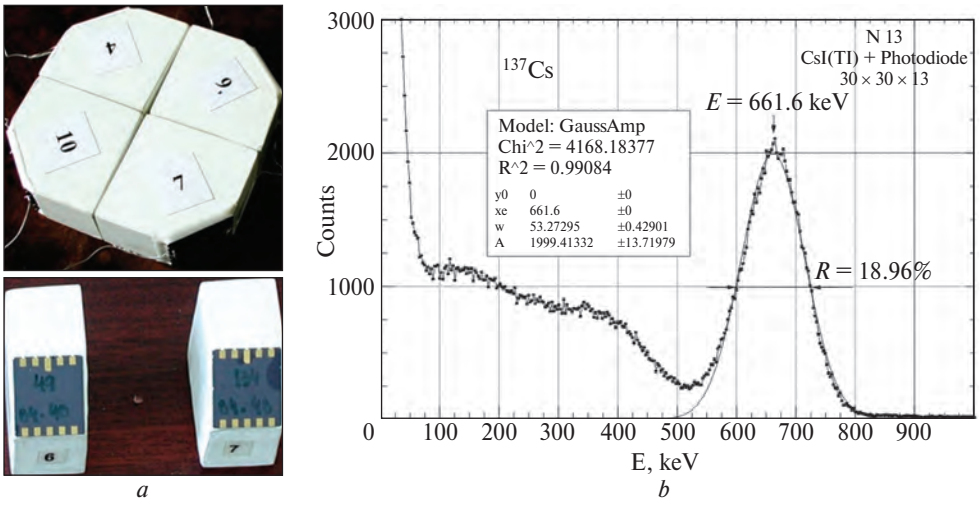

Fig. 3. Scintillation detectors coupled with the large-area silicon photodiodes (*a*); an example of ^{137}Cs isotope gamma-quanta energy spectrum obtained from CsI(Tl) detector (*b*)

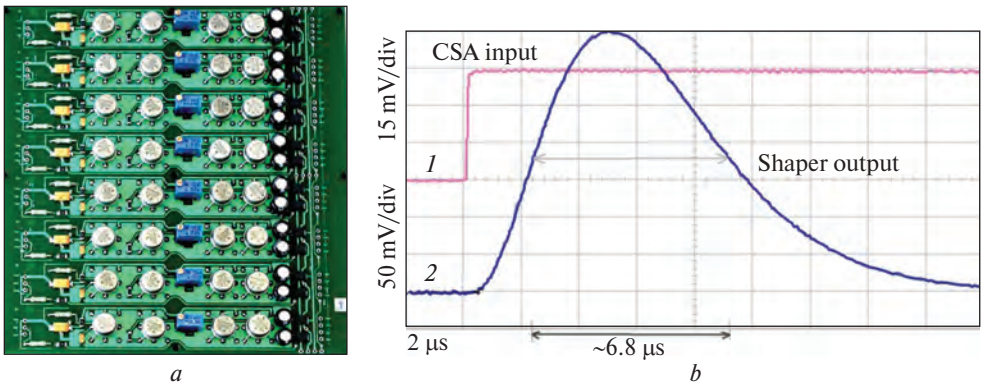

Fig. 4. A view of 8-channel' printed board of analog signal processing (*a*); the form of shaper' output quasi-gaussian signal as a response to step-like signal at the CSA test input (*b*)

photomultiplier in detector D4. The size of each of the 36 square elements of the silicon matrix detector is 7.3 × 7.3 mm^2, which yields an average angular resolution of about 8° in the general field of view of the telescope for high-energy particles. Fig. 2 represents a common view of position-sensitive silicon matrix detector, an example of resulting measurements of one selected matrix element with the isotope ^{207}Bi conversion β-particles, and the dependence of energy resolution for the energy $E = 482$ keV on the temperature.

In Fig. 3 it is shown a common view of CsI(Tl) single crystal scintillation detectors of the D3 layer coupled with the silicon PIN large area photodiode, and example of ^{137}Cs isotope gamma-quanta energy spectrum obtained from one of the D3 layer CsI(Tl) detectors.

Table 1 represents the energy ranges of registered electrons, protons and channels of mixed particle population.

Each element of the two silicon matrix detectors had their own analog signal processing channel. In total, 64 channels mounted on eight printed boards served 2 × 32 elements of matrices. In such a way we reached very high signal-to-noise, such that the total active area 20 cm^2 of D1 and D2 layer comprised electronic noises equivalent of one element with the area of 7.3 × 7.3 mm^2. The full width at half maximum (FWHM) of output from shapers' signals is of about 6.8 microseconds so that the upper limit of count rate for each element is at about $f \approx 150$ kHz. In Fig. 4 the 8-channel' printed board of analog signal processing is shown and the form of the output signal as a response to the test step-like signal is plotted.

The soft X-ray spectrophotometer SphinX

The structural scheme and a common view of the SphinX device are shown in Fig. 5. SphinX was equipped with four XR-100CR detectors provided by Amptek Inc., USA. These detectors were 500 μm thick, pure silicon PIN diodes with entrance windows covered with 12.7 μm thick beryllium foil. Each detector also had a temperature sensor, Peltier cooler, and FET transistor inside the package. Detectors

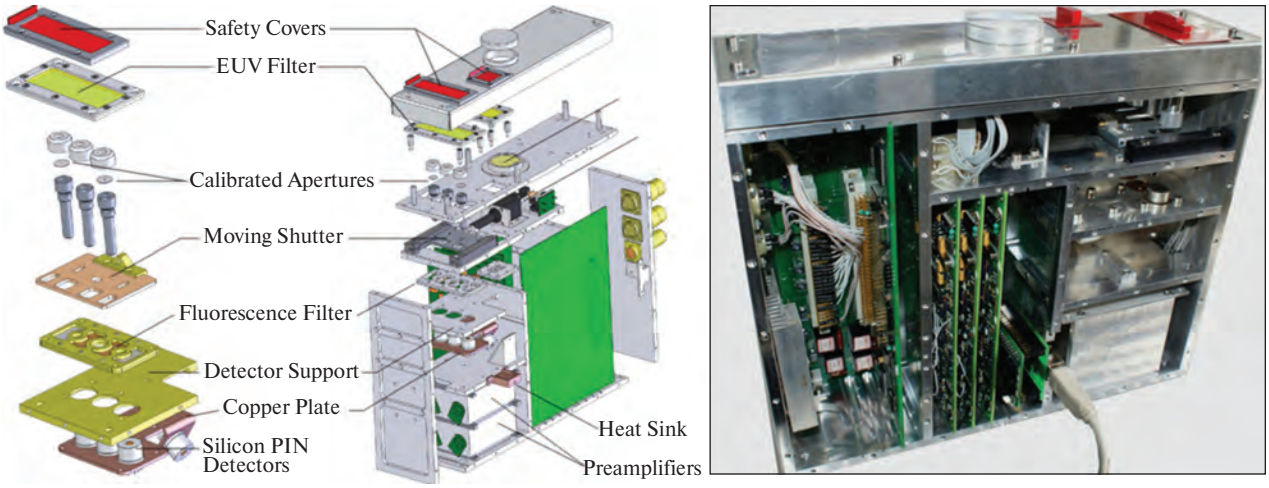

Fig. 5. Detailed structural scheme (*a*) and a common view of the soft solar X-ray spectrophotometer SphinX (b)

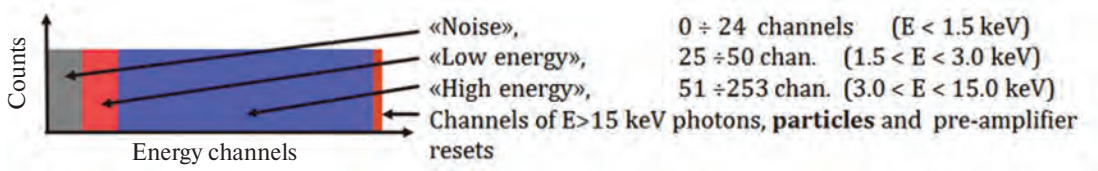

Fig. 6. Structure of information from SphinX in basic mode: 256-channel' energy spectra from D1 detector

were operated in flight at temperatures below −20 °C. Detector assembly came up with one detector (D1) of entrance aperture 21.50 mm^2 (the nominal factory entrance-window area), the second one (D2) with an aperture of 0.495 mm^2 for measuring moderate X-ray fluxes, and the third (D3) with an aperture of 0.01008 mm^2 for measurements of strong flux [5, 6].

Each measuring channel consisted of a detector, amplifier and shaper system whose output was read by an analog-to-digital converter and sent to an on-board computer. SphinX had spectral and event-counting modes of measurement. In the event-counting mode, every single pulse that appeared at the amplifier–shaper output was processed and information on the pulse amplitude and time of occurrence stored in memory. The pulse amplitude was converted to a channel number in the spectrometer's 256 channel space. Thus, all multichannel analyzers had 256 energy channels covering the nominal energy range of 0.0 – 15.0 keV.

Individual pulse-arrival times were determined with 1 μs accuracy. The pulses had different origins. The pulse amplitude was proportional to the photon energy. Pulses were also produced when energetic particles hit the detector's sensitive volume. Another source of pulses was the measurement channel electronics itself. It had to be reset every couple of seconds. After resets, additional pulses were produced at the amplifier's output. Many particle- and reset-originating pulses had a large amplitude and thus are seen in the last SphinX energy channel (bin 256), which allows one to identify them.

Table 1

Energy ranges of registered electrons and protons

Particle sort	Energy range [MeV]	Remark
Electrons	0.35 – 0.95 1.2 – 2.3 > 2.3	Provided by D2 silicon matrix detector and two first energy channels of D3 CsI(Tl) scintillator
Protons	7.4 – 10.0; 15.6 – 55.2 in 9 channels; > 55.2	Provided by D2 silicon matrix detector and 10 energy channels of D3 CsI(Tl) scintillator
Electrons + protons	0.18 – 0.51 (electrons) + 3.5 – 3.7 (protons)	Channel of mixed particle registration
Electrons + protons	0.55 – 0.95 (electrons) + 3.7 – 7.4 (protons)	Channel of mixed particle registration

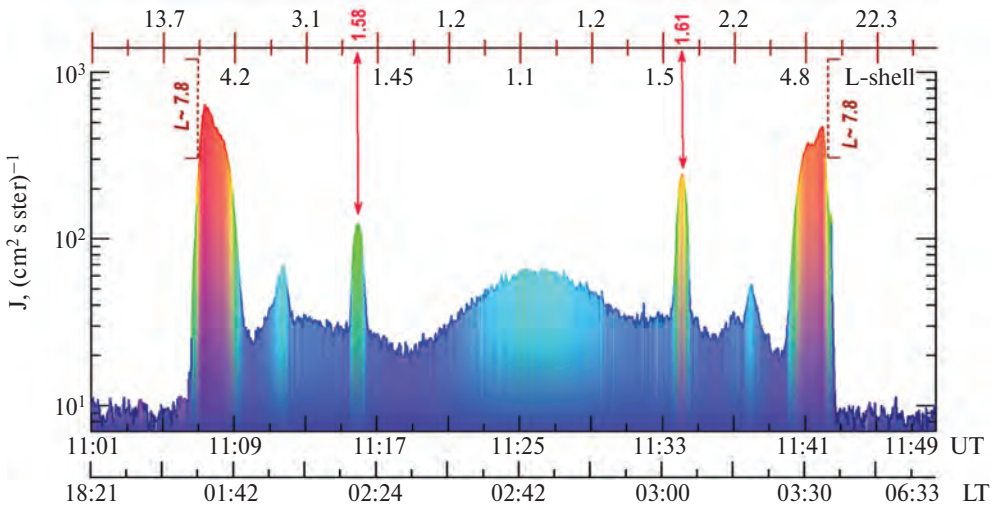

Fig. 7. Particle flux in the 1st channel of mixed particle registration (see Table 1) on May 6, 2009 on the ascending ascending part of the satellite orbit. UT is universal time; LT is local time

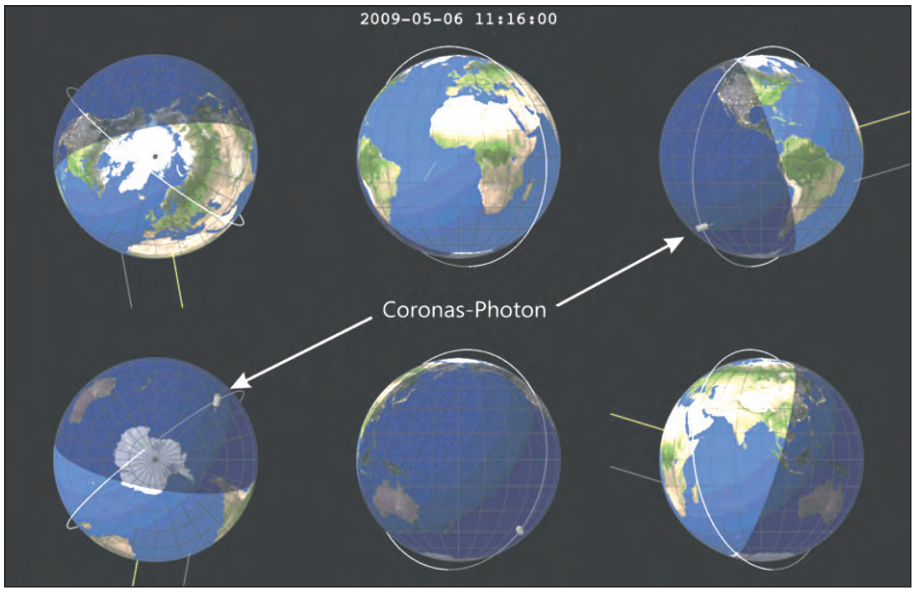

Fig. 8. Satellite position at the time of registration of the 3rd electron belt on May 6 in the Southern hemisphere

During the mission, SphinX recorded 256-channel and ancillary broadband, 4-channel spectra (so-called basic mode spectra). The first channel of the basic mode spectra contains mainly electronic noise. In the second and third channels solar X-ray flux was recorded in the energy ranges 1.5–3.0 keV and 3.0–14.9 keV for the D1 detector and 1.0–3.0 keV and 3.0–14.9 keV for the other detectors. The last channel of the basic mode contains the events caused by energetic particles and the instrument resets (Fig. 6).

Some selected results of the data processing

Possessing high sensitivity to low particle fluxes the STEP-F instrument detected in 2009 a three belt's structure of electron fluxes in the channel of mixed particle registration (see Table 1). Fig. 7 represents data on electron fluxes in the energy range 180 keV ≤ E_e ≤ 510 keV with 2-seconds' temporal resolution collected on the one of 15 ascending parts of the satellite orbit covering latitude range from – 82.5° South to + 82.5° North on May 6, 2009. Satellite crossed Van Allen outer and inner radiation belts in both hemispheres at the longitude range out from the South Atlantic magnetic Anomaly. Fig. 7 reveals presence of the third, additional belt being crossed by the satellite at $L \approx 1.58$ in Southern hemisphere, and at $L \approx 1.61$ in the Northern hemisphere. It is clearly seen that there is no vanishing quantity of low energy electrons within the magnetosphere at $L \leq 7.8$ into whole latitude span, while the background fluxes of the particles outside the closed lines of geomagnetic field is less 3—6 times.

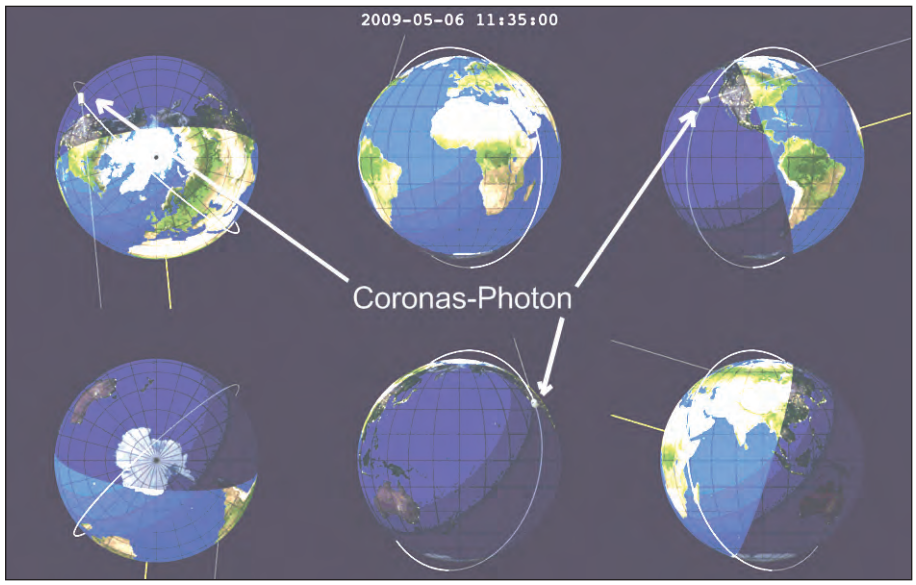

Fig. 9. Satellite position at the time of registration of the 3rd electron belt on May 6 in the Northern hemisphere

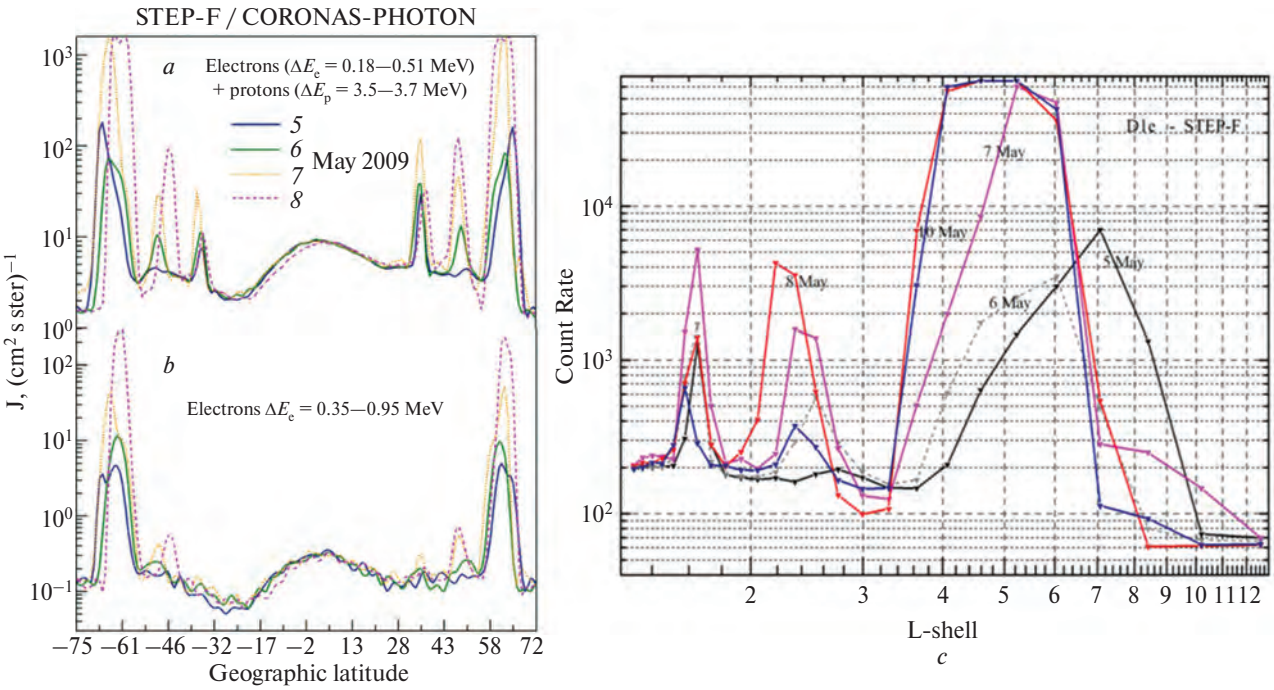

Fig. 10. Particle fluxes in the channel of mixed particle registration (*a*) and in the electron channel of energies ΔE = = 0.35—0.95 MeV (*b*) over the period of 5—10 May 2009. Different colors / lines represent individual days as indicated. (*c*) is distribution of particle fluxes by McIlwain *L*-shells

Fig. 8 and Fig. 9 demonstrate satellite position at the times of registration the 3rd, additional inner electron radiation belt at $L \approx 1.6$ in both hemispheres during the low solar and geomagnetic activity of May 2009. Each frame consists of 6 views. From the left to right a view from the North Pole and at Equatorial plane at 0 and 180 degrees of the longitudes is shown on the top raw. The view from the South Pole and at Equatorial plane at 90 and 270 degrees of the longitudes is shown on the lower series from the left to right too. As it can be seen from both Figures the additional inner electron radiation belt was observed at nighttime of the LT, far from the South Atlantic Anomaly zone.

Fig. 10 represents data with 30-seconds' temporal resolution collected on every 9th ascending parts of satellite orbit over the period from May 5 to May 10, 2009. Also, Fig. 10 reveals presence and stability of the registration of the third, additional inner belt being crossed by the satellite at −35÷−32 degrees South, and at ~36÷42 degrees North.

The persistent presence of the third belt on lower L-shell and the temporal variation of electron population in both belts are observed depending on the overall level of geomagnetic activity.

The two inner radiation belts on $L \approx 2.28$, and $L \approx 1.61$ were detected in the energy band $\Delta E_e = 0.18 \div 0.51$ MeV, the other particle channels did not confirm the fact of presence of the new belt. It can be concluded that the narrow belt at $L \approx 1.6$ is populated by the particles with energies not higher than 0.5 MeV.

Both inner radiation belts are seen on geographical longitudes that do not coincide with the South Atlantic Anomaly longitudes.

We carried out the comparison of the data extracted from the highest ADC channel of the SphinX spectrophotometer with the STEP-F recordings. As a result, Det1 and Det2 detectors of SphinX are sensitive to electrons and the secondary γ-quanta, generated by the magnetospheric high energy electrons. The latter allowed us to introduce the concept of effective lower energy thresholds for electron registration (E_{thr1} and E_{thr2}) by Det1 and Det2 detectors, respectively.

The analysis of averaged over 14 days of May 2009 L-shell values with maximum particle count rates vs. electron energy allowed us to determine values of effective lower threshold energies E_{thr1} and E_{thr2}. We determined also the lower threshold energy of the D4e channel, where D4 is the bottom-most scintillation detector of the STEP-F instrument' detector head. In Fig. 11 it is shown a dependence of L-shells with the largest particle fluxes, as a function of the electron energy for the South Atlantic Anomaly region. As a basic point the energies of D2e (electrons with energies $E_e = 0.35 \div 0.95$ MeV) and D1p (electrons with energies $E_e = 0.55 \div 0.95$ MeV + + protons with energies $E_p = 3.7 \div 7.4$ MeV) energy channels of STEP-F were chosen.

Fig. 11 demonstrates that the values of E_{thr1} and E_{thr2} are closely near, assumed values ~ 500 keV and ~475 keV for Det1 and Det2 of SphinX, respectively. Large dispersion of these values is determined by a poor

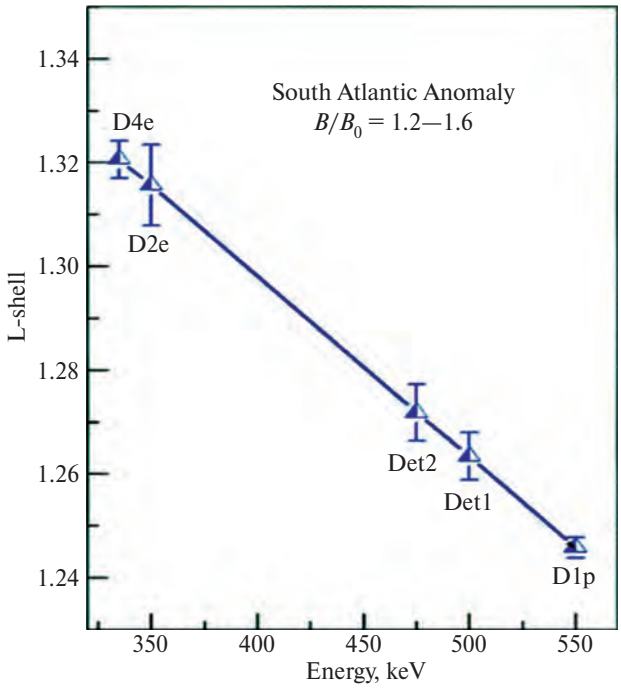

Fig. 11. Dependence of averaged L-shell values corresponding to maximum electron flux densities on the particle energy

statistic (14 days analyzed), from one side, and by the diurnal displacement of the satellite position on the longitude at fixed latitude relative to the initial day.

The bottom threshold energy of the D4e channel of STEP-F device is $E_{D4e} \approx 335$ keV as can be seen in Fig. 11. E_{D4e} values varied from day to day in the energy range from 230 to 350 keV during May 1—14, 2009, probably due to variation of electron energy spectrum slope.

Contours of the South Atlantic Anomaly as seen by STEP-F

The CORONAS-Photon orbit crosses all longitudes between ± 82° 15 times during the diurnal period. This allowed us to construct daily maps of the particle content at the height of ~550 km in terms of high energy charged particle fluxes. Such an approach for

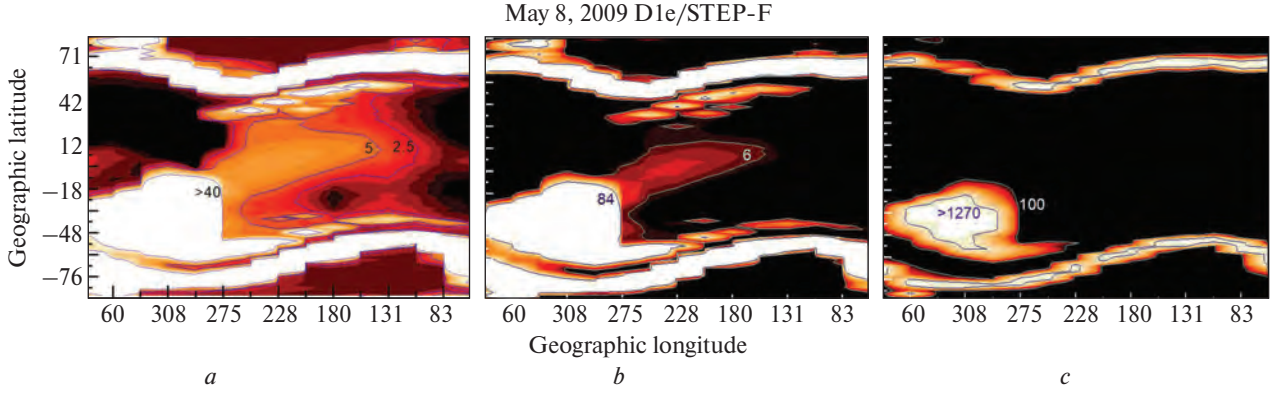

Fig. 12. A view of the SAA and radiation belts as seen by STEP-F in various intensity ranges. Explanations are given in the text

the electrons in the energy range $\Delta E_e = 0.18 \div 0.51$ MeV gave us the possibility to see the contours of the South Atlantic Anomaly having in mind high sensitivity of STEP-F to extremely low particle fluxes and the binding of the particle trajectories to the geomagnetic field lines.

Results of the 1st channel of mixed particle registration (see Table 1) data processing applied for May 8, 2009, are shown in Figure 12. The three maps in a shade of red are presented for particle intensity limits from 1 to 40 (Fig. 12, *a*), from 5 to 100 (Fig. 12, *b*) and from 100 to 1500 (Fig. 12, *c*) electrons / cm^2 s sr.

The higher the strength of the geomagnetic field in the region of the SAA, the more precipitating electrons are recorded by the STEP-F (Fig. 12, *c*). But negligible fluxes of precipitating particles are seen in the near equator zones up to projections of inner radiation belts onto altitude of the satellite trajectory in the northern hemisphere in a wide range of geographic longitudes from ~120 to ~275 degrees (Fig. 12, *a*). Whereas the azimuthal drift of electrons according to the 3rd adiabatic invariant it is envisaged that the SAA dimensions are much larger in comparison with the current classical concept.

Conclusions

1. Specific uncommon technical solutions adopted in the construction of the Satellite Telescope of Electrons and Protons STEP-F and the solar soft X-ray spectrophotometer SphinX allowed finding out some new patterns in the behavior of the high energy charged particles of the magnetospheric origin. Particularly, the utilization of silicon matrix-type configuration in the first two detecting layers of the STEP-F detector head allowed reaching a very high signal to noise ratio. This led to the detection of very weak particle fluxes outside of the regions of Van Allen outer and inner radiation belts and SAA including low latitudes and near-equatorial zone. Recording of the scientific information in the SphinX' spectral mode allowed finding extremely useful data in the last channel of the energy spectra on the variations of low and intermediate energies particles in the Earth's magnetosphere. Cross-analysis of data derived from both instruments led to estimating of the effective lower energy thresholds for primary particles seen by the SphinX sensors in the last ADC channel.

2. Specific features in the design of both space-borne based instruments enabled us to reveal the existence of new (third) steady electron radiation belts located below the Van Allen electron inner belt, on $L \approx 1.6$ for particle energies $E \leq 500$ keV, with significantly varying particle fluxes in response to a weak substorm in the magnetosphere. New ideas about dimensions of the South Atlantic Anomaly through the STEP-F particle detector measurements have been developed.

REFERENCES

1. Dudnik O. Radiation environment at Low Earth Orbits. *Consultations on modelling and analysis of orbital background in X-ray detectors*. September 19–20, 2019. Wroclaw, Poland. Programme. http://www.cbk.pan.wroc.pl//conferences/meeting_2019/meeting_2019.html.

2. Dudnik O.V., Sylwester J., Kowaliński M., Barylak J. Utilization of design features of the particle telescope STEP-F and solar x-ray spectrophotometer SphinX for exploration of the Earth's radiation belt properties. *Proceedings SPIE*. 2019. Vol. 11176 "Photonics Applications in Astronomy, Communications, Industry, and High-Energy Physics Experiments". P. 111763L-1–111763L-10. https://doi.org/10.1117/12.2537296.

3. Dudnik O.V., Sylwester J., Podgórski P. Combined study of radiation belts by the satellite particle telescope STEP-F and solar soft X-ray photometer SphinX during recent deep minimum of solar activity. *Proceedings of 23rd National Slovak Solar Physics Meeting*. Liptovský Mikuláљ, Slovakia, 30 May – 3 June, 2016. ISBN 978-80-85221-92-3 (on DVDs). Publisher: Slovak central observatory, Hurbanovo. P. 1–6.

4. Dudnik O.V., Persikov V.K., Zalyubovsky I.I., Timakova T.G., Kurbatov E.V., Kotov Yu.D., Yurov V.N. High-sensitivity STEP-F spectrometer–telescope for high-energy particles of the CORONAS-PHOTON satellite experiment. *Solar System Research*. 2011. Vol. 45, Iss. 3, P. 212–220. https://doi.org/10.1134/S0038094611020043.

5. Gburek S., Sylwester J., Kowalinski M., Bakala J., Kordylewski Z., Podgorski P., Plocieniak P., et al. SphinX soft X-ray spectrophotometer: science objectives, design and performance. 2011. *Solar System Research*. Vol. 45, Iss. 3, P. 189–199. https://doi.org/10.1134/S003809461102006.

6. Gburek S., Sylwester J., Kowalinski M., Bakala J., Kordylewski Z., Podgorski P., Plocieniak S., et al. SphinX: The Solar Photometer in X-Rays. *Solar Physics*. 2013. Vol. 283, Iss. 2. P. 631–649. https://doi.org/10.1007/s11207-012-0201-8.

LIST OF IMPLEMENTING ORGANIZATIONS

No.	Organization	E-mail
1	Educational and Scientific Center "Institute of Biology and Medicine" of Taras Shevchenko National University of Kyiv	decanat_bf@univ.kiev.ua
2	Institute for Scintillation Materials of NAS of Ukraine	info@isma.kharkov.ua
3	Institute for Safety Problems of Nuclear Power Plants of NAS of Ukraine	ispnpp@ispnpp.kiev.ua
4	Institute of Ecology of the Carpathians of NAS of Ukraine	ecoinst@mail.lviv.ua
5	Institute of Food Biotechnology and Genomics of NAS of Ukraine	office.ifbg@nas.gov.ua
6	Institute of Ionosphere of NAS and MES of Ukraine	iion@kpi.kharkov.ua
7	Institute of Radio Astronomy of NAS of Ukraine	rai@ri.kharkov.ua
8	Institute of Technical Mechanics of NAS of Ukraine and SSA of Ukraine	office.itm@nas.gov.ua
9	Karpenko Physico-Mechanical Institute of NAS of Ukraine	pminasu@ipm.lviv.ua
10	Lviv Center of Space Research Institute of NAS and SSA of Ukraine	vakor@isr.lviv.ua
11	M.G. Kholodny Institute of Botany of NAS of Ukraine	inst@botany.kiev.ua
12	M.M. Gryshko National Botanical Garden of NAS of Ukraine	nbg@nbg.kiev.ua
13	Main Astronomical Observatory of NAS of Ukraine	office.mao.kiev.ua
14	Main Center of Special Monitoring, National Space Facilities Control And Test Center	ncuvkz@spacecenter.gov.ua
15	National Aerospace University "Kharkiv Aviation Institute"	khai@khai.edu
16	National Aviation University	post@nau.edu.ua
17	National Space Facilities Control and Test Center	ncuvkz@spacecenter.gov.ua
18	National Technical University of Ukraine "Igor Sikorsky Kyiv Polytechnic Institute"	mail@kpi.ua
19	Oleksandr Dovzhenko Hlukhiv National pedagogical university	gnpuoffice@gmail.com
20	Palladin Institute of Biochemistry of NAS of Ukraine	secretar@biochem.kiev.ua
21	Poltava Gravimetric Observatory of Institute of Geophysics of NAS of Ukraine	pgo@poltava.ukrtel.net
22	Private Joint Stock Company "Research and Production Complex "KURS"	npk_kurs@ukr.net
23	Private Joint Stock Company "ELMIZ"	info@elmiz.com
24	Scientific Production Company "Alex Detector" LLC	konstructor_a@ukr.net
25	Space Research Institute of NAS of Ukraine and SSA of Ukraine	ikd@ikd.kiev.ua
26	State Institution "Scientific Centre for Aerospace Research of the Earth of Institute of Geological Sciences of NAS of Ukraine"	casre@casre.kiev.ua
27	Taras Shevchenko National University of Kyiv	rector@univ.net.ua
28	V.N. Karazin Kharkiv National University	univer@karazin.ua
29	V.N. Karazin Kharkiv National University, Institute of Astronomy	sky@astron.kharkov.ua

Звіт для COSPAR узагальнює результати космічних досліджень, проведених протягом 2018—2020 років. У цьому виданні представлено сучасний стан української космічної науки за такими напрямами: космічна астрономія та астрофізика, спостереження Землі та навколоземні космічні дослідження, науки про життя, космічні технології та науки про матеріали. Низку робіт присвячено створенню наукового обладнання для перспективних космічних місій. Значну увагу приділено прикладним дослідженням космічного моніторингу Землі. Видання може бути корисним для широкого кола читачів, які цікавляться космічними дослідженнями.

Наукове видання

НАЦІОНАЛЬНА АКАДЕМІЯ НАУК УКРАЇНИ

КОСМІЧНІ ДОСЛІДЖЕННЯ В УКРАЇНІ 2018—2020

Звіт підготовлений
Інститутом космічних досліджень
НАН України та ДКА України

Англійською мовою

Науковий редактор
ФЕДОРОВ Олег Павлович

Художнє оформлення
Є.О. Ільницького
Технічний редактор
Т.М. Шендерович
Комп'ютерна верстка
О.А. Бурдік

Підписано до друку 25.01.2021. Формат 60 × 84/8.
Ум. друк. арк. 17,75. Обл.-вид. арк. 22,84.
Тираж 50 прим. Зам. № 6215

Видавець і виготовлювач
Видавничий дім «Академперіодика» НАН України
01004, Київ-4, вул. Терещенківська,4

Свідоцтво про внесення до державного реєстру суб'єктів
видавничої справи серії ДК № 544 від 27.07.2001 р.